THE UNIVERSITY *of* EDINBURGH

Testing theories of Large Scale Structure Formation and Growth using Galaxy Surveys

Qianjun Hang

Doctor of Philosophy
The University of Edinburgh
May 2021

Lay summary

Cosmology is the study of the origin and evolution of the Universe as a whole. Although a seemly daunting question to ask, we now have a pretty good understanding about the history of the Universe thanks to profound theoretical insights and breathtaking observational evidence. The Universe started from a Big Bang about 13.8 billion years ago. At its early times, the Universe was extremely hot, dense, and uniform with only tiny fluctuations generated by quantum interactions. This is supported by the detection of the *Cosmic microwave background* radiation (CMB), the afterglow of the Big Bang. Then, the Universe expanded and cooled, while those fluctuations grew under the attraction of gravity, eventually becoming the *large-scale structures* of the Universe. When the temperature became sufficiently low, stars and galaxies formed within these structures, leading to the observable Universe today. There are three main contents of the Universe. The particles that make up the surrounding materials such as ourselves, baryons, only takes up 5% of the total content. The rest of the Universe is *dark*. Observations of distant supernovae suggest that the expansion of the Universe is accelerating, yielding 70% of the content to be the repulsive *dark energy*. Studies of galaxy rotation curves and clusters of galaxies require that as much as 80% of the total matter is *dark matter*, a particle beyond our current knowledge that only interacts gravitationally.

The success of this ΛCDM *model* in explaining a spectrum of independent observations is in fact a slightly awkward case. We do not know anything about dark energy and dark matter! Dark energy is supposed to arise from vacuum. Similar to boiling water, the vacuum is actually full of 'bubbles' of particle-antiparticle pairs that are instantaneously created and annihilated. The resultant vacuum energy, according to quantum theory calculations, is 100 orders of magnitude larger than what is required by the cosmological model. On the other hand, the search for dark matter has been carried out extensively by particle

physicists but to no avail. It is thus speculated that our understanding of the cosmological model is not complete, and alternative models have been proposed, for example, modifications to the theory of gravity. These models, although designed to reproduce the observed cosmos today, often alter the formation and evolution history of the large-scale structures. The focus of this thesis is to test the theory of cosmic structure formation using large galaxy surveys.

One of the probes of structure formation is *redshift-space distortions*. Very much analogous to the case where one can infer the speed of an ambulance by the pitch change of the siren, the recession speed of a galaxy due to the expansion of the Universe can be inferred by the frequency change of its emitted light, or the *redshift*. We can convert the redshifts into distances, hence study the large-scale structures by the spatial distribution of the galaxies. However, this is not entirely correct, because galaxies can have additional velocities, called *peculiar velocities*. This additional component distorts the observed spatial distribution. On large scales (at least 1000 times the size of the milky way), peculiar velocities are directly related to the *growth rate* of large-scale structures: galaxies fall into the gravitational potential generated by these structures. In Chapter 2, I use this effect to measure the growth rate using the GAMA survey [168], and show that it is consistent with the consensus cosmology. Specifically, I showcase the consistency of this measurement using different types of galaxies and galaxy groups.

Structure formation also generates specific features on the CMB. One such feature is *gravitational lensing*, the bending of light due to gravity. The effect is a small distortion of the CMB image, in a way similar to looking at it through an uneven glass. Another feature, the *Integrated Sachs-Wolfe* (ISW) effect, is present at recent epoch when dark energy started to dominate. In this effect, the gravitational potential generated by large-scale structures evolves with time, causing a net change in the CMB photon energy via gravitational redshift. These small imprints can be measured statistically by *cross-correlation* of the galaxy density and the CMB, thus providing a test for the ΛCDM model. In Chapter 5, I carry out this measurement using galaxies from the DESI Legacy Survey [68] and the CMB maps from the *Planck* Collaboration [226, 228]. While I find an ISW signal consistent with theoretical expectation, the lensing signal is significantly lower. In combination with other lensing results, this points to a possible tension within the ΛCDM paradigm.

Superstructures, the most dense and empty regions of the Universe, are also

fascinating objects for studying structure formation. Recently, a number of works on supervoids claim an excess ISW signal that is several times the prediction of the standard model. Such discrepancy, if real, can be a compelling evidence for non-standard dark energy. To test these claims, I construct a catalogue of superclusters and supervoids using the DESI Legacy Survey, and measure the stacked CMB lensing and ISW signals at centres of these superstructures. In Chapter 6, I show that, by comparison with a cosmological simulation, no excess ISW signal is observed. The claimed signal is thus likely overestimated due to selection and statistical fluctuation, often referred to as the look-elsewhere effect.

The interesting tension between the lensing measurements and the CMB shown in this work and other literature will need more evidence to be resolved. Luckily, a number of next generation galaxy surveys are underway, including DESI, LSST, Euclid, and the CMB Stage 4 experiments. These high precision experiments, covering large sky area and reaching incredible depth, will soon open up an unprecedented view of the Universe that would allow us to further test and fill in the missing pieces for the cosmological model.

Abstract

The distribution of galaxies in the Universe is not random: rather, galaxies cluster in a structured way. The formation and growth of these large-scale structures (LSS) provides powerful dynamical probes for cosmology. This thesis explores two of these probes, namely redshift-space distortion (RSD) and the imprints of LSS on the Cosmic Microwave Background (CMB). Using galaxy surveys, I test the theory of structure growth in the context of the ΛCDM cosmological model.

RSD probes the velocity field of LSS, which is influenced by the growth of matter fluctuations. I use the galaxy and group catalogues in GAMA survey to test the robustness of RSD in recovering unbiased growth rate $f\sigma_8$ with different tracers. Specifically, galaxies are split into red and blue subsamples, and groups are divided into three stellar mass bins. The 2D group-galaxy cross-correlation function between these subsamples are interpreted by a linear model and a small-scale Finger of God convolution. Given an appropriate minimum fitting scale, I show that the subsamples give consistent growth rate, $f\sigma_8 = 0.25 \pm 0.15$, also in agreement with the *Planck* 2018 results.

The imprints of LSS on the CMB correspond to the effects of weak gravitational lensing and the Integrated Sachs-Wolfe (ISW) effect. I measure these effects using the public DESI Legacy Survey, exploiting its large sky coverage and substantial depth for tomographic studies. After careful selection of galaxies and correction for various systematic effects, I assign photometric redshifts to galaxies based on $g - r$, $r - z$, and $z - W_1$ colours, and construct four tomographic redshift bins in $0 < z < 0.8$. The photo-z errors are accounted for using the galaxy auto- and cross-correlations between these redshift bins.

Having a clean galaxy sample, I measure the cross-correlation C_ℓ between the galaxy density fields and the *Planck* CMB temperature and lensing convergence maps. The amplitudes of these measurements relative to the ΛCDM prediction

using the fiducial *Planck* 2018 best-fit cosmology are $A_\kappa = 0.901 \pm 0.026$ and $A_{\rm ISW} = 0.98 \pm 0.35$. While the ISW result is consistent with the fiducial cosmology, the CMB lensing result is noticeably lower. This low amplitude is interpreted in terms of a lower Ω_m in combination with the total CMB lensing constraints.

Finally, to address the excess stacked ISW signal from supervoids claimed in literature, I construct a superstructure catalogue using the four tomographic bins in the DESI Legacy Survey, and measure their stacked CMB lensing and ISW signals. The results are compared to the ΛCDM prediction from a mock catalogue that is based on N-body simulations and carefully matched to the data. I find a similar discrepancy in the lensing amplitude as in the cross-correlation scenario. Here, it is mainly contributed by density peaks at the higher redshift end. I also show that the detection of ISW signal from superstructure stacking is only mild, but is consistent with the ΛCDM prediction with a 95% upper limit of $A_{\rm ISW} = 1.51$ using the full sample. Testing a range of superstructure subsamples, I demonstrate that the claimed excess signal may be due to look-elsewhere effect.

Declaration

I declare that this thesis was composed by myself, that the work contained herein is my own except where explicitly stated otherwise in the text, and that this work has not been submitted for any other degree or professional qualification except as specified. In particular, Section 5.2.5-5.2.7 were composed by John Peacock and Shadab Alam, the authors on the paper in which Chapter 5 was published. I reproduce these sections in this thesis as to maintain the clarity of discussion from that work. The mock catalogue used in Chapter 6 and the lensing convergence map are produced by Shadab Alam, and the ISW maps are produced by Yan-Chuan Cai. The corresponding descriptions in Chapter 6 are composed by these authors. This part is included to maintain the clarity of this work.

Part of Chapter 3, the entirety of Chapter 4 & 5 of this work have been published in [114].

(*Qianjun Hang, May 2021*)

Acknowledgements

I would like to first thank my supervisors, John Peacock, Shadab Alam, and Yan-Chuan Cai, with all my heart. During the past four years, they have always supported and guided me with enormous patience and care, in both my academic development and personal well-being. I have greatly enjoyed and will definitely miss the inspiring discussions and critical opinions on those Tuesday morning meetings. It is truly a pleasure to learn from and work with them. I would also like to thank my examiners: Florian Beutler and Blake Sherwin, for reading through my thesis with great patience and giving many constructive comments.

To my beloved mum, dad, and grandparents: thank you for your unconditional love, support, and encouragement along the journey. You have taught me to take an interest in everything, and never be afraid of failing. Especially, I am grateful and proud that I can always share my thoughts and get the best advice from my mother like a great friend. I would also like to extend my gratitude to Perry Wang (and his wonderful family); although it is a four-and-half-hour train journey from London to Edinburgh, your visits and companion from time to time have always recharged me for my PhD life.

I would also like to thank my PhD comrades at the IfA: Rohit Kondapally, Dylan Robson, Niall Whiteford, Marios Kalomenopoulos, Qianli Xia, Amanda Ibsen, Lara Alegre, Gennaro Di Pietro, Aaron Bradley, and Ben Moews (names are ordered by the distance from my office). Whether it was over a cup of coffee in the IfA kitchen, or on the way back from work, chatting with you has always brought me a great deal of encouragement and happiness. Special thanks to my officemates: Jaime Villasenor and Andrea Incatasciato for help watering my cactus (and also being great officemates, of course). My PhD life in Edinburgh is not complete without the amazing kendo clubs; all the sweating practices as well as heartwarming friendships are very much appreciated.

It has been an unusual and life-changing year for the most of us as the globe has been hit by the Coronavirus. There are many people who have risked their own lives to save others, or have devoted enormous efforts in developing the vaccine during the last one-and-a-half year. Therefore, lastly, I would like to dedicate my sincerest gratitude and respect to those who have fought or are still fighting on the frontline against COVID-19 during this on-going global pandemic.

Contents

List of Figures

List of Tables

Chapter 1

Background in Cosmology

Cosmology is perhaps the scientific field that concerns the biggest subject of all: the Universe. During the past century or so, we have established a decent model to describe of how the Universe has begun and evolved to what it looks like today. In this Chapter, I will give a brief introduction to the standard cosmological model and set up the background necessary for the rest of the thesis. I will start with a brief overview of General Relativity, the fundamental framework use in cosmology, in Section 1.1. Then, with a few general assumptions, we will see that the evolution of the Universe on large scales is well described by the Friedmann-Robertson-Walker (FRW) metric with a time-dependent expansion factor in Section 1.2. As we go to smaller scales, these assumptions break down, allowing structures to form in the Universe. I will describe in Section 1.3 how these small perturbations grow and evolve under gravity before they collapse to form haloes and galaxies, and how these structures can be related to the observables in modern cosmological studies. This altogether establishes the standard ΛCDM model, which allows us to describe the Universe quite precisely with only seven parameters. However, the model has two unknown contents that are suggested by its name, dark energy (Λ) and cold dark matter (CDM), and they happen to make up most of the Universe. A few main cosmological probes are listed in Section 1.4, providing almost consistent constraints on these parameters. Interestingly, tension between some of these parameter has also started to emerge, as I will briefly discuss in Section 1.5. Finally, I will mention the statistical tools used in cosmological analysis in Section 1.6, before ending this Chapter by giving a brief outline for this thesis in Section 1.7.

1.1 The Framework of General Relativity

General Relativity is one of the greatest discoveries in physics, because it introduces the important notion that the Nature should be described in a frame-independent, or *covariant* way. Tracing back to the Michelson–Morley experiment in 1887, it was the discovery of constant speed of light in the vacuum that has deepened the thought of relative motion and given rise to Special Relativity. Later on, based the Equivalence Principle, which states that the inertial mass is the same as the gravitational mass, Einstein was able to include gravity into the framework and formulated General Relativity. This has revolutionised our view of physics profoundly ever since. The idea was summed up concisely by physicist John Wheeler: "*Space-time tells matter how to move; matter tells space-time how to curve*".

Given the coordinate x^μ, where $\mu = 0, 1, 2, 3$, the line element ds of the space-time is given by

$$ds^2 = g_{\mu\nu} dx^\mu dx^\nu, \tag{1.1}$$

where $g_{\mu\nu}$ is the *metric*. The metric signature adopted in this thesis is $(+, -, -, -)$. The equation of motion is given by the geodesic equation:

$$\ddot{x}^\mu + \Gamma^\mu{}_{\nu\lambda} \dot{x}^\nu \dot{x}^\lambda = 0, \tag{1.2}$$

where the dot denotes derivatives with respect to the affine parameter, and the affine connection, $\Gamma^\mu_{\nu\lambda}$, is a function of the metric and its derivatives:

$$\Gamma^\mu{}_{\nu\lambda} = \frac{g^{\mu\alpha}}{2}(\partial_\lambda g_{\nu\alpha} + \partial_\nu g_{\lambda\alpha} - \partial_\alpha g_{\nu\lambda}). \tag{1.3}$$

A special case is the flat *Minkowski* metric $\eta_{\mu\nu} = (1, -1, -1, -1)$, where $\Gamma^\mu{}_{\nu\lambda} = 0$, and Eq. 1.2 gives the usual linear motion. In general, however, the space-time can be curved. The curvature is manifested in the non-vanishing Riemann tensor arising from parallel transportation of a vector. Consider parallel transportation around a parallelogram with sides a^μ and b^μ for a vector V^μ. The change between the original and transported vector is given by:

$$\delta V^\mu = R^\mu{}_{\nu\lambda\eta} V^\nu a^\lambda b^\eta, \tag{1.4}$$

where the Riemann tensor is given by

$$R^{\mu}{}_{\sigma\alpha\beta} = \partial_\alpha \Gamma^{\mu}{}_{\sigma\beta} - \partial_\beta \Gamma^{\mu}{}_{\sigma\alpha} + \Gamma^{\mu}{}_{\alpha\nu}\Gamma^{\nu}{}_{\sigma\beta} - \Gamma^{\mu}{}_{\beta\nu}\Gamma^{\nu}{}_{\sigma\alpha}. \tag{1.5}$$

Notice that the Riemann tensor involves the second derivative of the metric and is therefore a measure of the *curvature* of the space-time. The Riemann tensor has a number of symmetries, and among them the Bianchi Identity allows one to get:

$$\nabla_\nu R^{\nu}{}_{\mu} = \frac{1}{2}\nabla_\mu R, \tag{1.6}$$

where $R_{\mu\nu} = R^{\alpha}{}_{\mu\nu\alpha}$ is the Ricci tensor, and $R = R^{\mu}{}_{\mu}$ is the Ricci scalar. Eq. 1.6 can be rearranged to give the Einstein tensor,

$$G^{\mu\nu} = R^{\mu\nu} - \frac{1}{2}g^{\mu\nu}R, \tag{1.7}$$

such that the covariant divergence $\nabla_\mu G^{\mu\nu} = 0$.

The source of the space time is given by the energy-momentum tensor, $T^{\mu\nu}$. The conservation of energy and momentum requires that $\partial_\mu T^{\mu\nu} = 0$ in the local frame. Covariance requires that this equation holds generally, i.e., $\nabla_\mu T^{\mu\nu} = 0$. Therefore, to link the curvature of the space-time with its source, the simplest approach is to have $G^{\mu\nu}$ proportional to $T^{\mu\nu}$. In Newtonian limit, this constant can be computed and one arrives at the Einstein's field equation:

$$G_{\mu\nu} = -\frac{8\pi G}{c^4}T_{\mu\nu}. \tag{1.8}$$

In principle, nothing stops us from adding other terms into this equation as long as they have vanishing covariant divergence. The simplest such term is the metric tensor multiplied by an arbitrary constant Λ:

$$G_{\mu\nu} + \Lambda g_{\mu\nu} = -\frac{8\pi G}{c^4}T_{\mu\nu}. \tag{1.9}$$

We shall see in the next Section that this is the cosmological constant.

More complicated terms can also be added to this equation. In fact the above equation can be derived from the Einstein-Hilbert action:

$$S = \int \left[\frac{c^4}{16\pi G}(R - 2\Lambda) + \mathcal{L}_M\right]\sqrt{-g}\, d^4x, \tag{1.10}$$

where $\mathcal{L}_M$ is the Lagrangian for the source fields, by requiring $\delta S = 0$ given a

change of the metric $\delta g_{\mu\nu}$. Theories that involve additional terms in the square bracket in the action are generally referred to as *modified gravity* theories. For example, one class of terms is functions of the Ricci scalar, $f(R)$, called the $f(R)$ gravity. These theories lead to exotic physical effects that may provide alternative solution to dark energy and dark matter, or have the potential to resolve the tension in the cosmological parameters. A thorough review of modified gravity theories can be found in [51]. For now, we shall assume standard GR and carry on with Eq. 1.9 for the cosmological model.

1.2 Cosmological model

1.2.1 Homogeneity and isotropy assumptions

The cosmological model is constructed based on the *cosmological principle*: on large scales, the Universe is homogeneous and isotropic, i.e., the universe looks the same at all locations and in all directions. This is a fair assumption, because observations of distant galaxies do not suggest that our location in the Universe is special, nor any particular direction is preferred. It also implies that the same physical laws are valid everywhere in the Universe. Based on these assumptions, one may write down a metric that has the following properties: (1) the metric is spatially symmetric; (2) it can only be a function of time; and (3) it must have the same geometry everywhere. The resultant cosmological metric is the Friedmann-Robertson-Walker (FRW) metric, which takes the form:

$$c^2 d\tau^2 = c^2 dt^2 - R^2(t) \left[\frac{dr^2}{1 - kr^2} + r^2 \sin^2\theta d\phi^2 + r^2 d\theta^2 \right], \tag{1.11}$$

where the evolution of the space is characterised by the arbitrary function $R(t)$, and the curvature is characterised by the constant k, with $k = -1, 0, 1$ corresponding to closed, flat, and open universe respectively. It is common to define the *scale factor* $a(t) \equiv R(t)/R(t = t_0)$, such that $a = 1$ at today.

The Universe is assumed to be filled with perfect fluid, where the density ρ and pressure p are functions of time only. The energy-momentum tensor takes the covariant form,

$$T_{\mu\nu} = \left(\rho + \frac{p}{c^2}\right) u_\mu u_\nu + p g_{\mu\nu}, \tag{1.12}$$

where u^μ is the 4-momentum of the fluid. It is interesting to note that, one can

interpret the cosmological constant term in Eq. 1.9 as an energy density with *negative* pressure, and whose equation of state yields

$$w = \frac{p}{\rho c^2} = -1. \tag{1.13}$$

Therefore, Λ is often referred to as *dark energy*. Solving Eq. 1.9 in the rest frame of the fluid, we arrive at the Friedmann equations:

$$H^2 = \frac{8\pi G\rho}{3} - \frac{kc^2}{a^2} + \frac{\Lambda c^2}{3}, \tag{1.14}$$

$$\frac{\ddot{a}}{a} = -\frac{4\pi G}{3}\left(\rho + \frac{3p}{c^2}\right) + \frac{\Lambda c^2}{3}, \tag{1.15}$$

where

$$H \equiv \frac{\dot{a}}{a} \tag{1.16}$$

is the Hubble parameter, and dot denotes derivative with respect to t.

These equations immediately suggest that the Universe is in general not static. The fate of the Universe, whether it expands or collapses, depends on the matter content of the Universe and its curvature. Combining Eq. 1.14 and 1.15, one gets

$$\dot{\rho} + 3\frac{\dot{a}}{a}\left(\rho + \frac{p}{c^2}\right) = 0. \tag{1.17}$$

This allows us to compute the time dependence of the content of the universe given its equation of state, and solve for the evolution of the scale factor. There are three types of content below.

- **Matter (dust)**: This includes all non-relativistic baryons and dark matter. Because these particles are non-relativistic, their sound speed $c_s^2 = \delta p/\delta\rho$ is much smaller than the speed of light. Thus, the pressure can be neglected, i.e. $w = 0$. This implies that $\rho_m \propto a^{-3}$, i.e., the density decreases with the expansion of space. In a matter dominated Universe, Eq. 1.14 shows that $a \propto t^{2/3}$, and Eq. 1.15 gives $\ddot{a} < 0$. This implies that the universe starts from a singularity, or Big Bang, and expands with deceleration.

- **Radiation**: This includes photon and relativistic neutrinos. The equation of state for radiation is $w = 1/3$, and this shows that $\rho \propto a^{-4}$. This dependence can also be understood physically from the expansion of the space as well as the 'redshifting' of the photon energy $E = h/\lambda$. Substituting this into Eq. 1.14 and 1.15 again gives $a \propto t^{1/2}$ and $\ddot{a} < 0$

in a radiation dominated universe.

- **Dark energy**: The dark energy equation of state in Eq. 1.13 means that this energy density is a constant, as indicated in the Λ term in Eq. 1.14. In a dark energy dominated universe, $a \propto \exp(\sqrt{\Lambda c^2/3}\, t)$, i.e., the universe expands exponentially. We shall see that observations from supernova suggest that the Universe is expanding and accelerating. This is one of the strong evidences that Λ is nonzero.

The real Universe is a mixture of these contents. To make comparison between different species, it is convenient to define the critical density of the Universe today with $k = \Lambda = 0$:

$$\rho_c \equiv \frac{3H_0^2}{8\pi G} \approx 1.88 \times 10^{-26} h^2 \,\mathrm{kg\,m^{-3}}, \tag{1.18}$$

which is about 5 hydrogen atoms per cubic meter, and use the fractional density $\Omega_i = \rho_i/\rho_c$ (usually defined at today with explicit a dependence). H_0 is usually written in unit $100h\,\mathrm{kms^{-1}Mpc^{-1}}$, where h is a parameter of order unity. Eq.(1.14) can then be recast into:

$$H^2 = H_0^2 \left[\Omega_\Lambda + \Omega_m a^{-3} + \Omega_r a^{-4} - (\Omega - 1) a^{-2}\right]. \tag{1.19}$$

Here, Ω_Λ is the fractional dark energy density, $\Omega_m = \Omega_b + \Omega_{\rm DM}$ is the fractional matter density consisting of baryonic matter and dark matter, Ω_r is the fractional radiation density, and $\Omega = \Omega_\Lambda + \Omega_m + \Omega_r$. The last term corresponds to curvature: the open, flat, and closed universe corresponds to $\Omega > 1$, $\Omega = 1$, and $\Omega < 1$ respectively.

Given the dependence of the scale factor on each species, assuming no fine tuning of Ω_i and negligible curvature, the very early universe is dominated by radiation, and then by matter, before it is completely taken over by dark energy. An important time scale is the matter-radiation equality at

$$a_{\rm eq} = \frac{\Omega_r}{\Omega_m} = \frac{4.2 \times 10^{-5}}{\Omega_m h^2}. \tag{1.20}$$

As we shall see near the end of this Chapter, these parameters have been accurately determined by various cosmological observations. To the lowest significant digit, a cosmological model with $h = 0.7$, $\Omega = 1$, $\Omega_\Lambda = 0.7$, $\Omega_m = 0.3$,

$\Omega_b = 0.05$, $\Omega_{\rm DM} = 0.25$, and negligible Ω_r provides a good description of these observations. Given the measured density parameters above, it is perhaps a surprise to find that dark energy has only become dominant today[1]. These parameters suggest that the Universe is spatially flat and is expanding with acceleration. It is also interesting that the matter content is dominated by the unknown (cold) *dark matter*, which is about five times the amount of the normal baryonic matter. The standard model of cosmology is therefore referred to as the ΛCDM model.

1.2.2 Redshift and distance measures

In an expanding universe, the *physical* coordinate $\mathbf{r}$ expands with the scale factor. It is convenient to define the *comoving* coordinate $\mathbf{x}$, where $\mathbf{r} = a(t)\mathbf{x}$, meaning that $\mathbf{x}$ does not change as the Universe evolves. The velocity due to expansion for a physical distance r is given by $v = \dot{r} = H(t)r$. This apparent motion is referred to as the *Hubble flow*.

Due to the Hubble flow, galaxies appear to move away from us. Their radial velocity can be directly measured from the *redshift* of the galaxy characteristic emission lines:

$$z \equiv \frac{\lambda_o - \lambda_e}{\lambda_e}, \tag{1.21}$$

where λ_o is the wavelength observed and λ_e is the wavelength emitted. The change in the wavelength is given by the Doppler effect for a small increment in distance: $d\lambda = \lambda\, dv/c = \lambda\, H(t) dr/c$. Now the time of propagation is given by $dt = dr/c$, thus $d\lambda/\lambda = da/a$. This integrates to

$$\frac{\lambda_o}{\lambda_e} = \frac{a_o}{a_e}. \tag{1.22}$$

Therefore, one can relate the redshift and the scale factor via

$$z + 1 = \frac{1}{a}, \tag{1.23}$$

where the observed time is set to today.

With these tools, we can determine the distance to observed galaxies. In the local

[1] This has lead to the question of 'Why now?'

Universe, the distance can be approximated by the *Hubble law*:

$$d = v/H_0. \tag{1.24}$$

For more distant objects, $H(t)$ can no longer be approximated as a constant and one needs the following integral to compute the comoving distance:

$$\chi(z) = \int_{t_0}^{t} \frac{c\,dt'}{a(t')} = \int_0^z \frac{c\,dz'}{H(z')}. \tag{1.25}$$

It should be noted that this distance determined redshifts may not correspond to the true distance – as we shall see later, the redshift can also have a component arising from the galaxy *peculiar velocity*. This additional velocity actually encodes important cosmological information.

There are two other useful distance measures. The angular diameter distance is given by

$$D_A(z) = \sqrt{\frac{R^2\pi}{\Omega}}, \tag{1.26}$$

where R is the radius of the source observed, and Ω is the solid angle subtended. Since the proper size of the source is given by its comoving size multiplied by the scale factor, we find that $D_A(z) = \chi(z)/(1+z)$. The other one is the luminosity distance

$$D_L(z) = \sqrt{\frac{L}{4\pi S}}, \tag{1.27}$$

where L is the luminosity of the source at frequency, and S is its measured flux. The photon energy is redshifted, and the arrival time is dilated, so that the the measured flux $S = S_0/(1+z)^2$. Therefore, the luminosity distance is related to the comoving distance via $D_L(z) = \chi(z)(1+z)$.

1.2.3 Recombination

One of the greatest success of the cosmological model is the prediction of a relic radiation background from *recombination*, an important epoch during the evolution of the Universe. In the very early universe, photons are constantly scattering off protons and electrons. While hydrogen atoms can be formed, they are also constantly ionised by these high energy photons. As the universe expands, the temperature drops as $T \propto 1/a$, and the number density of ionised (electrons and protons) and neutral components (hydrogen) also drops with

$n_i \propto T^{3/2} \exp(\mu_i - m_i c^2/k_B T)$ in thermal equilibrium, where μ_i is the chemical potential. When the reaction rate is lower than the expansion rate, the Universe becomes neutral. Computation of the ionised fraction of the universe suggest that this happens at $z \sim 1000$. From around this time, a photon rarely interacts with the neutral hydrogen and is able to propagate freely. This is often referred to as *last scattering* or recombination. This afterglow of the Big Bang reaches us from every direction in the form of a background radiation. Due to constant scattering, these photons have a perfect black body spectrum with a temperature redshifted with time: $T_0 = T(z)/(1+z) \sim 3\text{K}$, corresponding to microwave frequencies. It is the earliest radiation that we could detect – the Universe is electromagnetically opaque before this era due to the photon scattering[2].

This Cosmic Microwave Background (CMB) was first predicted by G. Gamow and first observed by Penzias & Wilson [216]. This provided a strong evidence for Big Bang. Subsequently, it is measured by a series of satellite missions. The Cosmic Background Explorer (COBE) measured CMB to high precision and confirmed that the spectrum is a perfect black body with a temperature of $T = 2.73\text{K}$. Later on, the measurements from Wilkinson Microwave Anisotropy Probe (WMAP) allowed determination of cosmological parameters to percent level precision via the study of CMB anisotropies, and stated the era of 'precision cosmology'. This was succeeded by the *Planck* mission, and along with the polarisation data, has provided one of the tightest constraints on our current cosmological model today (see Section 1.4.2). More recently, higher precision CMB experiments are carried out as well as being planned, such as SPT, ACT, and CMB-S4.

1.2.4 Inflation

The CMB is extremely uniform across the whole sky with fluctuations of only one part in 10^5. The comoving particle horizon, which defines the size of causal interaction at the time of recombination is given by

$$\chi_{ph}(z) = \int_0^{t_{\text{CMB}}} \frac{c\,dt}{a(z)}. \tag{1.28}$$

Assume a matter dominated Universe, $\chi_{ph} \sim 180\,h^{-1}\,\text{Mpc}$, corresponding to an angular size of only $\sim 1^\circ$ on the sky – most of the last scattering surface was not

[2]Most of our current observations are based on electromagnetic waves, which cannot probe the epoch before recombination. However, gravitational waves can propagate through this early era, and is considered a potential future probe for the very early universe before recombination.

causally connected. How is the CMB so uniform across the whole sky?

This is referred to as the *horizon problem*, and *inflation* is proposed as a solution. The idea is that there is a period where the scale factor grows exponentially, $a(t) \propto \exp(Ht)$ just like the vacuum dominated case. This allows a small patch of the sky to rapidly grow large enough to cover the whole observable universe today. However, inflation needs to end at some point, or otherwise the Universe today would be completely empty. Such mechanism can be generated by a dynamical scalar field with Lagrangian:

$$\mathcal{L} = \frac{1}{2}\partial^\mu\phi\partial_\mu\phi - V(\phi), \tag{1.29}$$

where $V(\phi)$ is the potential. One can work out the energy-momentum tensor $T^{\mu\nu}$ of the field from Noether's theorem, and read off the density and pressure:

$$\rho_\phi = \frac{1}{2}\dot{\phi}^2 + V(\phi), \tag{1.30}$$

$$p_\phi = \frac{1}{2}\dot{\phi}^2 - V(\phi). \tag{1.31}$$

In this equations, I have assumed that $\phi = \phi(t)$ is homogeneous and thus ignored the terms involving gradients of ϕ. This is fine because as the space expands exponentially, any small spatial perturbations are quickly damped away. We recognise that the equation of state is now

$$w = \frac{\frac{1}{2}\dot{\phi}^2 - V(\phi)}{\frac{1}{2}\dot{\phi}^2 + V(\phi)}, \tag{1.32}$$

and requiring $\dot{\phi}^2 \ll V(\phi)$ gives the vacuum $w = -1$, which generates the exponential growth. We expect that the potential during the inflation era would be flat until the end of the inflation. The equation of motion is given by

$$\ddot{\phi} + 3H\dot{\phi} + V'(\phi) = 0, \tag{1.33}$$

where $V' = dV/d\phi$. In order to keep $\dot{\phi}$ small, we also require that the first term in the above equation is negligible. Together, these conditions are referred to as the *slow-roll approximation*, and can be recasted into the two Hubble slow-roll

parameters[3]:

$$\epsilon \equiv \frac{\dot{H}}{H^2} \sim \frac{\dot{\phi}^2}{V(\phi)}, \tag{1.34}$$

$$\eta \equiv -\frac{\ddot{\phi}}{H\dot{\phi}}. \tag{1.35}$$

After expanding for about 60 e-folds or so, these parameter become $\mathcal{O}(1)$ and ϕ is attracted to the minimum of the potential, hereby exiting the inflation epoch.

It is noticeable that inflation not only solves the horizon problem, but also provides an explanation for the *flatness problem*. This problem refers to that, given the measured curvature being almost zero at the current epoch, the initial curvature must be finely tuned to be extremely small. From Eq. 1.19, the time dependence of the curvature term is

$$1 - \Omega(z) = \frac{H_0^2}{H^2(z)a^2(z)}(1 - \Omega). \tag{1.36}$$

Thus, tracing back to the neutrino freeze-out time, for example, where $a \sim 10^{-10}$ and the Universe was radiation dominated, the curvature term has to be as small as $\sim 10^{-15}$. This is solved by including the inflation epoch, because the exponential expansion of the space essentially stretch out any initial curvature and naturally result in a flat Universe as we observe today.

At the end of the inflation, the fluctuations in the scalar field $\delta\phi$ also provide seeds for density fluctuations that later evolve into the large scale structures of the Universe. We shall see in Section 1.3.2 that inflation is able to predict the shape, or the *spectral index* of the initial power spectrum that matches well with observation.

1.2.5 The dark sector

Dark Matter

The existence of dark matter has been demonstrated by a range of evidence from astrophysical and cosmological observations. One set of evidence comes from the observations of galaxy clusters. In 1933, Zwicky [318] showed that the velocity

[3]There are also potential slow-roll parameters, which control the flatness of the potential. These two sets of slow-roll parameters are equivalent in the limit $\epsilon \to 0$ and $\eta \to 0$.

dispersion of galaxies in the Coma cluster is much larger than the escape velocity given the total mass of the cluster estimated from its luminous components. This indicates that there must be a much larger gravitational potential that hold these galaxies together. X-ray observations of clusters show high gas temperature from clusters of galaxies, indicating high thermal pressure which has to be balance out by the gravitational potential. Again, this gravitational potential is much larger than expected from luminous matter and gas. Furthermore, massive clusters bend the light from distant background galaxies, resulting in strong *gravitational lensing* effect. The distorted image, often looking like a ring or symmetric arcs, provides a direct determination of the mass of the lens. The three independent cluster mass estimation turns out to agree well, showing that about 80% of the total mass is invisible (see [10] for a thorough review).

Another set of evidence comes from the measurements of the rotational curves of spiral galaxies. According to Newtonian mechanics, the rotational velocity at radius R from the disk centre enclosing a mass M is given by

$$v^2(R) = \frac{GM(R)}{R}. \tag{1.37}$$

The rotational velocity can be measured from the Doppler effect of luminous tracers such as stars and HI gas in the disk of these galaxies, and the total visible mass can also be estimated from empirical relations such as the mass-to-light ratio. If the galaxy is composed solely of visible matter, then most of its mass will be concentrated within the size of the disk, beyond which the rotational curve would drop as a function of R. In 1978, Rubin et al. [246] showed that the measured rotational curve of spiral galaxies actually flattens, indicating that the enclosed mass is much larger. Such an effect is also measured in the Milky Way. It is now known that most galaxies are surrounded by *dark matter haloes*.

Big Bang nucleosynthesis (BBN) also provides strong evidence for dark matter. The early Universe has high temperature which allows particles to be constantly created and annihilated. As the Universe expands (and temperature drops as $T \propto 1/a$), the rate of interaction eventually falls below the Hubble parameter, and the species 'freeze out', i.e., the comoving number density becomes conserved. The primordial abundance of elements, especially that of helium (He^4) and deuterium (D), determined from e.g. metal poor intergalactic gas, is a good indicator of the thermal history since the Big Bang. The basic idea is the following. Neutrons and protons are in equilibrium in the early Universe through the interaction

with electrons and neutrinos. This is no longer true at $k_BT \sim 1$MeV when the electron neutrino decouples, and neutrons decay into proton only. Neutrons and protons can also combine to form deuterium through $\mathrm{p} + \mathrm{n} \rightarrow \mathrm{D} + \gamma$. As the temperature continues to drop, not enough energetic photons are around to reverse the process, and the deuteriums begin to form helium $2\mathrm{D} \rightarrow \mathrm{He}^4$. At the end of this process, the free neutrons and protons (and electrons) are almost all in the form of hydrogen (H) and He^4. Elements heavier than He^4 are hard to be produced primordially from two colliding He^4 or H atoms due to unstable nuclei and low number density. The abundance of these elements are sensitive to the baryon-to-photon ratio, which is directly proportional to Ω_b, since the photon number density can be derived from the Cosmic Microwave Background (CMB). Measurements of these elements show that $\Omega_b \approx 0.04$, indicating that only $\Omega_b/\Omega_m \sim 20\%$ of total matter is made up of baryonic matter. For a thorough review on BBN see [293].

Finally, various cosmological probes are sensitive to Ω_b. For example, the Baryon Acoustic Oscillations (BAO) – the sound horizon of the coupled baryon-photon fluctuations, and the relative amplitude of the acoustic peaks of the CMB anisotropy can be used to constraint Ω_b. We will leave detailed discussion of these probes to Section 1.4.

Before leaving this topic, I would like to briefly mention possible candidates for dark matter. For a while, neutrinos had been considered a very probable candidate due to their small cross-section to interact with the other Standard Model particles. However, there are two problems with neutrinos being dark matter. Firstly, their abundance can be computed from the corresponding photon number density as determined from the CMB temperature:

$$\Omega_\nu h^2 = \frac{\sum m_\nu}{91.5\mathrm{eV}}. \tag{1.38}$$

Neutrino oscillation experiments give constraints on the squared mass difference of the three neutrino species, which are of order $\sim 10^{-3} - 10^{-5}$eV, and the upper bound of electron neutrino from particle physics experiment is about 2eV. Together, this means that $\Omega_\nu \lesssim 0.12$ (taking $h \sim 0.7$), and so the neutrino fraction is not large enough to account for all of the dark matter. Another problem is that given the small mass, neutrinos have substantial thermal velocity, a phenomenon called *free streaming*. This prevents them from clustering on small scales. Thus, they would suppress the growth of small structures in the

universe, and this is in contrast to what we observe, for example, from the galaxy power spectrum. In fact, all *hot* dark matter like neutrinos can be ruled out, and this is why we often refer to the name *cold* dark matter. Another promising candidate is Weakly Interacting Massive Particles (WIMP). These particles could arise from extensions of the Standard Model motivated by the Hierarchy Problem, with a mass scale of $m_X \sim 100\text{GeV} - 10\text{TeV}$. Using the cross-section of weak interactions, their abundance can be computed, and it turns out that the relic density is comparable to that of CDM, $\Omega_X \sim 0.3$. This is often referred to as the 'WIMP miracle'. However, the search for WIMPs, along with other Supersymmetry particles, has not shown any convincing detections. Finally, well motivated from particle physics to solve the strong CP problem, QCD axions are also considered a candidate for dark matter. In contrast to WIMPs, they are very light particles with a mass $m_a \sim 10^{-3}\text{eV}(10^{10}\text{GeV}/f_a)$, where f_a is the Peccei-Quinn scale and is a free parameter [212]. To obtain a relic density comparable to observation, $\Omega_a h^2 \sim 10^{11}\text{GeV}/f_a$, the axion mass would be of order $\lesssim 10^{-5}\text{eV}$, yielding $f_a \gtrsim 10^{12}\text{GeV}$. This is referred to as the 'axion window'. It is noticeable, however, that the natural scale of f_a is $\sim 10^{16} - 10^{18}\text{GeV}$ from String Theory. Other types of axions (or axion-like particles) are proposed that have desired dark matter properties but do not solve the CP problem (e.g. fuzzy dark matter). The search for this particle, along with its related physical effects, are also ongoing, and has not provided convincing evidence of its existence yet. A review on the dark matter candidate can be found in e.g. [83].

Dark Energy

We now know from cosmological observations that the dark energy density parameter, Ω_Λ is about 0.7. Given the critical density $\rho_c = 3H_0^2/(8\pi G)$, the vacuum energy density is of the order $(10^{-12}\text{GeV})^4$ in natural units. This has raised the question of fine-tuning of the vacuum energy and the smallness of the cosmological constant. From Quantum Mechanics, we know that the zero-point energy of massless field is given by $E = \langle 0|H|0\rangle = \hbar\omega/2$. This has been experimentally verified, for example, in Casimir effect [155] and X-ray diffraction of lattice [315]. Therefore, the total energy density of the vacuum is given by integrating the equation in phase space,

$$\rho_{vac}c^2 = \frac{4\pi\hbar}{(2\pi)^3}\int_0^\infty \omega^3\, d\omega. \tag{1.39}$$

This expression clearly diverges. One could introduce a UV cutoff, Λ, as the upper limit, by arguing that there is a minimum scale in the space, i.e., a lattice. A natural scale to assume is the Planck scale, $\Lambda = \sqrt{\hbar c/(8\pi G)}$, above which quantum gravity would need to be considered, and is beyond our current understanding with the Standard Model. In this case we get a total vacuum energy of order $(10^{18}\text{GeV})^4$ – some 120 orders of magnitude difference between this naive prediction and the measured value. Of course, this naive computation needs to be taken cautiously. Firstly, it is unknown if this expression actually breaks down at much smaller energy scales, since QFT has only been tested up to the QCD scale. Secondly, we will need to consider all types of particles in the standard model and their interactions, rather than the single massless scalar field case. Thirdly, it is a common practice in QFT that such divergence can be avoided by *renormalisation* of the theory, and the observables turn out to be finite. After all, the observable is sensitive the the change of the energy, rather than its absolute value. In this sense, the vacuum energy can be 'renormalised' to any value. However, it is unsatisfactory that the choice of this 'free' parameter has to be finely tuned across many orders of magnitudes to be so small. This is often referred to as the cosmological constant problem.

One solution is that the cosmological constant is generated by other dynamical (scalar) fields, for example, in a scenario similar to the inflation field. This in general allows some evolution of the dark energy equation of state, i.e., $w = w(t)$, which can alter the evolution of large scale structures and their formation, and is a key aspect for the design of modern galaxy surveys to clarify. The evolution of w can be tested through two kinds of methods, geometrical and dynamical probes. The former refers to the precise measurements of the cosmic distance scale. Recall that for arbitrary w, considering $k = \Lambda = 0$, Eq.(1.14) and (1.15) together give $d\rho/da = -3(1+w)\rho/a$. This means that the dark energy density equation has the dependence

$$\rho \propto e^{\int -3(1+w)d\ln a}. \tag{1.40}$$

Therefore, the Hubble equation is then modified to

$$H^2(a) = H_0^2\left[\Omega_\Lambda e^{\int -3(1+w)d\ln a} + \Omega_m a^{-3} + \Omega_r a^{-4} - (\Omega - 1)a^{-2}\right]. \tag{1.41}$$

It is then clear that, by Eq.(1.25), non-trivial dependence of w on time can affect the comoving distance measure. Thus, geometric probes such as BAO are able to

test these effects. A complication is that such measurements also depend on the value of the matter density Ω_m, and to get tight constraints on w, we will also need high precision measurements in Ω_m. The dynamical probe the dark energy equation of state is through the growth of structures. As will be explained later, the density fluctuation is governed by the following equation:

$$\ddot{\delta} + 2H\dot{\delta} = 4\pi G\rho_0\delta.$$

This is a wave equation with a 'drag' term induced by the Hubble expansion. Therefore, the *growth rate* of large scale structures are also sensitive to the specific form of the dark energy equation of state.

1.3 Structure formation

The very existence of galaxies and stars shows that the homogeneity assumption of the Universe is not valid on small scales. It is also revealed in galaxy surveys that the distribution of galaxies is inhomogeneous and anisotropic, such as shown in Fig. 1.1. We can model these structures by introducing small perturbations to the density (and the metric) in the early Universe, and evolve them to the present. This is described in Section 1.3.1 as the linear perturbation theory. The two-point statistics of the density fluctuations are introduced in Section 1.3.2, namely the power spectrum and the correlation function. In Section 1.3.3, I will also discuss an important observational effect in the measured correlation function: redshift space distortions. Eventually, the small perturbations grow to $\mathcal{O}(1)$, and the perturbation theory breaks down. To account for non-linearity, the theoretical approach is to expand to higher order. The advantage of this method is that it does not involve additional parameters – non-linearities are computed from first principles. However, computation becomes complicated quickly before one can approach much smaller scales. An alternative approach is phenomenological models that are tested against N-body simulations, such as the halo model introduced in Section 1.3.4. It states that when the local density exceeds some critical value, the matter within the overdense region should collapse under gravity and form a gravitationally bound structure, or haloes. The large and small scales can then be described by the statistical distribution of different haloes and a single halo profile respectively. The connection between galaxies and haloes is discussed briefly in Section 1.3.5. Finally, there are also empirical

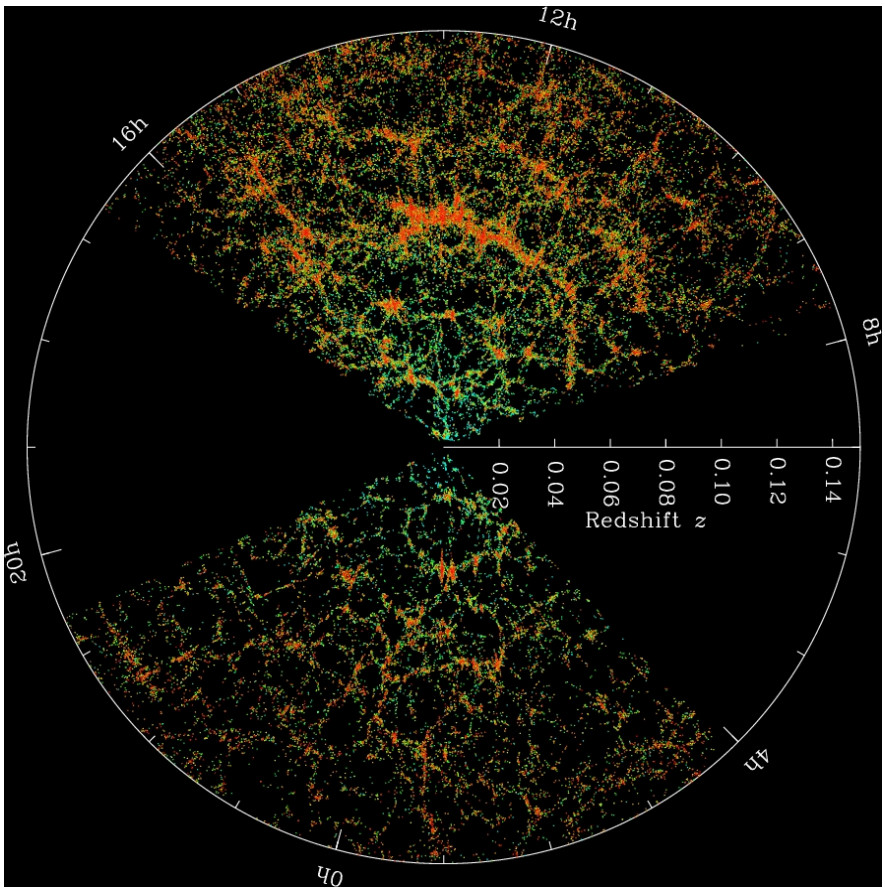

Figure 1.1 *The Solan Digital Sky Survey (SDSS) map of the Universe. Each dot is a galaxy; the colour is the $g-r$ colour of that galaxy. Credit: M. Blanton and SDSS.*

approaches towards the non-linear scales via parameterised models that explicitly match observations. These various approaches have been applied intensively in cosmological studies, and conveniently, there are many numerical packages that can generate non-linear matter power spectrum based on empirical fitting formula with different cosmological parameters, e.g. the HALOFIT [276, 282], and CAMB [163].

1.3.1 The linear perturbation theory

The density field $\rho(\mathbf{x}, t)$ fluctuates around a homogeneous mean background density $\bar{\rho}(t)$. The density fluctuation is defined as

$$\delta(\mathbf{x}, t) = \frac{\rho(\mathbf{x}, t) - \bar{\rho}(t)}{\bar{\rho}(t)}, \tag{1.42}$$

where $\delta > 0$ corresponds to *overdensity*, and $-1 \leq \delta < 0$ refers to *underdensity* compared to the background. The linear assumption, $|\delta| \ll 1$, is valid in two scenarios. Firstly, given that the CMB fluctuations are very much Gaussian and of order 10^{-5}, this assumption should hold in the early Universe. Secondly, it should be valid on very large comoving scales $\gg 100\,h^{-1}\,\mathrm{Mpc}$, regardless of epoch, because the homogeneous and isotropic assumption holds well even up to today. In these linear regimes, one can compute the equation of motion to first order in δ. In the following text, I will adopt the Newtonian limit where the gravitational field is weak, and when perturbation is much smaller than the horizon scale. This provides an intuitive way to work out the dynamics of the perturbation. The full relativistic treatment is more complicated and involves introducing perturbations to the metric and the energy momentum tensor (for details, see e.g., [301]). In this more rigorous approach, perturbations beyond scalar modes are in principle present: the vector perturbations correspond to the vorticity field, and the tensor perturbations produce small gravitational waves. The effect of vector perturbations corresponding to vorticity can be safely neglected, because they dissipate quickly with the expansion of the universe. The tensor perturbations are in fact predicted by inflation, but it has not yet been observed. For the following analysis, we shall ignore the tensor modes, and quote results from the relativistic approach directly when needed.

We adopt the non-relativistic fluid approximation. There are three equations that govern the dynamics of density.

- Continuity equation:
$$\frac{\partial \rho}{\partial t} = -\nabla_r \cdot (\rho \mathbf{U}), \tag{1.43}$$
where $\mathbf{U}$ is the velocity field of the fluid. The derivative ∇ and the partial time derivative are with respect to the proper distance $\mathbf{r}$.

- Euler equation (or conservation of momentum):
$$\left(\frac{\partial}{\partial t} + \mathbf{U} \cdot \nabla_r\right) \mathbf{U} = -\frac{\nabla_r p}{\rho} - \nabla_r \Phi. \tag{1.44}$$

- Poisson equation:
$$\nabla_r^2 \Phi = 4\pi G \rho - \Lambda. \tag{1.45}$$
Since Λ domination only happens at late times, we will ignore its contribution for the following discussion.

To distinguish the dynamics from Hubble expansion, we solve these equations in the comoving coordinates $\mathbf{x}$ where $\mathbf{r} = a(t)\mathbf{x}$. The velocity then is given by $\mathbf{U} = \dot{\mathbf{r}} = H\mathbf{r} + \mathbf{v}$, where the first term corresponds to the Hubble flow, and the second term is the *peculiar velocity*. The zeroth order equations are solved by the background cosmological model, e.g., Eq. 1.17. The first order equations can be rearranged into:

$$\ddot{\delta} + 2H\dot{\delta} - \frac{c_s^2}{a^2}\nabla_x^2\delta = 4\pi G\bar{\rho}\delta, \tag{1.46}$$

where $c_s^2 = \delta p/\delta\rho$ is the sound speed of the fluid, and the derivative is with respect to the comoving coordinates, ∇_x. This is essentially a wave equation with a friction term given by the expansion of the background universe, and a driving term given by the competing effect of pressure and gravity. In Fourier space, Eq. 1.46 becomes $\ddot{\delta}_{\mathbf{k}} + 2H\dot{\delta}_{\mathbf{k}} + (c_s^2/a^2)(k^2 - k_J^2)\delta_{\mathbf{k}} = 0$, where $\mathbf{k}$ is the comoving wave vector, and $k_J = \sqrt{4\pi G\bar{\rho}}/c_s$ is the *Jeans scale*. Below the Jeans scale ($k > k_J$), pressure dominates, and the density perturbation has an oscillatory solution, also referred to as *acoustic waves*. Above the Jeans scale ($k < k_J$), gravity dominates and the density evolves with time according to a power law. In the case of cold dark matter and baryonic matter after decoupling, the pressure term can be ignored, and Eq. 1.46 only involves time derivatives of δ. Thus, one can separate the temporal and spatial dependences of the density perturbation, i.e. $\delta(\mathbf{x}, t) = D(t)\delta_0(\mathbf{x})$. During matter domination, $a \propto t^{2/3}$, and we find a growing solution $D_+(t) \propto a$ and a decaying solution $D_-(t) \propto t^{-1}$; the latter quickly becomes negligible. It is commonly adopted that $D_+(t_0) = 1$, and

$$\delta(\mathbf{x}, t) = D_+(t)\delta_0(\mathbf{x}). \tag{1.47}$$

In radiation dominated era, $D_+(t) \propto t \propto a^2$ from relativistic computations (for more detail, see e.g., [204]). From here on, we will drop the '+' on the growth factor $D_+(z)$ as we will only consider the growing mode.

The peculiar velocity field

The peculiar velocity $\mathbf{v}$ can also be solved from Eq. 1.43-1.45. In the linear regime and using comoving coordinates, the Eq. 1.44 with negligible pressure becomes

$$\frac{\partial\mathbf{v}}{\partial t} + H\mathbf{v} = -\frac{\nabla_x\Phi}{a}, \tag{1.48}$$

where Φ is the Newtonian potential which satisfies the linearised Poisson equation. It is convenient to define the comoving velocity $\mathbf{u}$ such that $\mathbf{v} = a\mathbf{u}$, and Eq. 1.48 becomes $\partial\mathbf{u}/\partial t + 2H\mathbf{u} = -\nabla_x\Phi/a^2$. We can now drop the subscript x on the spatial derivative as we work consistently in comoving space. The inhomogeneous solution, where the RHS of the equation is set to zero, yields a decaying function with $|\mathbf{u}| \propto 1/a^2$. This soon becomes negligible. The homogeneous solution yields that $\mathbf{u}$ is along the direction of the potential gradient and thus can be expressed as a gradient of a scalar convergence θ, i.e., $\mathbf{u} = \nabla\theta$.

The comoving peculiar velocity is related to the density perturbation via the linearised continuity equation:

$$\frac{\partial\delta}{\partial t} + \nabla \cdot \mathbf{u} = 0. \tag{1.49}$$

Substituting Eq. 1.47 we find that in Fourier space,

$$\tilde{\mathbf{u}} = -iHf\delta_{\mathbf{k}}\frac{\mathbf{k}}{k^2}. \tag{1.50}$$

where

$$f \equiv \frac{\partial \ln D}{\partial \ln a} \approx \Omega_m^{\gamma} \tag{1.51}$$

is the *growth rate* of the density perturbation. In the last expression, the power is $\gamma \approx 0.55$ in GR [152, 299]. Conveniently, the peculiar velocity is completely determined by the density field in the linear regime. Thus, by measuring galaxy peculiar velocities, one can constrain the growth rate of the large scale structures. It is an important parameter for testing theories of gravity on cosmological scales, as will be discussed in more detail Section 1.3.3.

1.3.2 Descriptive statistics

Correlation function

The n-point functions are defined as

$$\xi^n(\mathbf{x}_1, \mathbf{x}_2, ...\mathbf{x}_n) = \langle\delta(\mathbf{x}_1)\delta(\mathbf{x}_2)...\delta(\mathbf{x}_n)\rangle, \tag{1.52}$$

where the bracket represents ensemble average[4]. If δ is a Gaussian random field, the 2-point function will be able to capture all statistical features. This is a good approximation in the early universe, for example, for the CMB analysis, because the CMB fluctuations are extremely close to Gaussian distributed. For the local universe, the $n = 2$ case is also most commonly adopted for its simplicity to model and convenience to construct an estimator for observational purposes; both modelling and observation get hugely complicated even at the *bispectrum* ($n = 3$) level, not to mention higher order statistics. However, it should be noted that as structures grow, the distribution of δ deviates significantly from Gaussian; it is more appropriately described by a lognormal distribution at low redshifts [55, 56]. Non-linearity also induces coupling between different scales, making the evolution of the density perturbation difficult to model. Thus, there are many efforts towards trying to capture these non-Gaussian properties beyond the 2-point functions, for example, using 1-point function (PDF of the density field) and 3-point functions, e.g.[96, 259, 274, 294]. In this thesis, we will focus on 2-point statistics only,

The 2-point function can be related to the excess probability of finding a pair of galaxies at positions $\mathbf{x}_{1,2}$ each in a volume dV with a mean number density $\bar{n}$:

$$P = (\bar{n}\, dV)^2 \left[1 + \xi(\mathbf{x_1}, \mathbf{x_2})\right], \tag{1.53}$$

when compared to a random distribution, where $\xi = 0$. Assuming isotropy (since there is no preferred direction for the inhomogeneity), $\xi(\mathbf{x_1}, \mathbf{x_2}) = \xi(r)$, where $r = |\mathbf{x}_1 - \mathbf{x}_2|$. This definition is used to construct estimators for the correlation function, and the average is taken over many such galaxy pairs. The ensemble average in Eq. 1.52 is replace by an average over volume (or galaxy pairs) here because we assume the *ergodic hypothesis*, which states that the statistical properties at different parts of the universe are the same. One of the commonly used estimators is the Davis-Peebles estimator [63]:

$$\xi(r) = \frac{DD}{DR} - 1. \tag{1.54}$$

Here D denotes data and R denotes random points in the same volume. A quantity like DR is the number of data and random pairs separated by distance r, normalised by the number of data and randoms in the volume. This is to account

[4]The ensemble average refers to averaging over many such samples. Ideally, this requires averaging over many realisations of the universe at positions $\mathbf{x_1}, ...\mathbf{x_n}$. However, as we shall see below, due to the homogeneity of the universe, this average can be performed spatially instead.

for the fact that normally the number of random points used is much larger than data points in order to reduce noise. Another commonly used estimator is the Landy-Szalay estimator [156], which has the improvement of better noise suppression compared to Eq. 1.54:

$$\xi(r) = \frac{DD - 2DR + RR}{RR}. \tag{1.55}$$

In actual observations, the correlation function is not isotropic due to the peculiar velocities of galaxies along the line of sight, as we will soon discuss in Section 1.3.3. To reduce the anisotropic effect, it is often useful to measure the *projected* correlation function

$$w_p(r_p) = \int_{-\infty}^{\infty} \xi(r_p, \pi)\, d\pi, \tag{1.56}$$

where (r_p, π) are the separation of the pair perpendicular and parallel to the line of sight, and $r^2 = r_p^2 + \pi^2$. With this, one can then invert the relation to find the isotropic 3D correlation function via the inverse Abel transform:

$$\xi(r) = -\frac{1}{\pi} \int_r^{\infty} \frac{dw_p(y)}{dy} \frac{dy}{\sqrt{y^2 - r^2}}. \tag{1.57}$$

It should be emphasised that these expressions assume a distant observer, and there is no selection as a function of distance (or redshifts).

In some cases, the distance to individual galaxy is not well determined (e.g., in a photometric survey), and the clustering is measured via the angular correlation function, $w_p(\theta)$, which counts galaxy pairs given an angular separation θ. This is related, but not to be confused with the above expressions that count pairs in 3D. In the case of angular correlation functions, the interpretation of the signal also requires the overall redshift distribution $N(z)$ of the galaxy sample.

Power spectrum

The power spectrum is the 2-point correlation function in Fourier space. In the linear regime, each Fourier mode of the perturbation evolves independently, making the power spectrum convenient for theoretical computations. Assuming zero curvature, the density perturbation can be decomposed into plane waves,

$\delta(\mathbf{x}) = \sum \delta_{\mathbf{k}} \exp(i\mathbf{k}\cdot\mathbf{x})$, and the Fourier coefficients are given by

$$\delta_{\mathbf{k}} = \frac{1}{(2\pi)^3}\int \delta(\mathbf{x}) e^{-i\mathbf{k}\cdot\mathbf{x}}\, d^3\mathbf{x}. \tag{1.58}$$

In the continuum limit, the power spectrum is defined as:

$$\langle \delta_{\mathbf{k}} \delta^*_{\mathbf{k}'} \rangle = \frac{1}{(2\pi)^3} P(k) \delta^3(\mathbf{k} - \mathbf{k}'), \tag{1.59}$$

where $\delta^3(\mathbf{k} - \mathbf{k}')$ is the Dirac delta function and $k \equiv |\mathbf{k}|$. In the linear regime, according to Eq. 1.47, the temporal and spatial dependence of the power spectrum are separable, i.e. $P(k, z) = D^2(z)P_0(k)$, where $P_0(k)$ is the power spectrum at $z = 0$. The power spectrum and the 2-point function is linked by the 3D Fourier transform. Integrating out the solid angle, the isotropic correlation function can be expressed as

$$\xi(r) = \frac{4\pi}{(2\pi)^3}\int_0^\infty P(k)\frac{\sin(kr)}{kr} k^2 dk. \tag{1.60}$$

The total variance of the field is given by integrating over the full phase space,

$$\langle \delta^2 \rangle = \frac{1}{2\pi^2}\int P(k) k^2\, dk = \int \Delta^2(k) d\ln k, \tag{1.61}$$

where

$$\Delta^2(k) \equiv \frac{P(k)k^3}{2\pi^2} \tag{1.62}$$

is the dimensionless power spectrum. This integral is divergent at large k given the shape of the power spectrum: as we shall see shortly, the small scale power is approximately $\propto k^{-3}$ in linear theory, and non-linearities further enhance the power. Thus, the variance is usually defined with a smoothing at some scale R:

$$\sigma_R^2(z) = \frac{1}{2\pi^2}\int_0^\infty P(k, z)|\tilde{W}(Rk)|^2 k^2 dk, \tag{1.63}$$

where $\tilde{W}(kR)$ is the Fourier transform of the smoothing function. It is common to adopt the spherical top-hat filter:

$$W(r) = \begin{cases} (4\pi R^3/3)^{-1}, & \text{if } r \le R, \\ 0, & \text{otherwise.} \end{cases}$$

In this case, σ_R simply tells us the rms overdensity enclosed in a sphere of radius R. It is conventional to use $R = 8h^{-1}$Mpc with $z = 0$ to define the *normalisation*

of the power spectrum, σ_8, which has a measured value of about 0.8. There is a subtlety that the σ_8 parameter is often quoted as the linear extrapolation with the linear growth factor $D(t)$. In general, however, the variance σ_R^2 would also include the non-linear scale, and thus has a different definition.

Shape of the matter power spectrum

The linear matter power spectrum can be written as

$$P(k, z) = D^2(z) A k^{n_s} T^2(k), \tag{1.64}$$

where $A \propto \sigma_8^2$ is the normalisation amplitude, n_s is the *spectral index*, which characterise the initial power spectrum, and $T(k)$ is the *transfer function*, which encodes the deviation from the initial power law due to the growth of structure. I will give a qualitative description of the last two terms in Eq. 1.64 below.

The power law form comes from the argument that the power spectrum has to be featureless due to the lack of a characteristic scale in the early universe. The corresponding functional form is a power law. The power index is postulated to be $n_s = 1$ because then the fluctuation of gravitational potential is constant, which is expected in as a result of scale invariance [115, 215]. This is known as the *Harrison-Peebles-Zel'dovich spectrum*. Such a constant potential fluctuation is also predicted by inflationary models, via introducing perturbations to the scalar field $\delta\phi$. It can be shown (see e.g. [204]) that the initial power actually deviates from unity by a small amount which is related to the slow-roll parameters (Eq. 1.34 and 1.35):

$$1 - n = 6\epsilon - 2\eta. \tag{1.65}$$

Indeed the measured n_s is slightly lower than unity. This small deviation is called the *tilt* of the power spectrum, and can be used to constrain inflationary models.

The transfer function $T(k)$ captures deviation from the initial power law. The main effect is the suppression of the growth of matter fluctuation at radiation domination due to pressure. This is reflected in a scaled dependent way via the horizon size of the perturbation. Given the size of the horizon $\chi_H(z)$, perturbation modes that are smaller than the horizon, i.e. $k > 1/\chi_H$, are in causal contact, thus often called modes that have *entered the horizon*. Large scale modes with $k < 1/\chi_H$, on the other hand, are unaffected by physical interactions such as pressure or free streaming. On sub-horizon scales, during

radiation domination, the matter fluctuation eases to grow. This can be seen qualitatively from Eq. 1.46: ignoring the pressure term for dark matter, δ varies on the characteristic expansion time scale $\sim 1/H$. Thus, the RHS of the equation is $\sim H^2\delta \sim (8\pi G/3)\rho_r\delta \gg 4\pi G\rho_m\delta$, much larger than the LHS, i.e. the gravity term is negligible. We ignore the contribution of radiation density on the LHS, because it oscillates fast with baryons. Well within the horizon, radiation can be treated as a uniform background field. This means that a perturbation mode which grows $\propto a^2$ during the radiation dominated era ($a < a_{eq}$) will stop growing once it enters the horizon, and start to grow again $\propto a$ when matter dominates ($a > a_{eq}$). Compared to modes that enter the horizon during matter domination, their amplitude is suppressed by a factor of $(a_{\rm enter}/a_{eq})^2$. One can show that the horizon scale at radiation domination is given by $\chi_H \sim 1/k \propto a$, and defining the horizon scale at matter-radiation equality as $\chi_{eq} \sim 1/k_{eq}$, we can see that the power at $k > k_{eq}$ is suppressed by $1/k^2$. This is referred to as the *Mészáros effect*. Therefore, qualitatively, the transfer function is

$$T(k) \approx \begin{cases} 1, & \text{if } k \ll k_{eq}, \\ k^{-2}, & \text{if } k \gg k_{eq}. \end{cases}$$

The full transfer function can be computed numerically. The exact transition scale depends on k_{eq}, which in turn depends on the matter density Ω_m. Therefore, the shape of the power spectrum provides a constraint on Ω_m.

Acoustic Oscillations

Although only a small portion of the total matter density, baryons also leave distinct features on the matter power spectrum via Baryon Acoustic Oscillations (BAO). At very early times, baryons and photons are tightly coupled due to the constant Compton scattering, and they can be treated as coupled relativistic fluid until recombination at $z \approx 1000$. As we saw in Eq. 1.46, the pressure term in the density perturbation gives rise to acoustic oscillations of the perturbation with a sound speed of c_s, at scales smaller than the Jeans scale. For radiation, the sound speed is $c/\sqrt{3}$[5], thus the *sound horizon* – the maximum distance of a sound wave could travel in a given epoch – is roughly $1/\sqrt{3}$ of the horizon scale. This oscillation can be solved exactly in radiation dominated era using relativistic

[5]For the baryon-photon fluid, there is a slight deviation because while the pressure is supported by photons, the density is a sum of photon and baryon. The deviation is proportional to $\Omega_b/\Omega_r \ll 1$ at early epochs, so we ignore it here.

perturbation theory. One finds that the potential evolves as

$$\Phi_k(\tau) = 3\Phi_k(0)\frac{\sin x - x\cos x}{x^3}, \quad x \equiv \frac{kc\tau}{\sqrt{3}}. \tag{1.66}$$

Here, τ is the conformal time, where $dt = ad\tau$, and $c\tau = \chi_H$ is the comoving horizon. Thus, on the sub-sound-horizon scale, $x \gg 1$, the potential oscillates with a decaying amplitude $\propto 1/\tau^2 \propto 1/a^2$. On super-sound-horizon scale, $x \ll 1$ and the potential tends to a constant. This oscillatory behaviour of the photon-baryon fluid leaves an imprint on the CMB, referred to as the *acoustic peaks*, and they are used to provide some of the most precise constraints on the cosmological parameters (see Section 1.4.2).

After reaching the *drag epoch* at $z \sim 500$, the photon pressure can no longer support baryons from collapsing under gravity, and the baryonic matter co-evolve with dark matter with a similar spatial distribution. This can be solved by the following coupled equations ignoring pressure:

$$\ddot{\delta}_b + 2H\dot{\delta}_b = 4\pi G\sum_{b,c}\bar{\rho}_i\delta_i, \tag{1.67}$$

$$\ddot{\delta}_c + 2H\dot{\delta}_c = 4\pi G\sum_{b,c}\bar{\rho}_i\delta_i. \tag{1.68}$$

The solutions to these equations suggest that δ_b and δ_c tend to the same after large enough time. This oscillatory feature from baryons before decoupling, often referred to as the BAO wiggles, thus also leave an imprint on the total matter power spectrum, with an amplitude proportional to $\Omega_b/\Omega_c \sim 20\%$.

In configuration space, this oscillatory feature corresponds to a bump with a characteristic scale of the sound horizon at the time of recombination in the 2-point correlation function. The location of this bump corresponds to the sound horizon at recombination (or the drag epoch, to be more rigorous), which is the largest wavelength of the acoustic oscillation. This is given by [12, 16]

$$d_s = \int_0^{a_{\rm drag}} \frac{c_s\,da}{a^2H(a)} \sim 147\,{\rm Mpc}\left(\frac{\Omega_b h^2}{0.0224}\right)^{-0.13}\left(\frac{\Omega_m h^2}{0.1424}\right)^{-0.26}, \tag{1.69}$$

where $a_{\rm drag}$ is the redshift at the drag epoch, and the sound speed c_s of the photon-baryon fluid is given by $c_s = (c/\sqrt{3})/\sqrt{1+(3/4)(\Omega_b(z)/\Omega_\gamma(z))}$. Here we use the full expression for c_s because at later times as the correction from Ω_b/Ω_γ becomes relevant given that the current measurements from galaxy surveys are

up to percent level. The BAO is another pillar of the cosmological probes, and it provides tight constraints on the matter density and the Hubble parameter H_0 (see Section 1.4.3).

1.3.3 Redshift-space distortion

The measured correlation function from observations relies on the determination of the distance to galaxies, which in turn depends on their redshifts. As mentioned above, due to peculiar velocity, the measured redshift of a galaxy would have an additional contribution from the Doppler effect of the peculiar velocity via

$$1 + z_{obs} \approx (1 + z_H)(1 + |\mathbf{v}|\mu/c), \tag{1.70}$$

where μ is the cosine of the angle between the peculiar velocity and the line of sight, and $|\mathbf{v}| \ll c$. Because the comoving distance to galaxies are determined from redshift via Eq. 1.25, the radial distance to the galaxies are 'distorted' by the peculiar velocity. This results in a measured galaxy 2-point function that is anisotropic, referred to as the Redshift-space distortion (RSD) effect.

The mapping between real and redshift space and its effect on the power spectrum was quantified by [137] with the notion of the displacement field. Subsequently, the effect was discussed by [86, 111, 164, 178] including configuration space. Let the true position in real space be denoted by superscript r, and the observed position in redshift space by s. Mass conservation yields $(1 + \delta^r)\, d^3\mathbf{x}_r = (1 + \delta^s)\, d^3\mathbf{x}_s$. The redshift space position differs from the real space position by $\mathbf{x}_s = \mathbf{x}_r + \mathbf{d}$, where $\mathbf{d} = \mathbf{v}/aH$ is the comoving displacement field. In Fourier space, the mapping is given by:

$$1 + \delta^s_{\mathbf{k}} = \int (1 + \delta^r)\, e^{i\mathbf{k}\cdot\mathbf{x}_s} \left|\frac{\partial \mathbf{x}_r}{\partial \mathbf{x}_s}\right| d^3\mathbf{x}_s,$$

where to first order, the Jacobian is given by $|\partial\mathbf{x}_s/\partial\mathbf{x}_r|^{-1} \approx (1 - \nabla_r \cdot \mathbf{d})$.

Since the effect is only along the line of sight, we can replace $\nabla_r \cdot \mathbf{d}$ by $\partial d_y/\partial y$, where y is the coordinate along the line of sight. We will also adopt the distant observer assumption, where $y^r \approx y^s$. From Eq. 1.50, the Fourier transform of the displacement is $\mathbf{d}_\mathbf{k} = -if(\delta_\mathbf{k}/k)\hat{\mathbf{k}}$, and the component along the line of sight is $d_y = |\mathbf{d}_\mathbf{k}|\mu$, where $\mu = k_y/k$ is the cosine of the angle between the wave vector and the line of sight. Altogether, this gives $\delta^s_\mathbf{k} = \delta^r_\mathbf{k}\,(1 + f\mu^2)$. Thus, the power

spectrum in redshift space, P^s, is then related to that in real space, P^r, by

$$P^s(k,\mu) = (1 + f\mu^2)^2 P^r(k). \tag{1.71}$$

I emphasise that this is valid only for distant observers, where the radial vectors pointing to the pair of galaxies are assumed to be parallel. This is a good approximation for galaxy surveys with a pencil-beam like survey geometry, such as the GAMA fields studied in Chapter 2. In general, however, this assumption breaks down for galaxy pairs that are widely separated, and one need to account for the *wide angle effect*, see e.g. [26, 45, 176, 233, 310].

For the galaxy power spectrum, $P_g(k) = b_g^2 P(k)$, Eq. 1.71 becomes $P_g^s(k,\mu) = (b_g + f\mu^2)^2 P^r(k)$, since the velocity is assumed to be unbiased given that it responds directly to the matter distribution. It it thus useful to define the distortion parameter $\beta \equiv f/b$ such that:

$$P_g^s(k,\mu) = (1 + \beta\mu^2)^2 P_g^r(k). \tag{1.72}$$

Given the dependence of μ in Eq. 1.71, the power spectrum can be expanded into multipoles of Legendre polynomials $L_\ell(k)$, where $\ell = 0, 2, 4$. The quadrupole-to-monopole ratio directly measures the distortion parameter [54].

In configuration space, the 2-point correlation function in redshift space can be expressed in terms of multipoles [111]:

$$\xi^s(r,\mu) = \xi_0(r)L_0(\mu) + \xi_2(r)L_2(\mu) + \xi_4(r)L_4(\mu), \tag{1.73}$$

where ξ_ℓ is given by real space isotropic correlation function $\xi(r)$ and its higher moments:

$$\xi_0 = \left(1 + \frac{2}{3}f + \frac{1}{5}f^2\right)\xi(r), \tag{1.74}$$

$$\xi_2 = \left(\frac{4}{3}f + \frac{4}{7}f^2\right)[\xi(r) - \bar{\xi}(r)], \tag{1.75}$$

$$\xi_4 = \frac{8}{35}f^2\left[\xi(r) + \frac{5}{2}\bar{\xi}(r) - \frac{7}{2}\bar{\bar{\xi}}(r)\right], \tag{1.76}$$

with

$$\bar{\xi}(r) = 3r^{-3} \int_0^r \xi(s) s^2 ds, \tag{1.77}$$

$$\bar{\bar{\xi}}(r) = 5r^{-5} \int_0^r \xi(s) s^4 ds. \tag{1.78}$$

In practice, higher order (even) multipoles are present due to non-linear scale effects (e.g. the Finger of God effect which will be introduced shortly), and the multipoles also deviate from the linear expression Eq. 1.74-1.76. Odd multipoles can also be non-zero – although at a much smaller amplitude – due to relativistic effects such as lensing and gravitational redshift [27, 35, 305]. However, at the cost of losing some information, it is still a common practice to compress the full degree of freedom of the 2D $\xi^s(r, \mu)$ into the lowest few even multipoles via:

$$\xi_\ell^{obs} = \frac{2\ell + 1}{2} \int_{-1}^{1} \xi^s(r, \mu) L_\ell(\mu)\, d\mu. \tag{1.79}$$

1.3.4 Nonlinear growth

Spherical collapse

Linear perturbation breaks down at late times, when $\delta \sim \mathcal{O}(1)$. Furthermore, the fluid approximation becomes invalid when the density becomes too large and shell crossing happens. To study the density evolution beyond linearity, N-body simulations are usually employed, where a huge system of collisionless dark matter particles are placed initially with a Gaussian distribution, and then evolved under gravity with a background cosmology. The *spherical collapse* model [103, 213] provides an intuitive picture that explains well the observations from these N-body simulations. In this picture, we consider a patch of overdensity with mass $M(< r_i)$ enclosed within some radius r_i initially. The patch would expand slightly slower than the background expansion rate due to gravity, while this will lead to more enhanced overdensity. At some point, if the overdensity is sufficiently large, the patch would break away from the background expansion and collapse under gravity. A thorough review on non-linear growth and halo model can be found in [58].

In the following text, I will assume spherical symmetry. Extensions to non-

spherical models were first discussed in [186], and more details could be found in e.g. [214]. I will also assume a matter dominated universe with $\Omega_m = 1$ and negligible pressure. The inclusion of dark energy is discussed in e.g. [174, 301]. The spherical model works given that the initial density of the sphere is larger than the dark energy density, which is true until the recent epoch. According to Birkhoff Theorem, the dynamics of a spherical mass distribution can be described by the homogenous and isotropic FRW metric. Thus, Eq.1.15 applies and the *proper* radius of the overdense sphere enclosing mass M satisfies the equation of motion:

$$\ddot{r} = -\frac{GM}{r^2}. \tag{1.80}$$

The equation has the parametric solution

$$r = A(1 - \cos\theta), \tag{1.81}$$

$$t = B(\theta - \sin\theta), \tag{1.82}$$

where $A^3/B^2 = GM$.

Linear theory is recovered close to $t = 0$. Expansion in small θ gives $r(t)$ in the linear regime:

$$r \approx \frac{A}{2}\left(\frac{6t}{B}\right)^{2/3}\left[1 - \frac{1}{20}\left(\frac{6t}{B}\right)^{2/3}\right]. \tag{1.83}$$

The leading order term is $r \propto a(t) \propto t^{2/3}$, consistent as found in Section 1.2.1. The second term implies an overdensity

$$\delta^{\rm L} \approx \frac{3}{20}\left(\frac{6t}{B}\right)^{2/3}, \tag{1.84}$$

which is also what we found in Section 1.3.1.

As the sphere continues to expand, it soon reaches two critical phases. The first phase is at $\theta = \pi$, where a maximum radius $r = 2A$ is reached at time $t = \pi B$, known as the *turnaround*. At this point, the linearly extrapolated density of the sphere is $\delta^{\rm L} \approx 1.06$, i.e., linear theory already fails at this time. Past this point, the radius begins to shrink. The second phase is at $\theta = 2\pi$, where $r = 0$ and $t = 2\pi B$, i.e. the sphere now collapse into a singularity. By the time of collapse, the linearly extrapolated overdensity is

$$\delta_c \equiv \delta^L(\theta = 2\pi) = \frac{3}{20}(12\pi)^{2/3} \approx 1.69, \tag{1.85}$$

whereas the actual overdensity of the sphere is

$$1 + \delta = \frac{r_L^3}{r^3} = 18\pi^2 \approx 178. \tag{1.86}$$

In a real physical situation, an overdense sphere rarely collapses to a singularity because this would require perfectly spherical orbits and no fluctuations in the density or gravitational potential. Rather, the sphere would *virialise* and reach equilibrium. According to Virial Theorem this happens when the potential energy of the sphere is twice its kinetic energy at $\theta = 3\pi/2$. The spherical collapse model thus says that a region with an extrapolated linear density $\delta > \delta_c$ would collapse and form a virialised region with an actual density that is ~ 200[6] times the background density ρ_c (Eq. 1.18). These collapsed regions are called *dark matter haloes*.

Halo mass function

Based on spherical collapse, Press & Schechter [232] proposed a model for the number density of dark matter haloes in a given mass range and redshift. In this model, the probability to find the overdensity between δ and $\delta + d\delta$ in a sphere of radius R at redshift z is given by a Gaussian distribution:

$$P(> R, z)\, d\delta = \frac{1}{\sqrt{2\pi}\sigma_R(z)} \exp\left(-\frac{\delta^2}{2\sigma_R^2(z)}\right) d\delta, \tag{1.87}$$

where $\sigma_R(z)$ is given by Eq.(1.63). This parameter is often quoted as a function of mass enclosed by the radius, $M = 4\pi\rho_m R^3/3$. In Eq. 1.87, I have used $> R$ because the variance is calculated by 'blurring' out structures smaller than the scale R, thus only haloes larger than this scale would contribute to the probability. We also notice that σ_R would be a decreasing function of R or M – a larger smoothing would reduce the variance of the perturbation. The fraction of collapsed matter at redshift z with radius $> R$ is then given by integrating this function from δ_c

$$F(R, z) = \int_{\delta_c}^{\infty} P(R, z)\, d\delta = \frac{1}{2}\mathrm{erf}\left(\frac{\nu(R, z)}{\sqrt{2}}\right), \tag{1.88}$$

[6]It is common to use $\rho = 200\rho_c$ to define the virialised mass, often referred to as M_{200}, although some literature adopt $\rho = 178\rho_c$ at the time of collapse.

where the peak height ν is given by

$$\nu \equiv \frac{\delta_c}{\sigma_R(z)}. \tag{1.89}$$

This expression receives a factor of two correction [32, 77, 209]. A qualitative explanation is that at fixed redshift, when $\nu \to 0$ corresponding to the low mass end, we expect that all matter would have collapsed, thus $F \to 1$.

The number density of haloes at redshift z with mass larger than M can then be calculated, which is simply given by $n(M, z) = 2(\rho_m/M)F(M, z)$. It is more commonly expressed as the differential number density per logarithmic mass bin, or known as the *halo mass function*:

$$\frac{dn(M, z)}{d\ln M} = \sqrt{\frac{2}{\pi}} \frac{\rho_c \Omega_m}{M} \frac{d\ln \sigma_M^{-1}}{d\ln M} \nu e^{-\nu^2/2}. \tag{1.90}$$

Adopting the power spectrum in the form Eq. 1.64 with $n_s = 1$, the M dependence of the variance is:

$$\sigma_M^2 \propto \int_0^\infty |T(k)|^2 |f(kR(M))|^2 k^3 dk. \tag{1.91}$$

For large mass, the integral is dominated by small k, for which $T(k) \to 1$. Then by a simple change of variable, $\sigma_M^2 \propto R^{-4} \propto M^{-4/3}$. For low mass, the integral is dominated by large k, where $T(k)$ falls as $\ln k/k^2$ [127], so the overall behaviour is $\sigma_M^2 \propto \log R$. Therefore, Eq.(1.90) falls roughly as a power law of M at small mass, and exponentially at large M. This behaviour is in general agreement with observations [279] and numerical simulations, although deviations are reported in [102, 132, 159], and generalised forms are proposed, for example, the Sheth-Tormen mass function [266].

Nevertheless, this model has a few implications. Firstly, it implies that structures are formed in a hierarchical manner: lower mass objects form first, and larger mass objects are formed later via mass accumulation or merging between different haloes. Another implication is that the number density of haloes is cosmology dependent. Specifically, the shape at the high mass end, corresponding to clusters and superclusters, is highly sensitive for parameters such as Ω_m. Thus, cluster counts are used to constrain cosmology, e.g. [2, 17], although a range of observational systematics such as mass calibration and sample completeness can greatly complicate the analysis.

Halo profile

The mass distribution inside a dark matter halo can be extracted from N-body simulations. It was first shown in [193] that the profile has a universal form even across different simulations, which can be fitted by the following Navarro-Frenk-White (NFW) profile:

$$\rho(r) = \frac{\rho^*}{(r/r^*)(1 + r/r^*)^2}, \tag{1.92}$$

where ρ^* and r^* are free parameters. When $r \gg r^*$, ρ decays as $\propto 1/r^3$ and the total mass enclosed diverges logarithmically; when $r \ll r^*$, the density diverges as $1/r$. This behaviour at $r \to 0$ is referred to as *cuspy*. The halo mass profile can be inferred from the profile of galaxies and galaxy clusters, although interpretations should be taken with care. In the case of galaxies, baryonic effects are important near the galaxy centre, and observations have suggested a core rather than cusp in the centre. The profiles measured from galaxy clusters, on the other hand, show good agreement with the NFW profile [166]. This is often referred to as the core-cusp problem.

The NFW profile is often expressed in terms of the virial radius r_{200}, which corresponds to the radius within which the mean density is 200 times the critical density $\rho_c(z)$, and the *concentration* parameter, defined as

$$c \equiv \frac{r_{200}}{r^*}. \tag{1.93}$$

The NFW profile deviates from simulations at small scales, where it underestimates the actual density, and the true relation should be much steeper [91]. A number of profiles are subsequently proposed to capture this trend, e.g. [194, 195], and a commonly adopted profile is [194]:

$$\ln\left(\frac{\rho_\alpha}{\rho_{-2}}\right) = -\frac{2}{\alpha}\left[\left(\frac{r}{r_{-2}}\right)^\alpha - 1\right], \tag{1.94}$$

where α is a free parameter and r_{-2} is a characteristic radius at which the slope of the profile $d\ln\rho/d\ln r = -2$. This fitting formula can capture a variety of trends with different α.

Halo bias

The statistical distributions of dark matter haloes are different from those of the matter density field – haloes only form at peaks of the density field. Thus, the density fluctuations measured from haloes δ_h are *biased* compared to δ. This difference is captured by the bias parameter which can depend on the halo mass and redshift,

$$\delta_h = b(M, z)\delta. \tag{1.95}$$

Notice that this is only true for linear scales. On small scales, the bias can take the non-linear form [148].

In the spherical collapse model, overdense regions, given a smoothing scale of R, with $\delta_R > \delta_c$ collapse to form haloes. However, objects that reside in large-scale overdensity collapse sooner than in large-scale underdensity. This can be understood in the picture of *peak-background split*, where we split the density perturbation into large and small scale components, $\delta = \delta_L + \delta_S$. In the absence of δ_L, the region would collapse if $\delta_S > \delta_c$. With a slightly positive δ_L, the region could collapse with $\delta_S < \delta_c$, and vice versa for a slightly negatively δ_L. This is equivalent to modulating δ_c for the large scale modes. Let $F(> \nu)$ be the cumulative collapsed fraction as in Eq. 1.88, and $G = -dF/d\ln\nu$ be the collapsed fraction between $\ln\nu$ and $\ln\nu + d\ln\nu$. Given a small change ϵ in δ_c, the collapsed fraction changes to $\Delta G = -(\partial G/\partial\delta_c)\epsilon = -(dG/d\ln\nu)\epsilon/\delta_c$, the negative sign because $\epsilon < 0$ corresponds to a lower threshold, thus higher collapsed fraction. The Lagrangian bias is $b_L\epsilon = \Delta G/G$, and thus the bias is given by

$$b(\nu) = 1 + b_L = 1 - \frac{1}{\delta_c}\frac{d\ln G}{d\ln\nu}. \tag{1.96}$$

For the Press-Schechter formula, the bias has a simple form [53, 182]

$$b(\nu) = 1 + \frac{\nu^2 - 1}{\delta_c}. \tag{1.97}$$

The bias increase monotonically as a function of halo mass at fixed redshift given Eq. 1.89. It tends to a constant as $\nu \to 0$, and rises steeply at large ν. At fixed mass, the bias also rises with redshift. Because of the deviation of the mass function predicted from the Press-Schechter formula from simulations, often empirical formula are used (e.g., [205, 267, 289]). An example of the halo bias-halo mass relation adopting the empirical formula in [205] is shown in Fig. 1.2 at

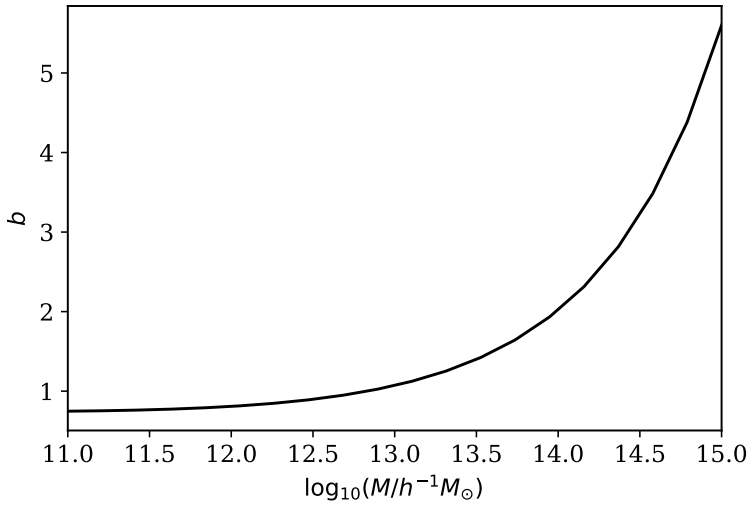

Figure 1.2 *Halo bias as a function of halo mass calculated from fitting formula given in Peacock [205].*

$z = 0$.

Given a distribution of halo masses, $f(M)$, the mean halo bias of the sample can be computed via

$$\langle b \rangle = \int f(M)\, b(\nu)\, dM. \tag{1.98}$$

If $f(M)$ is the halo mass function, then the above integral gives $\langle b \rangle = 1$.

1.3.5 From dark matter to galaxies

Dark matter haloes are not directly measurable. In practice, we could only observe luminous matter, i.e., galaxies. Because galaxies reside in dark matter haloes, we expect the galaxy density fluctuation, δ_g, to be also biased compared to the underlying matter fluctuation $\delta_g = b_g\, \delta$, similar to the haloes [302]. Again, this relation holds only on large linear scales [136], and the galaxy bias in non-linear regime can be more complicated (see discussion in [66]). On linear scales, we can measure the galaxy bias in surveys by measuring the power spectrum or correlation function, and compare it with the theoretical prediction, i.e. $P_g(k) = b_g^2\, P(k)$ and $\xi_g(r) = b_g^2\, \xi(r)$.

Observations show that galaxy bias has a strong dependence on galaxy luminosity. The measurements from SDSS survey [311] showed that the dependence resembles the mass dependence of the halo bias, implying that the galaxy luminosity is strongly correlated with the halo mass. [311] further showed that at fixed

luminosity, the galaxy bias also depends on the galaxy colour, which also strongly correlate with the age of the galaxy. The fact that red galaxies have a larger bias, or are more clustered than blue galaxies implies that red galaxies are preferentially found in higher mass haloes. Moreover, the clustering of red galaxies on small scales, in the *1-halo regime*, is further enhanced, i.e., the galaxy bias is also scale-dependent in this case. This can be explained by that large haloes would contain a central galaxy that is likely blue, and one or more satellite galaxies that are likely red. We shall come back to the colour dependence in Chapter 2.

The complex dependence of galaxy bias on galaxy properties originates from the physics of galaxy formation and evolution, for which a more detailed discussion would perhaps yield the length a whole thesis. A thorough review is given by [300]. In short, the different galaxy properties are a collaborative result of various baryonic processes, e.g. star formation, merging, and feedback from supernovae and AGN, which are also related to the formation and merging of the underlying dark matter haloes. The aim of studying the *galaxy-halo connection* is to quantify statistically the relation between galaxy and halo properties. Empirical methods include abundance matching [296], i.e., matching galaxy properties such as stellar mass to the halo mass by rank and studying the stellar mass to halo mass ratio (SHMR), halo occupation distribution (HOD) [210], i.e., specifying the probability of finding a number of galaxies given the halo mass, and conditional luminosity function [309], i.e., specifying the galaxy luminosity function given the halo mass. These methods can also be applied to dark-matter-only simulations to produce realistic mock galaxy catalogues. With the aid of hydrodynamical simulations and semi-analytic models, these baryonic processes can also be studied in detail (see [278] for a thorough review). Due to the complicated nature to predict galaxy bias, it is usually treated as a free parameter, or relevant parameters in the galaxy properties are marginalised over in cosmological studies.

1.4 Current cosmological constraints

1.4.1 The distance ladder

We have seen in Section 1.2.2 that the distance-redshift relation is cosmology dependent. By measuring the distances and redshifts to galaxies independently,

one can determine the current expansion rate, the Hubble constant H_0, as well as constrain the density parameters. The earliest distance-redshift relation is measured at $z \sim 0$ from extragalactic nebulae [128, 275], and the results showed a linear relation between the radial velocity and the distance of these nebulae. The slope of this relation is gives H_0 according to Eq. 1.24. This was a direct evidence for the expansion of the Universe. To obtain more accurate measurements, one needs to extend this relation to higher redshifts, because the local relation can be affected by large peculiar velocities. While redshifts can be obtained from spectroscopic or photometric observations, the direct determination of distances are more difficult. This is achieved via the *distance ladder*: the cosmic distances are calibrated against a set of local galaxies.

The first part of the ladder extends up to the Large Magellanic Cloud (LMC), about 50 kpc away. Its distance can be most precisely determined via the illuminated ring from the explosion of Supernova 1987A. The inclination of the ring can be determined from its ellipticity (since the ring is expected to be almost circular), and the size of the ring can be estimated via the time delay of the illumination between the close and far part of the ring. These together determines the physical size of the ring, which can then be turned into a radial distance given the apparent angular size. Another precise distance determination to the LMC is using eclipsing binaries for late-type stars [222]. For these stars, the angular size can be determined using accurately calibrated relation between their surface brightness and colour. This angular diameter distance can then be compared to the dimension obtained from spectroscopic or photometric data. These methods give the distance to LMC up to 2%.

The next part of the ladder comes from the calibrated period-luminosity relation of Cepheids – a type of highly luminous pulsating stars. The distance can be extracted from the luminosity L given the observed flux or apparent magnitude (Eq. 1.27). This relation is calibrated accurately to few percent level using a large sample of Cepheids found in galaxies with known distance, such as LMC and NGC 4258 (at a distance of ~ 7 Mpc). Due to the high luminosity, Cepheids can be observed at large distance, thus extending the distance-redshift relation to higher redshifts.

The furthest part of the ladder consists of the light curves of Supernova Type Ia (SNe Ia). SNe Ia are explosions of white dwarfs – stars at the end of their evolution that are highly compact and supported by electron degeneracy pressure only. White dwarfs explode when if their masses exceed the Chandrasekhar limit,

about $1.4M_\odot$. It is expected then that all SNe Ia undergo similar physical process, thus their maximum luminosity and light curve would be the same. However, this is not entire true as pointed out in [112, 221] – there is a (correlated) scatter observed in maximum luminosity and the shape of the light curve. Fortunately this can be carefully calibrated [88, 220, 241]. Due to their high luminosity, SNe Ia can be observed to as far as $z \sim 1$. At this scale, the local Hubble law is not valid and one needs the full expression of $H(z)$ (Eq. 1.14) which depends on the density parameters. The high redshift SNe Ia measurements preferred $\Omega_m \sim 0.3$ and $\Omega_\Lambda \sim 0.7$, thus provided a direct piece of evidence for a non-zero dark energy and the accelerated expansion of the Universe [219, 242]. Fig. 1.3 shows a recent compilation of the distance ladder measurements of the distance-redshift relation in [243].

More recent measurements on the Hubble parameter from the distance ladder yields a precision of 2%. [244] reported $H_0 = 74.03 \pm 1.42$ km/s/Mpc from 70 Cepheids observed by the Hubble Space Telescope. We shall see that this highly precise result obtain from the low redshift universe is in tension with that measured from the early universe in Section 1.5.

1.4.2 CMB anisotropy

We have mentioned in Section 1.2.4 that the CMB is not isotropic – there are fluctuations at the order of 10μK. The primary CMB fluctuations originates from the photon-baryon interaction up to the recombination epoch, and can be understood at roughly three scales. Since the CMB fluctuations are usually analysed in spherical harmonic space (the analogue of Fourier transform on a sphere), I will quote the angular scales θ on the CMB in terms of the spherical harmonic wave number $\ell \sim \pi/\theta$. The horizon scale χ_H corresponds to $\theta \sim 1^\circ$ on the CMB sky, or $\ell \sim 100$.

At superhorizon scales, i.e., structures on the CMB with length scales $L > \chi_H$, photons and baryons only interact gravitationally through the *Sachs-Wolfe effect*: photons propagating from a high density region to a low density region are gravitationally redshifted, and vice versa. Therefore, the fluctuations in the photon frequency corresponds to those in the matter density, and the temperature power spectrum would have the same shape as the matter power spectrum at $\ell \lesssim 100$. Below the sound horizon at recombination, $L \lesssim \chi_s = \chi_H/\sqrt{3}$, baryons and photons behave like coupled fluid and the density fluctuations oscillate, as

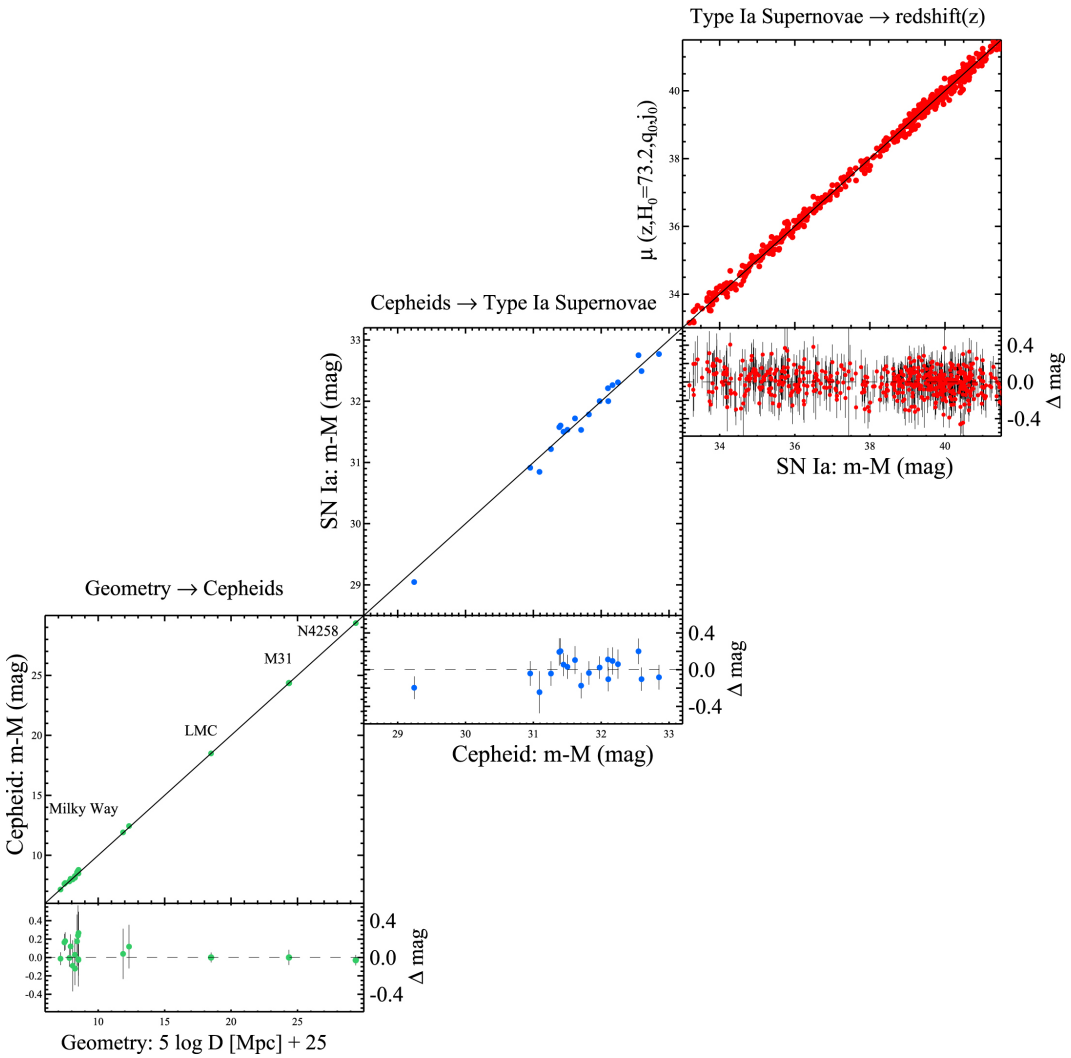

Figure 1.3 *The distance ladder adopted from Riess et al. [243]. The x-axis shows calibrated distance which are used to calibrate the distance indicators on the y-axis via absolute magnitude M or Hubble parameter H_0.*

mentioned in Section 1.3.2. The wavelength that can experience a full oscillation at this epoch is the sound horizon, and subsequent smaller wavelengths are present at integer multiples of the corresponding frequency. These waves are shown as *acoustic peaks* on the CMB power spectrum, with the first peak located around $\ell \sim 200$. Although we have assumed $\Omega_m = 1$ in this case, in general, the location of the peak is (most) sensitive to the curvature parameter Ω. The precise determination of the peak positions in combination with CMB lensing [7] thus put a tight constraint on the curvature $1 - \Omega = -0.0027^{+0.0039}_{-0.0038}$ [123], suggesting that the Universe is very close to flat. Lastly, recombination did not happen instantaneously – the last scattering surface has a finite width of $\Delta z \sim 80$ due to the finite mean free path of the photons. This scale $\theta \sim 5'$, or $\ell \sim 2500$, is the smallest scale where anisotropic structures can be resolved. At small scales, photon diffusion also causes *Silk damping* [270], which damps the acoustic peaks exponentially at small scales. A thorough review of the CMB features can be found in [126].

The CMB temperature power spectrum (TT) is shown in Fig. 1.4, where the data points are measured by the *Planck* satellite [227]. The above features are clearly present, and the agreement between data and theory is remarkable. The cosmological dependence of these features gives the tightest parameter constraints so far: $\Omega_c h^2 = 0.120 \pm 0.001$, $\Omega_b h^2 = 0.0224 \pm 0.0001$, $n_s = 0.965 \pm 0.004$, $H_0 = 67.4 \pm 0.5\,\mathrm{km\,s^{-1}\,Mpc^{-1}}$ and $\sigma_8 = 0.811 \pm 0.006$. In addition, the CMB power spectrum in combination with other cosmological probes also provide constraints on the optical depth of reionisation, the dark energy equation of stats, relativistic effective degree of freedom, and upper limit of neutrino mass.

There are additional CMB probes. For example, the polarisation of the CMB photons is measured by *Planck*. Its auto power spectrum (EE) and the cross power spectrum with temperature (TE) show excellent agreement with the best-fit model determined from TT only [227]. Secondary CMB fluctuations are also be explored: these are the perturbations to the CMB photons due to large scale structures and ionised gas from the recombination epoch to today. Such effects include CMB lensing, Integrated Sachs-Wolfe (ISW) effect, and Sunyaev-Zel'dovich (SZ) effect. The former two will be discussed in more detail in Chapter 3. A general discussion of the CMB anisotropy and its measurements can be found in [256].

[7] Without lensing, the curvature parameter is degenerate with other parameters such as Ω_Λ and h, as discussed in detail in [73].

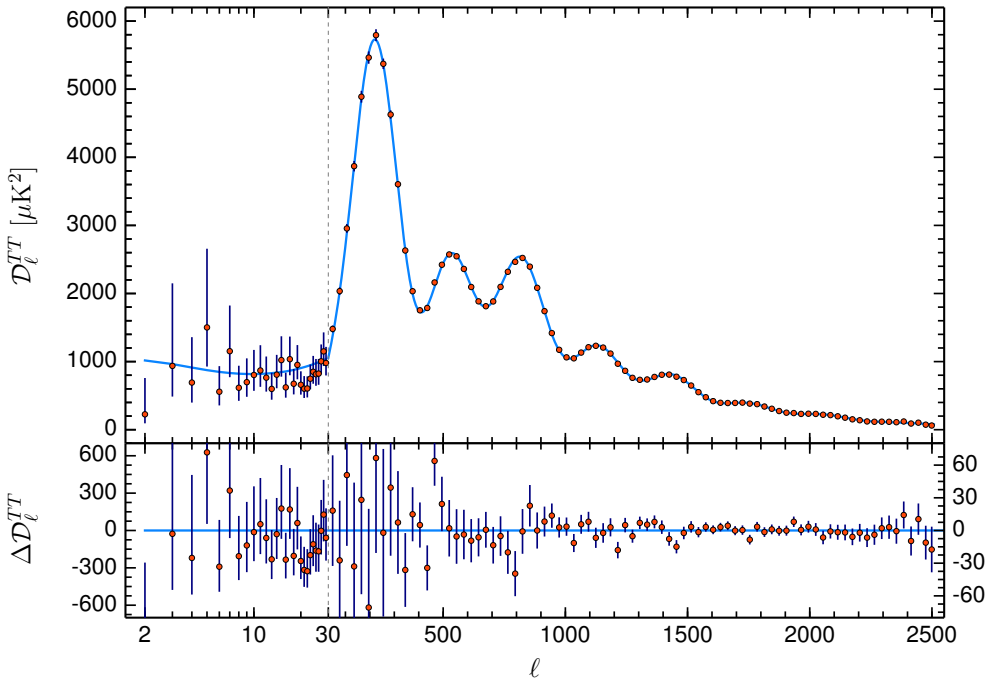

Figure 1.4 *Upper: The CMB temperature power spectrum adopted from Planck Collaboration et al. [227]. The measured data are shown in red dots and the best-fit theory is shown in blue. Lower: The residual difference between data and best-fit theory.*

1.4.3 BAO

The sound wave from the coupled baryon-photon plasma before recombination is also visible in the correlation function ξ, as we saw in Section 1.3.2. This Baryon Acoustic Oscillation (BAO) has a characteristic comoving scale $d_s \sim 150\,\mathrm{Mpc}$ (Eq. 1.69). The exact location of this peak at a given redshift provides a direct measure for the geometry of the Universe. Therefore, BAO is also referred to as the *standard ruler*.

BAO can be measured in the 3D galaxy correlation function using large redshift surveys (e.g. [12, 75, 218, 320]). At the BAO scale, linear galaxy bias is a good approximation, thus the shape of the matter power spectrum can be measured. At a given redshift z, the scale transverse to the line-of-sight gives the angular diameter distance $D_A(z)$, whereas the direction along the line-of-sight gives the comoving separation $cz/H(z)$. Thus, the result is usually presented as the spherically averaged BAO scale

$$D_V(z) = \left(D_A^2(z) \frac{cz}{H(z)} \right)^{1/3} . \tag{1.99}$$

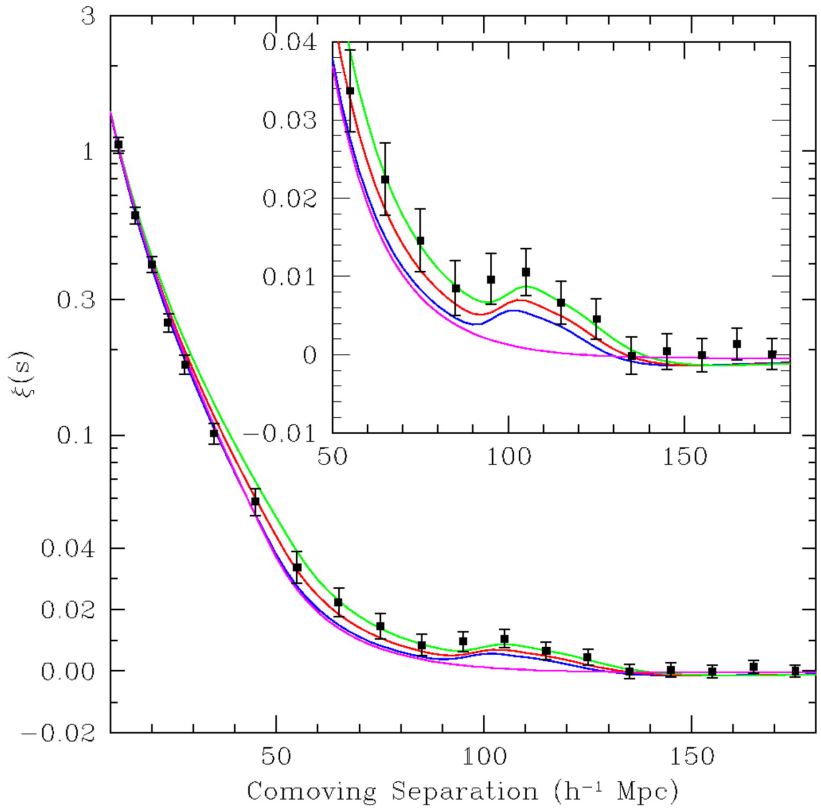

Figure 1.5 *The measured correlation function of luminous red galaxies in SDSS (black data points), adopted from Eisenstein et al. [75]. The solid lines of different colours show theoretical prediction with different $\Omega_m h^2$: 0.12 (green), 0.13 (red), and 0.14 (blue), with other parameters fixed. The magenta line shows a pure CDM prediction, where the BAO peak is absent.*

Fig. 1.5 shows one of the first measurements of the BAO from the SDSS luminous red galaxies [75], where the feature is clearly visible and the BAO scale is constrained up to 5%.

In principle, the peak position can be affect by the peculiar velocity of the galaxies. Due to the large scale and low amplitude of the BAO peak, it is also difficult to measure with high statistical significance in practice. Thus, it is a common practice to use the *reconstruction* technique, where the measured galaxy density fluctuation is 'moved back' according to the inferred peculiar velocity from gravitational potential, allowing the original density field to be reconstructed [76, 263]. The application to the SDSS DR7 data has improved the measurement precision of D_V from 3.5% to 1.9% [203]. The inferred distance-redshift relation from the BAO measurements gives cosmological parameter constraints that

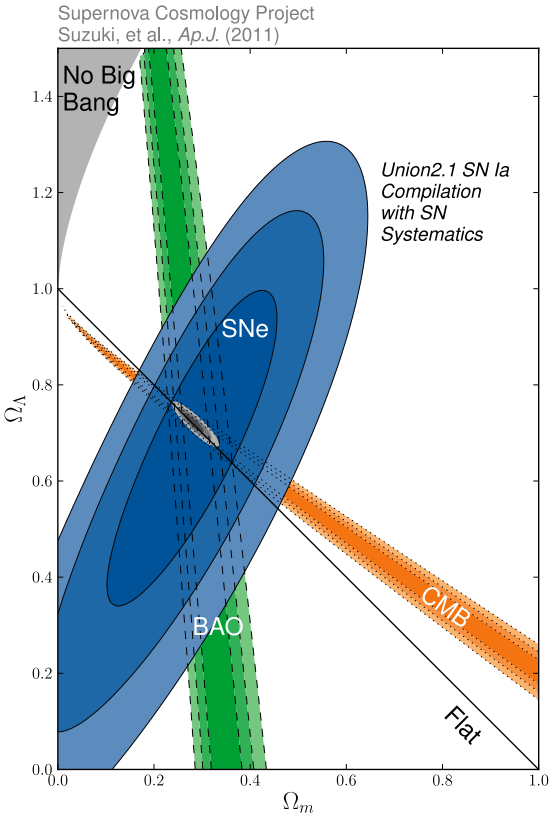

Figure 1.6 *The combined constraints on matter and dark energy density from various different cosmological probes, adopted from the Supernova Cosmology Project and Suzuki et al. [281]. Due to the different degeneracy directions, the combination provides a tight constraints on the two parameters.*

are consistent with those obtained from the CMB probes [16, 320], providing independent and strong evidence for the ΛCDM model.

The constraints on Ω_m and Ω_Λ from the probes that have been described so far are shown in Fig. 1.6.

1.4.4 RSD

The afore mentioned distance ladder and BAO are *geometric* probes of the Universe, i.e. they constrain cosmological parameters via determining a particular scale. RSD, on the other hand, is a *dynamical* probe, where cosmological information in velocities are used. As mentioned in Section 1.3.3, the measured galaxy redshift consists of a component from Hubble flow and a component from peculiar velocities. The radial distances determined from redshifts are 'distorted', leading to an anisotropic 2-point correlation function.

The RSD effect can be understood intuitively by considering the line-of-sight peculiar velocity on two scales as follows. On linear scales, the Kaiser effect (see Section 1.3.3) dominates. Taking a spherically symmetric distribution of galaxies in a cluster, the galaxies have a infall velocity towards the centre of the cluster due to gravity. A galaxy closer to us would then have a slightly lager redshift and consequently a larger apparent distance due to the infall velocity, whereas a galaxy further away would have the velocity pointing the opposite direction, giving a smaller apparent distance. Therefore, the apparent pair separation shortens along the radial direction, leading to a squashing effect along the line of sight in the measured $\xi(r_p, \pi)$. On smaller scales, the 'Fingers of God' effect dominates – these elongated filament-like structures are apparent in galaxy distributions such as Fig. 1.1. Take the spherical cluster as an example, now focusing on the inner virialised region, where galaxies have large velocity dispersions. These velocities move the galaxies around over a large range in redshift space, increasing significantly the pair separation, and giving rise to an elongated smearing effect at small r_p in $\xi(r_p, \pi)$. The two features can be observed clearly in the 2D anisotropic correlation function measured from the 2dF Galaxy Redshift Survey [117, 211] shown in Fig. 1.7.

Cosmological information is encoded in the peculiar velocity on the linear scale through the growth rate f of the large scale structure (Eq. 1.51). To account for galaxy bias, the measured distortion parameter is $\beta = f/b_g$. Because galaxy bias and the normalisation of the power spectrum is degenerate, such that $b_g\sigma_8 =$ const, the measurement can also be recast into constraint on $f(z)\sigma_8(z)$ at redshift z. The dependence on z can be used to constrain the power γ in $f \sim {\Omega_m}^\gamma$. A deviation from $\gamma \approx 0.55$ could indicate deviation from GR, such as modified gravity [20, 84]. Recent constraints on $f\sigma_8$ over a wide range of redshift have a percent level precision and are consistent with the concordance cosmological model (see Fig. 1.8). Interpreting the RSD measurements on smaller scales is challenging – the main difficulties are accounting for the non-linearities in the coupling of density and velocities as well as scale-dependent galaxy bias. However, going into smaller scales have the advantage of a greatly improved signal-to-noise. Thus, improved non-linear models have been considered in e.g. [133, 258, 283]. I will introduce some of these models in Section 2.2.

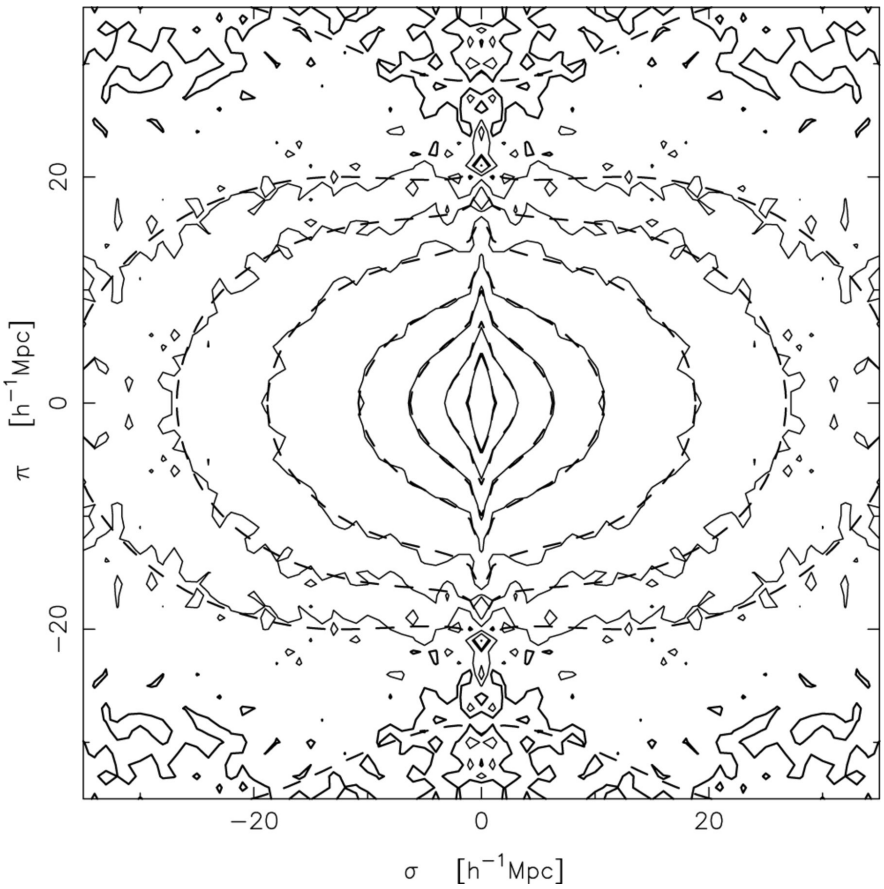

Figure 1.7 *The measured 2D correlation function from the 2dF Galaxy Redshift Survey, adopted from Hawkins et al. [117]. (σ, π) denotes the directions perpendicular and parallel to the line of sight respectively. The smooth dashed contour levels show the best-fit model.*

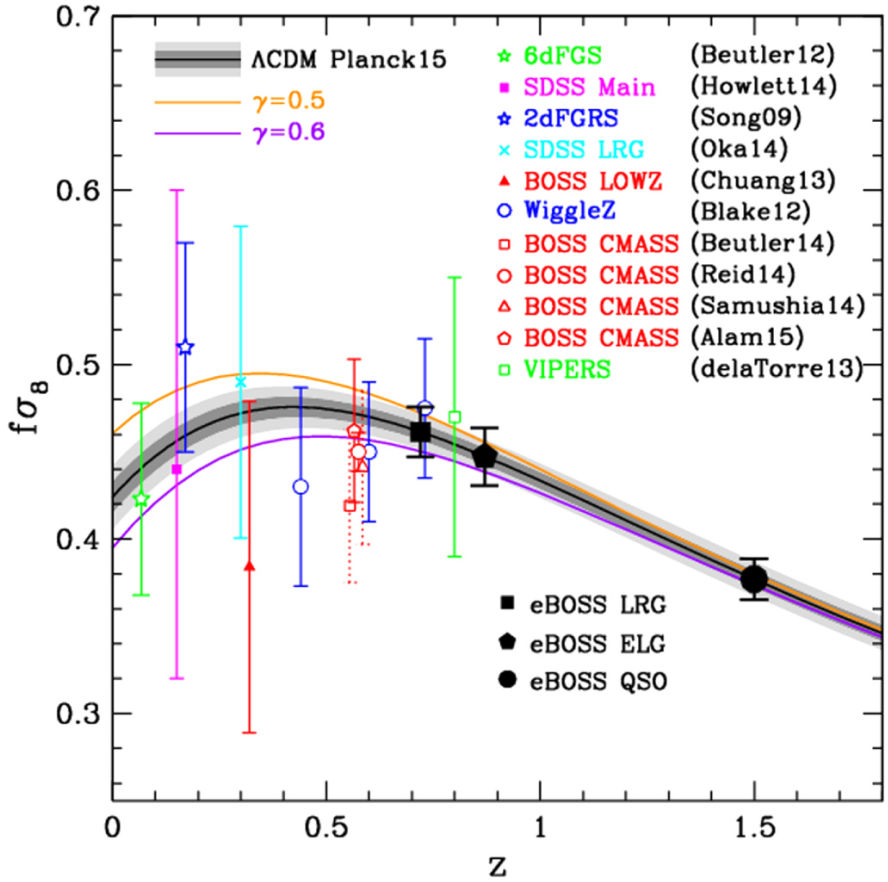

Figure 1.8 *Constraints on the growth rate $f\sigma_8$ from various redshift surveys adopted from Dawson et al. [64]. The solid line with grey band shows the ΛCDM prediction from the* Planck *2015 parameters.*

1.4.5 Weak lensing

The light from distant galaxies can be deflected along its path by the gravitational tidal fields generated by large scale structures. Thus, the image of an observed galaxy can be distorted. In the presence of a large galaxy cluster, for example, the background galaxy can be deformed into multiple ring-like images. The deformation allows one to deduce the mass of the foreground lens. This phenomenon is called *strong* lensing. The same can happen when the gravitational field is weak, generated by the matter perturbations along the line of sight, hence *weak* lensing. In this case, the photons are deflected multiple times with tiny deflection angles, and the resultant distortions are only at percent level. However, just as powerful as strong lensing, weak lensing allows us to infer *directly* the projected matter fluctuation along the path of the photons without the complication of galaxy bias. In order to measure this signal, however, one needs not only excellent image quality, but also averaging over a large ensemble of galaxies, because each galaxy would have an intrinsic shape that is in general not circular. The measured distortion is called *cosmic shear*. For a detailed review see [19].

The distortions of galaxies due to large scale structures are correlated: at higher density peaks, the distortions are stronger. Thus, the shear correlation function $\xi_+(\theta)$, which measures the excess shear between pairs with respect to a random distribution, has information on the matter power spectrum $P(k)$. Through the Poisson equation (Eq. 1.45), the potential is related to the density perturbation via $\Phi_k = (3/2)H_0^2\,\Omega_m\,\delta_k/k^2$, thus the measurement is highly sensitive to the total matter density Ω_m and the total clustering σ_8. The lensing kernel is a function of distance, thus the distance-redshift relation gives additional dependence on Ω_m. In particular, the signal depends on the combination $S_8 = \sigma_8(\Omega_m/0.3)^q$, where $q \approx 0.5$.

There are two major systematics in weak lensing. One is instrumental – the point spread function (PSF) smears the image of the galaxies (it could easily overwhelm the lensing signal) and needs to be corrected before one can extract the galaxy shape parameters. The other one is of astronomical origin, called the *intrinsic alignment*. Suppose the observed shear is given by an intrinsic term plus the cosmic shear: $\epsilon_o = \epsilon_i + \gamma$. The shear correlation function has the following components:

$$\langle \epsilon_o^1 \epsilon_o^2 \rangle = \langle \epsilon_i^1 \epsilon_i^2 \rangle + \langle \epsilon_i^1 \gamma^2 \rangle + \langle \gamma^1 \epsilon_i^2 \rangle + \langle \gamma^1 \gamma^2 \rangle, \tag{1.100}$$

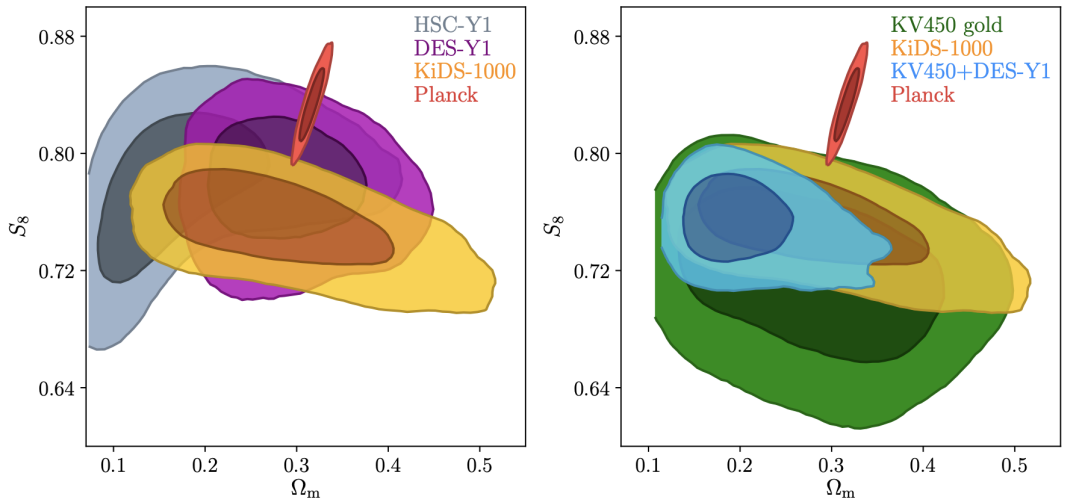

Figure 1.9 *The constraints in the parameter plane $S_8 = \sigma_8(\Omega_m/0.3)^{0.5}$ and Ω_m from several weak lensing surveys and the Planck 2018 cosmological result, adopted from Asgari et al. [15].*

where the superscripts 1 and 2 denote the two galaxies in the pair, and $\langle ... \rangle$ denotes the average over all such pairs. The first term corresponds to the correlation between intrinsic shapes of the two galaxies. This term is contributed by very nearby galaxies influenced by the same local gravitational tidal field. The second and third term arise from pairs that are separated at different redshifts. Because shear is sensitive to the projected tidal fields, γ^1 of the galaxy at higher redshift is affect by the tidal field at the lower redshift, which then correlates with ϵ_i^2 of the other galaxy. What we are interested in is the last term corresponding purely to cosmic shear $\langle \gamma^1 \gamma^2 \rangle$. Although the first few terms are of lower order compared to the last term, they need to be carefully accounted for to achieve high precision and reliable results. Efforts in conducting such careful weak lensing analysis include the Canada-France-Hawaii Lensing Survey (CFHTLenS; [139]), the Kilo-Degree Survey (KiDS; [95, 121]), the Dark Energy Survey (DES; [291]), and the Hyper Suprime-Cam (HSC; [108, 119]). The cosmological constraints from these weak lensing experiments are summarised in Fig. 1.9, and the most up-to-date S_8 parameter is measured to be $S_8 = 0.759^{+0.024}_{-0.021}$ from the KiDS-1000 survey [15].

1.5 Beyond the standard model

It is impressive how various cosmological probes presented in Section 1.4 turned out to provide consistent parameter constraints over the last few decades. This has established the ΛCDM model as the standard cosmological model – any proposal beyond this standard model has to also pass all of these independent observational tests, which is truly non-trivial. On the other hand, with better technology and larger telescopes, the constraints have reached a sufficiently high precision that in recent years, two major tensions have emerged within the ΛCDM paradigm.

The H_0 tension: The measurements of the Hubble constant H_0 from the early and late universe disagree with each other. The late universe measurements, favouring $h \sim 0.74$, consists mainly of the distance ladder (see Section 1.4.1), reaching a precision of $1-2\%$. Recently, measurements from strong lensing time-delay (e.g., [29, 306]) also provide independent constraints with competitive precision of 2.4%. The early universe measurements, preferring $h \sim 0.68$, mainly come from the CMB analysis by the *Planck* Collaboration (see Section 1.4.2) and BAO (see Section 1.4.3) in combination with other probes such as BBN. As shown in Fig. 1.10, the two sets of measurements are consistent within their own groups, but are discrepant from each other at 4.4σ as claimed by [244]. This corresponds to a ~ 0.002 probability that this discrepancy is due to a statistical fluctuation. It is noticeable that recently the detections of gravitational wave allow another measure of the distance. If the electromagnetic counterpart of the gravitational wave event can be identified, then one can measure H_0, a method referred to as *gravitational-wave standard siren* [1, 48, 257]. Currently, the constraints on H_0 provided by this method is rather wide, but within the next few years with more detections of such events, it is expected that this independent method will provide competitive constraints.

'Lensing is low': This is a tension in the $\Omega_m - \sigma_8$ parameter plane between several weak lensing measurements and the CMB results from the *Planck* Collaboration. As can be seen from Fig. 1.9 (it shows the $S_8 - \Omega_m$ plane instead), while some surveys such as DES-Y1 and HSC-Y1 are consistent with *Planck*, the recent KiDS-1000 and a combination of the lensing surveys (KV540+DES-Y1) show a discrepancy at 3σ level [15]. Discussion regarding to the tension from these measurements can be found in e.g. [134, 292]. We will come back to this topic in Section 5.2.5.

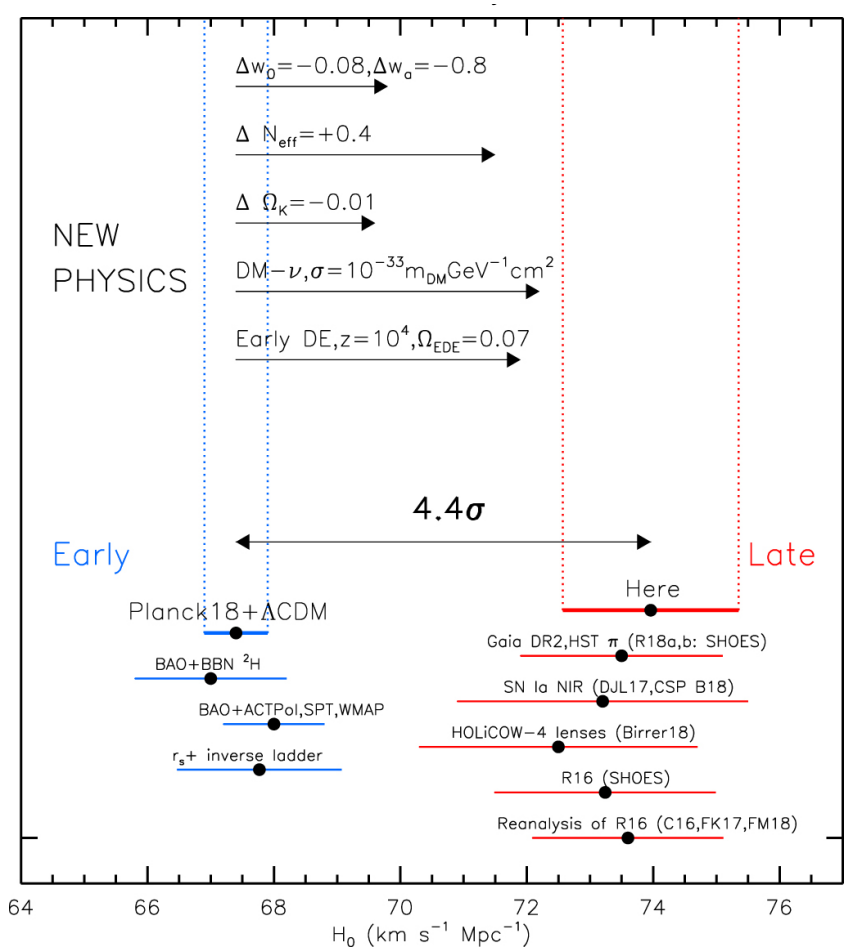

Figure 1.10 *The measurements of the Hubble parameter H_0 split by the early- and late-universe probes adopted from Riess et al. [244]. The black errors on the top shows several non-standard models which reduce the 4.4σ tension between the early-universe (blue) and late-universe (red) measurements.*

The origin of the these tensions is not yet clear. A first and conservative explanation is systematic errors not accounted for by either one of or both groups of experiments. There have been many efforts devoted to check the robustness of these results from both sides, while none of the systematic errors investigated are large enough to close the gap (e.g. [74, 122, 244]). A bolder step would be to seek explanations beyond the standard ΛCDM model. For example, a few suggestions to ease the Hubble tension are listed on top of Fig. 1.10: (a) A change in the dark energy equation of state Δw_0, or time-dependent equation of state, Δw_a, where the equation of state is modified to $w(a) = w_0 + a\Delta w_a$; (b) A change in the effective number of relativistic species $\Delta N_{\rm eff}$; (c) A slightly open universe $\Delta\Omega_k < 0$; (d) Dark matter interaction with a cross-section of σ; (e) Early dark energy at redshift $z = 10^4$. A thorough review on possible extensions to the ΛCDM model can be found in e.g., [187, 236].

1.6 Statistics

1.6.1 Bayesian inference

There are two main types of statistical inferences: frequentist and Bayesian. The frequentist's approach refers to obtaining the probability of an event by repeated measurements. A simple example is flipping a coin – by flipping the coin many times, the number of appearances of head and tail tends to the same, indicating that the probability of getting either is 1/2. This method, however, does not work well for small samples, and certainly does not work for cosmological inferences, because there is only one observable universe. For this reason, Bayesian inference, based on Bayes' theorem, is widely adopted in cosmology. The Bayes' theorem states that, for two events A and B, the conditional probability of A given B satisfies

$$P(A|B) = \frac{P(A)P(B|A)}{P(B)}. \tag{1.101}$$

In the context of cosmological analysis, A and B correspond to model (M) and data (D) respectively, where the model depends on a set of parameters θ. The function $P(M(\theta)|D)$ is the *posterior*, which tells us the probability distribution of the model parameters given the data, and it is what we are most interested in. The function $P(M(\theta))$ is the *prior*, indicating our *a priori* knowledge on the parameters. For example, if a parameter is measured from other experiments to

be $\theta \pm \Delta\theta$, then a Gaussian prior can be used with mean and std of the measured value. It is also common to adopt a *flat* or *uniform* prior, where no knowledge is assumed at all for the parameter, except perhaps for a plausible (wide enough) upper and lower bound. The function $P(D|M(\theta))$ is proportional to the *likelihood* $\mathcal{L}$, which can be calculated from assessing the goodness of fit of the model to the data. Let the observables be an N-dimensional vector $\mathbf{y}$, and let $\mathbf{y}_m$ be the value of these observables obtained from the model. Defining $\mathbf{v} = \mathbf{y} - \mathbf{y}_m$, the likelihood is given by

$$\mathcal{L} = \frac{1}{(2\pi)^{N/2}|\mathbf{C}|^{1/2}} e^{-\mathbf{v}^T \mathbf{C}^{-1} \mathbf{v}/2}, \tag{1.102}$$

where $\mathbf{C}$ is the *covariance matrix*. The covariance matrix can be computed analytically if Gaussian distribution is assumed. However, non-Gaussianity can arise on small non-linear scales. In this case, the covariance can be estimated from mock realisations. For M such realisations labelled by the superscript k, the covariance is given by

$$C_{ij} = \frac{1}{M-1} \sum_{k}^{M} (v_i^k - \bar{v}_i)(v_j^k - \bar{v}_j), \tag{1.103}$$

where $\bar{\mathbf{v}}$ is the mean of the realisations. It is noticeable that $\chi^2 = \mathbf{v}^T \mathbf{C}^{-1} \mathbf{v}$. Therefore, if $\mathbf{C}$ is not sensitive to change in model parameters, then $\ln \mathcal{L} = \text{const} - \chi^2/2$, and so maximising the likelihood is the same as minimising the χ^2. Finally, $P(D)$ is a probability that depends on the data only. Therefore, for parameter inferences, it is irrelevant and can be simply treated as the normalisation of the posterior.

1.6.2 Internal Sampling

A robust covariance matrix is thus essential for getting unbiased likelihood and posterior distribution. As mentioned above, in the non-Gaussian case, estimating an accurate covariance matrix usually requires running a large ensemble of realisations, and it can be computationally expensive. An alternative route is *internal sampling*, where subsamples of the data are used as realisations. The advantage of internal sampling is that the covariance can be estimated in a model-independent way. For more details on cosmological studies using internal sampling, see e.g. [200] for galaxy 2-point functions and [90] for cosmic shear correlation functions.

A common method is *Jackknife resampling*, where the different parts of the data are rejected to form subsamples (see [181] for a thorough review). For example, for N independent data points drawn from some distribution, we reject one datapoint each time, and form a set of subsamples each with $N-1$ points. The covariance of the full data is then estimated by the covariance of these subsamples multiplied by $N-1$ to account for correlations between different subsamples. In cosmological data, this method is usually applied at the field level – the survey region is divided into equal area units. Then one unit is masked out in turn, while the remaining $N-1$ units are treated as data subsamples that are used for data compression and analysis. The covariance matrix can then be estimated from the final products of these subsamples. Notice that this method can be cosmic variance limited, because the variations on the scale of the survey coverage or larger are not captured.

The noise in the estimated covariance matrix from finite number of subsamples can lead to singular determinant or biased likelihood and χ^2. This can be treated with *eigenvalue decomposition*. If the orthonormal eigenvectors of the covariance matrix, $\mathbf{u}_i$, are used as a basis, then the χ^2 is simply

$$\chi^2 = \sum_i^N a_i^2 \, \lambda_i^{-1}, \tag{1.104}$$

where the λ_i's are the eigenvalues of the covariance, and $a_i = \mathbf{v} \cdot \mathbf{u}_i$ are the coordinates of $\mathbf{v}$. Thus, small eigenvalues that correspond to singular modes will dominate the χ^2. One can then reject modes with $\lambda_i < \lambda_c$ for some λ_c, such that the sum in χ^2 only runs through non-singular modes.

Another way to regulate the estimated covariance matrix is employing the *shrinkage estimator* [230, 253]. In this method, the analytic covariance matrix from theory, $\mathbf{C}^{\rm th}$, is combined with the estimated covariance matrix from internal sampling, $\mathbf{C}^{\rm IS}$, via $\mathbf{C} = \alpha\mathbf{C}^{\rm th} + (1-\alpha)\mathbf{C}^{\rm IS}$, with $0 < \alpha < 1$. Although the analytic covariance matrix is noise-free, it is usually not applied directly to the analysis because it can be biased. The covariance matrix obtained from internal sampling, on the other hand, is unbiased but noisy. The parameter α can be optimally chosen such that the estimated covariance is non-singular and has minimum variance with respect to the true covariance.

1.6.3 MCMC

In a low dimensional parameter space, the posterior can be computed by a grid search in the prior space. However, when the number of parameter increases, the computation soon becomes order N^D, where N is the number of samples taken in each parameter and D is the dimension. In this case, the posterior can be efficiently computed using the *Monte-Carlo Markov-Chain* (MCMC) sampling method [162]. A commonly implemented MCMC algorithm is the *Metropolis-Hastings algorithm*. This method works by starting at a random point in the parameter space, $\mathbf{a}$ associated with a likelihood $\mathcal{L}_0$. The algorithm then takes a random step $\Delta\mathbf{a}$ to arrive at a new point with likelihood $\mathcal{L}$. If $\mathcal{L} > \mathcal{L}_0$, the new point, or *candidate sample*, is kept; otherwise, it is rejected with some probability $p < 1$ given by the probability density ratio between the new and the old points. In this way, the chain will not be trapped at minima, allowing full exploration of the parameter space. The process is then repeated, generating a *chain* of points in the parameter space that eventually converges to the maximum likelihood value. The determination of the step size $\Delta\mathbf{a}$ is crucial to the efficiency of the algorithm: steps that are too large can easily miss the minimum, while steps that are too small take a very long time to converge. The function that is used to optimise the step size is called the *proposal function*. Adjacent points in the MCMC chain are correlated, and it is common to keep points between every other or more points. The initial points of the chain are also also disregarded because they likely to be biased. This process is often referred to as *burn in*. The convergence of the MCMC chain can be tested via the *Gelman-Rubin test* [37], which assesses the variance between different chains and within the chains.

Marginalisation can be done straightforwardly with MCMC, because it generates a set of points in the parameter space with density $\rho(\mathbf{x})$ proportional to the PDF. Thus, marginalisation with respect to one parameter corresponds to summing over all points spanning that dimension, i.e., $\rho(x) = \sum_i \rho(x, y_i)$. *Pseudo-marginalisation* is sometimes applied, where instead of taking the full distribution along a dimension, the maximum likelihood value is taken. For example, for two parameters x and y, the pseudo-marginalised PDF of x is approximated to be

$$\rho(x) = \int \rho(x, y)\, dy \propto \rho\left(x, y_{\max}(x)\right). \tag{1.105}$$

1.7 Thesis outline

The aim of this chapter is to present a coherent background in cosmology and its current status. I have briefly introduced how General Relativity provides the appropriate formalism (so far) to describe space and time in Section 1.1. I then showed, in Section 1.2, that a simple cosmological model based on homogeneity and isotropy provides a good description of the observable Universe on large scales as well as the expansion history since the Big Bang. In Section 1.3, we have seen how, by introducing small inhomogeneities into the early Universe, structures can grow and evolve on linear and non-linear scales, and how this can be measured statistically using large galaxy surveys. In Section 1.4, I briefly mentioned a few main cosmological probes and their constraints on the ΛCDM model. In Section 1.5, we saw that with the shrinking error bars on the parameter, tensions have emerged. Whether this is due to systematic errors or new physics is currently unresolved, although future experiments may provide more insight into these issues. Finally, Section 1.6 briefly summarised statistical tools that are commonly adopted for cosmological parameter inference.

My work presented in the rest of this thesis fits into the big picture by further testing the theory of structure formation using galaxy survey data. The work contains two major parts. In the first part, I tested the RSD method using different density tracers represented by different types of galaxies and galaxy groups. In the second part, I measured the secondary CMB anisotropies arising from CMB lensing and ISW effect via their correlation with nearby galaxy density fields. The thesis is thus organised in the following way. In Chapter 2 I will present my work on measuring and modelling the group-galaxy cross-correlation using the GAMA survey. In Chapter 3 I will discuss in detail the CMB lensing and ISW effect, and how these are related to the galaxy density fields. To conduct such analysis, I processed data from the DESI Legacy Survey in order to produce galaxy density maps in four tomographic redshift bins. This is described in Chapter 4. The results of the cosmological analysis are presented in Chapter 5 & 6: Chapter 5 shows the angular cross-correlation between the CMB and galaxy density maps, and Chapter 6 shows the stacked CMB signal from superstructures. Finally, in Chapter 7, I give closing remarks and discuss possible future works.

Chapter 2

Group-galaxy cross-correlations in GAMA

2.1 Introduction

The large-scale structure in the galaxy distribution has a long history of providing cosmological information. The first constituents of the inhomogeneous galaxy density field to be identified were the rich clusters, which today we see as marking the sites of exceptionally massive haloes of dark matter. Further down the halo mass spectrum, we find less rich groups of galaxies, and below them systems like the Local Group that are dominated by a single L_* galaxy. All these systems have been familiar constituents of the Universe since the first telescopic explorations of the sky, but it took rather longer to appreciate that they were connected as part of the cosmic web of voids & filaments (see e.g. [206] for some selective history). In part, the history here showed a complex interaction of theory and observation, since redshift surveys through the 1980s lacked the depth and sampling to reveal the cosmic web with complete clarity. For a period, it was therefore a question of asking whether the real Universe displayed the same structures that were predicted in numerical simulations of structure formation in the Cold Dark Matter model [33]. But since those times, there has been an increasing confidence that galaxy groups are indeed particularly extreme nonlinear points in the general field of cosmic density fluctuations, and this makes them interesting in two ways. First of all, groups are readily identified in galaxy surveys, providing a relatively robust dataset; secondly, their nonlinear nature makes them an informative probe

of theory. Modelling nonlinear behaviour is by its nature challenging compared to linear theory, but by studying structure formation further into the nonlinear regime, we have the chance to test the robustness of our cosmological conclusions.

Our specific aim in this direction is to use galaxy groups as a probe of the cosmological peculiar velocity field. Such deviations from uniform expansion must exist through continuity, and density concentrations such as groups should be associated with an average infall velocity in regions surrounding the groups. The amplitude of these velocities depends in part on the strength of gravity on cosmological scales, and the peculiar velocity field has thus increasingly been seen as a means of probing the nature of gravity and testing alternative theories. Although it is possible to probe peculiar velocities directly using absolute distance indicators, the most powerful tool has been Redshift-space distortions (RSD). These arise inevitably in the study of the 3D galaxy distribution because the distances to galaxies observed on the sky are inferred from their redshifts, z, via the standard relation:

$$d(z) = \int_0^z \frac{c\,dz'}{H(z')}. \tag{2.1}$$

As we have seen in Chapter 1, this equation does not give the true distances, because Doppler shifts from the peculiar velocities modify the observed redshift: $1 + z \rightarrow (1 + z)(1 + v_r/c)$, where v_r is the radial component of the peculiar velocity. If we then use the observed redshift as if it were a true indicator of distance, we obtain a distribution of galaxies in 'redshift space' – in which the apparent properties of galaxy clustering are distorted in an anisotropic way.

As a recap, these distortions have a character that depends on scale: outside of large density concentrations, galaxies fall coherently together under gravity; while inside of haloes, the orbital velocities are effectively randomised. RSD due to coherent flows in the linear regime were first studied by Kaiser [137]. The growth factor f is defined by:

$$f \equiv \frac{\partial \ln \delta}{\partial \ln a} \simeq \Omega_m(z)^{0.55}, \tag{2.2}$$

where a is the expansion factor, and Ω_m is the matter fraction; the approximation for $f(\Omega_m)$ only applies for flat ΛCDM models in standard gravity [152]. In Fourier space, and in the small-angle limit of a distant observer, the matter power spectra in redshift space and in real space are related by:

$$P_m^s(k, \mu) = P_m^r(k)\,(1 + f\mu^2)^2, \tag{2.3}$$

where μ is the cosine of the angle between the wave-vector k and the line of sight. This simple equation was highly influential from its first appearance, as it offered the chance of measuring Ω_m from measuring the RSD anisotropy. But eventually goals shifted as Ω_m became very well determined from other routes (especially the CMB). Following [107], the modern view is therefore to emphasise that the growth rate for a given density is also proportional to the strength of gravity, so that RSD can be used as a test of theories of gravity.

RSD has been measured using various surveys to constrain cosmological parameters. For example, it was measured in the 2dFGRS survey using the dispersion model for the FOG [117, 211], and in the SDSS survey using the Gaussian streaming model [9, 238]. For the GAMA survey, Loveday et al. [170] had measured pair-wise velocity dispersion to small scales with different luminosity. The above studies had focused on galaxy auto-correlations.

The difficulty of modelling RSD is that truly linear modes are rare. In observation, large scales are affected by cosmic variance due to the finite survey volume. McDonald & Seljak [177] proposed the use of multiple tracers to beat cosmic variance, although in practice the improvement is slight because the tracer density has to be high enough such that the signal is not shot-noise dominated. Using multiple galaxy tracers to measure growth rate has been done in e.g. Mohammad et al. [185], who used blue galaxies for their reduced non-linearities, and Blake et al. [31], who used different galaxy subsamples in the GAMA survey. To gain more information, one needs to probe smaller scales, where the effect of non-linearity can systematically bias the results [319]. One of the solutions is to use galaxy groups to probe the velocity field. Due to the small random virial velocity at the group centre, the coherent large-scale infall velocities of groups are dominant down to intermediate and small scales. The the group auto-correlation would thus have negligible FOG, ideal for the extraction of linear growth rate [184, 202]. In practice, the group catalogue in GAMA is sparse and measurements of the auto-correlation will have high statistical noise. The cross-correlation between groups and galaxies can thus effectively improve the statistical power as well as reduce the non-linear pairwise velocities at small scales. The aim of the work in this Chapter is to test the robustness of RSD methods in the intermediate scales using multiple tracers. By cross-correlating galaxies of red and blue types, and groups in different mass bins, we examine the consistency of the inferred cosmological results between the subsamples. We briefly review a few RSD models in Section 2.2, and apply the extension of the Hamilton model in

configuration space proposed by Mohammad et al. [184] for the GAMA sample.

The GAMA data set and its mocks are detailed in Section 2.3 and 2.4 respectively, followed by Section 2.5 where we introduce the statistics for measuring the 2-point function in the data. In Section 2.6 we present 2D-correlation function measurements for sub-samples. In Section 2.7 we discuss modelling for galaxy-group cross-correlation: the model is validated in Section 2.7.1 with the GAMA mocks, and we present the fitting of GAMA data in Section 2.7.2. Finally, the work is summarised in Section 2.8.

2.2 RSD models

2.2.1 The streaming model

An alternative description of RSD to the linear Kaiser model (see Section 1.3.3) is the streaming model [63, 214], based on the definition that the two point correlation function is the excess probability of finding a pair of galaxies within a radius r compared to Poisson distribution. The probability of finding a pair of galaxies at two locations $\mathbf{x}_1$ and $\mathbf{x}_2$ in real space is

$$dP = \bar{n}^2[1 + \xi(r)]d^3\mathbf{x}_1 d^3\mathbf{x}_2, \tag{2.4}$$

where $\bar{n}$ is the mean number density of the galaxies. In redshift space, this is modified by a velocity distribution, $\mathcal{P}(v)$, which affects the line of sight component of the coordinate by shifting the coordinate y with $y - \mu v_{12}(r)$, where v_{12} is the scale-dependent *pairwise velocity*. Denoting redshift space coordinates as s, the probability of finding a pair is

$$dP = \bar{n}^2[1 + \xi(r)]\mathcal{P}\left(r_\pi - y - \frac{y}{r}v_{12}(r)\right)\, dy\, d^3\mathbf{s}_1 d^3\mathbf{s}_2. \tag{2.5}$$

The redshift space coordinates and the real space coordinates are related in the following way

$$s_\parallel = r_\pi = y + v_{12}/aH, \tag{2.6}$$

$$s_\perp = r_p, \tag{2.7}$$

$$r = \sqrt{y^2 + r_p^2}. \tag{2.8}$$

This gives the relation between redshift and real space two-point functions,

$$1 + \xi^s(s_p, s_\pi) = \int [1 + \xi(r)]\, \mathcal{P}\left(r_\pi - y - \frac{y}{r} v_{12}(r)\right) dy. \tag{2.9}$$

One then needs to specify the velocity distribution $\mathcal{P}$.

It was pointed out by Fisher [85] that in order for this model to be consistent with the Kaiser description in the linear regime, $\mathcal{P}(v)$ needs to be a joint Gaussian distribution of both velocity and density. The mean pairwise velocity is the weighted average of the velocity difference for each pair by density $\langle(\mathbf{v} - \mathbf{v}')(1 + \delta)(1 + \delta')\rangle$, and the dispersion is given by the second moment of the velocity $\langle v_i v_j' \rangle$. This is referred to as the Gaussian Streaming Model (GSM). In the linear theory limit

$$1 + \xi^s(s_\parallel, s_\perp) = \int [1 + \xi(r)] \frac{1}{\sqrt{2\pi\sigma_-^2}} \exp - \frac{[r_\pi - y - (y/r)v_{12}(r)]^2}{2\sigma_-^2(r)} dy. \tag{2.10}$$

The pairwise velocity and dispersion can be computed in terms of the real space correlation function. The radial pairwise velocity $v_{12}(r)$ can be computed by solving the pair conservation equation [214]. In linear theory, the mean pairwise velocity is

$$v_{12}(r) = -\frac{2}{3} aHrf\bar{\xi}(r), \tag{2.11}$$

where $\bar{\xi}$ is the volume averaged correlation function given by Eq. 1.77. It is shown in [135] that the the higher order correction to the pairwise velocity can be solved by perturbation theory. To first order:

$$v_{12}(r) = -\frac{2}{3} aHrf\tilde{\xi}(r)[1 + \nu\tilde{\xi}(r)], \tag{2.12}$$

where

$$\tilde{\xi}(r) = \frac{\bar{\xi}(r)}{1 + \xi(r)}. \tag{2.13}$$

This gives a better description of the mean velocity in N-body simulations. In principle, ν is a function of the logarithmic slope of the (leading order) two point correlation function, which can also depend on scale. Moreover, ν is more sensitive to the transition scale between the linear and non-linear regime.

The scale-dependent velocity dispersion, $\sigma(r)$ in the linear regime takes a more complicated form (see Eq.15 of [85]). [214] suggests that the full form would depend on the three point function. The extension of $\sigma(r)$ into quasilinear scales

is therefore non-trivial [183]. [268] adopted a halo model description, and showed good consistency down to scales $r \sim 0.1\,h^{-1}\,\mathrm{Mpc}$ with N-body simulations.

2.2.2 Non-linear scales

On small scales, the velocity due to virialised motion becomes large and the linear assumption breaks down. This is shown clearly by the Finger of God (FOG) effect [131] at small separations perpendicular to the line of sight in the correlation function in Fig. 1.7. The small-scale pairwise velocity distribution from N-body simulations shows deviation from Gaussian, and is closer to an exponential distribution with no strong scale dependence [265]. Following this, [208] proposed the *dispersion model*, where in Fourier space, the large k modes of the anisotropic power spectrum in Eq. 1.72 is damped by a Lorentzian function $D(k\mu) = 1/(1 + k^2\mu^2\sigma_{12}^2/2)$, and σ_{12} is a scale-independent free parameter characterising FOG only. In configuration space, this is equivalent to a convolution along the line of sight r_π with the exponential distribution:

$$\tilde{D}(r_\pi) = \frac{1}{\sqrt{2}\sigma_{12}} \exp\left(-\sqrt{2}H_0 r_\pi/\sigma_{12}\right). \tag{2.14}$$

Furthermore, it is common to replace the linear power spectrum in Eq. 1.72 by the non-linear one because the transverse direction unaffected by RSD should be exactly the same as in real-space[1]. It is discussed in [30] that this rather simple model is actually among the best-performing models when fitting down to small scales of order $10\,h^{-1}\,\mathrm{Mpc}$. The parameter σ_{12} may be inferred by adopting a HOD analysis [118, 238, 248]

There are multiple challenges in extending the analytical model to the non-linear regime from first principles. Nonlinearities alter the small scale shape of the matter power spectrum and correlate the density and velocity fluctuations. Thus, they can introduce systematic bias in the inferred cosmological parameters [319]. The difference between the matter field and haloes is explored in [269, 288, 303]. Accounting for these effect requires higher order expansion in Perturbation Theory as well as the inclusion of the velocity spectrum, $P_\theta(k)$, and the density-velocity cross spectrum, $P_{\delta\theta}(k)$ (e.g. [133, 283]). Galaxy bias can also be nonlinear and stochastic on small scales [65]. Furthermore, the approximate velocity dispersion in equation 2.14 fails to fit auto-correlation data on the smallest scales

[1] Assuming no significant wide angle effects.

[258]. More elaborate velocity distributions are proposed by e.g., [28, 237, 317] based on simulations. In [317], for example, the velocity profile is characterised by a 7-parameter joint PDF, $P(v_r, v_t|r)$, of the velocity along and perpendicular to the line of sight of the satellite galaxies with respect to the cluster centre.

2.2.3 Cross-correlation in redshift space

Linear model

The Hamilton model was extended to cross-correlation by Mohammad et al. [184]. Consider cross-correlation between groups and galaxies with galaxy bias denoted by $b_{\rm gal}$ and group bias by $b_{\rm grp}$. It is also useful to define the relative bias, b_{12}:

$$b_{12} \equiv b_{\rm gal}/b_{\rm grp}. \tag{2.15}$$

The cross power spectrum in redshift space is

$$P_c^s(k,\mu) = b_{\rm gal} b_{\rm grp}(1+\beta_{\rm gal}\mu^2)(1+b_{12}\beta_{\rm gal}\mu^2)P^r(k), \tag{2.16}$$

where $\beta_{\rm gal} = f/b_{\rm gal}$. In configuration space, equations 1.74 – 1.76 are modified to

$$\xi_{0,c}(r) = \Big(1+\frac{1}{3}\beta_{\rm gal}(1+b_{12}) + \frac{1}{5}\beta_{\rm gal}^2 b_{12}\Big)\xi_c(r), \tag{2.17}$$

$$\xi_{2,c}(r) = \Big(\frac{2}{3}\beta_{\rm gal}(1+b_{12}) + \frac{4}{7}\beta_{\rm gal}^2 b_{12}\Big)[\xi_c(r) - \bar{\xi}_c(r)], \tag{2.18}$$

$$\xi_{4,c}(r) = \frac{8}{35}\beta_{\rm gal}^2 b_{12}\Big[\xi_c(r) + \frac{5}{2}\bar{\xi}_c(r) - \frac{7}{2}\bar{\bar{\xi}}_c(r)\Big], \tag{2.19}$$

where $\xi_c(r) = \left(b_{\rm gal}^2/b_{12}\right)\,\xi(r)$ and similarly for $\bar{\xi}_c$ and $\bar{\bar{\xi}}_c$.

The FOG term in the cross-correlation would be a convolution of the two velocity dispersions. In case of a Gaussian dispersion, the velocity dispersion would be $\sigma_{12}^2 = \sigma_{\rm gal}^2 + \sigma_{\rm grp}^2$. In case of the galaxy groups, we expect the dispersion to be small, given that the group centre would correspond to the halo centre. In that case, the total dispersion term would be close to that of galaxies. This model is applied to the analysis in Section 2.7.

One-halo and two-halo decomposition

A simple extension to the linear model is by separating the correlation function into two components: the 1-halo term and the 2-halo term (e.g., [268]). The 2-halo term takes the same form as the usual linear (or quasi-linear) RSD model, whereas the 1-halo term is given by the halo model. The 1-halo term can be approximated by a power law $\xi_{1\mathrm{h}} = (r_0/r)^\alpha$ or take the NFW profile $\xi_{1\mathrm{h}} = \alpha/x(1+x)^2$, where $x = r/r_0$. The FOG is modelled separately for each term, using exponential profiles with velocity dispersion $\sigma_{1\mathrm{h}}$ and σ_{lin} respectively. The model takes the form:

$$\xi_c^s = \xi_{1\mathrm{h}}(r \,|\, \alpha, r_0) * D(\sigma_{1\mathrm{h}}) + \frac{b_{\mathrm{gal}}^2}{b_{12}}\, \xi_{\mathrm{lin}}^s(r, \mu) * D(\sigma_{\mathrm{lin}}). \tag{2.20}$$

Compared to the linear model, this 1- and 2-halo decomposition contains three extra parameters α, r_0, and $\sigma_{1\mathrm{h}}$. The extra degrees of freedom could thus improve the model fitting at smaller scales. These 1-halo term parameters can be constrained by fitting the projected cross-correlation function. In this model, it has the form

$$w_p(r_p) = \frac{b_{\mathrm{gal}}^2}{b_{12}} \int \left[\left(\frac{r_0}{r} \right)^\alpha + \xi_{\mathrm{lin}}(r) \right] dr_\pi, \tag{2.21}$$

where $r^2 = r_p^2 + r_\pi^2$.

2.3 The Galaxy And Mass Assembly (GAMA) Survey

The Galaxy And Mass Assembly (GAMA DR2) spectroscopic survey [168], conducted by the Anglo-Australian Telescope, contains around 300,000 galaxies in five survey fields, with most galaxies concentrated at $z \sim 0.2$. The three main fields near the equator: G09, G12, and G15 are used here, each covering an area of 12×5 deg^2. The survey has an extinction-corrected r-band flux limit of $r < 19.8$. The overall redshift completeness of the equatorial region is 98.5% above the magnitude limit. This high completeness, thanks to repeated visits of each target in GAMA, is greatly advantageous for small scale galaxy and group studies compared to much larger surveys such as BOSS: fibre collision can lead to undercounts of close galaxy pairs and bias the measured galaxy 2-point correlation function [104]. Fig. 2.1 shows the survey geometry of the three GAMA main fields overlapped with a few other galaxy surveys.

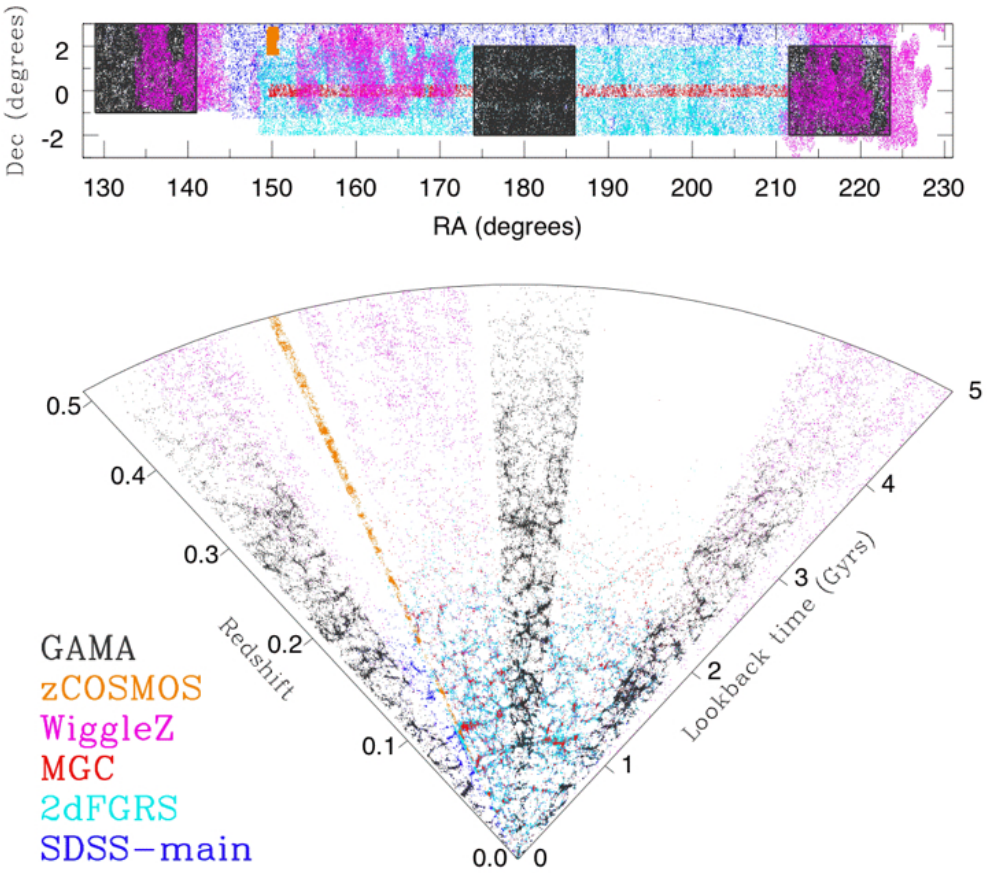

Figure 2.1 *The pencil beam of the three main fields, G09, G12, and G15 of the GAMA survey. The upper panel shows the RA and Dec of the three fields in black, and the lower panel shows the radial depth of the field in terms of redshift and lookback time. The figure is adopted from Driver et al. [70].*

Galaxies are selected with the following criteria: redshift quality $\texttt{nQ} \geq 3$, angular completeness mask $> 80\%$, and visual classification $\texttt{VIS\_CLASS} = 0, 1, 255$. The random catalogue is generated by [82] from the actual GAMA galaxy catalogue using a modified method following [52]. The idea of this method is to clone each galaxy n times and distribute them randomly within the maximum volume $V_{\rm max}$ that the galaxy can be observed given the survey magnitude limits,

$$n = n_{\rm clones} \frac{V_{\rm max}}{V_{\rm max,dc}}, \tag{2.22}$$

where $n_{\rm clones} = 400$ is the total number of randoms divided by data, and $V_{\rm max,dc}$ is the maximum volume weighted by overdensity $\Delta(z)$. This method is iterated until $\Delta(z)$ converges, and the redshift distribution of the resultant random catalogue is smooth without large scale features (see Fig. 4 in [82]).

The official GAMA group catalogue (G3C) is constructed by Robotham et al. [245]. Most of the groups are found within $z \lesssim 0.35$ (see Fig. 16 in [245]), thus we impose a redshift cut $0.1 < z < 0.3$ for the groups. The group catalogue is derived using an anisotropic friends-of-friends (FoF) algorithm. The idea is to link galaxies together if their separation is smaller than the *linking length* $\ell_{\rm FoF}$ that is related to the local overdensity. This linking length is defined separately for the radial direction and the projected plane: the $\ell_{\rm FoF}$ along the line of sight is much larger than the transverse direction, accounting for the effect of galaxy peculiar velocities (see an illustration in Fig. 2.2). The choice of $\ell_{\rm FoF}$ is crucial for groups found because a single group can be split into a few if $\ell_{\rm FoF}$ is too small, while several groups can merge if $\ell_{\rm FoF}$ is too large. Thus, the free parameters involved in determining $\ell_{\rm FoF}$ are adjusted against an N-body mock catalogue before they are applied to the actual data. To have consistently defined groups in the GAMA mocks (see Section 2.4), we do not use the official G3C catalogue. Instead, we apply a similar FoF group finder algorithm by Treyer et al. [290] to both data and mocks. This algorithm has also been applied to GAMA and other datasets [147, 172]. The main difference between the two algorithms is the parameterisation of the two linking lengths, and a detailed description of the algorithm and assessment of the group reconstruction quality can be found in the Appendix of [290].

The redshift distribution of the galaxies and groups in the GAMA survey is shown in Fig. 2.3. In addition to the above selections, we further split galaxies and groups into subsamples. The number of selected galaxies and groups in each

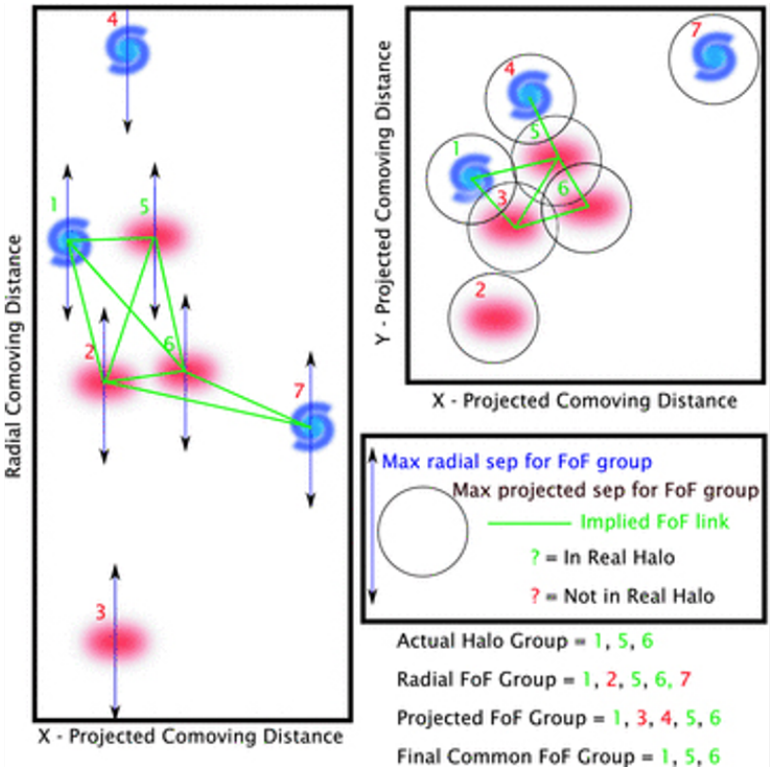

Figure 2.2 *A schematic diagram of the Friends-of-friends (FoF) algorithm applied to GAMA galaxies in order to construct the group catalogue. The figure is adopted from Robotham et al. [245].*

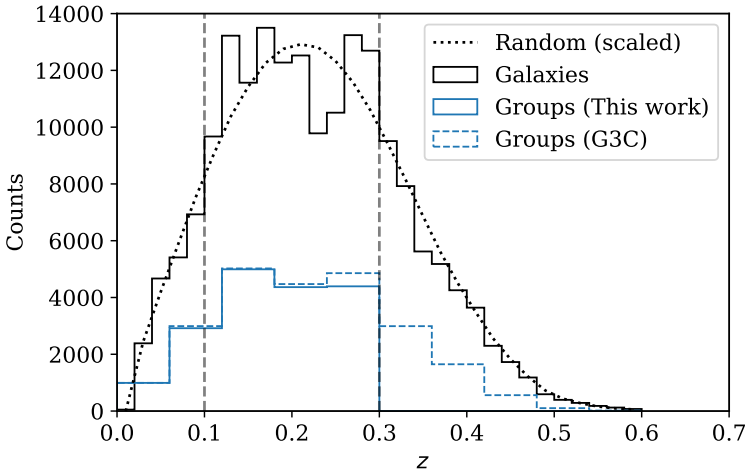

Figure 2.3 *Redshift distribution of the GAMA galaxies and groups. This work uses the redshift range* $0.1 < z < 0.3$.

Table 2.1 *Number of selected galaxies and groups from GAMA fields with redshifts* $0.1 < z < 0.3$ *and flux limit* $r < 19.8$. *Galaxies are split into red and blue subsamples, and groups are split into three stellar mass bins by 40%, 50%, and 10% by mass ranking from low to high.*

Number of		G09	G12	G15
Galaxies	Blue	17,335	18,719	19,053
	Red	20,584	22,155	21,141
	Total	37,919	40,874	40,194
Groups	LM	1,877	2,084	2,054
	MM	2,347	2,606	2,569
	HM	470	522	514
	Total	4,694	5,212	5,137

GAMA field and for each subsample is summarised in Table 2.1. We describe the selection in more detail below.

2.3.1 Galaxy colours: the red sequence and the blue cloud

In section 1.3.5, it is briefly mentioned that galaxy clustering is different for red and blue galaxies, and it can be qualitatively explained by their association with the dark matter haloes attributed to galaxy formation and evolution. The bimodality in galaxy colour and magnitude distribution is well known. It is found that galaxies are mainly concentrated in two regions in the colour-magnitude plane: there is a high luminosity 'red sequence' and a lower luminosity 'blue cloud'. The galaxies in between are often referred to as the 'green valley'.

Galaxy colours are closely associated with the age and star formation history of the galaxy. The luminous red galaxies tend to be older, with little or no star formation going on, while the less luminous, blue galaxies generally are younger with active star formation. It is also observed that the red population is rather tightly confined in colour, whereas the blue cloud has a much bigger spread. This trend can be explained by noting that the colour of old stellar populations do not change much with their age. The spread of colour in the blue cloud, on the other hand, suggests a range of stellar ages and different stages of star formation activities.

It is then interesting to split the GAMA galaxies into two tracer samples: red and blue, and study their two-point clustering with galaxy groups. To obtain the galaxy colours, we use the extinction corrected SDSS magnitudes from the `TilingCatv46` DMU (Database Migration Assistant for Unicode). It is, however, non-trivial to separate the two populations from a continuous distribution in colour and magnitude, and elaborate approaches have been discussed in e.g. [286]. For the purpose of this study, we adopt a simple quadratic cut in the apparent $g-i$ colour versus redshift plane:

$$g - i = 6.220z^2 + 1.383z + 0.831. \tag{2.23}$$

The specific form of the cut comes from matching the red and blue fraction at each redshift of GAMA data with the mocks, which is discussed in Section 2.4. The upper panel of Fig. 2.4 shows the bimodal distribution in $g-i$ colour and z for the GAMA data and the cut. The overall fraction of the red or blue galaxies is very close to 0.5, and it changes slightly with redshift: at the low redshift end, the red and blue fractions are similar, while towards higher redshifts, the fraction of red galaxies increases mildly until $z \sim 0.2$, and the difference in red and blue fraction becomes small at $z \sim 0.3$. We create random catalogues for the red and blue galaxy subsamples with matched redshift distribution.

2.3.2 Galaxy groups

Galaxy groups are assemblies of galaxies that are spatially close to each other, as we have seen in the group finding algorithm, and are tracers for density peaks. Compared to galaxy clusters, which typically have $N \gtrsim 50$ members per cluster, groups have fewer members and therefore probe lower mass haloes.

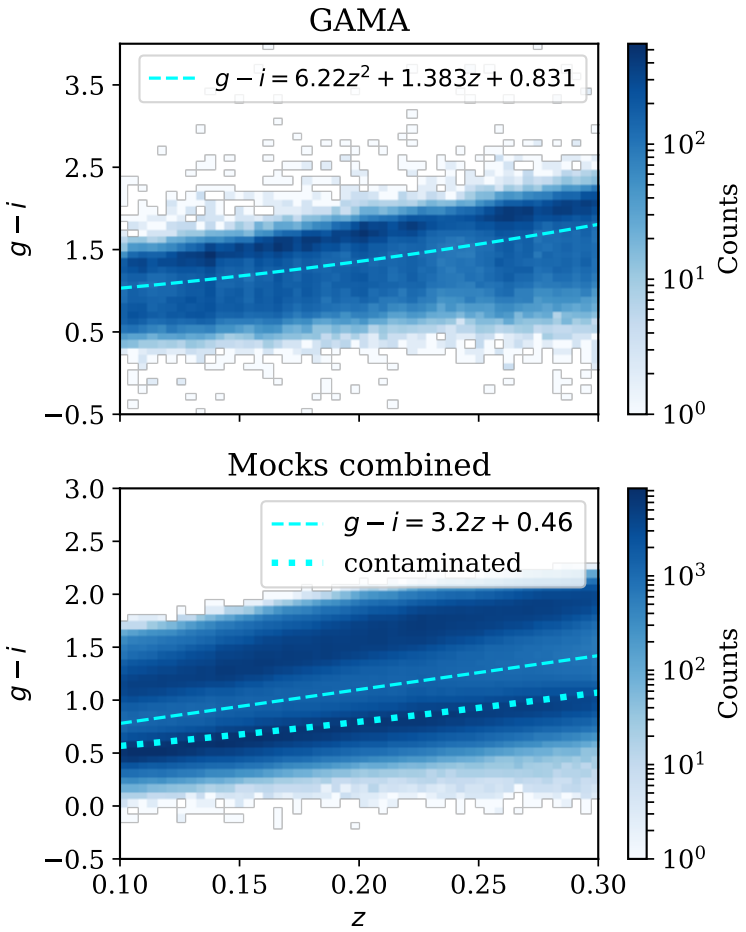

Figure 2.4 *Distribution of the $g-i$ colour of galaxies in redshift range $0.1 < z < 0.3$, for GAMA data (upper panel) and 25 mocks combined (lower panel). Red and blue populations are separated by the dashed black lines. The cut in GAMA is chosen such that GAMA and mocks have similar red and blue fraction at each redshift.*

Groups are accepted with group members ≥ 2, and the centre of the group is determined by the most (more) massive member in stellar mass. The 2-member systems make up 66% of the total groups in the GAMA data, but are likely to have poor fidelity. Thus, we emphasise that having the same group finder algorithm for the data and mocks is vital for these low-fidelity groups to be comparable. There are several approaches for determining the group centre. The simplest choice is to select the most massive member to be the central galaxy, and assume that it overlaps with the halo centre. Other approaches include determining a weighted centre by averaging over the positions of the group members, or iteratively excluding members that are most distantly separated (see e.g. [245]). The iterative centres are used in the G3C catalogue, and it is shown in [245] that the agreement with using the brightest group galaxy (BCG) as group centre is 95% for groups with $N \geq 5$, and for $2 \leq N \leq 4$, both BCG and iterative centres give highly consistent results compared with the mock, and the BCG centres are only degraded by about 3% compared to the iterative centres. The effects of different group centre choices on the group-galaxy cross-correlation concern mainly the 1-halo regime at $r \leq 1\,h^{-1}\,\mathrm{Mpc}$, and the correlation functions converge on larger scales [308].

The halo mass of GAMA groups is found to be tightly correlated with the group total luminosity in Han et al. [113], where they used maximum-likelihood weak-lensing analysis to determine the mass distribution of the GAMA groups with background SDSS photometric galaxies. The halo mass of groups is related to the r-band luminosity via:

$$M_h = M_p \left(\frac{L_{\mathrm{grp}}}{L_0} \right)^{\alpha}, \tag{2.24}$$

where

$$L_0 = 2 \times 10^{11} h^{-2} L_{\odot},$$

$$\log_{10}(M_p/h^{-1}M_{\odot}) = 13.48 - 0.08 \pm 0.12,$$

$$\alpha = 1.08 + 0.01 \pm 0.22.$$

In the expression of M_p and α, the three numbers refer for the best-fit value, bias, and the error. The luminosity is computed from the apparent r-band magnitude:

$$-2.5 \log(L/L_{\odot}) = m - K(z) - 5 \log(d_L) - 25 - M_{\odot}, \tag{2.25}$$

where $K(z)$ the k-correction up to $z = 0$ (`kcorr_z00`), d_L is the luminosity

distance, and $M_\odot = 4.67$ is the r-band absolute magnitude of the sun. The luminosity distance is expressed with unit $h^{-1}\,\mathrm{Mpc}$ so that the luminosity is expressed with unit $h^{-2}L_\odot$. The total luminosity of the group is computed in [245] by

$$L_{\mathrm{FoF}} = BL_{\mathrm{ob}} \frac{\int_{-30}^{-14} 10^{-0.4M_r}\phi_{\mathrm{GAMA}}(M_r)\,dM_r}{\int_{-30}^{M_{r-\mathrm{lim}}} 10^{-0.4M_r}\phi_{\mathrm{GAMA}}(M_r)\,dM_r}, \tag{2.26}$$

where L_{ob} is the total observed luminosity in r_{AB} band, $B = 1.04$ is the correction for median unbiased mean estimate for $N \geq 5$ groups, and $M_{r-\mathrm{lim}}$ is the absolute magnitude limit of the group depending on the redshift z. ϕ_{GAMA} is the luminosity function defined in [245]. The luminosity function at the faint end for GAMA galaxies is well approximated by $\phi \propto L^{-1}\exp(-L/L_*)$ [169]. Thus, we apply a redshift-dependent correction factor $\beta(z) = \exp(z^2/z_*^2)$ with $z_* = 0.33$ to each group instead, where z is the mean redshift of the group members. This correction factor has been checked using the G3C groups to produce a consistent total luminosity as `TotFluxProxy`.

The total stellar mass is another proxy for the total group mass. We use the `StellarMasses` DMU from Taylor et al. [285], where stellar population synthesis is used to model the optical photometry of the GAMA galaxies. Because the modelling uses rest frame luminosities, which depends on distance, the stellar mass is expressed in units of $h^{-2}{M_\odot}^2$. Furthermore, for each group, we correct the total stellar mass by the same redshift dependent factor as the total luminosity.

The calibration of the total stellar mass and the halo mass from weak lensing of the GAMA groups is shown in Fig. 2.5 for the official G3C groups (dashed line) and the group catalogue used in this work (solid line). The contours show 95%, 50%, and 20% of the total sample, and are highly consistent between the two group catalogues. We choose to divide groups into three stellar mass bins based on percentiles: the Low Mass (LM) bin consists of the least massive 40% groups, the Medium Mass (MM) bin corresponds to the middle 50%, and the High Mass (HM) bin contains the most massive 10%. The signal-to-noise of from high mass haloes is expected to be high, despite the low number in the HM bin.

[2]Notice that this is only approximately true, because the stellar mass to light ratio, M/L, which is used obtain the stellar mass, depends on age and is therefore specific to the choice of h. The stellar mass used here assumes $h = 0.72$.

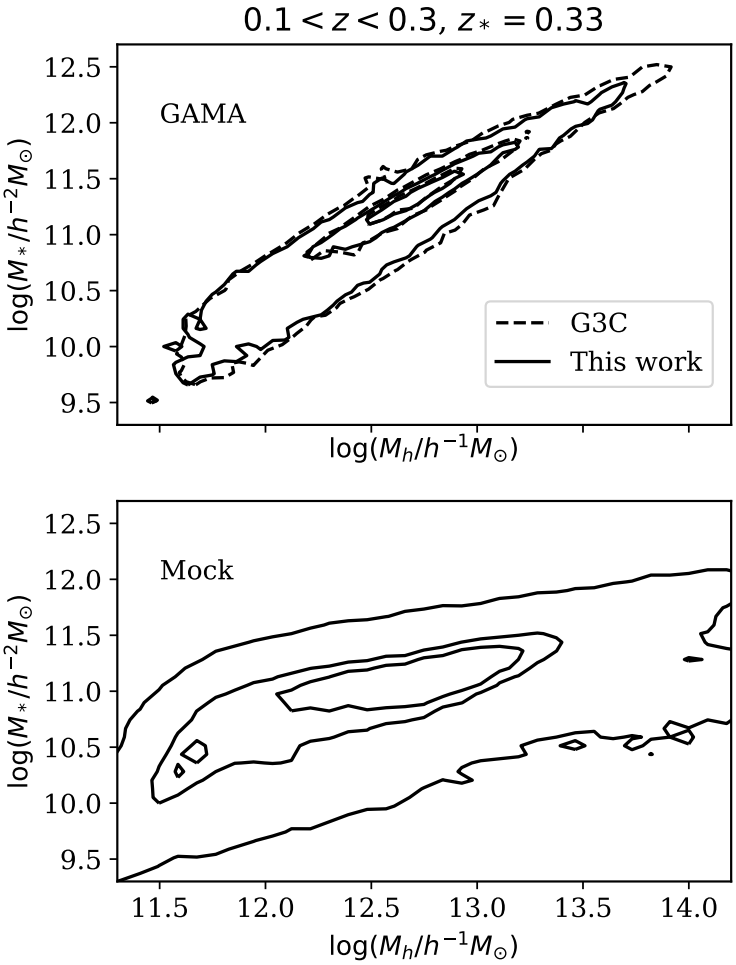

Figure 2.5 *Upper panel: Correlation between the total stellar mass, corrected by a factor* $\exp(z^2/z_*^2)$ *and the halo mass from the calibration from [113] for the GAMA groups with two or more members between redshifts* $0.1 < z < 0.3$*. The contours denote 95%, 50%, and 20% of the total sample. The solid lines show the groups used in this work using the group finder algorithm in [290], and the dashed lines show the the official G3C groups [245]. Lower panel: The same relation for the mock catalogue. In this case,* M_h *is not estimated from the luminosity, but directly taken as the arithmetic mean host halo mass of the group member. The difference in the distribution indicates that such estimator is not very reliable.*

2.4 The GAMA mock catalogue

There are two reasons for including mock catalogues: (1) to validate the RSD models and assess the bias on the recovered growth rate, and (2) to quantify the impact of cosmic variance via the construction of covariance matrices. We used 26 realisations of a lightcone mock catalogue based on the GALFORM semi-analytical galaxy formation [97]. The catalogue exploits the Millennium Simulation with WMAP7 cosmology [105]: $\sigma_8 = 0.81$, $\Omega_m = 0.27$, $h = 0.70$, and $n_s = 0.967$. These mocks are queried from the table `GAMA_v1...LC_multi_Gonzalez2014a` from the Durham hosted Virgo–Millennium Database1 [161]. For more details of the mock catalogue, see [82]. By Eq. 1.51, the fiducial value of growth rate at the mean redshift of the mocks, $z = 0.195$, is $f_{\rm fid} = 0.593$. The lightcone is constructed using the methods in Merson et al. [179], where, given an observer, the galaxy is placed at the epoch where it first enters the past lightcone of the observer. The galaxy trajectories are interpolated between snapshots. Each mock covers the five GAMA fields with the SDSS r-band apparent magnitude `SDSS_r_obs_app` < 21, and $z < 0.9$.

We use galaxies in the G09, G12, and G15 fields and apply the same selection in redshifts $0.1 < z < 0.3$ and the apparent r-band magnitude cut `SDSS_r_obs_app` $<$ 19.8. We also apply the same survey mask generated using the random catalogue. The masked areas are obtained by binning random galaxies in each field with an average of ~ 2000 counts in each bin. Pixels with counts smaller than five times the Poisson noise are masked. The total masked area in the three fields is about $0.14\,\mathrm{deg}^2$. Because the mock redshift distribution is not matched exactly with GAMA data and random (see Fig. 2.6), we create a random catalogue for these mocks by down-sampling the random catalogue for the GAMA data, such that the $n(z)$ matches the mean of 25 mocks.

2.4.1 Matched galaxy colour subsample

The red and blue subsamples for the mean of the mocks are separated by the empirical line given by

$$g - i = 0.46 + 3.2z, \tag{2.27}$$

as shown in the lower panel of Fig. 2.4. The line is chosen to go through the green valley of the mock galaxy $g - i$ colour. The GAMA galaxies have a

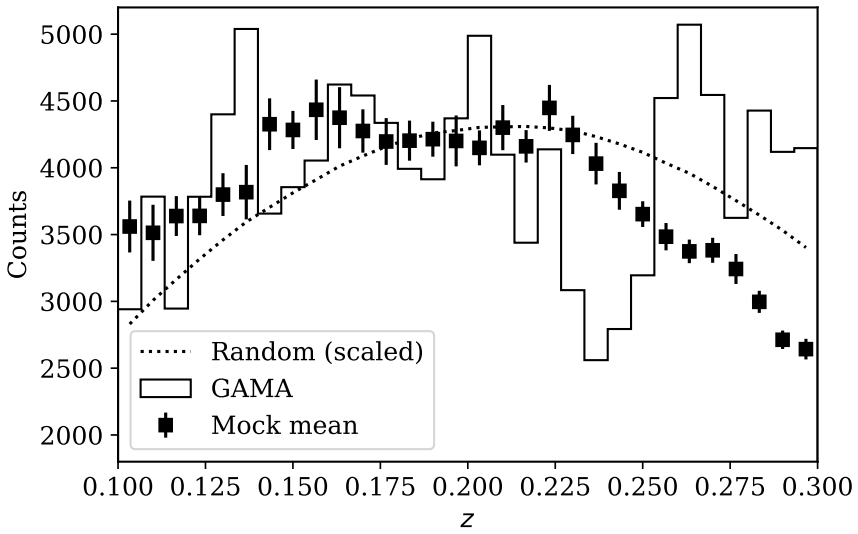

Figure 2.6 *The mean redshift distribution of the 25 GAMA mocks (square) is offset from that of the random sample (dotted line). A random catalogue is created for the mocks to have matched redshift distribution as the mock mean. The redshift distribution of the GAMA galaxy sample is also shown (histogram) for comparison.*

more concentrated red sequence overlapping with an extended blue population, without a distinct green valley in between. On the contrary, the mocks have a broader red population which is well separated from the blue population by a green valley. Since the mock catalogues have more distinctive separation for the two populations, we find the corresponding colour cut in the GAMA data by matching red and blue fractions in the two catalogues for 20 redshift bins in $0.1 < z < 0.3$. The cut is smoothed by fitting a second order polynomial, as shown in the upper panel of Fig. 2.4.

The contamination of the red and blue sub-samples in the GAMA data resulting from the colour cut is quantified in the following way: for each redshift bin, the red and blue sub-samples are fitted by a double Gaussian. It is a reasonable fit except for the green valley in the mocks, as shown in Fig. 2.7. Given a colour cut, the contamination of the red sub-sample is defined as the area under the blue Gaussian over the area under the red Gaussian, and similarly for the contamination of the blue sub-sample. Clearly, GAMA data contain a contaminated red sample and a pure blue sample. Therefore, we create a contaminated red sub-sample using the mock catalogues by placing the mock colour cut such that extra blue galaxies are included with the same level of contamination as GAMA data. The contaminated red cut in the mocks (see

Fig. 2.4) is smoothed by fitting a quadratic polynomial of the form

$$g - i = 2.43z^2 + 1.55z + 0.388. \tag{2.28}$$

2.4.2 Mock group catalogue

For mock groups, the stellar mass is computed by the sum of `diskstellarmass` and `bulgemass` of all group members, and corrected by the same redshift-dependent factor as the data. We do not estimate the group halo mass from the same mass-luminosity relation in Eq. 2.24. Instead, we use the host halo mass of the mock galaxy directly. Because some haloes contain more than one galaxy, for each group, we test the largest, the arithmetic mean, and the median halo mass of the group member, and find that they give similar results. We also test using the sum of unique host haloes in the group. This increases the total group halo mass in the lower mass end, but does not affect the higher mass end.

The stellar-halo mass relation of the groups using the total stellar mass and the arithmetic mean host halo mass of the group members is shown in the lower panel of Fig. 2.5. It is clear that the the mocks show a much large scatter in the $M_h - M_*$ plane and the slope is smaller compared to data, i.e., at fixed stellar mass, the halo mass is larger. The total stellar mass of the mock groups are also smaller by about 0.5 dex compared to data. The clear difference between data and the mocks shows that estimating the halo mass from luminosity using Eq. 2.24 is not very reliable. The luminosity is itself strongly correlated with stellar mass via the luminosity-mass relation, thus the upper panel of Fig. 2.5 does not show the true scatter of M_h at fixed M_* faithfully (or vice versa).

The comparison between the group and the halo catalogue also reveals interesting information. Across the mock realisations, the number of groups with two or more members is of order 1.4×10^4, and that of haloes is of order 8×10^3. Haloes containing one galaxy only are concentrated towards low M_h and low M_*, whereas haloes containing two or more members have a minimum $\log(M_h/h^{-1}M_\odot) \sim 11.5$. Therefore, the extended lower mass end in the lower panel of Fig. 2.5 shows that galaxies from different low mass haloes are identified in the same group. At the high halo mass end, the excess of small stellar mass groups indicates that the group finder breaks a small number of haloes with multiple galaxies into several smaller groups. This observation again emphasises the importance of

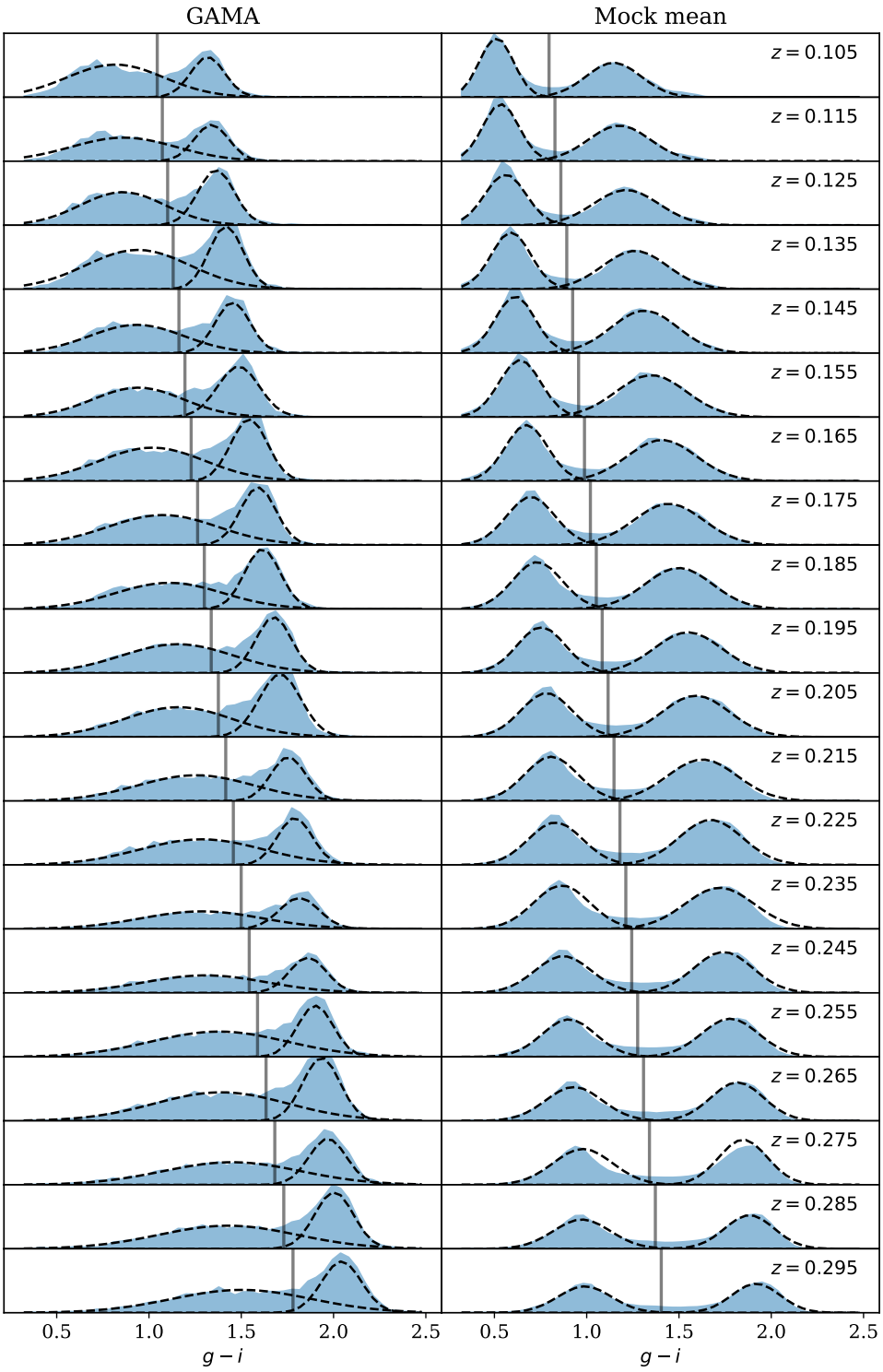

Figure 2.7 *The $g-i$ colour distribution of GAMA and mock mean (blue shaded region) in 20 redshift bins with $0.1 < z < 0.3$. The black dashed lines are double Gaussian fits to the distributions characterising the blue and red populations. The vertical grey cuts separate the red and blue populations in mock and data, with matched red and blue fraction of the total galaxy number.*

using a consistent group finder algorithm between the GAMA data and the mock catalogues. The mock group catalogues are separated into three stellar mass bins based on the 40%, 50%, and 10% percentiles as the data.

2.5 Measuring statistics

We measure the 2-point correlation function ξ of the groups and galaxies. For two objects located at $\mathbf{s}_1, \mathbf{s}_2$, the line of sight is defined as $\mathbf{l} = (\mathbf{s}_1 + \mathbf{s}_2)/2$. Their separation is given by $\mathbf{s} = \mathbf{s}_1 - \mathbf{s}_2$. The correlation function is then measured in bins of the separation parallel and perpendicular to the line of sight:

$$\pi = \frac{\mathbf{s} \cdot \mathbf{l}}{|\mathbf{l}|}, \quad r_p = \sqrt{\mathbf{s}^2 - \pi^2}. \tag{2.29}$$

As mentioned above, the survey mask and redshift distribution $n(z)$ are captured by the random catalogue. For the red and blue subsamples, the random $n(z)$ is adjusted by the smoothed, redshift-dependent red and blue fraction respectively. The group subsamples also have different $n(z)$, with lower mass groups concentrating at lower redshifts, and higher mass groups dominating at higher redshifts. We do not try to fit their redshift distribution due to their small sample sizes. Thus, the standard Landy-Szalay estimator, which requires random catalogues for both groups and galaxies, is not applicable here. Instead, we use the Davis-Peebles estimator:

$$\hat{\xi}(r_p, \pi) = \frac{D_1 D_2}{D_1 R_2} - 1, \tag{2.30}$$

where subscript 1 denotes groups and 2 denotes galaxies in the above case.

To break the degeneracy of galaxy and group biases, we also measure the 2-point function for the galaxy subsamples. In this case, we use the standard Landy-Szalay estimator:

$$\hat{\xi}(r_p, \pi) = \frac{DD - DR - 2DR}{RR}. \tag{2.31}$$

Although the latter is better at suppressing statistical noise, the two estimators make negligible difference for our sample. Throughout the analysis, the size of random galaxies used is 20 times that of data. The 2D correlation functions are measured with a bin width of $1\,h^{-1}\,\mathrm{Mpc}$ in both r_p and π. We take $|r_p| < 40\,h^{-1}\,\mathrm{Mpc}$, where both positive and negative r_p are counted in the same bin,

because ξ is symmetric around the transverse direction. Along the line of sight, we do not assume symmetry and take $\pi = [-40, 40]\, h^{-1}\,\mathrm{Mpc}$ instead, where positive and negative π are counted in different bins. It is interesting to check the line of sight symmetry because, as mentioned briefly in Section 1.3.3, additional effects such as gravitational redshift could give rise to a non-vanishing dipole in the cross-correlation function, leading to an asymmetry in the π direction.

For the convenience of model fitting, the information in the 2D correlation function is then compressed into the projected correlation function w_p with integral limits of $\pm\pi_{\max}$:

$$w_p(r_p) = \int_{-\pi_{\max}}^{\pi_{\max}} \xi(r_p, \pi) d\pi, \tag{2.32}$$

and multipoles ξ_0 and ξ_2:

$$\xi_\ell(r) = \frac{2\ell + 1}{2} \int_{-1}^{1} \xi(r, \mu) \mathcal{P}_\ell(\mu)\, d\mu,\ \ell = 0, 2, \tag{2.33}$$

where $\mu = \pi/|\mathbf{s}|$. We ignore ξ_4 because it is more sensitive to non-linearity. For the integral limit in Eq. 1.56, $\pi_{\max} = 40\, h^{-1}\,\mathrm{Mpc}$, the w_p is only weakly dependent on RSD parameters. The multipoles are computed by interpolating the 2D correlation function, and this is done consistently for both measurements and the model.

2.5.1 Likelihoods

The constraints of model parameters are computed using Bayesian likelihoods. The probability distribution of a set of parameters θ given the data D is

$$P(\theta|D) = \frac{P(D|\theta)P(\theta)}{P(D)}, \tag{2.34}$$

where $P(D|\theta)$ is proportional the likelihood $\mathcal{L}$, $P(\theta)$ is the prior distribution of the parameters, and $P(D)$ is treated as a normalisation. The covariance matrix is only weakly dependent on model parameters, allowing the approximation $\mathcal{L} \propto \exp(-\chi^2/2)$, where the χ^2 is defined as

$$\chi^2 = \sum_{i,j}^{m} [x(r_i) - y(r_i)] C_{ij}^{-1} [x(r_j) - y(r_j)] \tag{2.35}$$

for a data vector $x(r)$ and a model vector $y(r)$ with m bins in separation r. C_{ij} is the covariance matrix. The degree of freedom of χ^2-fitting is given by dof $= m-p$, where p is the number of parameters. For each subsample (e.g. LM-red), the data and mock vector includes both the group-galaxy cross-correlation and the auto-correlation of the corresponding galaxy subsample. We use the python package `emcee`[3] to explore the parameter space with uniform priors.

For N independent mock realisations, the estimator for the covariance matrix is

$$\hat{C}_{ij} = \frac{1}{N-1}\sum_{k=1}^{N}[x_k(r_i) - \langle x(r_i)\rangle][x_k(r_j) - \langle x(r_j)\rangle]. \tag{2.36}$$

The dimension of the covariance matrix needs to be smaller than N in order for it to be invertible [284]. This justifies the compression of the 2D-correlation function into w_p and multipoles. Due to the small number of mocks, we apply Jackknife re-sampling on the mocks by dividing each survey field 18 sub-regions, giving a total of $N_J = 54$ Jackknife samples for each mock. The covariance matrix for each mock sample is estimated using equation 2.36, with an extra factor $(N_J - 1)$ to account for correlations between Jackknife samples. We then average over the covariance matrices of the 25 mocks to obtain the final covariance matrix. It is pointed out in Escoffier et al. [78] that this method can reduce the noise on the covariance estimation, and fast approach the truth. However, it should be noted that these mocks are not completely independent, since they are constructed from the same simulation [97]. We compare the mean Jackknife errors with the scatters between mock realisations and find that they are consistent, with the only exception of the cross-correlations with blue samples, where the mean Jackknife error is smaller than the scatter between mocks by about 10%, especially at scales $r < 10\,h^{-1}\,\mathrm{Mpc}$. The covariance matrix is computed for each of the correlation configurations.

2.6 Cross-correlation measurements

In the following analysis, we will refer to the group subsamples as LM (low mass bin), MM (medium mass bin), and HM (high mass bin), and the cross-correlation between subsamples as e.g., LM-Red for low mass group cross-correlated with red galaxy subsamples. We measure the cross-correlation of all groups and galaxies

[3] http://dfm.io/emcee/current/

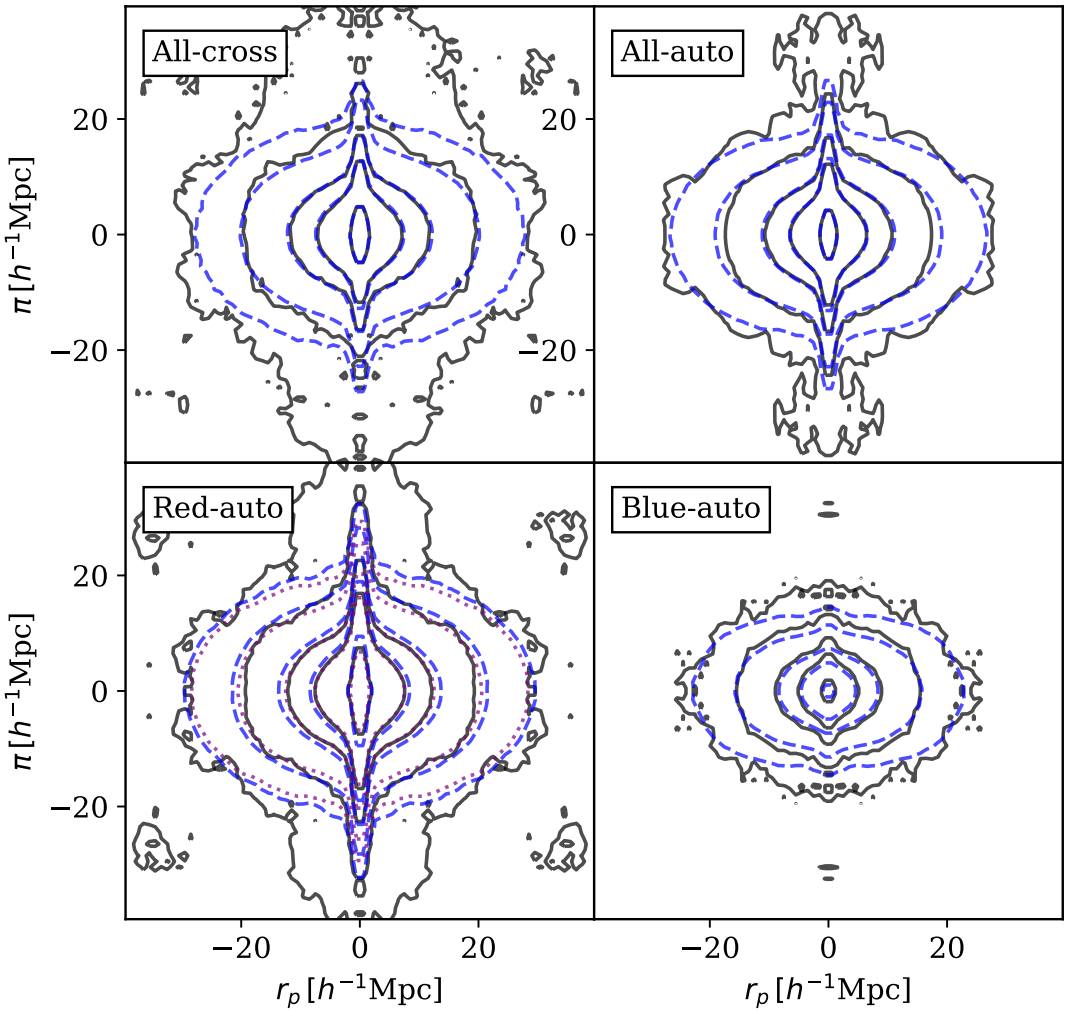

Figure 2.8 *2D group-galaxy cross-correlation with all galaxies and groups (top left), auto-correlation of all galaxies (top right), auto-correlation of red galaxies (bottom left), and auto-correlation of blue galaxies (bottom right) measured in GAMA (black solid lines) and the mean of mocks (blue dashed lines). The contour levels are* $\xi = (0.1, 0.2, 0.5, 1, 5)$. *In the 'Red auto' case, the purple dotted contours show the contaminated red galaxy subsample in the mocks. The bin size is* $1\,h^{-1}\,\mathrm{Mpc}$ *in both* r_p *and* π.

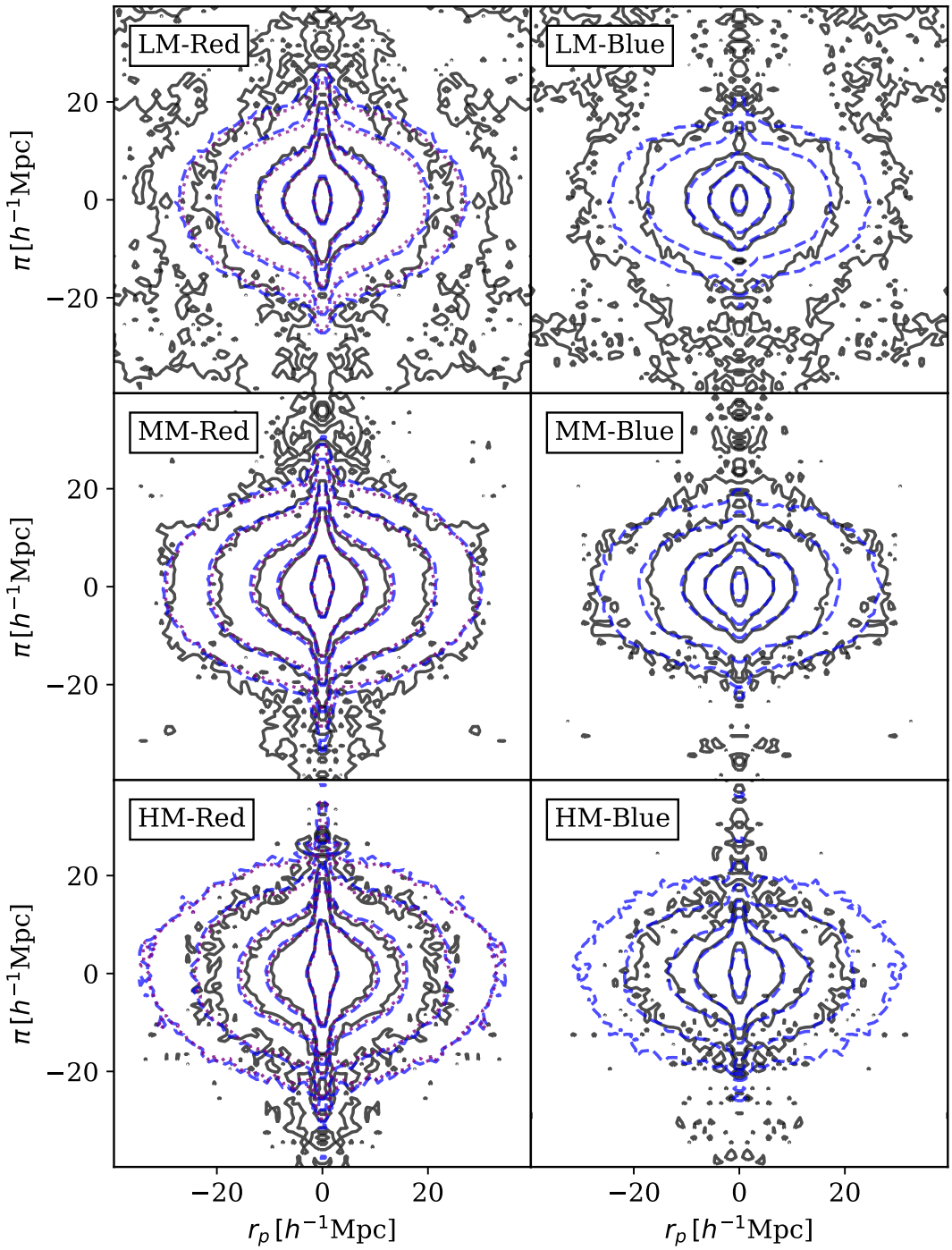

Figure 2.9 *Same as Fig. 2.8 but for group-galaxy cross-correlation with galaxies split in two colours and groups split in three mass bins from the GAMA data (black solid lines) and mean of the mocks (blue dashed lines). Lowest contour level in the high mass (HM) bins for the GAMA data is not shown due to large noise.*

(denoted as All), and those between the three group and two galaxy subsamples. In addition, we also measure the galaxy auto-correlations for all, red, and blue galaxies. This allows us to fit cross-correlation with the corresponding galaxy auto-correlation simultaneously to break the degeneracy between $b_{\rm gal}$ and b_{12}. We do not measure the auto-correlation for groups because it is tricky to construct randoms that match the group catalogue; the cross-correlation conveniently avoids this issue.

The measured 2D auto- and cross-correlations from GAMA and the mean of the mocks are shown in Fig. 2.8 and Fig. 2.9. For subsamples involving red galaxies, the mock results from the contaminated red sample is also shown in dotted purple contours. The effect of including bluer galaxies in the red subsample reduces the galaxy bias and the FOG slightly, resulting in a better agreement with data in the Red auto case. The agreement between data and the mocks in each of these measurement is well down to small scales ($\lesssim 15\,h^{-1}\,$Mpc). The only exception is with the blue galaxy auto-correlation, where the mock results seem to give a slightly smaller galaxy bias and the FOG. On larger scales, the agreement is not so well possibly due to the large noise – there are fewer pairs on larger scales. Cosmic variance also affects these large scales. In particular, the cross-correlation with low mass groups (LM-Red and LM-Blue in Fig. 2.9) is excessive on these scales, even higher than the MM and HM subsamples and resulting in poor agreement between the data and mocks for $\xi \lesssim 0.5$. This is also reflected in the projected correlation functions w_p as we shall see later on. This could be due to cosmic variance: there happen to be a spike in the distribution of GAMA galaxies at $0.1 < z < 0.2$, where the low mass groups are concentrated. It could give rise to a mismatch in the $n(z)$ of GAMA with its random catalogue. After inspecting each mock realisation, we believe that this signal is consistent with cosmic variance.

The upper panels in Fig. 2.8 show the group-galaxy cross-correlation and the galaxy auto-correlation for the full sample, and while the cross-correlation has a slightly higher amplitude, they show very similar trend. The lower panels in the same figure shows the auto-correlations for the red and blue galaxy subsamples, and their differences can be seen clearly. On large scales, the correlation function is amplified for the red galaxies compared to the blue galaxies, yielding a larger galaxy bias. This implies that red galaxies are preferentially associated with massive haloes (e.g. [106]). On small scales, the FOG effect is more dominant in the red galaxies than blue galaxies, showing a stronger non-linearity in the red subsample. This is consistent with the observation that red galaxies are likely to

be satellites while blue galaxies are likely centrals.

Fig. 2.9 shows the cross-correlations between the group and galaxy subsamples. The left and right panels show those involving red and blue galaxies, and the difference between the two shows a similar trend as observed in the auto-correlation case. The panels from top to bottom show low mass, medium mass, and high mass groups. The amplitude of the correlation function on large scales and the FOG on small scales increases significantly with increasing group mass. This is expected because larger groups are likely found in higher density peaks, and are strongly clustered with a higher bias. The virial velocities of galaxies on small scales are also expected to be larger for larger groups, thus the strongly increasing FOG with group mass.

Fig. 2.10 shows the projected correlation function w_p (red), the monopole ξ_0 (blue), and the quadrupole ξ_2 (orange) for data (solid circles) and the mean of mocks (open circles). For demonstration purposes, we have multiplied r_p to the projected correlation function, and r^2 to the multipoles. The cross-correlation is shown on the panel below its corresponding galaxy auto-correlation for each subsample. The error bars on the data points are adopted from the averaged Jackknife errors from the mocks. As we have seen from the 2D correlation functions, the data and mocks match closely in most cases, especially on small scales with $r \lesssim 10\,h^{-1}\,\mathrm{Mpc}$. On scales $r \gtrsim 15\,h^{-1}\,\mathrm{Mpc}$ the quadrupole of data becomes larger than the mocks, and a rise in w_p and monopole can also be seen at $r \gtrsim 20\,h^{-1}\,\mathrm{Mpc}$, but the size of the errors suggests no clear deviation of the data from the mocks. There is a more obvious difference in w_p between the data and mock in the LM cases, also seen clearly in the top panels in Fig. 2.9. Given that the data points are strongly correlated, such difference is also not statistically significant.

2.7 Model fitting

We adopt the linear RSD model in [184] with a non-linear power spectrum generated by HALOFIT [276, 282]. We test a set of minimum fitting scales, $r_{\mathrm{min}} = 2, 5, 10, 15, 20\,h^{-1}\,\mathrm{Mpc}$. We also include an extra parameter, the integral constraint I, which is a small constant added to the 2D correlation function. It accounts for the missing power from modes with wavelengths longer than the survey scale. The non-linear power spectrum is taken at $z = 0.195$ with σ_8 fixed

Table 2.2 *Range of the uniform priors of the RSD fitting parameters. For growth rate, the usual constraint from RSD is $f\sigma_8$, but we fix $\sigma_8 = 0.81$ in this analysis.*

Parameter	Range
b_{gal}	$[0.1, 2.5]$
b_{12}	$[0.1, 2.5]$
f	$[0, 2]$
σ_a [km/s]	$[100, 800]$
σ_c [km/s]	$[100, 800]$
I_a	$[0, 0.1]$
I_c	$[0, 0.1]$

to the mock fiducial value 0.81. Although the shape of the non-linear power spectrum at large k is sensitive to σ_8, this dependence is weak for the analysis here. Thus, we treat σ_8 as an overall factor completely degenerate with the linear biases. Fitting the auto- and cross-correlations together, there are in total seven free parameters, namely $b_{\rm gal}$, b_{12}, f, σ_a, σ_c, I_a and I_c. Due to the bin size in the 2D correlation function, the model is insensitive to dispersions smaller than $100\,{\rm kms}^{-1}$. For the GAMA data, we run MCMC at the optimum minimum scale for each subsample determined from mocks with uniform priors. The prior range is shown in Table 2.2.

2.7.1 Fitting Mocks

We test the model on each mock realisation using w_p, ξ_0, and ξ_2 shown in Fig. 2.10. For each subsample, the galaxy auto-correlation (shown in the rows labeled with 'Auto') and the group-galaxy cross-correlation (shown in the rows labeled with 'Cross') are fitted simultaneously. For example, on the third row of Fig. 2.10, the data points in each column show the same measured red galaxy auto-correlation, but the best-fit models can be sightly different from simultaneously fitting the cross-correlation in each column in the fourth row. The model (dashed lines) provides a good fit for the mocks in most cases, and except for those cases involving red galaxies, the fits are reasonable even down to $r < r_{\rm min}$. Fig. 2.11 shows the constraints on the model parameters by taking the mean and the standard deviation of the best-fit parameters from the mocks. The All sample is shown in black circles, subsamples using LM, MM, and HM groups are shown in square, triangle, and star markers, and subsamples involving red and blue galaxies are shown in their respective colours. We also include the contaminated

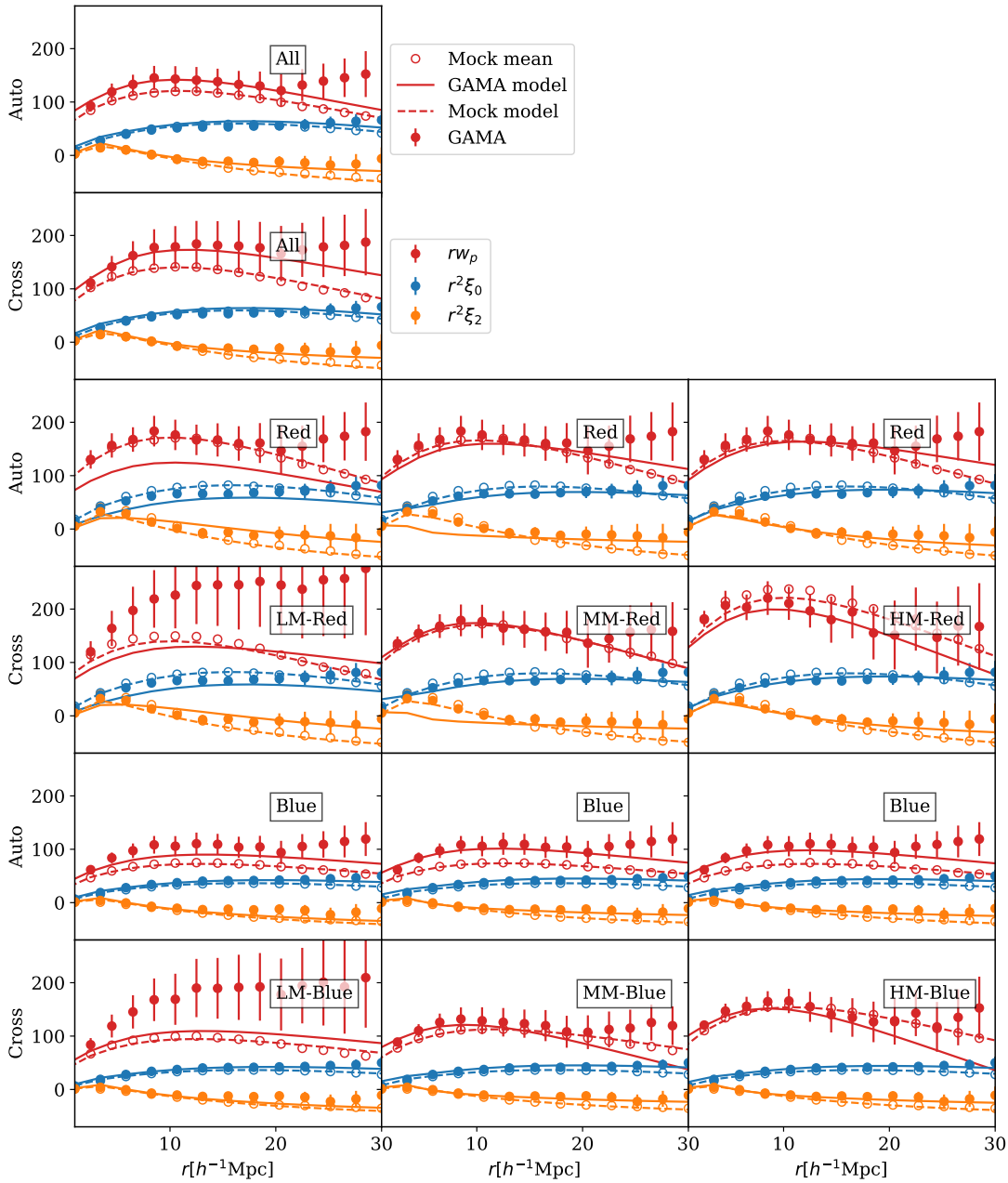

Figure 2.10 *The projected correlation w_p, the monopole ξ_0, and the quadrupole ξ_2 of the seven sub-samples All, LMred, MMred, HMred, LMblue, MMblue, HMblue measured from GAMA and the mean of the mocks, as well as their best-fit models. The w_p, ξ_0, ξ_2 are multiplied by powers of r to amplify the dynamics on large scales. For each of the seven sub-samples, we show both the galaxy auto-correlation and the cross-correlation, as used in our fitting method. GAMA data are shown in filled circles with error bars, and the mock means are shown in open circles. The solid and dashed lines are best-fit models to the data and the mean of the mocks using the linear model. All sub-samples involving blue galaxies, as well as the All case, are fitted with $r_{\mathrm{min}} = 10\,h^{-1}\,\mathrm{Mpc}$, the LMred case fitted with $r_{\mathrm{min}} = 15\,h^{-1}\,\mathrm{Mpc}$, and all other cases with $r_{\mathrm{min}} = 20\,h^{-1}\,\mathrm{Mpc}$.*

red galaxy subsample here, labelled by 'Red*'. The specific values of the best-fit parameters and its 1σ errors are summarised in Tab. 2.3.

The top panel of Fig. 2.11 shows the constraints on the growth rate f. The fiducial value with $\pm 10\%$ error is marked in the grey band. As expected, in all cases the model recovers the fiducial growth rate at $r_{\rm min} \geq 15\,h^{-1}\,{\rm Mpc}$, but the fitting including small scales ($r_{\rm min} \leq 5\,h^{-1}\,{\rm Mpc}$) are significantly biased. The overall growth rate seems to be under-estimated by about $5-10\%$, but this is much smaller than the statistical error. This means that the linear assumption is recovered at these scales and the measurement of f is consistent from different biased tracers. Comparison between the red and blue galaxy subsamples reveals that cross-correlation with blue galaxies recovers the growth factor f better than red galaxies. For the blue-galaxy cases, f is over-estimated at smallest $r_{\rm min} = 2\,h^{-1}\,{\rm Mpc}$, but with $r_{\rm min} \geq 10\,h^{-1}\,{\rm Mpc}$ it is measured within 10% of the fiducial value. For the MM-Red and HMred cases, the measured f is only within 10% of the fiducial value at $r_{\rm min} = 20\,h^{-1}\,{\rm Mpc}$, while for the LM-Red case this is $r_{\rm min} = 15\,h^{-1}\,{\rm Mpc}$. The contaminated red galaxy sample gives less biased measurements of f at small scales, and converges with the pure red sample at $r_{\rm min} \geq 15\,h^{-1}\,{\rm Mpc}$. This confirms that blue galaxies show smaller non-linearity compared to red galaxies.

The second and the third panels show the group and galaxy biases, $b_{\rm grp}$ and $b_{\rm gal}$. We see that this is determined consistently between different subsamples at $r_{\rm min} \geq 10\,h^{-1}\,{\rm Mpc}$. As observed in the 2D correlation functions, the group bias increases with higher group masses, and the red galaxies have a larger galaxy bias compared to the blue galaxies. The consistency between different subsamples and the convergence of the bias values as a function of $r_{\rm min}$ at sufficiently large scales indicate that linear bias model is a good approximation. The contaminated red galaxy sample shows a smaller galaxy bias here, due to the mixing with blue galaxies. The last two panels show the velocity dispersion, which determines the extent of the FOG convolution, in the auto- and cross-correlations. The results indicate an average velocity dispersion of $\sim 300\,{\rm kms}^{-1}$, consistent across different subsamples. There is a slight hint that σ_a is larger for the red galaxies compared to the blue galaxies, but it is not statistically significant. Beyond $r_{\rm min} = 10\,h^{-1}\,{\rm Mpc}$, the uncertainty in the measured σ_a and σ_c increases rapidly as the model becomes insensitive to the dispersion on large scales.

From this test, we choose to adopt $r_{\rm min} = 10\,h^{-1}\,{\rm Mpc}$ for all subsamples involving blue galaxies and the All case, $r_{\rm min} = 15\,h^{-1}\,{\rm Mpc}$ for LM-Red, and

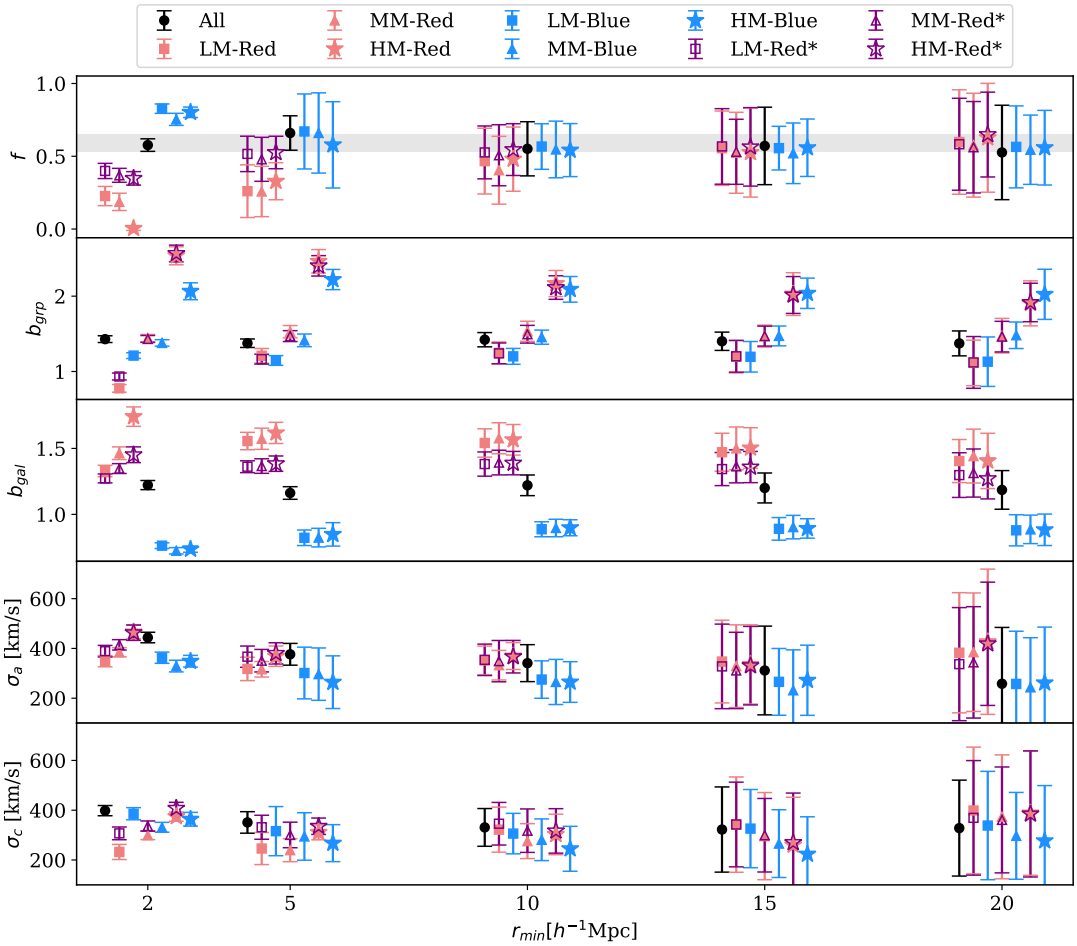

Figure 2.11 *The constraints on model parameters from fitting the mocks as a function of the minimum fitting scale, $r_{\rm min}$ for all galaxies and groups, and for the six subsamples split by galaxy colours and group masses. In addition, we also include the contaminated red subsample indicated by 'Red*'. The values and error bars are from the means and standard deviations of the 25 mocks. Data points at each $r_{\rm min}$ are displaced by $\pm 0.3\,h^{-1}\,$Mpc for clarity. The top panel shows the growth rate parameter, f, with the grey band marking $\pm 10\%$ regions around the fiducial value, $f = 0.593$. The middle panel shows the group and galaxy biases. The bottom panel shows the velocity dispersion for the auto- and cross-correlations.*

$r_{\rm min} = 20\,h^{-1}\,$Mpc for MM-Red and HM-Red respectively for this linear model. This choice is also taken in the best-fit models shown in Fig. 2.11.

2.7.2 Fitting GAMA

We then fit the data w_p, ξ_0, and ξ_2 for the auto- and cross-correlation simultaneously, shown in Fig. 2.10. The best-fit models are shown in solid lines. In this case, we quote the best-fit parameters from $r_{\rm min}$ based on the previous mock results and we use the mock covariance matrices. In all cases except those with red galaxies, the model provides reasonable fit even down to scales smaller than $r_{\rm min}$. With the red subsamples, the model does not capture the small scale behaviour of the quadrupole well in particular. In the LM cases, the best-fit models give smaller galaxy biases in the red and blue subsamples compared to MM and HM cases. Fig. 2.12-2.14 show the marginalised posteriors for f, $b_{\rm gal}$, and b_{12} from MCMC sampling for the All, red-galaxy, and blue-galaxy cases respectively. There is a degeneracy between f and $b_{\rm gal}$ because the RSD constraints the distortion parameter $\beta = f/b$. In Fig. 2.13 and 2.14, adding the galaxy auto-correlations breaks the degeneracy between the group and galaxy biases, and they provide distinction constraints on the b_{12} for groups in each mass bin.

Fig. 2.15 shows the the best-fit (filled markers) and mean-fit (open markers) parameters from MCMC fitting the GAMA data, taken at the optimal $r_{\rm min}$ for each subsample. The specific parameter values for the best-fit case can be found in Tab. 2.4. The symbols and colours are the as in Fig. 2.11. The error bars on the best-fit parameters are taken from the std of the 26 mocks, whereas the error bars on the mean-fit parameters are the 1σ deviation estimated from the marginalised posterior from MCMC. The two sets of constraints show good consistency. The growth rate is measured consistently across the six subsamples. The All case gives a constraint $f\sigma_8 = 0.25 \pm 0.15$. The constraint from *Planck* with 68% limit from TT, TE, EE+lowE+lensing is $f\sigma_8 = 0.47 \pm 0.01$ at the redshift $z = 0.195$ [227]. The mean value is lower than the Planck value, possibly due to the flattening of the quadrupoles at scales $r > 15\,h^{-1}\,$Mpc, as shown in Fig. 2.10, but the difference between the measurements is only 1.4σ. Therefore, they are consistent measurements.

The middle panels in Fig. 2.15 show the measured galaxy and group biases. For galaxy biases, the LM subsamples give a lower mean bias compared to the

Table 2.3 *Mock measurements using the linear RSD model. The values are at smallest $r_{\rm min}$ which gives f below 10% bias compared to the fiducial value.*

	All	LMred	LMblue	MMred	MMblue	HMred	HMblue
$r_{\rm min}$	10	15	10	20	10	20	10
$\bar{\chi}^2$/dof	61.9/101	44.7/75	62.7/101	29.8/49	62.4/101	30.1/49	62.8/101
f	0.55 ± 0.19	0.56 ± 0.26	0.57 ± 0.16	0.58 ± 0.36	0.55 ± 0.19	0.63 ± 0.37	0.54 ± 0.18
$b_{\rm gal}$	1.22 ± 0.08	1.47 ± 0.14	0.89 ± 0.06	1.44 ± 0.20	0.90 ± 0.07	1.41 ± 0.21	0.90 ± 0.06
b_{12}	0.86 ± 0.02	1.26 ± 0.17	0.74 ± 0.05	0.98 ± 0.10	0.62 ± 0.03	0.74 ± 0.09	0.43 ± 0.03
σ_a	341 ± 74	347 ± 166	275 ± 75	385 ± 238	265 ± 91	427 ± 292	265 ± 82
σ_c	331 ± 76	342 ± 119	306 ± 81	373 ± 249	281 ± 84	389 ± 250	245 ± 90
I_a	0.019 ± 0.012	0.028 ± 0.020	0.008 ± 0.007	0.029 ± 0.023	0.008 ± 0.006	0.023 ± 0.022	0.009 ± 0.006
I_c	0.021 ± 0.014	0.026 ± 0.031	0.014 ± 0.020	0.029 ± 0.026	0.015 ± 0.013	0.028 ± 0.029	0.023 ± 0.016
$b_{\rm grp}$	1.42 ± 0.09	1.20 ± 0.22	1.20 ± 0.11	1.48 ± 0.23	1.46 ± 0.09	1.90 ± 0.30	2.09 ± 0.17

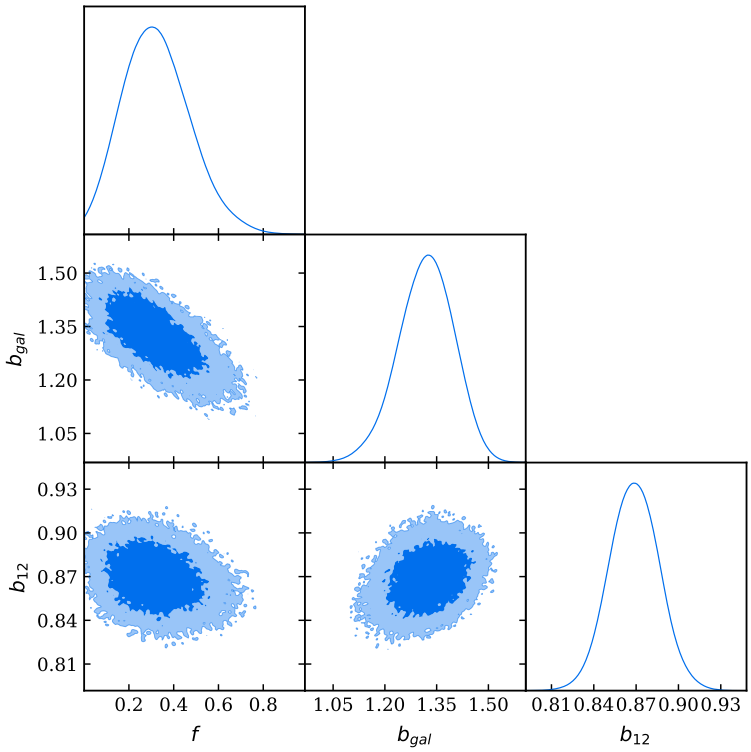

Figure 2.12 *The posterior distributions of the growth rate and biases of the cross-correlation with all galaxies and all groups in GAMA, marginalised over other parameters.*

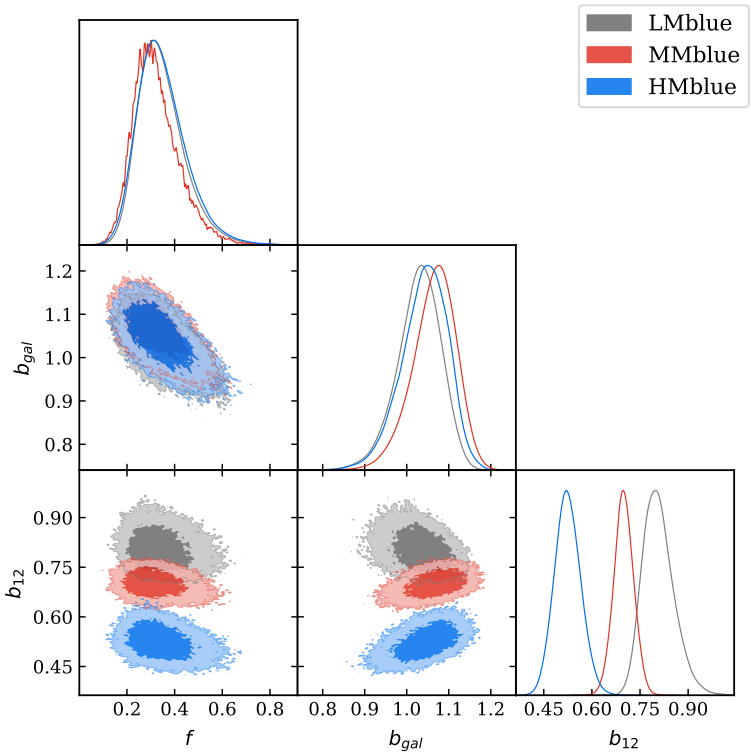

Figure 2.13 *Same as Fig. 2.12, but for blue galaxies cross-correlating groups in the three mass bins.*

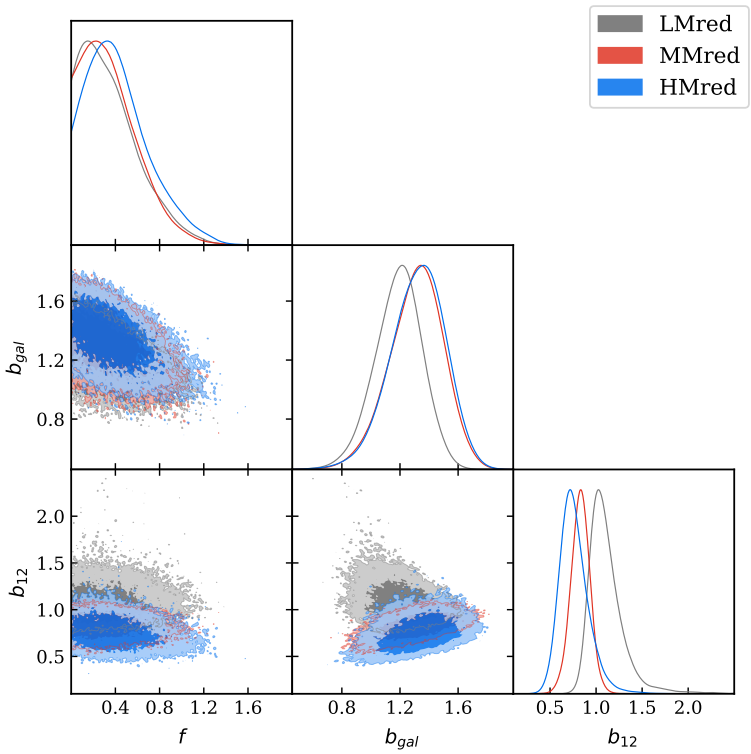

Figure 2.14 *Same as Fig. 2.12, but for red galaxies cross-correlating groups in the three mass bins.*

other two mass bins. Combining the measurements from different groups bins assuming independency, we find $b_{\rm gal} = 1.32 \pm 0.10$ for the red-galaxy subsample and $b_{\rm gal} = 1.04 \pm 0.04$ for the blue-galaxy subsample. The mean galaxy bias is $b_{\rm gal} = 1.33 \pm 0.08$, closer to the red galaxy bias. Combining the red and blue subsamples, the group biases for LM, MM, and HM bins are $b_{\rm grp} = 1.27 \pm 0.10$, 1.57 ± 0.08, 2.02 ± 0.15 respectively. The mean group bias is measured to be $b_{\rm grp} = 1.53 \pm 0.09$. The galaxy biases for the red and blue galaxies are consistent with other measurements using GAMA (e.g. [31]). The lower panels show the measured velocity dispersions for the auto- and cross-correlations. The results seem to suggest a consistent velocity dispersions between the auto- and cross-correlations, and between different group masses, but there is a preference of larger velocity dispersion in the red-galaxy subsamples than the blue ones. Combing the measurements from σ_c with different mass bins, we find $\sigma_c = 462 \pm 99\,{\rm kms}^{-1}$, $217 \pm 45\,{\rm kms}^{-1}$ for the red and blue subsamples respectively. The mean velocity dispersion for the whole sample is $\sigma_c = 245 \pm 76\,{\rm kms}^{-1}$. These velocities are also in good consistency with other measurements from GAMA (e.g. [31, 170]).

Group bias from the Halo Model

Having a proxy for the halo mass for each group, we attempt to compute the group bias in each mass bin. We compute this based on halo model mentioned in Section 1.3.4. For a given halo mass M, we compute the corresponding peak height ν as defined in Eq. 1.89 using the linear power spectrum at $z = 0.195$. The bias is then computed by

$$b(\nu) = 1 - \frac{1}{\delta_c}\frac{d\ln G}{d\ln \nu}, \tag{2.37}$$

where $\delta_c = 1.686$, $G = -dF(\nu)/d\ln\nu$, and we adopt the fitting formula for $F(\nu)$ in [205]:

$$F(\nu) = (1 + a\nu^b)^{-1}\exp(-c\nu^2) \tag{2.38}$$

with $(a, b, c) = (1.529, 0.704, 0.412)$. The group bias in a stellar mass bin is then computed by

$$\hat{b}_{\rm grp} = \sum_i^N f(M_h^i)\, b(M_h^i)/M_h^i\, \Delta\log(M_h), \tag{2.39}$$

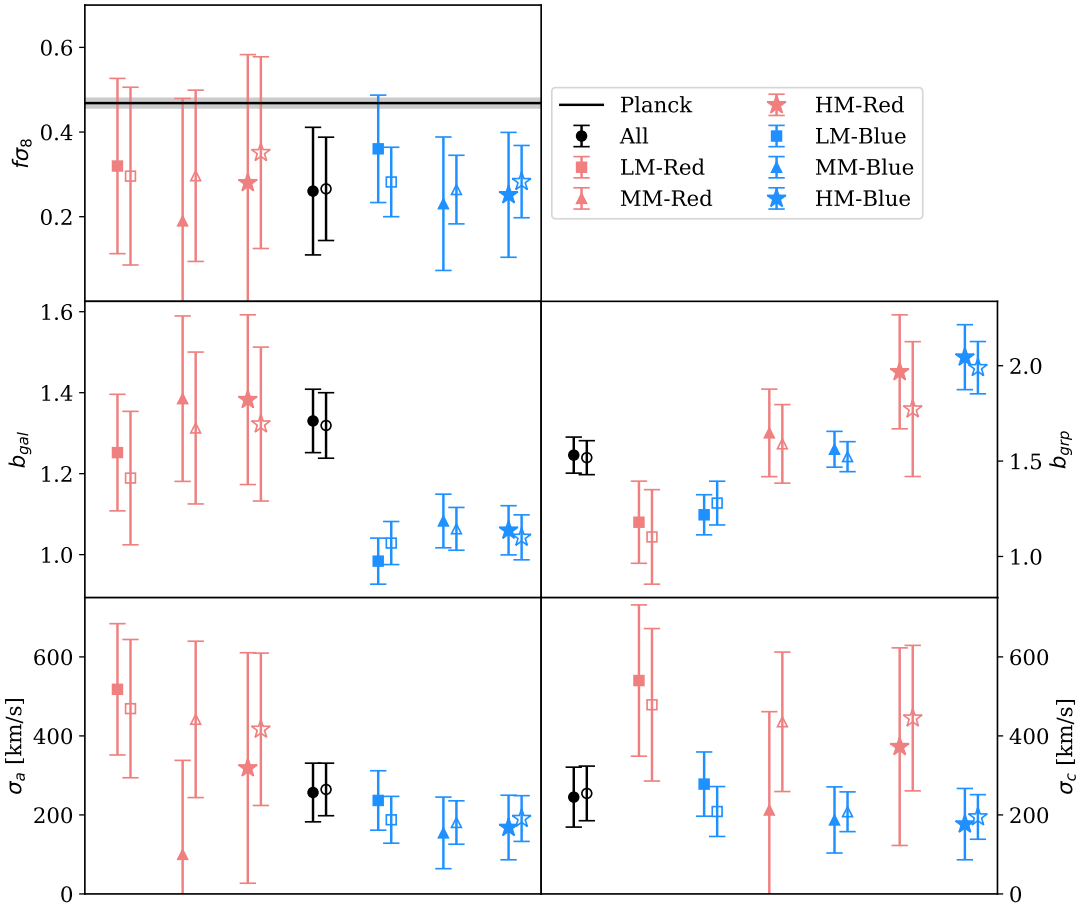

Figure 2.15 *Parameters fitting from the actual GAMA data at optimal minimum fitting scales for each sub-sample. The filled points show best-fit values with error bars from the scatter of 25 mocks. The unfilled points show the mean fit and* 1σ *deviation from MCMC sampling marginalising over other parameters. The black line in the top panel shows the Planck result and the grey band shows the using the TT, TE, EE+lowE+lensing 68% limits [227] at* $z = 0.195$.

Table 2.4 *GAMA measurements using the linear model. The values are at smallest $r_{\rm min}$ which gives f below 10% bias compared to the fiducial value.*

	All	LMred	LMblue	MMred	MMblue	HMred	HMblue
$r_{\rm min}$	10	15	10	20	10	20	10
$\bar{\chi}^2$/dof	74.7/101	37.4/75	78.2/101	19.2/49	77.0/101	33.7/49	74.3/101
f	0.32 ± 0.19	0.39 ± 0.26	0.44 ± 0.16	0.23 ± 0.36	0.28 ± 0.19	0.35 ± 0.37	0.31 ± 0.18
$b_{\rm gal}$	1.33 ± 0.08	1.25 ± 0.14	0.98 ± 0.06	1.39 ± 0.20	1.08 ± 0.07	1.38 ± 0.21	1.06 ± 0.06
b_{12}	0.87 ± 0.02	1.06 ± 0.17	0.81 ± 0.05	0.84 ± 0.10	0.69 ± 0.03	0.70 ± 0.09	0.52 ± 0.03
σ_a	257 ± 74	518 ± 166	237 ± 75	$100 + 238$	155 ± 91	319 ± 292	168 ± 82
σ_c	245 ± 76	540 ± 119	278 ± 81	212 ± 249	187 ± 84	372 ± 250	177 ± 90
I_a	0.011 ± 0.012	0.014 ± 0.020	$0.000 + 0.007$	$0.000 + 0.023$	$0.000 + 0.006$	$0.000 + 0.022$	$0.000 + 0.006$
I_c	$0.000 + 0.014$	$0.000 + 0.031$	$0.000 + 0.020$	0.018 ± 0.026	0.028 ± 0.013	0.036 ± 0.029	0.040 ± 0.016
$b_{\rm grp}$	1.53 ± 0.09	1.18 ± 0.22	1.29 ± 0.11	1.65 ± 0.23	1.56 ± 0.09	1.97 ± 0.30	2.04 ± 0.17

Table 2.5 *Group bias for the full sample, and for the LM, MM, and HM stellar mass bins, computed from the fitting formula given in [205] and measured from the 2-point correlation functions using the mocks and the GAMA data. For the mock groups, the halo mass in each stellar mass bin is based on the arithmetic mean host halo mass of the member galaxies. For the data, the mass-luminosity relation in [113] is used to compute the group halo mass, and the uncertainty of this relation is included as a convolution to the halo mass distribution in each stellar mass bin. The measured values is from combining the red and blue subsamples in Tab. 2.3 and 2.4 assuming independency.*

	Groups	$b_{\rm grp}$ (predicted)	$b_{\rm grp}$ (measured)
Mocks	All	1.13	1.42 ± 0.09
	LM	0.96	1.20 ± 0.11
	MM	1.16	1.46 ± 0.09
	HM	1.70	2.04 ± 0.17
GAMA	All	1.07	1.53 ± 0.09
	LM	0.92	1.27 ± 0.10
	MM	1.11	1.57 ± 0.08
	HM	1.42	2.02 ± 0.15

where $f(M_h)$ is the halo mass distribution in that stellar mass bin, and we take N logarithmic bins in the corresponding halo mass range with width $\Delta \log(M_h)$. Different halo mass definitions for groups in the mock catalogue results in biases differing by $< 10\%$, and we use the arithmetic mean host halo mass here. For GAMA, we include the uncertainty in the halo mass from the uncertainties in the parameters M_p and α from Eq. 2.24:

$$\sigma_{\log M_h} = \sigma_{\log M_p} + \sigma_\alpha \log(L_{\rm grp}/L_0), \tag{2.40}$$

where $\sigma_{\log M_p}$ and σ_α are given in below Eq. 2.24. For each mass bin $\log M_h^i$, we then convolve the number of objects by a Gaussian with $\sigma_{\log M_h}$. The predicted and measured group biases (combining the red and blue galaxy subsamples in the measured case) using mocks and GAMA data are summarised in Table 2.5.

We see that the predicted group bias are all smaller than the fitted values by $25\% - 50\%$. The predicted bias can match the measured values if the mass is increased by a factor of $2 - 3.5$ from HM to LM bins for mocks, and $3 - 6$ for data. For mocks, if the sum of the halo mass from members in unique host haloes is used as the group halo mass, then the group bias is increased to $b_{\rm grp} = 1.21, 1.03, 1.23, 1.80$ for the All, LM, MM, and HM cases respectively. This is closer to but still smaller than the measured bias values by about $1-2\sigma$, especially in the lower stellar mass bins. For data, increasing the dispersion in $\log M_h$ by a

factor of two only increases the bias in each bin by a few per cent. As indicated by Fig. 2.5, M_h estimated from total luminosity may not represent the true halo mass of the group. While the true scatter can be much larger, the mean slope of M_* as a function of M_h can also be smaller, indicating that at fixed M_*, the mean halo mass can be larger, leading to a larger group bias.

2.8 Conclusion

In this work, we present measurements of the 2D cross-correlation function $\xi(r_p, \pi)$ between groups and galaxies using the GAMA data in the redshift range $0.1 < z < 0.3$. The groups are found using a FoF algorithm from [290], and are subdivided into three stellar mass bins (LM: 40%, MM: 50%, and HM: 10%). We calibrate the corresponding halo mass for the groups using the relation in [113]. The galaxies are split into red and blue colours using a cut in the $g - i$ vs z plane. This altogether gives six cross-correlation subsamples. We use the 26 GAMA lightcone mocks from [82] for the purpose of testing the RSD models on a series of minimum fitting scales $r_{\rm min}$, and of constructing Jackknife covariance matrices to capture the sample variance between the GAMA fields. There are a few differences between the mocks and the GAMA data, including the mock mean redshift distribution, the bimodal $g - i$ colour distribution, and the total stellar mass of the groups. We match them carefully with the data subsamples. The measured 2D correlation functions show good consistency between the data and the mocks down to scales $r_p, \pi \leq 15\,h^{-1}\,$Mpc. At larger scales, the correlation functions are noise dominated. The measurements show distinct bias and FOG features for subsamples involving different galaxy colours and group masses.

The linear RSD model in [184] is adopted for this work with a non-linear power spectrum generated by HALOFIT [276, 282]. We fit the model to the projected correlation w_p and the multipoles ξ_0, ξ_2, and include the galaxy auto-correlation for each cross-correlation subsample to break the degeneracy between the galaxy and group bias. Applying the model to the mocks with σ_8 fixed to the fiducial value, we find that the growth rate f is recovered with negligible bias compared to the variance between the mocks at minimum fitting scales of $r_{\rm min} = 10 - 20\,h^{-1}\,$Mpc, depending on the subsample: the blue galaxy subsamples are more linear, and can be fitted to smaller scales compared to the red galaxy subsamples. Different subsamples also give consistent galaxy and group biases. The same model is then applied to the GAMA data, fitted down to the optimal $r_{\rm min}$ for

each subsample. We use MCMC sampling to marginalise over the biases, velocity dispersions, and integral constraints, and recover consistent growth rates from each subsample. The full sample gives a growth rate of $f\sigma_8 = 0.25 \pm 0.15$ at mean redshift $z = 0.195$, consistent with the *Planck* value of $f\sigma_8 = 0.47 \pm 0.01$. Using the halo mass of the groups, we attempt to predict the group bias from the halo model. However, in both mocks and the data, we find that the bias is underestimated by $25 - 50\%$. The discrepancy is partially alleviated in the mock case by using the sum of the unique halo mass, rather than the arithmetic mean halo mass of the group members. In data, the discrepancy suggests that the estimated halo mass from total luminosity and its scatter at fixed stellar mass is not very reliable.

The linear model adopted in this work is can only provide unbiased fitting results at relatively large scales, where the signal-to-noise of the GAMA sample is limited. Thus, an extension of this work will be to apply more sophisticated models, such as the 1-halo and 2-halo decomposition mentioned in Section 2.2.3, that can allow unbiased results at smaller scales. In principle, the much higher signal to noise can lead to a much tighter constraint on $f\sigma_8$, and the distinctive small scale features for different subsamples can also be explored. Currently, another limiting factor of this work is the relatively small sky coverage of GAMA, leading to large noise at large pair separation. In the future, however, the same analysis can be applied to larger datasets, such as the Bright Galaxy Sample in the Dark Energy Spectroscopic Instrument (DESI) survey [175], where the linear model may provide improved constraints on $f\sigma_8$ from different tracer samples.

Chapter 3

Cross-correlation of large scale structures and the CMB

We now turn to another cosmological probe for the growth of structures: the correlation between large scale structures and the CMB. Photons emitted from the CMB are perturbed by the presence of gravitational potentials sourced by matter, imprinting secondary features on the CMB that correlate with the foreground matter overdensity. By measuring the density field in the local Universe through galaxy surveys, one can pull out this correlation signal via cross-correlation or stacking. Tomographic analysis can demonstrate further the evolution of this correlation with the growth of structure, providing constraints on the cosmological parameters Ω_m and σ_8. I will present in Chapter 5 and 6 the measurements of this signal using the DESI Legacy Survey galaxies and the *Planck* 2018 CMB maps. Before I talk about the practical details of the survey and measurements, I will go through the theoretical background of these correlations in this Chapter.

The gravitational perturbations to the photon trajectory is discussed in Section 3.1. The temporal effect (Section 3.1.1) is changes in the peak and troughs of the CMB temperature fluctuations on relatively large scales, referred to as the Integrated Sachs-Wolfe (ISW) effect. The spatial effect (Section 3.1.2) is weak gravitational lensing, which distorts the CMB fluctuations and induces non-Gaussianity that can be used to reconstruct the *CMB lensing convergence* map. Then, in Section 3.2, I will show how these effects can be formulated into predicting the angular cross-correlation in spherical harmonic space, C_ℓ, between galaxy fields and the CMB. This serves as the theory section for Chapter 5.

In Section 3.3, I will discuss how the ISW signal can be predicted from the lensing convergence field in linear theory, and from the non-linear evolution of the matter density field. This serves as the theory section for Chapter 6, where we use a mock catalogue to predict the stacked CMB lensing and ISW signals from superstructures.

3.1 Perturbation to the photon geodesic

In the Newtonian gauge, the perturbed FRW metric is given by [189]:

$$ds^2 = -(1+2\Psi)dt^2 + a(t)^2(1-2\Phi)\delta_{ij}dx^i dx^j, \tag{3.1}$$

where $\Psi \ll 1$ and $\Phi \ll 1$ are two scalar potentials. The potential Φ satisfies the Poisson equation (Eq. 1.45), whereas the gradient of the other potential, $\nabla\Psi$, corresponds to the acceleration of non-relativistic particles. As we shall see below, the deflection of relativistic particles always comes with the combination $\Psi + \Phi$. In the absence of anisotropic stress, the off-diagonal terms in $T^{\mu\nu}$, the two potentials are equal, i.e. $\Phi = \Psi$. This is a result of the perturbed Einstein equation (see e.g. [188]). In most cases, the anisotropic stress is negligible, but it can arise in, e.g. neutrino free-streaming [171].

The photon geodesic equation is given by

$$\frac{d^2x^\mu}{d\lambda^2} + \Gamma^\mu_{\nu\sigma}\frac{dx^\nu}{d\lambda}\frac{dx^\sigma}{d\lambda} = 0. \tag{3.2}$$

The goal is to obtain the first order perturbations arising from these potentials. To do so, we first look at the unperturbed geodesic equation. Let the photon four momentum be $P^\mu = dx^\mu/d\lambda$. It satisfies $P^\mu P_\mu = 0$, so that

$$P^0 = a|P|. \tag{3.3}$$

The time component of Eq. 3.2 is

$$\frac{dP^0}{d\lambda} + a\frac{da}{dt}|P|^2 = 0. \tag{3.4}$$

This can be rewritten as $dP^0/d\lambda + d\ln a/d\lambda(P^0) = 0$, which gives the solution

$P^0 \propto 1/a$. Therefore, choosing the normalisation, we have

$$P^\mu = (1/a, 1/a^2 e^i), \quad \Sigma_i e^i = 1. \tag{3.5}$$

3.1.1 Temporal part: the ISW effect

We first look at the perturbation in the temporal component of Eq. 3.2. For a more thorough discussion of the ISW effect and its derivation , see the notes by [198], where the following derivation is based on. It is more convenient to work with conformal time, where $k^0 = \dot{\tau}$, and the dot is the derivative with respect to the affine parameter.

We start with Eq. 3.1 with conformal time $d\tau = dt/a$:

$$ds^2 = a(\tau)^2[-(1+2\Psi)d\tau^2 + (1-2\Phi)\delta_{ij}dx^i dx^j]. \tag{3.6}$$

We shall work with the scaled metric $\hat{g}_{\mu\nu} = g_{\mu\nu}/a^2$ to simplify the computation. Since the two metrics are conformal, the photon geodesic is the same. Notice that the affine parameter in $g_{\mu\nu}$ is however not affine in $\hat{g}_{\mu\nu}$. We first find the affine parameter in $\hat{g}_{\mu\nu}$. The following manipulations can be found in e.g. [49].

First, one can show that the Christoffel symbols for the two metrics are linked via

$$\Gamma^\mu_{\nu\rho} = \hat{\Gamma}^\mu_{\nu\rho} + \hat{S}^\mu_{\nu\rho}, \tag{3.7}$$

where

$$\hat{S}^\mu_{\nu\rho} = \frac{1}{a}[\delta^\mu_\nu \partial_\rho a + \delta^\mu_\rho \partial_\nu a - \hat{g}_{\nu\rho}\partial^\mu a]. \tag{3.8}$$

Let ρ and λ be the affine parameters of $g_{\mu\nu}$ and $\hat{g}_{\mu\nu}$ respectively. The affine parameters satisfy the geodesic equation

$$\frac{dx^\nu}{d\rho}\nabla_\nu\left(\frac{dx^\mu}{d\rho}\right) = 0, \tag{3.9}$$

$$\frac{dx^\nu}{d\lambda}\hat{\nabla}_\nu\left(\frac{dx^\mu}{d\lambda}\right) = 0, \tag{3.10}$$

where ∇ is the covariant derivative. The two parameters can be linked by taking

the derivative with respect to λ in $g_{\mu\nu}$:

$$\frac{dx^\nu}{d\lambda}\nabla_\nu\left(\frac{dx^\mu}{d\lambda}\right) = \frac{dx^\mu}{d\rho}\frac{dx^\nu}{d\lambda}\nabla_\nu\left(\frac{d\rho}{d\lambda}\right) = \frac{dx^\mu}{d\lambda}\frac{d}{d\lambda}\ln\left(\frac{d\rho}{d\lambda}\right), \tag{3.11}$$

where the second step used Eq. 3.9. Now substituting Eq. 3.7 into the left hand side of the above equation, it becomes

$$\frac{dx^\nu}{d\lambda}\left[\partial_\nu\left(\frac{dx^\mu}{d\lambda}\right) + \hat{\Gamma}^\mu_{\nu\rho}\frac{dx^\rho}{d\lambda} + \hat{S}^\mu_{\nu\rho}\frac{dx^\rho}{d\lambda}\right], \tag{3.12}$$

The first two terms combine to give zero according to Eq. 3.10, leaving

$$\hat{S}^\mu_{\nu\rho}\frac{dx^\nu}{d\lambda}\frac{dx^\rho}{d\lambda} = \frac{dx^\mu}{d\lambda}\frac{d}{d\lambda}\ln\left(\frac{d\rho}{d\lambda}\right). \tag{3.13}$$

Substituting Eq. 3.8, one finds that the third term in Eq. 3.8 drops out because of the null geodesic, getting:

$$2\ln a = \ln\left(\frac{d\rho}{d\lambda}\right) + c, \tag{3.14}$$

where c is a constant. Choosing it to be one, we have that $d\rho = a^2 d\lambda$.

Let the photon four-momentum in the conformal metric $\hat{g}_{\mu\nu}$ be $\hat{k}^\mu = dx^\mu/d\lambda$. Therefore, $k^\mu = \hat{k}^\mu/a^2$. The photon geodesic in Eq. 3.10 is given by

$$\frac{d\hat{k}^\mu}{d\lambda} + \hat{\Gamma}^\mu_{\nu\rho}\hat{k}^\nu\hat{k}^\rho = 0. \tag{3.15}$$

The ISW effect concerns the perturbed photon energy, i.e., the $\mu = 0$ term:

$$\frac{d\hat{k}^0}{d\lambda} + \partial_\tau\Psi\,(\hat{k}^0)^2 + 2\partial_i\Psi\,\hat{k}^0\hat{k}^i - \partial_\tau\Phi\,(\hat{k}^i)^2 = 0. \tag{3.16}$$

Now let $\hat{k}^\mu = \hat{k}^\mu_0 + \delta\hat{k}^\mu$. Since the potentials are of first order, at zeroth order, $\hat{k}^\mu_0$ is constant, i.e., $(1, e_i)$, where e_i is a unit vector. We have chosen such that $d\lambda = d\tau$. At first order, one can integrate Eq. 3.16. We recognise that

$$\frac{d\Psi}{d\lambda} = \hat{k}^\nu\partial_\nu\Psi, \tag{3.17}$$

so that Eq. 3.16 at first order becomes

$$\frac{d\delta\hat{k}^0}{d\lambda} = 2\frac{d\Psi}{d\lambda} - (\partial_\tau\Psi + \partial_\tau\Phi). \tag{3.18}$$

Let the emission time be τ_* and receive time be τ_0, the perturbed photon energy is

$$\delta\hat{k}^0(\tau_0) - \delta\hat{k}^0(\tau_*) = -2[\Psi(\tau_0) - \Psi(\tau_*)] + \int_{\tau_*}^{\tau_0} (\partial_\tau\Psi + \partial_\tau\Phi)\, d\tau. \tag{3.19}$$

Thus, the perturbed photon four-momentum is $k^\mu = a^{-2}(1 + \delta\hat{k}^0, e_i)$. Indeed, one would expect that, in an expanding universe, the photon energy decreases as a^{-2}. The photon energy measured by the observer moving at velocity u^μ, is

$$E = g_{\mu\nu}k^\mu u^\nu. \tag{3.20}$$

Since the background fluid speed is small, the velocity vector to first order is $u^\mu = 1/a(1 - \Psi, v_i)$, with v_i a first order quantity, such that $g_{\mu\nu}u^\mu u^\nu = -1$. This gives the measured energy to first order,

$$E = -\frac{1}{a}(1 + \Psi + a^2\delta k^0 - \mathbf{v}\cdot\mathbf{e}). \tag{3.21}$$

The measured photon energy decreases with a^{-1}, which is related to the redshift. The redshift is given by the ratio of energy emitted and received, i.e.,$1 + z_* = E_*/E_0 = (1/a_*)(1 + \Delta)$, where

$$\Delta = -a^2\delta k^0\big|_{\tau_*}^{\tau_0} - \Psi\big|_{\tau_*}^{\tau_0} + \mathbf{v}\cdot\mathbf{e}\big|_{\tau_*}^{\tau_0}. \tag{3.22}$$

Finally, the temperature is proportional to $1 + z$, giving $d\ln T = d\ln(1 + z)$. Therefore,

$$\left.\frac{\delta T}{T}\right|_{\tau_0} = \left.\frac{\delta T}{T}\right|_{\tau_*} + \frac{1}{c^2}[\Psi(\tau_0) - \Psi(\tau_*)] + \left.\frac{\mathbf{v}\cdot\mathbf{e}}{c}\right|_{\tau_*}^{\tau_0} - \frac{1}{c^2}\int_{\tau_*}^{\tau_0} (\partial_\tau\Psi + \partial_\tau\Phi)\, d\tau. \tag{3.23}$$

In the above equation, we have restored the factors of speed of light, c. The first term refers to the primordial temperature fluctuation at last scattering. The second term refers to the gravitational redshift of the photon at today and last scattering. The third term shows the Doppler effect of the observer. The last term is the Integrated Sachs-Wolfe effect, depending on the time evolution of the two potentials, and becomes significant as dark energy becomes dominant. In linear perturbation theory, the potentials are related to the density fluctuation directly through the Poisson equation

$$\nabla^2\Phi = 4\pi G\rho\delta/a. \tag{3.24}$$

It is therefore correlated with the matter distribution at late times.

3.1.2 Spatial part: the CMB lensing convergence κ

The aim here is to compute the spatial perturbation of the photon geodesic in the presence of Ψ and Φ. To put the result in a form which corresponds to the observable, it is convenient to change the coordinate system to $x^i = r(\theta_1, \theta_2, 1) = r\,\vec{\theta}$, where the z direction points towards the source located far away, and the x and y axis are aligned with the lens and source plane. We use the small angle approximation here. In this case, we have $dt = -a\,dr$, the minus sign since the origin is set to today. In the analysis, we would like to express the variable in terms of the vector $\vec{\theta}$, which tells us how much the 2D *image* of the source is changed by the perturbation.

The photon momentum is given by $P^\mu = dx^\mu/d\lambda$, where λ is the affine parameter; it satisfies $P^\mu P_\mu = 0$. Let the spatial part be $p^2 = g_{ij}P^iP^j$, then

$$-(P^0)^2(1+2\Psi) + p^2 = 0, \tag{3.25}$$

and from Eq.3.5 we know that $p \propto 1/a$. The spatial part of Eq. 3.2 to first order is

$$\frac{d^2x^i}{d\lambda^2} + \Gamma^i_{00}\left(\frac{dt}{d\lambda}\right)^2 + \Gamma^i_{0j}\frac{dt}{d\lambda}\frac{dx^j}{d\lambda} + \Gamma^i_{jk}\frac{dx^j}{d\lambda}\frac{dx^k}{d\lambda} = 0, \tag{3.26}$$

where the Christoffel symbols are:

$$\Gamma^i_{00} = a^{-2}\partial_i\Psi \tag{3.27}$$

$$\Gamma^i_{0j} = \delta^i_j(H - \dot{\Phi}) \tag{3.28}$$

$$\Gamma^i_{jk} = \delta^{im}\delta_{jk}\partial_m\Phi - \delta^i_k\partial_j\Phi - \delta^i_j\partial_k\Phi. \tag{3.29}$$

We rewrite Eq. 3.26 terms of derivatives with respect to r. We can write $d/d\lambda = (dt/d\lambda)(dr/dt)d/dr$. In general we need to consider $d/d\lambda = \partial/\partial x^\mu dx^\mu/d\lambda$, but in fact there is only one variable here, which is r because we have $\theta^i = \theta^i(r)$. Notice that θ^i are very small, so all terms containing the product of θ^i and the potentials drop out. The last term is only contributes with $j = k = 3$. Combining with Eq. 3.25, and with some cancellations, we get

$$\frac{d^2(r\theta^i)}{dr^2} = -\delta^{ij}\partial_j(\Psi + \Phi). \tag{3.30}$$

One can now integrate the equation twice to get the source location, θ_s^i, in terms of the imaged location, θ_m^i

$$\theta_s^i = \theta_m^i - \frac{\delta^{ij}}{r}\int_0^r dr \int_0^{r'} dr'' \partial_j(\Psi + \Phi). \tag{3.31}$$

Reverse the integral order and change the limits of the r' integral to $[r'', r]$, and integrate over this variable to get the expression:

$$\theta_s^i = \theta_m^i - \delta^{ij}\int_0^r dr'' \frac{r - r''}{r}\partial_j(\Psi + \Phi). \tag{3.32}$$

Define the distortion matrix as

$$A_{ij} = \frac{\partial \theta_s^i}{\partial \theta_m^j} = I + \xi_{ij}. \tag{3.33}$$

The matrix ξ_{ij} is symmetric given the expression, and the three degrees of freedom can be written as

$$\xi = \begin{pmatrix} -\kappa - \gamma_1 & -\gamma_2 \\ -\gamma_2 & -\kappa + \gamma_1 \end{pmatrix}, \tag{3.34}$$

where the diagonal part proportional to the identity is the *convergence* or magnification, κ, which changes the size of the image. The γ_i are referred to as *shear*, and they change the shape of the image. Therefore we get

$$\kappa = -\frac{1}{2}(\xi_{11} + \xi_{22}) = \frac{1}{2}\int_0^r dr'' \nabla_{2D}^2(\Psi + \Phi)\frac{r''(r - r'')}{r}, \tag{3.35}$$

where the extra r'' comes from converting the derivative of θ to the coordinate derivative. The convergence is linked to the lensing potential.

In terms of CMB lensing, the source is at the last scattering surface, $r = r_{\rm LS}$. The lensing potential, ψ, is defined such that the distorted displacement is given by its gradient, $\Delta\theta = \nabla_{\hat{n}}\psi$. From Eq. 3.32 we can write

$$\psi(\hat{n}) = -\int_0^{r_{\rm LS}} dr \frac{r_{\rm LS} - r}{r r_{\rm LS}}(\Psi + \Phi). \tag{3.36}$$

In spherical harmonic space, then, one can write

$$\kappa(\hat{n}) = \sum_{\ell m} \kappa_{\ell m} Y_{\ell m}(\hat{n}), \tag{3.37}$$

and similarly for ψ. Recording that $r^2\nabla^2 Y_{\ell m} = -\ell(\ell+1)Y_{\ell m}$, the lensing convergence and lensing potential thus has a simple relation

$$\kappa_{\ell m} = \frac{1}{2}\ell(\ell+1)\psi_{\ell m}. \tag{3.38}$$

3.2 Angular cross-correlation C_ℓ between tracers and CMB

To measure the lensing and ISW signals associated with a galaxy sample, the galaxy auto-correlations (gg) and the cross-correlations with CMB lensing ($g\kappa$) and with CMB temperature (gT) are employed. The following theoretical predictions for these quantities in the ΛCDM model are presented in spherical harmonic space and follow the notation in Peacock & Bilicki [207]. In the rest of this Chapter, we will assume $\Psi = \Phi$.

The galaxy harmonic auto-correlation in the Limber–Kaiser approximation [138, 165] is given by

$$\frac{\ell(\ell+1)}{2\pi}C_\ell^{gg} = \frac{\pi}{\ell}\int b^2\Delta^2(k=\ell/r,z)\,p^2(z)\,\frac{H(z)}{c}r\,dz, \tag{3.39}$$

where b is galaxy bias, $\Delta^2(k,z)$ is the dimensionless matter power spectrum at redshift z ($\Delta^2(k,z) = k^3P_{\delta\delta}(k,z)/2\pi^2$), and $p(z)$ is the redshift probability distribution function: $\int p(z)\,dz = 1$. Note that the corresponding equation, (7), in [207] is misprinted and lacks the factor $\ell(\ell+1)/2\pi$. For the case of galaxy cross-correlations between different tomographic slices, $p^2(z) \to p_1(z)p_2(z)$ in Eq. 3.39, where $p_1(z)$ and $p_2(z)$ are the redshift probability distributions of the two slices. There are also different biases for the two slices, $b^2 \to b_1b_2$, although for tomographic slices with a single sample selection, the bias is purely a function of redshift. Note that the above theory ignores distortions from peculiar velocities and treats redshift as an exact radial coordinate. This would not be correct for shells with width $\sim 10\,h^{-1}\,$Mpc, but is negligible for the much thicker shells that we consider [199].

Similarly, the theoretical galaxy-lensing convergence cross power spectrum is

computed by

$$\frac{\ell(\ell+1)}{2\pi}C_\ell^{g\kappa} = \frac{\pi}{\ell}\int b\Delta^2(k=\ell/r,z)\,p(z)K(r)\,r\,dz, \tag{3.40}$$

where the lensing kernel is given by

$$K(r) = \frac{3H_0^2\Omega_m}{2c^2a}\frac{r(r_{\rm LS}-r)}{r_{\rm LS}}. \tag{3.41}$$

Finally, the galaxy ISW cross-correlation is given by

$$\frac{\ell(\ell+1)}{2\pi}C_\ell^{gT} = T_{\rm CMB}\,\frac{2\pi}{c^3}\int b\,\Delta^2_{\delta\dot\Phi}(k=\ell/r,z)/k\,p(z)\,a\,dz. \tag{3.42}$$

$\Delta^2_{\delta\dot\Phi}(k,z)$ is the dimensionless matter-$\dot\Phi$ cross-power spectrum. In linear theory, $\delta(t,\mathbf{x}) = D(t)\delta(0,\mathbf{x})$. In Fourier space, Eq. 3.24 becomes $-k^2\Phi = 3/2H_0^2\Omega_m D(t)\delta(k)$. Therefore, the time derivative of the potential can be expressed as

$$\dot\Phi = \frac{3H_0^2\Omega_m}{2k^2}\frac{H(z)(1-f_g(z))}{a}D(z)\delta(k), \tag{3.43}$$

where $f_g \equiv d\ln D/d\ln a \simeq \Omega_m^{0.55}(z)$ is the growth rate [e.g. 5, 59, 93, 124, 225]. Thus,

$$\Delta^2_{\delta\dot\Phi}(k,z) = \frac{3H_0^2\Omega_m}{2k^2}\frac{H(z)\,(1-f_g(z))}{a}\Delta^2(k,z). \tag{3.44}$$

N-body simulations have suggested that small deviations from linear theory for C_ℓ^{gT} occur at $\ell \gtrsim 50$, and Eq. 3.42 becomes inaccurate [38, 39, 43, 57, 261, 277]. This can be alleviated by using the full nonlinear matter power spectrum in Eq. 3.44, e.g. HALOFIT, while still assuming a linear coupling between the density and velocity fields [39].

The above expressions for angular power spectra assume spatial flatness. The Limber-Kaiser approximation is inaccurate at large scales [e.g. 125, 297]. The agreement between the small angle approximation and the exact computation is about 15% in power at $\ell = 10$, but quickly improving to $< 1\%$ for $\ell > 30$. In practice these deviations are statistically negligible, as we exclude the largest-scale modes with $\ell < 10$ from our fitting, to allow for possible complications from combining several surveys in the sky (see Chapter 4). Because of cosmic variance, those very large-scale perturbations contain little statistical power. Note also that in principle the bias parameter may depend on scale, although it should tend to a constant in the linear limit as $k \to 0$; in practice we do allow for this scale dependence (see Section 5.1).

In summary, combinations of Eqs 3.39, 3.40 & 3.42 can be used to predict measurements from observations, and should in principle allow us to determine both cosmological parameters and nuisance parameters such as galaxy bias and uncertainties in the true redshift distribution of the galaxy samples. Most directly, one can determine the amplitudes of the CMB lensing and ISW signals associated with the late-time LSS galaxies, relative to the prediction of a fiducial cosmological model.

3.3 Predicting stacked signal

Another way to measure these imprints of large scale structures on the CMB sky is via stacking: the CMB maps are stacked at the locations of selected density peaks and troughs. This is similar to measuring the angular cross-correlation function in configuration space, $w(\theta)$. I will use this stacking technique in Chapter 6 to study the CMB lensing and ISW signals around superstructures in the DESI Legacy Survey. In this case, the modelling of this signal is non-trivial, because we will need to model small scales and targeting on specific structures means we cannot directly use the full distribution of δ. I will discuss below two possible ways one can model this effect. Due to the complication, it is also common to use mock galaxy samples and simulated CMB maps to predict the measured signals.

3.3.1 Non-linear density evolution

One can use the stacked density profile at the peaks or troughs to predict the signal. This method applies to thin tomographic bins or 3D voids/clusters. Taking voids as an example, the void profile is found by the void-galaxy cross-correlation function, and the RSD effect can be alleviated by integrating along the line of sight. Spherical symmetry is a good approximation for the average void profile. Thus, one can use the inverse Abel transformation to obtain the spherically symmetric 3D void profile, $\delta_v(r, z)$ centred at the mean redshift z of the galaxy sample. One can then use non-linear density evolution and spherical collapse to find the full evolution of the density profile. This can be done by numerically solving (e.g. see Eq.11 in [295])

$$y'' + \left(\frac{1}{2} + \frac{3}{2}\Omega_\Lambda(t)\right) y' + \frac{\Omega_m(t)}{2}\left(y^3 - 1\right) y = 0, \tag{3.45}$$

where the prime denotes derivative with respect to $\ln a$, and y is related to δ via

$$\rho_m(t) = \bar{\rho}_m(t) y(t)^{-3}. \tag{3.46}$$

Alternatively, the mapping between linear and non-linear density can be approximated, e.g. $1 + \delta_{NL} = (1 - D(t)\delta_L/\delta_c)^{-\delta_c}$ from Eq.B1 in [154]. Then the density can be evolved to different redshifts for each r. This density profile then allows one to straightforwardly compute the lensing convergence by integrating along the line of sight with the lensing kernel (Eq. 3.41).

For the ISW signal, one needs to compute the time derivative of the potential $\dot{\Phi}$. The corresponding spherically symmetric gravitational field $\Phi(r, z)$ for the 3D density fluctuation can computed for each redshift z by integrating the Poisson equation:

$$\Phi(r, z) = -\frac{3}{2}\frac{H_0^2 \Omega_m}{a}\left[\frac{1}{r}\int_0^r \delta(r', z) r'^2 dr' + \int_r^\infty \delta(r', z) r' dr'\right]. \tag{3.47}$$

The stacked ISW temperature at a given angular position $\hat{n}$ is then obtained through this integral

$$\Delta T(\hat{n}) = -T_0 \frac{2}{c^2}\int \frac{\partial \Phi}{\partial z}\Big|_{\rm 2D}(\hat{n}, z)\, dz, \tag{3.48}$$

where $\partial\Phi/\partial z|_{\rm 2D}(\hat{n}, z)$ is a 2D slice at redshift z of the full 3D potential $\partial\Phi/\partial z$ generated at the void centre. In this way, the derivative of Φ is projected in space and integrated in time.

3.3.2 Quasi-linear approach

Alternatively, one can also link the two observables – lensing and ISW effects – by making the assumption that density and velocity are linearly coupled. This should be true on linear scales where the ISW effect is most significant. Given the lensing convergence κ map, the lensing potential ψ map can be computed in spherical harmonic space using Eq. 3.38. The lensing potential is related to the 3D gravitational potential Φ via

$$\psi(\hat{n}) = -\frac{2}{c^2}\int \frac{r_{\rm LS} - r}{r_{\rm LS} r}\Phi(\hat{n}, r)\, dr, \tag{3.49}$$

where $r_{\rm LS}$ is the comoving distance to the CMB. The ISW signal is related to the time derivative of the gravitational potential via

$$\Delta T(\hat{n}) = -T_0 \frac{2}{c^2} \int \dot{\Phi}(\hat{n}, t)\, dt. \tag{3.50}$$

From the Poisson equation $\nabla^2\Phi = (3/2)H_0^2\Omega_m\delta/a$, it follows that in linear theory, $\nabla^2\dot{\Phi} = -H(1-f)\nabla^2\Phi$. Notice that the $\dot{\Phi}$ here is not fully linear – because the 3D potential Φ can have non-linear contributions, and the 'linear' assumption here is only between the density and velocity coupling.

Given a thin shell centred around redshift z_0 with edges $[z_0 - \Delta z, z_0 + \Delta z]$, one can make the approximations

$$\psi(\hat{n}, z_0) \approx -\frac{2}{c^2} \frac{r_{\rm LS} - r_0}{r_{\rm LS} r_0} \frac{c}{H(z_0)} \int_{z_0-\Delta z}^{z_0+\Delta z} \Phi(\hat{n}, z)\, dz, \tag{3.51}$$

$$\Delta T(\hat{n}, z_0) \approx -T_0 \frac{2}{c^2} a(z_0) \left[1 - f(z_0)\right] \int_{z_0-\Delta z}^{z_0+\Delta z} \Phi(\hat{n}, z)\, dz. \tag{3.52}$$

Combining these two equations we have

$$\Delta T(\hat{n}, z_0) \approx T_0 a(z_0) \left[1 - f(z_0)\right] \frac{r_{\rm LS} r_0}{r_{\rm LS} - r_0} \frac{H(z_0)}{c} \psi(\hat{n}). \tag{3.53}$$

This approach allows us to directly construct quasi-linear ISW signals from lensing potentials. We will check the validity of this method in Chapter 6 using simulations.

Chapter 4

Galaxy data from the DESI Legacy Imaging Survey

A major part of this thesis concerns the study of the correlation between large scale structures and the CMB. The dataset used for mapping out the large scale structures is the DESI Legacy Imaging Survey. Purposed for the Dark Energy Spectroscopic Instrument (DESI) target selection, this public imaging survey covers a vast sky area in both the north and south hemisphere, and also reaches a substantial depth, down to $g = 24.0$, $r = 23.4$, and $z = 22.5$. It is much deeper than alternative large-area imaging such as SDSS or Pan-STARRS, thus is invaluable for tomographic cross-correlation studies. However, as we shall see, some efforts are required to bring the dataset to a high quality that can be used for cosmological studies. This chapter is devoted to the procedure towards constructing reliable tomographic galaxy density maps. These procedures include various survey selections, systematic corrections, and photometric redshift assignments. Having set up the stage in this chapter, we will discuss the galaxy clustering and their CMB correlations in detail in Chapter 5.

4.1 The DESI Legacy Imaging Survey

Altogether covering an area of 17,739 deg^2, the DESI Legacy Imaging Survey [68] is divided around Dec = 33° in J2000 coordinates, a combination of four different projects observed using three different instruments on three different telescopes,

namely, DECaLs, BASS, and MzLS.

DECaLS The Dark Energy Camera Legacy Survey (DECaLS) is observed using the Dark Energy Camera (DECam; [87]) based on the 4m Blanco telescope at the Cerro Tololo Inter-American Observatory, Chile. DECam has high sensitivity in the wavelength range of $400 - 1000$nm, which is optimal in obtaining the photometry in grz bands. The overall survey area is about 9000 deg^2, covering regions with Dec $\leq 32^\circ$ in the North Galactic Cap (NGC) and and Dec $\leq 34^\circ$ in the South Galactic Cap (SGC). Part of the data is directly adopted from the Dark Energy Survey (DES; [287]), which covers about 5000 deg^2 area in the SGC.

BASS The Beijing-Arizona Sky Survey (BASS; [316]) is observed by the 90Prime camera [304] at the prime focus of the Bok 2.3m telescope at Kitt Peak, Arizona. The survey covers about 5000 deg^2 in the NGC at Dec $\geq 32^\circ$, and supplies the g and r band photometry matched with DECaLS for the DESI Legacy Survey.

MzLS The Mayall z-band Legacy Survey (MzLS) is observed by the MOSAIC-3 camera [67] at the prime focus of the 4m Mayall telescope at Kitt Peak National Observatory, Arizona. The imaging covers the same sky area as BASS. The z-band filter is matched to the DECam filter bandpass.

We use the publicly available Data Release 8[1] (DR8) of the DESI Legacy Survey. The sources are processed and extracted using `Tractor`[2] [157], which in general involves the following procedures. Firstly, the sky is subtracted on each CCD iteratively, and its PSF is estimated. Then, using several weighted stacks of the images, sources are detected above a 6σ-threshold. Finally, the `Tractor` models the source with a set of parametric light profiles, producing a catalogue containing source information such as positions, fluxes, and morphologies. In addition to the three optical bands grz, for each optically observed source, the Legacy Survey also include its mid-infrared photometry from the WISE [307] satellite. These fluxes are centred at 3.4μm, 4.6μm, and 12μm, namely the W_1, W_2, and W_3 bands. The WISE photometry is also measured using the `Tractor` algorithm with 'forced photometry', i.e., forcing the location and shape of the model, since WISE has a lower spatial resolution compared to the optical surveys.

[1] `http://legacysurvey.org/dr8/`
[2] `https://github.com/dstndstn/tractor`

4.1.1 Galaxy selection

We apply the following selections and corrections to the DESI Legacy Survey data at the catalogue level.

Firstly, the catalogue contains stars, galaxies, and quasars. For our purpose of constructing tracers for the large scale structure, we would like to only select galaxies. A convenient way to do so is by looking at the morphology types of the source. There are six morphology types fitted by the `Tractor` algorithm (except the last one), namely:

1. PSF: point sources;
2. REX: round exponential galaxies with a variable radius;
3. DEV: deVaucouleurs profiles for elliptical galaxies;
4. EXP: exponential profiles for spiral galaxies;
5. SER: Sersic profiles;
6. DUP: Gaia sources that are coincident with an extended source.

The majority of the sources are in the first four morphology types. The point sources mainly contain stars and quasars. Objects of this type are thus excluded. This is also confirmed by cross-matching galaxies from spectroscopic surveys to the DESI Legacy Survey, where only a small fraction of galaxies are identified as PSF objects. The resultant sources may still contain some stars and quasars. This can be separated in the colour space. Since we also select objects implicitly in the three dimensional colour space of $g-r$, $r-z$, and $z-W_1$ via photometric redshift assignment, the contamination is thus small.

Secondly, we require `FLUX_G|R|Z|W1`> 0, i.e. fluxes in these four bands are detected. Because of the shallower effective depth of the W_2 and W_3 bands, we only make use of W_1. This is to ensure successful determination of photometric redshifts. Fluxes are corrected using `MW_TRANSMISSION_G|R|Z|W1` for Galactic extinction correction. These values are derived from the maps in [254] to account for the dust absorption near the Galactic Plane. This largely removes the survey depth dependence as a function of galactic coordinates. However, there are still residual correlations, which we attempt to remove at the galaxy density map level in Section 4.3.1.

The survey does not have a uniform depth over the entire footprint. The main difference in depth is between the deep DES region and the rest of the survey. Magnitude cuts are applied with $g < 24$, $r < 22$, and $W_1 < 19.5$, where all magnitudes are computed by $m = 22.5 - 2.5 \log_{10}(\text{flux})$. The cuts in g and r are chosen as reasonable completeness limits from inspection of the number counts. The cut in W_1 further removes faint objects that are not well covered by the calibration sample. We experimented with imposing a brighter cut, and found that our main results were essentially unchanged if all limits were made 0.5 mag. brighter.

Finally, Bitmasks[3] are used to generate a survey completeness map, with the following Bits masked:

- Bit 0: touches a pixel that is outside the primary region of a brick;
- Bit 1: touches a pixel within the locus of a bright star;
- Bit 5-7: masks in grz bands;
- Bit 11-13: touches a pixel within the locus of a medium bright star, large galaxy, or globular cluster.

To convert the mask to appropriate resolution for this work, we generate large number of randoms and bin them into a HEALPIX map [98] with $N_{\text{side}} = 128$, corresponding to a pixel area of $0.2\,\text{deg}^2$. The completeness map is obtained from the ratio of the number of randoms in each HEALPIX pixel with and without masking. The map is then upgraded to $N_{\text{side}} = 1024$ which is the resolution used for most of our analyses. Fig. 4.1 shows the completeness map of the Legacy Survey footprint.

4.2 Photometric redshifts

One of the key pieces of information needed for interpreting observations of CMB-galaxy cross-correlations is the redshift distribution of the galaxy sample. A variety of methods have been developed over many years to estimate either the redshifts of individual galaxies or the redshift distribution of a galaxy sample using broad band photometry (see Schmidt et al. 2020 for a review). Generally

[3] `http://legacysurvey.org/dr8/bitmasks`

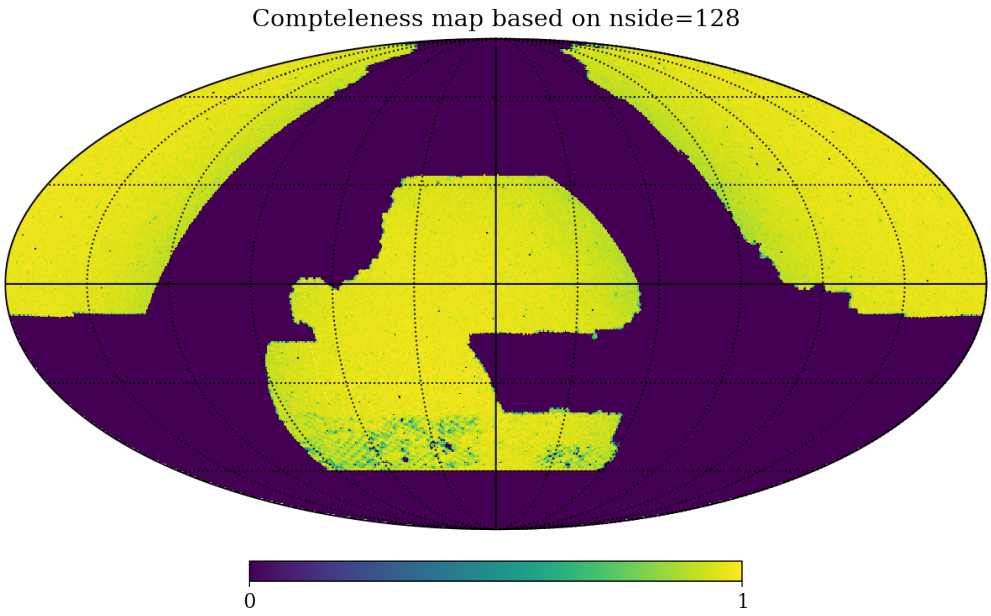

Figure 4.1 *The completeness map of the DESI Legacy Survey. The higher intensity denotes regions with higher completeness.*

photo-z estimates are either template based (e.g. LePhare Arnouts et al. 1999; BPZ Benítez 2000; EAZY Brammer et al. 2008) or data-driven methods (e.g. TPZ Carrasco Kind & Brunner 2013; SkyNet Graff et al. 2014; GPz Almosallam et al. 2016; ANNZ2 Sadeh et al. 2016; METAPhoR Cavuoti et al. 2017; Delight Leistedt & Hogg 2017; CMN Graham et al. 2018; CHIPPR Malz & Hogg 2020) . There have been several attempts to compare the accuracy and precision of various photometric redshift methods [34, 120, 235, 249] with no strong winner.

Our approach is direct and empirical, based on using observed spectroscopy to assign a redshift to a given location in multi-colour space. In parallel with this work, a public catalogue of photometric redshifts for the Legacy Survey was made available by Zhou et al. [314]; Z20 hereafter. Although they used similar spectroscopic calibration samples, their approach differs somewhat from ours, being based on machine learning. The advantage of this is that we are able to look in detail at the sensitivity of our results to the properties of the photometric redshifts.

4.2.1 Spectroscopic calibration samples

We use a number of spectroscopic surveys that overlap with the DESI Legacy Survey footprint to calibrate photometric redshifts. These surveys and their details are listed below.

GAMA DR2 The Galaxy and And Mass Assembly (GAMA) survey [168] is a spectroscopic survey conducted by the Anglo-Australian Telescope, down to $r < 19.8$ mag over a sky area of $\sim 286\text{deg}^2$. We select samples with $z > 0.01$ and redshift quality `NQ`≥ 3. The GAMA sample has been rejection sampled to remove the dip in density around $z = 0.23$; this is known to represent a rare LSS fluctuation, which we do not wish to imprint on our photo-z estimates.

BOSS DR12 The Baryon Oscillation Spectroscopic Survey (BOSS) [8] is part of SDSS-III. The main sample consists of LOWZ ($z \lesssim 0.4$) and CMASS ($0.4 < z < 0.7$) galaxy samples. The LOWZ sample has a set of colour-magnitude cuts that are similar to Luminous Red Galaxies (LRG), whereas the CMASS sample is selected with a bluer extension. We remove very low redshift samples with $z > 0.01$.

eBOSS DR16 The extended BOSS survey [6] consists of three target classes: LRG, ELG (Emission Line Galaxies), and QSO (Quasars). Since we aim to remove quasars in our selected catalogue, we only use the LRG and ELG sample for calibration. The LRG sample covers a mean redshift of 0.7, whereas the ELG sample covers $0.7 < z < 1.1$. We remove very low redshift samples with $z > 0.01$.

VIPERS DR2 The VIMOS Public Extragalactic Redshift Survey [260] is a spectroscopic survey conducted by the Very Large Telescope (VLT) at the European Southern Observatory (ESO). The survey covers an overall area of $\sim 23.5\text{deg}^2$, with a redshift overage of $0.5 < z < 1.2$, and a magnitude limit of $i < 22.5$. We select sources with $z > 0.01$, `zflg`≥ 3, and `classFlg`≥ 0.

DEEP2 DR2 The DEEP2 Redshift Survey [196] is a spectroscopic survey conducted by the DEIMOS spectrograph on the Keck II telescope. The survey has a limiting magnitude of $R_{AB} = 24.1$, with redshifts extending to 1.4. We select sources with $z > 0.01$ and flag `ZQUALITY`≥ 3. This survey is useful in covering the high redshift tail of the DESI Legacy Survey sample.

In addition, we also include two photometric surveys for their highly accurate photometric redshifts.

COSMOS The Cosmic Evolution Survey [130] is a deep, wide area, multi-wavelength survey. We use the COSMOS2015 photo-z catalogue [153], which has an accuracy of 0.007 and less than 0.5% catastrophic failures. Since COSMOS is much deeper than the DESI Legacy Survey, we choose sources with `r_MAG_APER2` < 23 to match with the DECaLS sample. This is another survey which we use to cover the high redshift tail of our selected galaxy sample.

DESY1A1 redMaGiC The Dark Energy Survey [47] is conducted using DECam mounted at the Blanco 4m telescope. We use the Y1 redMaGiC Catalogue, consisting of LRG samples in the photometric redshift range $0.15 < z < 0.9$. The photometric redshift has an uncertainty of $0.017(1 + z)$. We use this sample as a 'space filler' as will be explained below.

Altogether, the calibration sample contains 1.26×10^6 galaxies, roughly covering the redshift range $0 < z < 1$. The majority of these datasets overlap with DECaLS, and galaxies in the calibration data sets are matched with DECaLs objects based on their nearest neighbours using the python routine `cKDTree` within a distance of 0.5°.

4.2.2 Photo-z assignment in multi-dimensional colour space

The redshifts from the original calibration samples will be referred to as 'spectroscopic' or 'true' from this point onward, in order to make a distinction with the inferred photometric redshifts. All calibration samples except DESY1A1 redMaGiC [47] are binned in 3-dimensional grids of $g-r$, $r-z$, and $z-W_1$ with a pixel width of about 0.03. The range of the colours are: $-0.5 < g-r < 2.5$, $-2 < r-z < 3$, and $-2 < z-W_1 < 4$. Pixels containing more than 5 objects from the calibration samples are assigned the mean redshift of these objects. The DES sample is processed in the same way to fill out pixels that are not calibrated in this initial pass. We then apply this calibration to the full Legacy Survey: objects that fall in pixels that lack a redshift calibration are excluded, thus selecting objects that occupy the same colour space as our calibration sample. The assigned photometric redshift is the mean redshift for the colour pixel, plus a random top-hat dither of ± 0.005 so that digitisation artefacts are not apparent in the $N(z)$ distributions. Fig. 4.2 compares the inferred photometric redshifts with the true redshifts of all the calibration sample, and Fig. 4.3 shows the break down for each sample including both DECaLS and BASS+MzLS. The general agreement is good, with 68% of the sample having photometric redshifts within ± 0.027 of

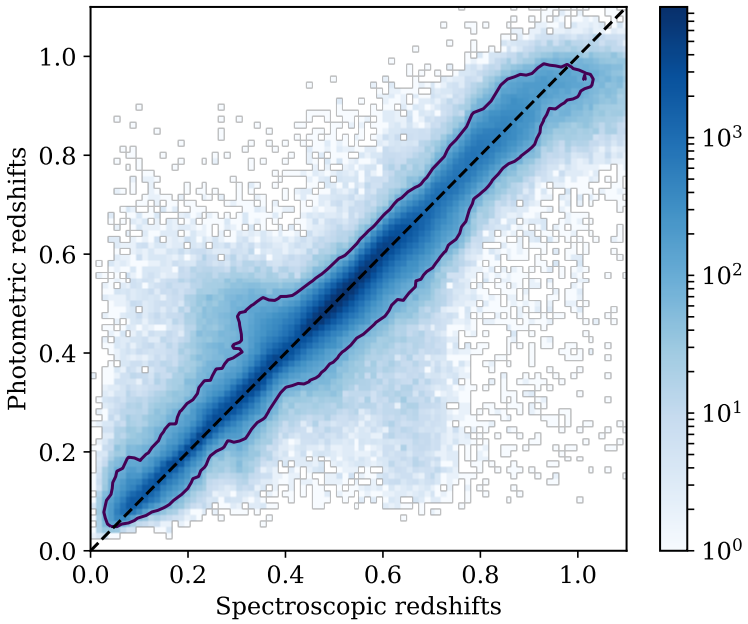

Figure 4.2 *Photometric redshifts inferred from $g-r$, $r-z$, and $z-W_1$ colours, versus the spectroscopic redshifts for the calibration samples. The contour shows the 95% interval. The colour bar indicates the number of galaxies in each pixel.*

their spectroscopic redshifts. However, a small proportion of the objects with true redshifts $0.2 < z < 0.4$ are assigned photometric redshifts between $0.4 < z < 0.6$. The inferred redshifts are also underestimated beyond $z = 0.9$, as usual: this estimation method means that $\langle z_{\rm spec} \rangle$ should be unbiased at given $z_{\rm phot}$, so that a bias in $\langle z_{\rm phot} \rangle$ at given $z_{\rm spec}$ is inevitable at the extremes of the distribution.

Photometric redshifts are assigned to 78.6% of the selected Legacy Survey objects, yielding a primary sample of approximately 49 million galaxies (see Table 4.1 for details). The lost 21.4% objects will lead to higher shot noise, but this is a small price to pay for excluding objects where the photometric redshift cannot be reliably calibrated. The redshift distribution of our final sample is shown in Fig. 4.4 as solid line histogram.

We can compare this distribution with the corresponding $N(z)$ for the public Legacy Survey photometric redshifts made available by Z20; this is shown in Fig. 4.4 as shaded histogram. The two distributions are generally in good consistency with each other; both distributions show some weak features, indicating that LSS in the calibrating samples has still propagated into the final photo-zs to some extent. With broad tomographic bins, we expect that such

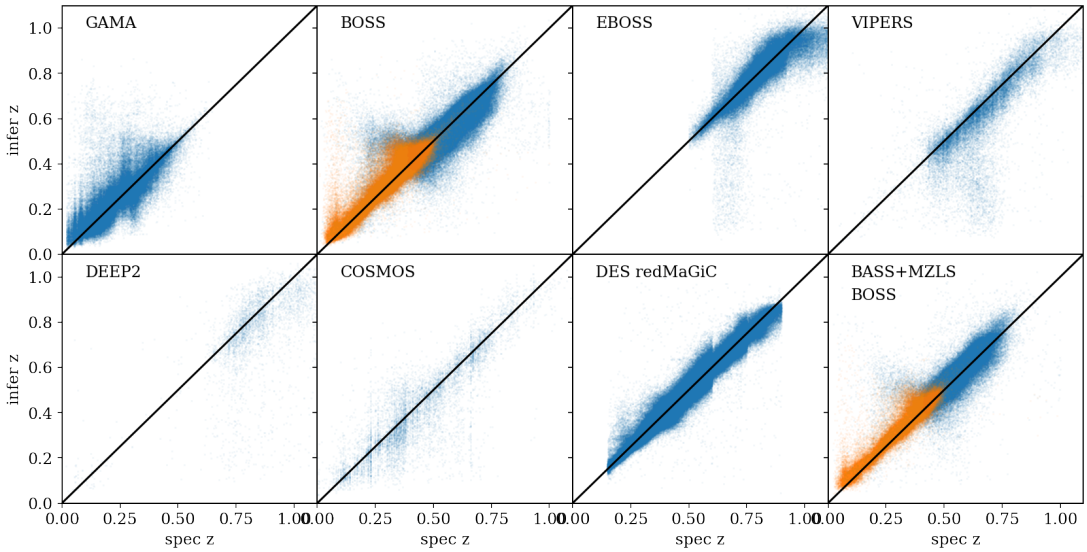

Figure 4.3 *The assigned photometric redshift and true redshift for each of the spectroscopic samples used: GAMA, BOSS (CMASS in blue and LOWZ in orange), eBOSS (LRG and ELG), VIPERS (field 1 and 4), DEEP2, COSMOS, and DES redMaGiC. All panels show the calibration with DECaLS, except for the last panel, which shows the calibration with BASS+MzLS.*

structure will be unimportant, but it will be helpful to compare the results from two rather different photo-z catalogues (see Section 4.2.4). We divide our samples into four tomographic slices, illustrated by the grey dotted lines in Fig. 4.4. The redshift ranges are: bin 0: $0 < z \leq 0.3$; bin 1: $0.3 < z \leq 0.45$; bin 2: $0.45 < z \leq 0.6$; bin 3: $0.6 < z \leq 0.8$. Our photo-z data and accompanying software can be accessed at `https://gitlab.com/qianjunhang/desi-legacy-survey-cross-correlations`.

4.2.3 Photometric redshift error distribution

For the calibration sample, the distribution of $\delta z \equiv z_{\rm spec} - z_{\rm phot}$ as a function of $z_{\rm phot}$, can be well modelled by the modified Lorentzian function,

$$L(x) = \frac{N}{(1 + ((x - x_0)/\sigma)^2/2a)^a}, \tag{4.1}$$

where x_0, σ, and a are parameters that control the mean. width, and fall-off of the distribution, and N is the normalisation such that $\int_{-\infty}^{+\infty} L(x)\,dx = 1$. For each of the tomographic bins, we fit σ and a, while x_0 is fixed to zero. The results for calibration sample is shown in Fig. 4.5, and their best-fit parameters

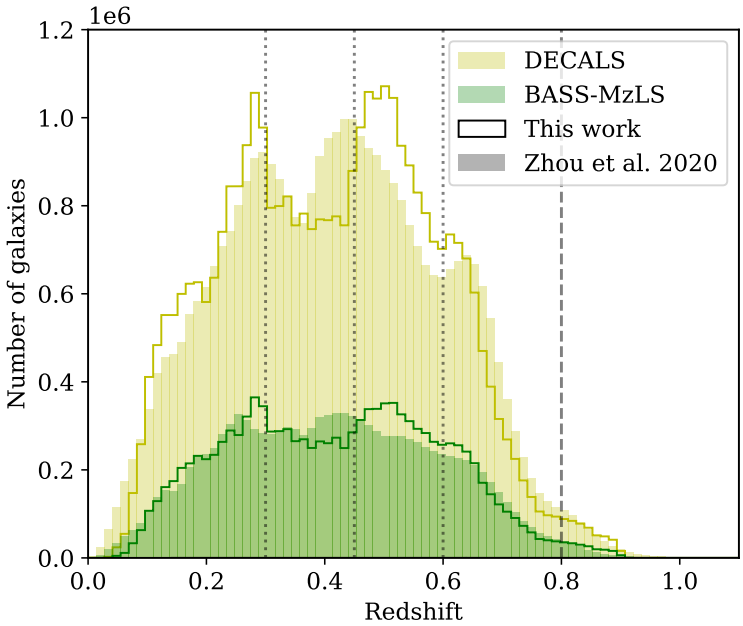

Figure 4.4 *Photometric redshift distribution of galaxies after selection, in the DECALS (yellow) and BASS-MzLS (green) regions respectively. We compare our photometric redshifts (shown as a solid line histogram) with the corresponding redshifts from [314] (shown as a shaded histogram). Grey dotted lines show our four tomographic redshift bins in* $0 < z \leq 0.8$.

are summarised in Table 4.1. The inferred true redshift distribution $p(z)$ is then estimated by convolution of the raw distribution with the Lorentzian function, as shown in the black dashed line in Fig. 4.6. [252] have recently proposed a similar approach to marginalising over photo-z errors while restricting themselves to the case of Gaussian fields with an ad-hoc mixing matrix.

However, galaxies fainter than the calibration sample may not follow this δz distribution exactly. There is an irreducible scatter that arises because galaxy spectra are not universal in shape; but photometric measuring errors will increase the scatter for fainter objects. As shown below in Section 5.1, we are able to diagnose this using the galaxy cross-correlations between the different tomographic redshift slices. The width of the error distribution controls the degree of cross-correlation between the different tomographic slices, which is observed to be larger than predicted when using the directly calibrated $p(z)$ parameters from Table 4.1. The largest discrepancy occurs in the cross-correlation between redshift bin 1 and bin 2, which is almost double the predicted value. We therefore model the true error distribution in the photometric redshifts by allowing the tail a of each distribution to spread, while fixing the width σ to that

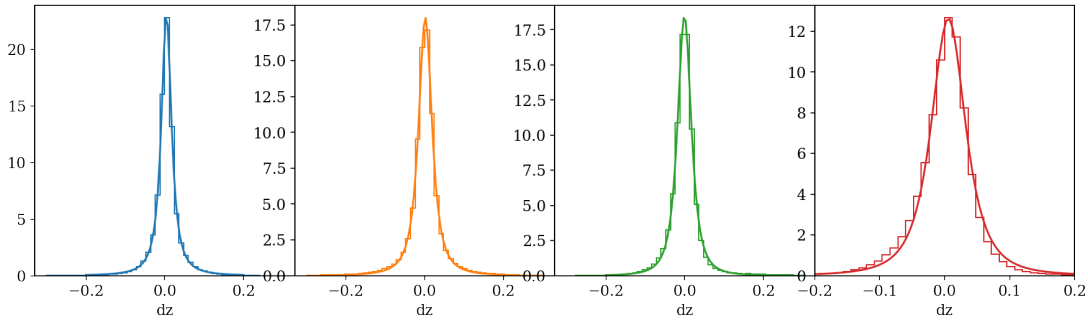

Figure 4.5 *The normalised histogram of $\delta z \equiv z_{\rm spec} - z_{\rm phot}$ as a function of $z_{\rm phot}$ in four tomographic bins for the spectroscopic calibration sample. From left to right, the distributions show bin 0 (blue), bin 1 (orange), bin 2 (green), and bin 3 (red). The smooth solid lines on top of the histograms show the best-fit error distribution in Eq. 4.1.*

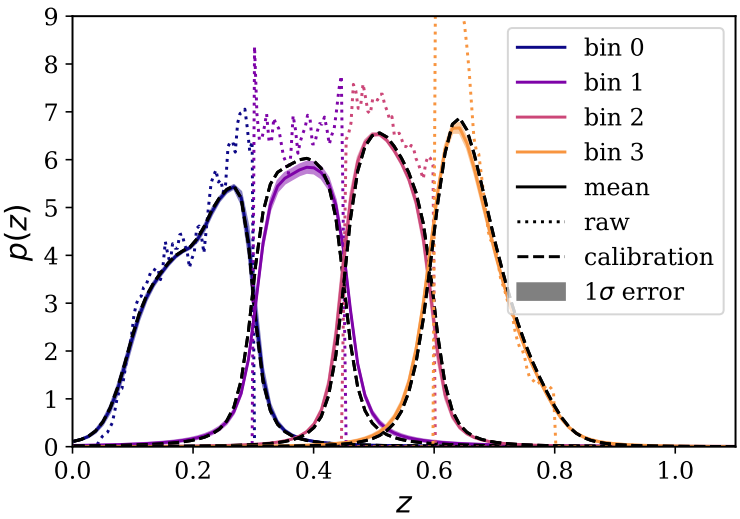

Figure 4.6 *Redshift distribution function, normalised such that for each redshift bin $\int p(z)\,dz = 1$. The dotted lines show the raw photometric redshift distribution with $|\Delta z| < 0.05$, the solid lines show the mean distribution (see text for details) and their 1-σ deviation using the 2-bias model (see Section 5.1.2), and the dashed lines show the distribution using parameters from spectroscopic calibration sample.*

Table 4.1 *Summary of the four tomographic redshift slices. The first row shows the number of galaxies in each redshift slice. The second row shows the effective volume of the redshift slice. The third and forth rows are parameters for the Lorentzian function (Eq. 4.1) fitted to redshift errors in each redshift bin derived from the calibration data sets; and the last two rows show the best-fit parameters derived empirically from the cross-correlations between the different tomographic bins (noting that σ is not varied in this exercise). The best-fit parameters refer to our photo-z data clipped with $|\Delta z| < 0.05$.*

Redshift bin	0: $0 < z \leq 0.3$	1: $0.3 < z \leq 0.45$	2: $0.45 < z \leq 0.6$	3: $0.6 < z \leq 0.8$
Number of galaxies	14 363 105	11 554 242	13 468 310	7 232 579
Volume $[(h^{-1}\mathrm{Gpc})^3]$	1.047	2.084	3.431	20.37
σ^{spec}	0.0122	0.0151	0.0155	0.0265
a^{spec}	1.257	1.319	1.476	2.028
a^{bf}	1.257	1.104	1.476	2.019
x_0^{bf}	-0.0010	0.0076	-0.0024	-0.0042

determined by the spectroscopic sample. We also allow a change in the mean x_0 of each bin, while requiring the sum of the mean shifts in the four bins to be zero. This results in 7 systematic nuisance parameters to marginalise over. We take 10 samples in each dimension of the 7-parameter space with appropriate upper and lower bounds, and for each point in the grid, we compute the χ^2 of the 10 galaxy auto- and cross-correlation between different redshift slices. The galaxy bias parameters in each case are fixed at the lowest-χ^2 values from the auto-correlation (which we fit using the 2-bias model up to $\ell = 500$). This is sufficient given the size of the error bar in the auto-correlations: the galaxy bias is very tightly constrained. Constraints on the cross-correlation amplitudes can then be marginalised over the photo-z parameters, i.e., weighted by the likelihoods of each set of parameters. The mean and 1-σ deviation of $p(z)$ weighted by the likelihoods of the $p(z)$ parameters are shown in Fig. 4.6. We leave the detail of this procedure to be discussed in Section 5.1.

4.2.4 Comparison with other photo-z

We present a detailed comparison between our photometric redshifts and those of Z20 [314], including the impact of the different photo-z options on our cosmological results. Firstly note that this comparison is only possible for the 78.6% of galaxies that lie in regions of multicolour space for which calibration data exist. Z20 give photometric redshifts for additional galaxies, and these are probably to be considered less reliable. Nevertheless, we can perform clustering analyses that use all the Z20 data, or just their redshifts for the same set of objects that we use, and this can give useful insight into the robustness of our conclusions. Fig. 4.7 compares the two photo-z catalogues in detail. For the objects in common, the median redshift difference is $|\Delta z| = 0.023$, and 68% of objects agree in photometric redshift to within 0.038 . The difference distribution has non-Gaussian tails, and we also therefore consider a 'clipped' selection where we retain only objects where the two estimates agree to within $|\Delta z| < 0.05$ (indicated by the black dashed line in Fig. 4.7): this is about twice as large as our photo-z 1-σ uncertainty, so the effect is to remove outlying objects in the tails of the error distribution. This removes a further 23.4% of the sample, but should provide a cleaner selection in the sense that object are more likely to lie in their nominal tomographic bin. The cross-correlations between the different bins confirm that this strategy is successful.

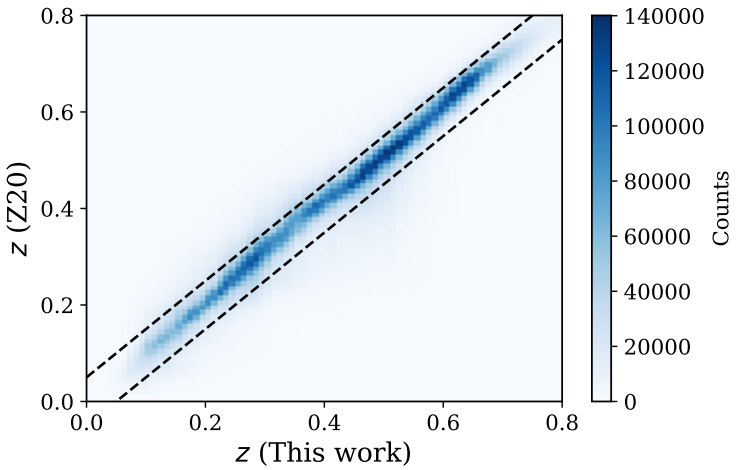

Figure 4.7 *Photometric redshifts inferred from $g-r$, $r-z$, and $z-W_1$ colours, versus that from Z20. The dotted lines mark $|\Delta_z| = 0.05$ interval. In the clipped sample, we only use objects inside the dashed line.*

Table 4.2 *Photo-z parameters for Z20, using spectroscopic calibration sample as well as the best-fit values from the galaxy clustering analysis.*

	bin 0	bin 1	bin 2	bin 3
$\sigma^{\rm spec}$	0.0075	0.0128	0.0150	0.0248
$a^{\rm spec}$	1.320	1.484	1.700	1.502
$a^{\rm bfit}$	1.320	1.110	1.697	1.502
$x_0^{\rm bfit}$	0.000	0.0003	−0.0002	−0.0001

Furthermore, there is a slight offset in the mean of the two samples, shown explicitly in the north and south part of the Legacy Survey in Fig. 4.8. We fit this offset for the south and north part of the survey separately using a cubic spline. Then we further create an 'offset' sample which has its redshifts corrected using the spline for $\Delta_z(z)$ to match with that of Z20. For this sample, the clipping of $|\Delta_z| = 0.05$ is applied after correcting for the offset, cutting 22.5% of the objects. Fig. 4.9 compares the raw redshift distributions of this work and Z20 for the three samples. The left panel shows the sample using redshifts inferred from $g-r$, $r-z$, and $z-W_1$ colours, the middle panel shows that from Z20, and the right panel shows that from the offset sample. The two photo-z distributions are close in all cases.

We find the photo-z convolution function parameters, $(\sigma^{\rm spec}, a^{\rm spec})$, for the Z20 samples using the same spectroscopic samples. We then follow the same procedures to find the best-fit $n(z)$. The parameters are summarised in Table 4.2

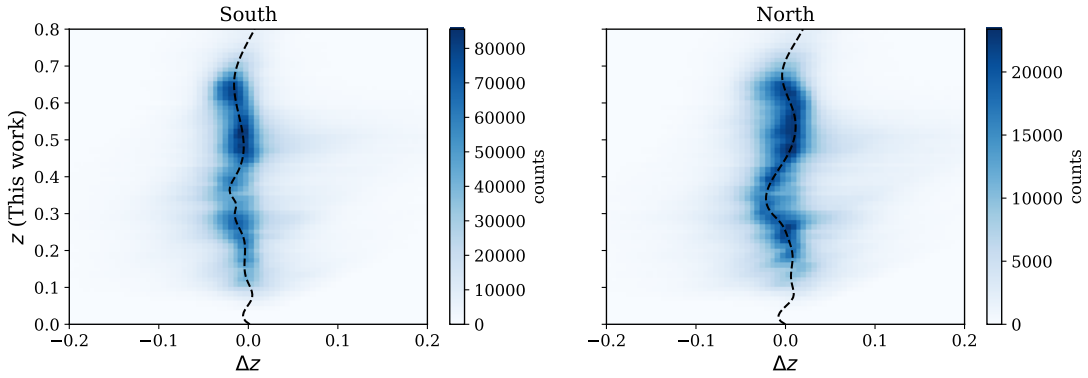

Figure 4.8 *Photometric redshifts inferred from $g-r$, $r-z$, and $z-W_1$ colours, versus the difference from the Z20 estimates. The dotted lines show a spline fit to Δz as a function of our photo-z, used for the offset correction.*

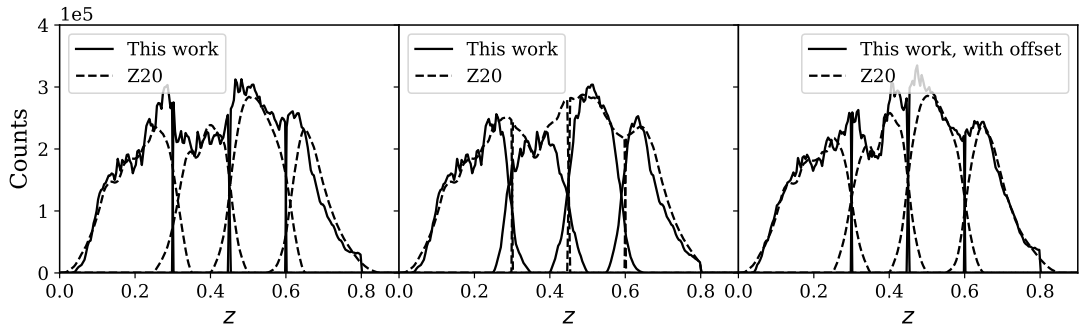

Figure 4.9 *The raw redshift distribution binned using photo-z obtained in this work (left), in Z20 (middle), and in this work with the correction for the offset (right), after a clipping of $|\Delta z| < 0.05$. The solid line shows the distribution of photo-z in this work, while the dashed line shows that from Z20.*

4.3 Galaxy density maps

Galaxies in each tomographic slice are binned in HEALPIX maps with $N_{\rm side} = 1024$. The density fluctuation, δ, in each pixel is then computed by

$$\delta = \frac{n}{\bar{n}} - 1, \tag{4.2}$$

where n is number of galaxies in the pixel, and $\bar{n}$ is the mean number of galaxies per pixel. Due to the slight differences in the photometric passbands for DECam, BASS, and MzLS, the surface density of the tomographic slices varies slightly, between 2% and 5%, in the north and south regions. For our purpose here, we compute δ for the north and south regions separately, and join the two regions at Dec $= 33^\circ$.

The density maps are correlated with various systematics, including observational conditions, survey depth, stellar density, and Galactic extinction. Most foreground contamination is captured by the completeness map. In addition, we use the ALLWISE total density map as a proxy for stellar density. We find little correlation with the $E(B-V)$ extinction map. The following corrections are applied to the density map to remove possible systematics.

4.3.1 Systematic corrections

To obtain an unbiased mean density, we compute $\bar{n}$ using pixels with completeness > 0.95 and stellar number $N_{\rm star} < 8.52 \times 10^3$ deg^{-2}, about 70% of the total unmasked pixels. The largest correlation with density comes from the completeness map. The galaxy count in each pixel is corrected by n/w, where w is the completeness in each pixel. Regions with $w < 0.86$ are masked, based on the binned one-dimensional relation between the completeness and mean density fluctuation in the bin, $\bar{\delta}$, such that the deviation of $\bar{\delta}$ from zero is smaller than 0.1. We also introduce a similar cut in stellar number at $N_{\rm star} < 1.29 \times 10^4$ deg^{-2}. The residual binned one-dimensional correlation between $\log_{10}(N_{\rm star})$ and mean δ in the bins is below 5% for all bins except for the highest redshift bin at the large stellar density end. We use 5th-order polynomials to fit for the residual correlation for each bin as a function of $\log_{10}(N_{\rm star})$ and subtract the residual mean density from the raw δ (see Fig. 4.10). The final corrected density maps are cross-correlated with the completeness map and stellar density map in each bin. The

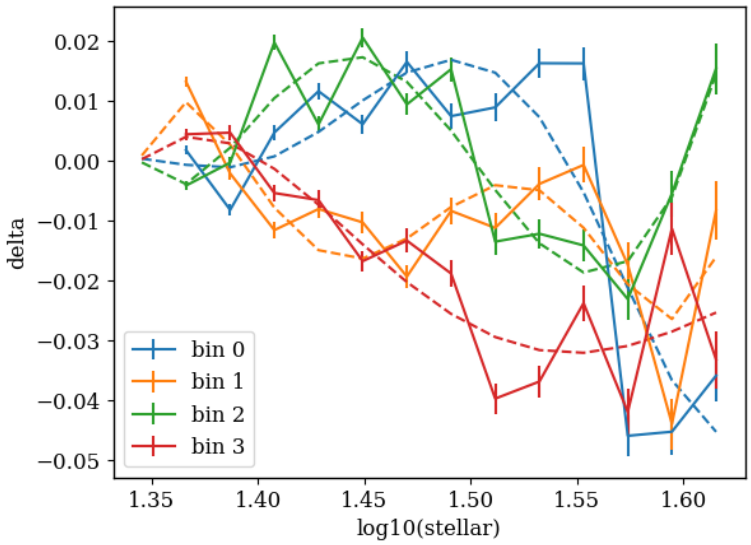

Figure 4.10 *The completeness weighted mean galaxy density fluctuation per pixel in bins of various stellar number density from ALLWISE total density map. The dashed lines show fitting of the relation using fifth order polynomials.*

resultant correlation is consistent with zero for the ℓ range used in the analysis (see Fig. 4.11 and 4.12). The corrected density fluctuations in the four redshift slices are shown in Fig. 4.13–4.16. For illustrative purpose, they are smoothed by a Gaussian symmetric beam with $\sigma = 20\,h^{-1}$ Mpc in comoving distance. We note that the photometric variations and correlations with various foreground maps for our sample are relatively small. This is driven by the magnitude cuts used in our selection. [141] provides a more detailed analysis of photometric systematics for a variety of galaxy samples.

To check the consistency between different survey regions: the BASS+MzLS,

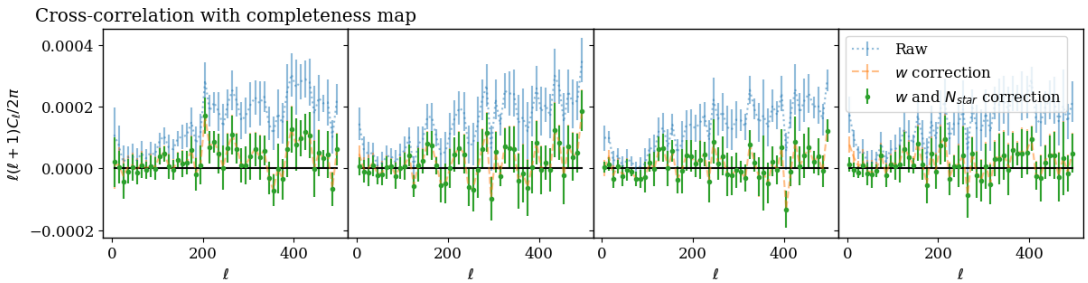

Figure 4.11 *The angular cross-correlation between galaxy density maps and the completeness map. The blue dotted curves show the correlation using raw density maps, the orange dashed curves show that using completeness weighted maps, and the green points show that using completeness weight and stellar number correction.*

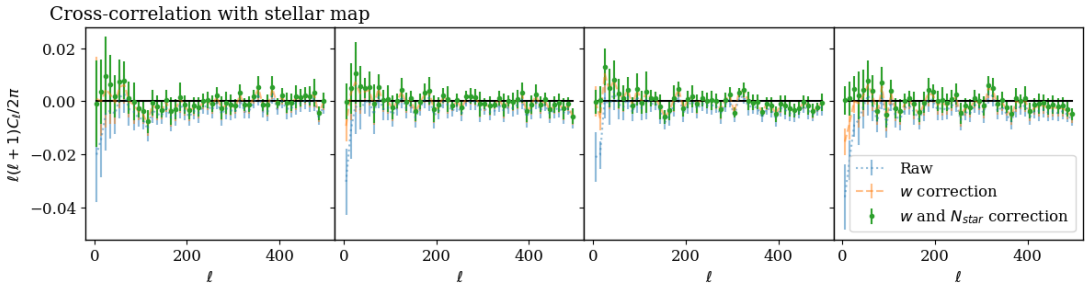

Figure 4.12 *Same as Fig. 4.11 but for the ALLWISE total density map. It cam be seem clearly that the stellar correction is only effective on large scales with $\ell < 50$, and is most effective for the highest redshift bin.*

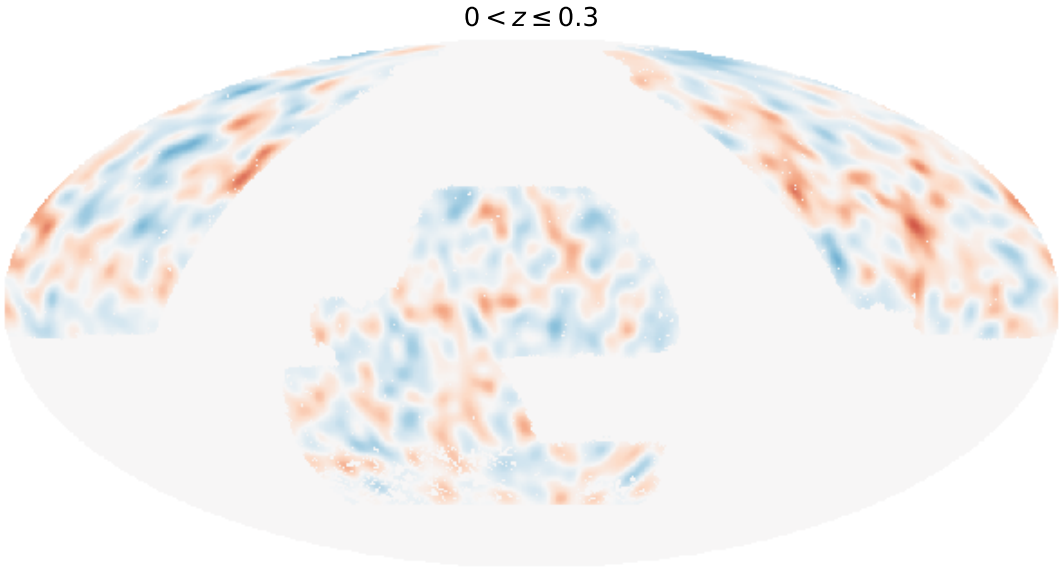

Figure 4.13 *The density fluctuation map for bin 0, with $0 < z \leq 0.3$. For illustrative purpose only, the map is smoothed by a Gaussian symmetric beam with comoving scale of $20\,h^{-1}\,\mathrm{Mpc}$. This map is made from the corresponding galaxy map via Eq. 4.2, and corrected by completeness and stellar density.*

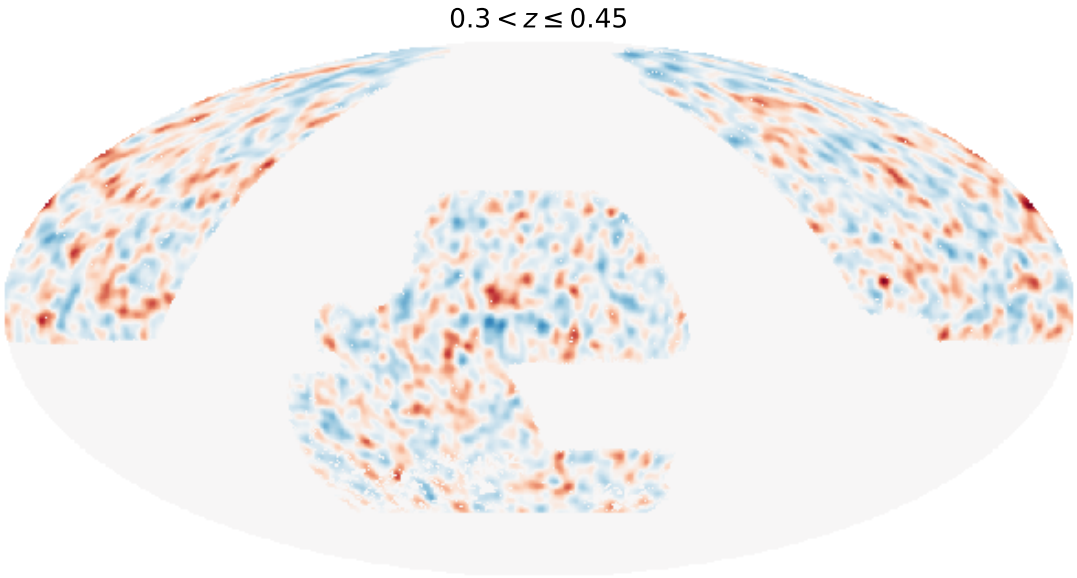

Figure 4.14 *Same as Fig. 4.13 but for bin 1, with* $0.3 < z \leq 0.45$.

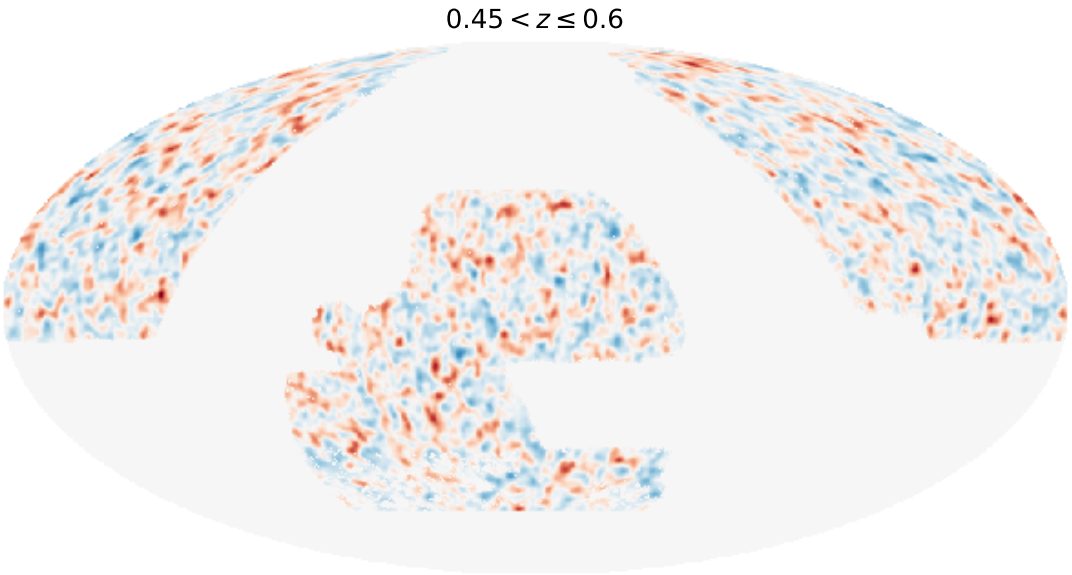

Figure 4.15 *Same as Fig. 4.13 but for bin 2, with* $0.45 < z \leq 0.6$.

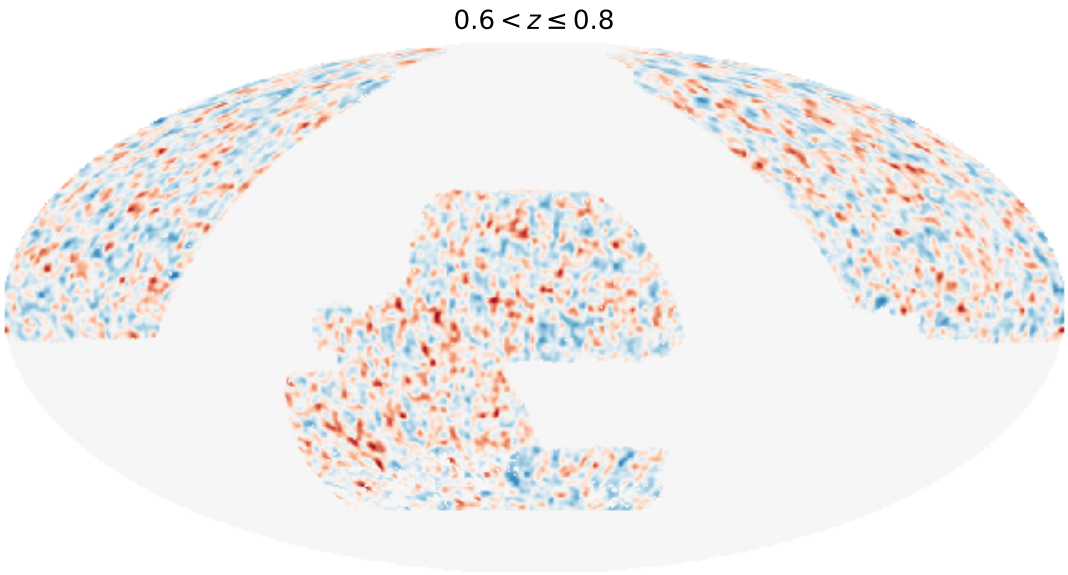

Figure 4.16 *Same as Fig. 4.13 but for bin 3, with* $0.6 < z \leq 0.8$.

DES footprint, and the DECsLS region (without DES), we look at the galaxy auto-correlations from these three independent regions. We use the systematic-corrected galaxy maps in the four redshift bins as well as the unbinned case. The results are shown in Fig. 4.17. We see that the measurements from the three regions are in good consistency with each other out to $\ell = 500$ in the unbinned case as well as split into four redshift bins. However, the auto-correlation from bin 3 in the DES and BASS+MzLS regions are different from the rest of the DECaLS. The χ^2 of the DES and BASS+MzLS regions against the best-fit model in bin 3 indicates about 2.5σ and 3.7σ inconsistency with $\ell_{\rm max} = 500$, whereas it is fully consistent with the DECaLS region. This can be due to the relatively large photo-z error at the high redshift tail. Because the number of galaxies in bin 3 accounts for only $\sim 15\%$ of the total sample, its contribution for the clustering in the combined case is relatively minor.

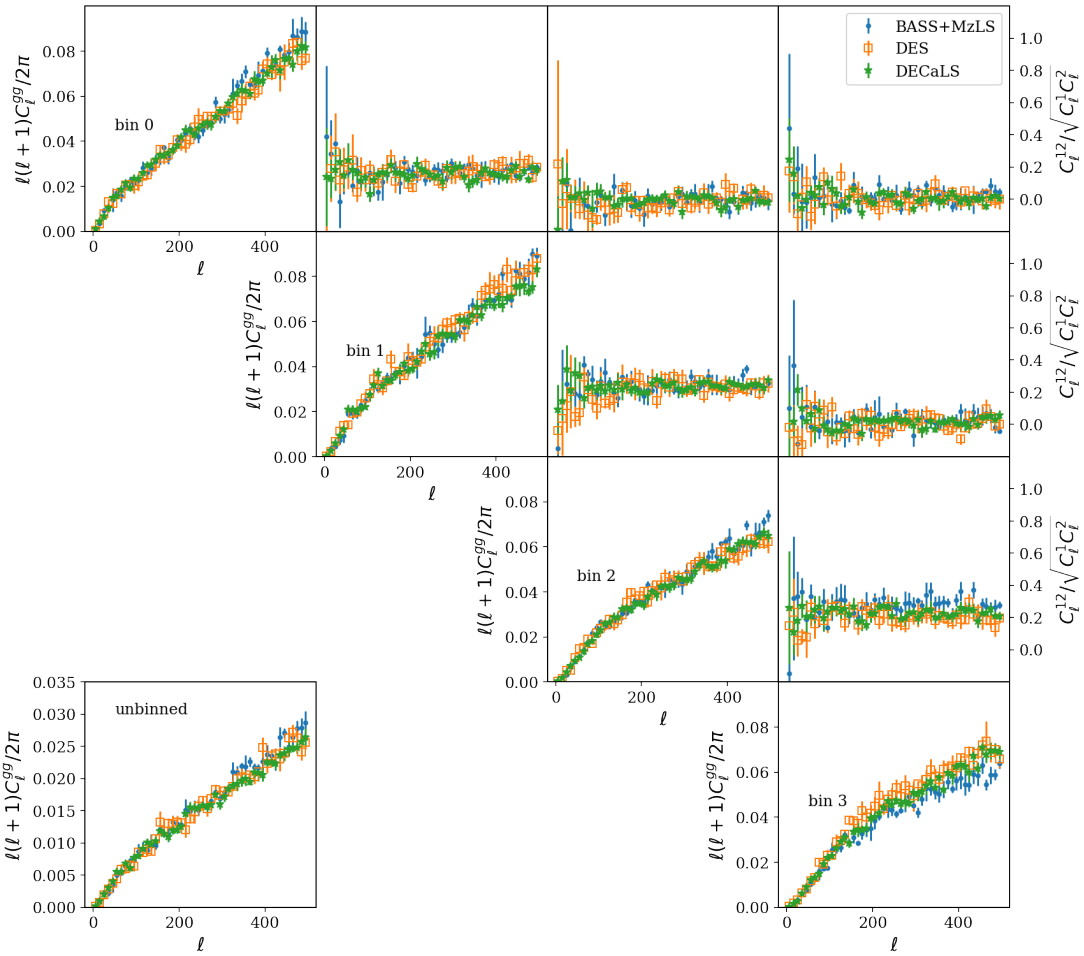

Figure 4.17 *The galaxy auto-correlations in four redshift bins and their cross-correlations, measured from three separate parts of the DESI Legacy Survey footprint: BASS+MzLS, DES, and DECaLS (without DES). The unbinned case is presented at the bottom left.*

Chapter 5

Imprints of galaxy clustering on the CMB from the DESI Legacy Imaging Survey

In this Chapter, we will exploit galaxy samples from Chapter 4 to measure the angular correlations between galaxy number density and the CMB. Observations of CMB lensing have progressed hugely in recent years, with a full sky map of lensing convergence delivered by *Planck* [223, 224, 228], and over 2100 deg^2 by ACTpol [61]. Here, we correlate the *Planck* lensing and temperature maps with LSS traced by galaxies. A particular aim is to measure the ISW effect, which has the attraction of providing an independent probe of dark energy. However, ISW detections have been challenging because the signal is largest at low multipoles where substantial cosmic variance is unavoidable; the effect has therefore been detected with only modest significance [e.g. 93, 124, 225]. The uncertainty of measurements for the redshift range beyond $z > 0.5$ is particularly large, with some having null, or anti-correlations between LSS and the CMB [251]. This regime is of particular interest as it may provide key evidence for distinguishing ΛCDM from early dark energy or modified gravity models (e.g. Renk et al. 2017). Recent examples of this sort of work include [280] for the ISW effect and [62, 69, 94, 149, 207, 272, 273] for CMB lensing. A particular goal for the present study is to extend the redshift range of the tomographic measurements from $z \lesssim 0.5$ to $z \simeq 1$ using the Legacy Survey.

We will be especially interested in comparing the amplitudes of the CMB lensing

and ISW signals with the predictions of the fiducial ΛCDM model, from Eqs 3.40 & 3.42. We use HALOFIT [276, 282] as implemented in CAMB [163] to model the non-linear matter power spectrum. The procedure can be summarised as follows:
• Constrain linear galaxy biases with the galaxy auto- and cross-correlations from the four redshift bins:

$$C_\ell^{g_i g_j} = b_i b_j C_\ell^{\delta\delta}. \tag{5.1}$$

Here, we allow the pdf of photo-zs to vary with nuisance parameters that will be marginalised over.
• Measure the amplitude of the lensing and ISW signals A_κ and $A_{\rm ISW}$ defined as

$$C_\ell^{g\kappa} = A_\kappa b C_\ell^{\delta\kappa}; \quad C_\ell^{gT} = A_{\rm ISW} b C_\ell^{\delta T}, \tag{5.2}$$

incorporating the constrained galaxy biases from the previous step.

The angular power C_ℓ is computed by converting a pixel map into its spherical harmonics $a_{\ell m}$ in HEALPY. For a masked map, we use the simplest pseudo-power estimate $\hat{C}_\ell = C_\ell^{\rm masked}/f_{\rm sky}$. We have verified that inaccuracies in this estimate are unimportant for this large sky coverage, especially given that we exclude $\ell < 10$ as further insurance against any residual large-scale systematics. We also impose an upper cutoff: throughout the analysis, we use modes in the range $10 \leq \ell < 500$. The $\ell > 500$ modes give very noisy measurements for cross-correlations between LSS and CMB, and the S/N for the amplitude of the cross-correlation signal has converged by this point. Linear bias is no longer a valid assumption beyond about $\ell = 250$, and we make allowance for scale-dependent bias as described in Section 5.1.2. We use a HEALPIX resolution of $N_{\rm side} = 1024$ for our analysis, and have tested that using finer maps would not alter the results. We correct for the pixel window function, although this is not a significant effect.

In the following analysis, we group every $M = 10$ ℓ-modes together such that

$$\langle C_\ell \rangle_{\rm group} = \frac{1}{M} \sum_{\ell'}^{\ell'+M-1} C_{\ell'}, \quad \ell' = M, 2M, ..., \tag{5.3}$$

and ℓ is the median value in each case. A simple error bar on each grouped data point can then be computed by

$$\sigma_\ell = \frac{1}{f_{\rm sky}} \sqrt{\frac{\langle C_\ell^2 \rangle - \langle C_\ell \rangle^2}{M-1}}. \tag{5.4}$$

The $f_{\rm sky}$ factor accounts for correlations between ℓ-modes due to the masked sky.

We use 50 lognormal simulations to test the effect of sky mask and shot noise. As an example, we show the results using bin 1 of our tomographic slice, and we focus on modes with $\ell \leq 300$, because the mask would especially correlate the low-ℓ modes. The upper panel of Fig. 5.1 shows the comparison between the mean C_ℓ of the simulated galaxy maps with or without mask and shot noise. We see that the deviation is large at low-ℓ but is only of order $\leq 5\%$, consistent within the statistical error. The lower amplitude at lower multipoles in the measured spectra compared to the input is likely caused by the survey mask. The bottom panel of the same figure shows the error estimated on these modes in simulations as well as the error on the actual data C_ℓ. The masked maps with shot noise show a slightly larger error, but is consistent with the error estimated on the data. The covariance matrix for $\hat{C}_\ell \equiv \ell(\ell+1)C_\ell/2\pi$ form the lognormal simulations is shown in Fig. 5.2. We see that it for can be well approximated by a diagonal covariance $\mathbf{C} = \mathrm{diag}(\sigma_\ell^2)$.

The χ^2 of a theoretical model is defined as

$$\chi^2 = \mathbf{d}^T \mathbf{C}^{-1} \mathbf{d}, \tag{5.5}$$

where the vector $\mathbf{d}$ has components $d_\ell = C_\ell^{\rm data} - C_\ell^{\rm th}$. The likelihood of a model parameter set $\mathbf{x}$ is given by

$$\mathcal{L}(\mathbf{x}) = \frac{e^{-\chi^2(\mathbf{x})/2}}{\int e^{-\chi^2(\mathbf{x})/2}\, d^n\mathbf{x}}, \tag{5.6}$$

where as usual we will take the likelihood to give the posterior on the parameters, assuming uninformative uniform priors.

The theory vector $C_\ell^{\rm th}$ contains the predictions from Eqs 3.39, 3.40 & 3.42 and We convert them to equivalent band power before comparing with data. It has the following free parameters: $\theta = \{A_\kappa, A_{\rm ISW}, a^i, x_0^i\}$. a^i and x_0^i are nuisance parameters to account for uncertainties for our photo-z calibration. We impose $\sum_i x_0^i = 0$, where the indices of the redshift bins are $i = 0, 1, 2, 3$, and so there are 7 degrees of freedom for the nuisance parameters. A_κ and $A_{\rm ISW}$ are the key parameters of interest, which characterise the amplitudes of the lensing and ISW signals relative to the fiducial model, as discussed above. All other cosmological parameters are fixed to the *Planck* 2018 cosmology, with $n_s = 0.965$, $\sigma_8 = 0.811$, $\Omega_m = 0.315$, $\Omega_{\rm b} = 0.0493$, and $H_0 = 67.4$ [227]. The cross-correlation

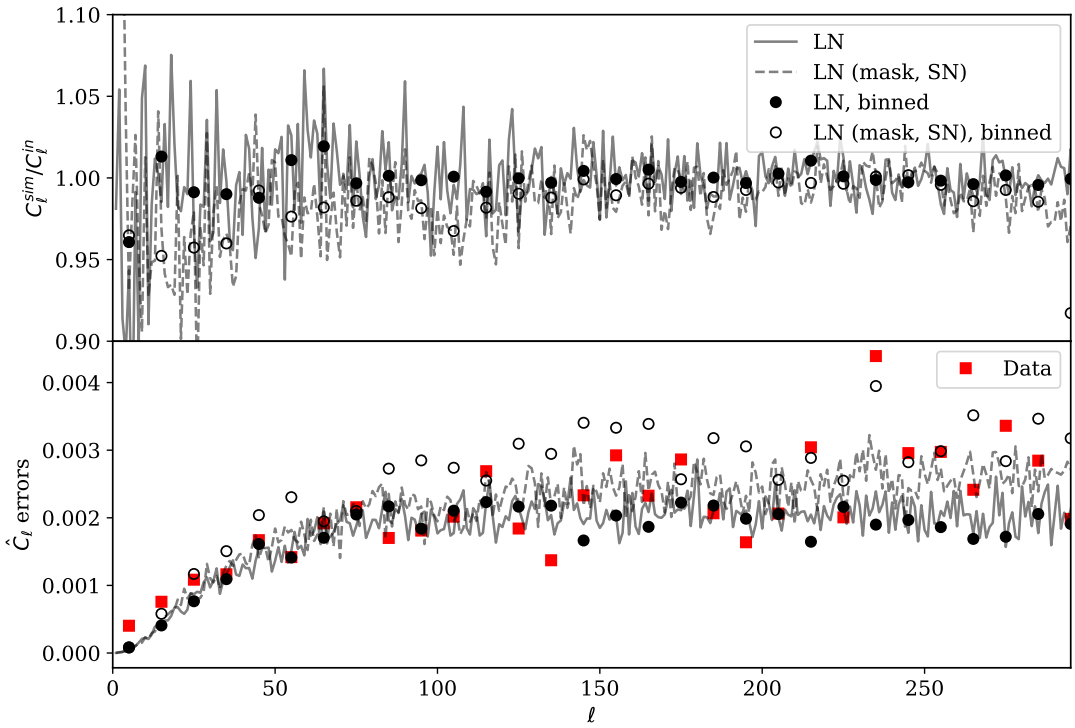

Figure 5.1 *The effect of survey mask and shot noise on the measured angular correlation C_ℓ demonstrated using lognormal simulations. As an example, we show the galaxy auto-correlation for bin 1 here. The upper panel shows the ratio of the mean C_ℓ from simulation compared to the input best-fit theoretical power spectrum, with the full or binned modes. The lower panel shows the errors on $\hat{C}_\ell \equiv \ell(\ell+1)C_\ell/2\pi$ from different realisations as well as the those on the actual data (red squares).*

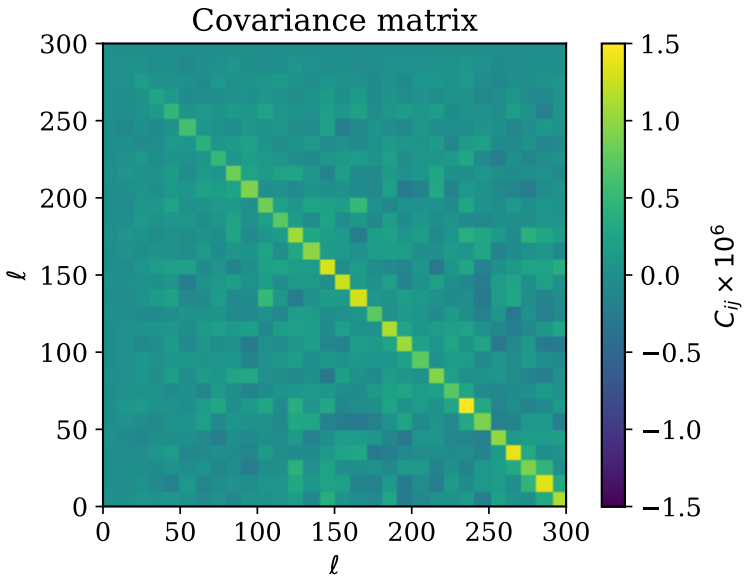

Figure 5.2 *The covariance matrix for bin 1 galaxy auto-correlation with* $\ell_{\rm max} = 300$ *from 50 lognormal simulations with mask and shot noise. The covariance matrix has very small correlation on the off-diagonal, and can be well approximated by using just the diagonal components.*

measurements are made using the CMB temperature and lensing κ maps and masks from the 2018 *Planck* data [226, 228]. Galaxy bias is a further nuisance parameter, but this will be constrained from data.

5.1 Galaxy auto- and cross-correlation

We now present the auto- and cross-correlations from the different tomographic bins. We will use the results to constrain galaxy bias and also to determine the empirical form of the photo-z error distribution. The galaxy auto-power requires shot noise to be subtracted. Given N_g galaxies in a redshift slice, the shot noise spectrum is given by $C_\ell^{\rm shot} = 4\pi f_{\rm sky}/N_g$. There is no correction to be made to the cross-power between the different bins. However, we also consider the cross-correlation between our data and that of Z20 and the computation of shot noise is more complicated in that case, since it depends on the numbers of galaxies that are in common to the two catalogues (which is non-zero even for cross-correlation).

Data points with error bars in Fig. 5.3 show the 10 measured galaxy auto- and cross-correlations for our data. The off-diagonals show the cross-correlation

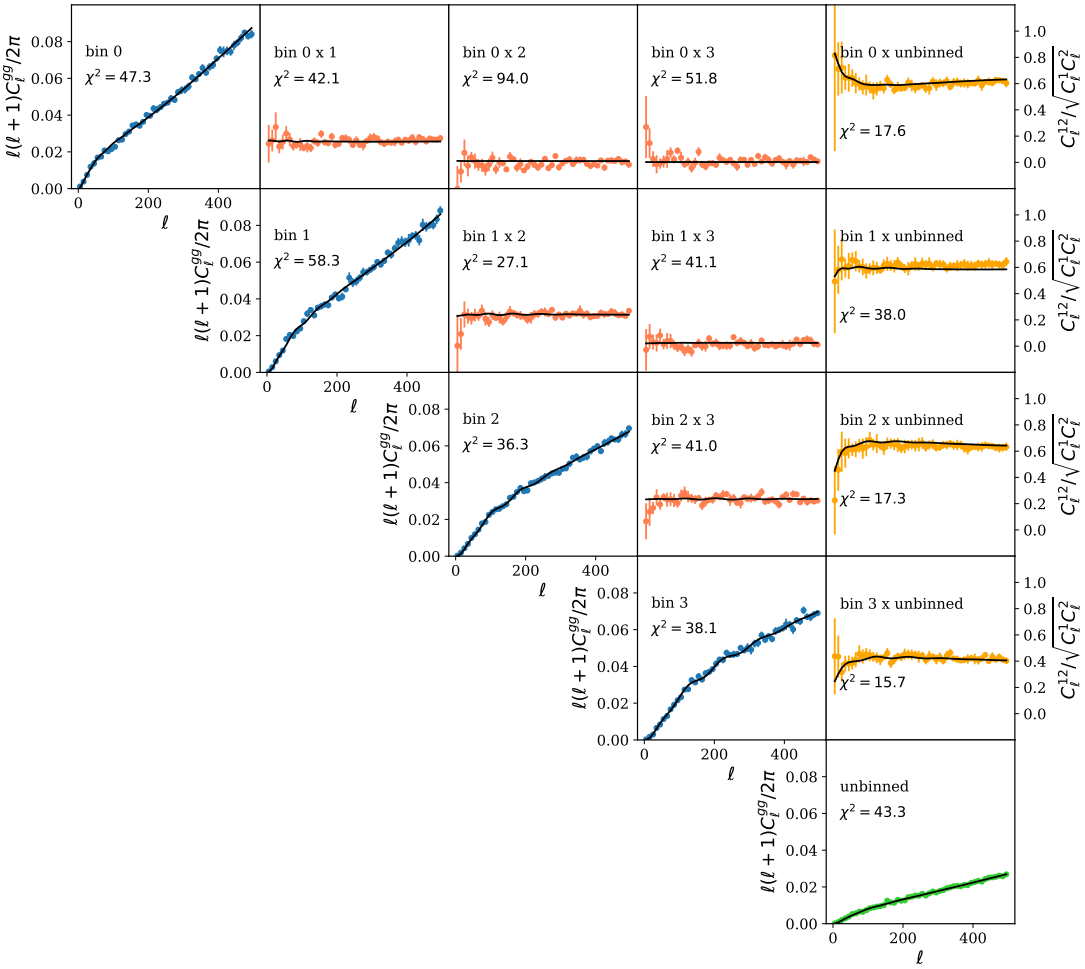

Figure 5.3 *The galaxy auto-correlation C_ℓ^{gg} for each redshift slice (diagonal) and cross-correlation coefficients between different slices (off-diagonal). The last column shows the auto- and cross-correlations with the unbinned case, with shot noise subtracted. Data is presented in groups of 10 modes. The black solid line shows the theory with the best-fit $p(z)$ and redshift-dependent bias. The fitting of $p(z)$ is performed simultaneously for all the sub-sections except the last column for modes in $10 < \ell < 500$, with a total DOF=$49 \times 10 - 7 = 483$ and the total $\chi^2 = 471$. The break-down of χ^2 is in each case is shown on the top left corner of each sub-section.*

coefficients, defined as

$$r_{ab} = \frac{C_\ell^{ab}}{\sqrt{C_\ell^a C_\ell^b}}, \tag{5.7}$$

where a, b refers to different redshift slices. These are independent of galaxy bias.

In this procedure of finding photometric redshift errors, we use only the large-scale modes with $\ell_{\rm max} = 500$ as discussed above. The cross-correlation coefficients are flat over a large range of ℓ, and is only dependent on the redshift distribution. Specifically, using constraints from the 10 auto- and cross-correlations of galaxy redshift bins, we compute χ^2's in the 7D nuisance parameter space $[a^i\ x_0^i]$ for $p(z)$. The fitting also excludes $\ell < 10$ modes. We use a 2-bias model, detailed in Section 5.1.2, to find the best-fit $p(z)$.

5.1.1 Lensing magnification bias

Finally, we note that the use of cross-correlations in calibrating $p(z)$ is potentially problematic because of lensing. Even with perfect redshift selection, some cross-correlation is expected between different tomographic slices because of magnification bias: lensing by the nearer slice will imprint an image of its density fluctuations on the more distant slice. Indeed, [149] argue strongly that magnification bias should be allowed for in CMB lensing tomography. However, we can see that such effects are unimportant here, as they should be largest for widely separated bins, and where the bin has the largest count slope. This should affect above all bin 3, with the highest mean redshift and the highest count slope (the slopes in slices 0–3 are respectively $s \equiv d\log_{10} N/dm = 0.19, 0.29, 0.41, 0.57$). But we see from Fig. 5.3 that bin 3 has no significant correlation with bins 0 and 1. The reason for our different conclusion regarding magnification bias is that our photo-zs are calibrated using the colours of spectroscopic objects, whereas [149] calibrated their photo-zs using the cross-clustering with a spectroscopic sample. Magnification bias can affect that cross-correlation and hence the inferred $p(z)$, but it has no effect on the numbers of objects at a given colour.

5.1.2 Non-linear bias and bias evolution

The galaxy auto-power data beyond $\ell \simeq 250$ cannot be fit well by a constant bias. Specifically, the ratio between $C_\ell^{\rm data}$ and $C_\ell^{\rm DM}$ are roughly constant at small and large ℓ, with a transition at intermediate scales corresponding to roughly the

transition between linear and non-linear scales. We allow for this by introducing two bias parameters for the linear and non-linear regimes separately:

$$C_\ell^{gg} = b_1^2 C_\ell^{\rm lin} + b_2^2 \Delta C_\ell^{\rm nl}, \tag{5.8}$$

where $C_\ell^{\rm lin}$ and the nonlinear correction $\Delta C_\ell^{\rm nl}$ are computed using the linear and additional non-linear components of the CAMB power spectrum. This simple model gives an excellent fit up to $\ell = 1000$. The best-fit linear and non-linear biases using the best-fit $p(z)$ are shown in Table 5.3. We note that b_2 is systematically larger than b_1, obeying the approximate relation $b_2 - 1 \simeq 1.9(b_1 - 1)$.

In the marginalised case, to speed up the computation, we approximate the best-fit biases by taking the ratio of the data with the linear and non-linear theory at different scales using

$$b_{1,2}^2 = \sum_\ell w(\ell) \frac{C_\ell^{\rm data}}{C_\ell^{\rm th}}, \quad w(\ell) = \frac{1/\sigma_\ell^2}{\sum_\ell (1/\sigma_\ell^2)}. \tag{5.9}$$

The transition scales are different for each redshift slice. For bias fitting, a good approximation is the scale at which the fraction of the nonlinear power becomes comparable to the measurement error. This ranges between $\ell \sim 100 - 200$ from low to high redshift slices. The drawback of this approximation is that the intermediate scales are hard to control, but it gives biases close to the lowest χ^2 value. In this case, the best-fit $p(z)$ gives $\chi^2 = 471$ with DOF $= 483$. The model parameters are shown in Table 4.1, and the convolved mean $p(z)$ with its 1σ deviation is shown in Fig. 4.6. The best-fit spectra are shown as black solid lines in Fig. 5.3, with the galaxy biases and break-down of χ^2 printed for each case. The measured galaxy biases and their errors for each redshift slice are shown in Table 5.3. We have checked that with $\ell_{\rm max} = 500$, the best-fit $p(z)$ model and the marginalised case give almost identical amplitude constraints on the cross-correlation of CMB lensing and ISW effects. Therefore, in the following analysis, we will carry out the modelling using the best-fit $p(z)$.

The linear and non-linear biases evolve with redshift, with b_1 increasing from 1.2 to 2.0 over redshift 0.2 to 0.7, although the trend is not quite monotonic (see Fig. 5.4). This is consistent with the expectation for luminosity-limited galaxy samples in which high-z galaxies are intrinsically brighter, thus those galaxies tend to occupy more massive dark matter haloes. In general, such evolution can be locally treated as a constant if the redshift bin is thin, or if the distribution

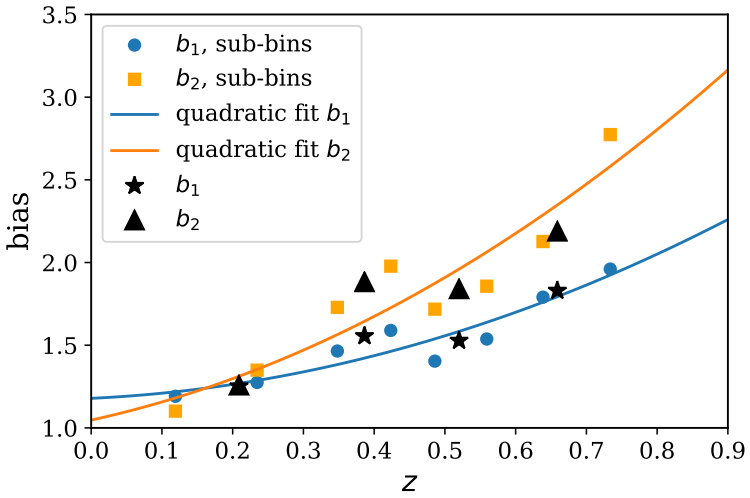

Figure 5.4 *Linear and non-linear bias parameters, b_1 and b_2 (Eq. 5.8), as a function of mean redshift. The circles show minimum-χ^2 bias measured in 8 sub-bins, the stars and triangles show that measured in 4 bins, and the solid lines show quadratic fits to the circles.*

Table 5.1 *The effective redshift and the perturbation to the quadratic fits of the bias evolution.*

Bin	0	1	2	3	unbinned
$z^{\rm eff}$	0.21	0.39	0.52	0.66	0.42
δb_1	−0.010	0.098	−0.033	0.029	−0.005
δb_2	−0.022	0.159	−0.056	−0.056	0.027

is symmetric. However, for bin 3, which has a tail towards higher redshifts, and for an analysis of the unbinned sample, such an approximation breaks down, and the full bias evolution needs to be included in the kernel. To determine the bias evolution more precisely, we sub-divided each bin into two bins. We approximate the redshift distribution of each sub-bin by convolution of the raw $p(z)$ with the best-fit photo-z error of that bin. Then for each sub-bin we fit linear and non-linear biases as above. These measurements are consistent with the 4-bin case. The biases as a function of the mean redshift in that bin can be fitted by a quadratic function (see Fig. 5.4). We only use the increasing part of the quadratic, and extrapolate the decreasing part beyond the function's minimal point by a constant. To match the auto-correlation amplitude, for each bin, we introduce a small correction $b_i(z) = (1 + \delta b_i) b_i^0(z)$, where $i = 1, 2$, $b_i^0(z)$ is the fitted quadratic curve, and $\delta b_i \ll 1$. We find δb_i by iteration, shown in Table 5.1.

This model agrees with our measurements very well in general, as seen in Fig. 5.3, with reasonable χ^2/DOF overall and for most individual spectra. The auto-power

for bin 1 has χ^2 on the high side, but we were unable to identify any systematics that could account for this (e.g. looking for discrepant sky sub-areas in the data). In any case, the look-elsewhere effect is clearly relevant here, with 10 spectra to consider. It is worth noting that χ^2 is nominal for bin 3, even though this has the largest volume and the lowest errors. Indeed, the precision of this bin and bin 2 is sufficient to show a clear signal from Baryon Acoustic Oscillations (BAO).

Overall, then, these cross-correlation results reassure us that the clustering of the galaxy samples and the calibration of the underlying $p(z)$ distributions is robust, and that the samples are ready for the cross-correlation analysis with the CMB.

5.1.3 Marginalising photo-z parameters

We marginalise our photometric redshift parameters in the following way. We look at 7 parameters: x_0, x_1, and x_2 are defined as in Eq. 4.1 for bin 0, 1, and 2 respectively, whereas for bin 3, $x_3 = -x_0 - x_1 - x_2$. We also use $f_i = a_i/a_i^{\rm spec}$ for the tail parameters. Wider tails mean smaller a, so we take the upper limit of f to be 1, i.e., we assume that the scatter of faint objects always increase the tails. We then run a grid search in the 7-dimensional parameter space, taking a 10 points in each parameter with range listed in Tab. 5.2 to compute the χ^2 of the 10 galaxy auto- and cross-correlations. MCMC is not adopted in this case for two reasons. Firstly, the prior range is hard to determine without a grid search, thus running a MCMC may result in longer computational time for convergence. Secondly, we would like to marginalise over these parameters, rather than interested in their detailed posterior distribution. A grid search should suffice our purpose for this analysis. As mentioned before, for each case, we fix the galaxy bias (linear and non-linear) at the lowest χ^2 values, and fit for modes $10 < \ell < 500$. Fig. 5.5 shows the likelihoods for this parameter search. The black lines on the diagonal points indicate the mean parameter values. The mean and $1-\sigma$ of the convolved redshift distribution $p(z)$ weighted by the likelihoods in each tomographic slice is shown in Fig. 4.6. We also propagate this likelihood to the computation of A_κ and $A_{\rm ISW}$. This is summarised in Table 5.3. It is clear that the marginalised constraints are similar to that coming from the the best-fit $p(z)$. Therefore, in the following analysis including the unbinned case, we use the best-fit $p(z)$ and its set of galaxy biases.

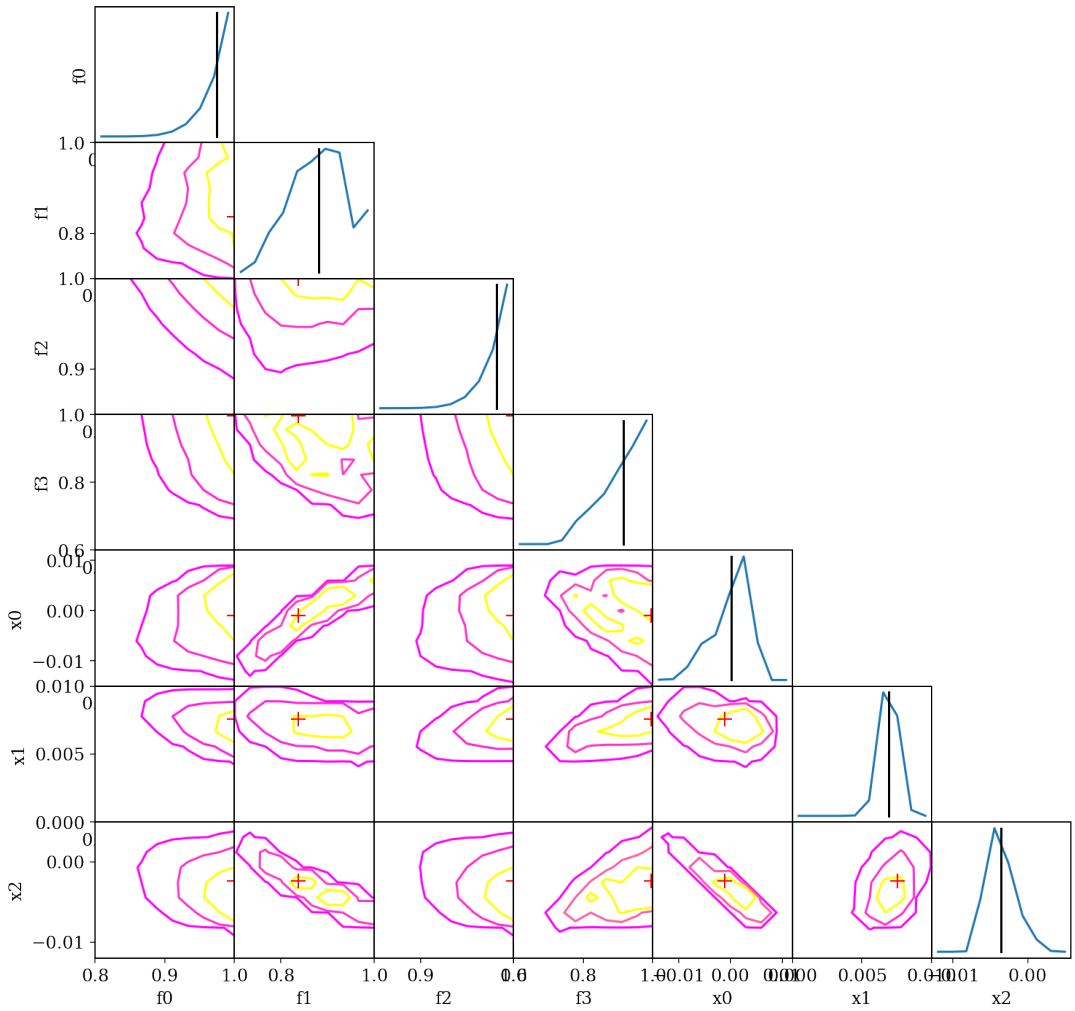

Figure 5.5 *The likelihood for the 7 photometric redshift parameters fitted to the 10 galaxy auto- and cross-correlations between the four tomographic bins. The likelihood is estimated based on a grid search with 10 points in each parameter. The black lines on the diagonal points indicate the mean parameter values.*

Table 5.2 *The range of the photo-z parameters used in fitting the 10 galaxy auto- and cross-correlations. We take 10 uniform points in each parameter to compute the likelihood. The $f_0 - f_3$ parameters controls the tail of the photo-z error. $f_i = 1$ indicates the same tail as the calibration sample, while $f_i < 1$ indicates a larger tail. The $x_0 - x_2$ parameters control the shifts in the mean redshifts of bin 0 to 2, and the shift in bin 3 is given by $x_3 = x_0 + x_1 + x_2$.*

Parameter	Range
f_0	$[0.7, 1]$
f_1	$[0.7, 1]$
f_2	$[0.7, 1]$
f_3	$[0.5, 1]$
x_0	$[-0.02, 0.01]$
x_1	$[-0.01, 0.02]$
x_2	$[-0.01, 0.01]$

5.2 Cross-correlation with CMB

5.2.1 The Planck CMB maps

The Planck 2018 lensing and temperature maps are shown in Fig. 5.6 and 5.7. In computing the galaxy-lensing cross-power signal, we encountered unexpected practical issues. The *Planck* CMB lensing data are made available as spherical harmonic coefficients, from which the required κ map can be obtained by using the `alm2map` routine within the HEALPY package. The maximum wavenumber is 2048 in the 2015 release and 4096 in the 2018 release. The 2015 map is already dominated by small-scale noise, but the noise spectrum in the 2018 map displays a nearly divergent spike at high ℓ: C_ℓ^κ increases from about 10^{-4} at $\ell = 3650$ to over unity at $\ell = 4096$. This creates numerical problems in reconstructing the map, so that e.g. making a map at $N_{\rm side} = 512$ directly yields a different answer to creating a map at 2048 and downgrading to 512. The spike at $\ell = 2048$ can be tamed by filtering the map, but a sufficiently large FWHM is required that modes at $\ell < 100$ would be affected. In practice, therefore, we chose to truncate the data at $\ell = 2048$, consistent with the 2015 data. With the adoption of a standard resolution of $N_{\rm side} = 1024$ for our analysis, the results were robust (and only slightly different from $N_{\rm side} = 512$).

A further issue concerned coordinate systems: the CMB maps are supplied in galactic coordinates, whereas we constructed our galaxy maps in equatorial

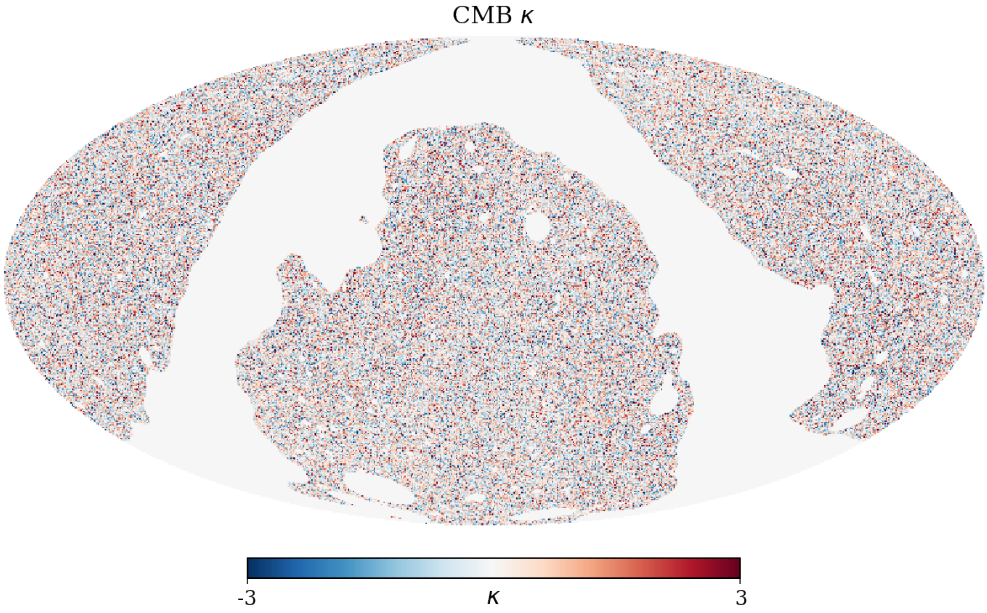

Figure 5.6 *The Planck 2018 CMB lensing convergence κ map with $\ell_{\rm max} = 2048$.*

coordinates. Facilities exist within HEALPY for performing the rotation in $a_{\ell m}$, but we found that the rotation generated artefacts in the lensing auto-power C_ℓ^κ, which we attribute to the extremely noisy nature of the lensing map, dominated by fluctuations on the inter-pixel scale. After tests at a range of resolutions, we are confident that this issue does not affect the regime of our measurements, out to $\ell = 500$.

5.2.2 Cross-correlation with the lensing convergence map

Fig. 5.8 shows the measured galaxy-κ cross-power, with the solid black lines showing the theory using the best-fit $p(z)$ and biases obtained from the galaxy auto- and cross-correlations. The black lines are not fits to the data points. To quantify the consistency between data and theory, we include a scaling factor for the lensing amplitude, A_κ, such that $C_\ell^{\rm th} = A_\kappa b C_\ell^{\rm DM}$. In terms of the two bias model, this is

$$C_\ell^{\rm th} = A_\kappa \left[b_1 C_\ell^{\rm DM;lin} + b_2 \Delta C_\ell^{\rm DM;nl} \right]. \tag{5.10}$$

The constraints on A_κ as a function of maximum ℓ-mode is shown in Fig. 5.9. The coloured points show measurements from individual tomographic slices, the black open circle shows the product of the four likelihoods, and the black solid points show that from the unbinned case. The mean and 1-σ deviation for each of these likelihoods are presented in Table 5.3.

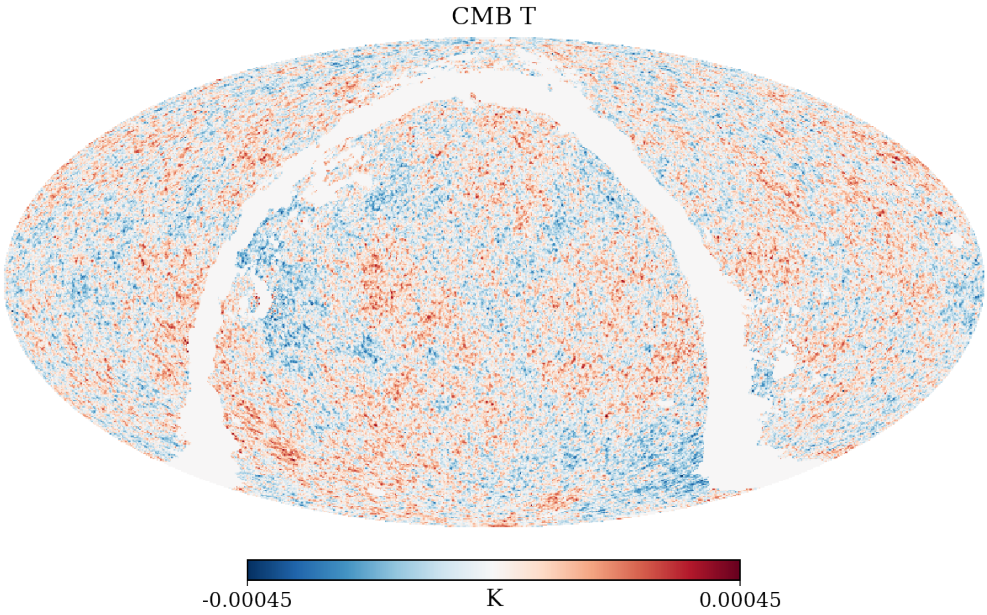

Figure 5.7 *The Planck 2018 CMB temperature map. The map has been smoothed by a Gaussian symmetric beam of FWHM= 5arcmin.*

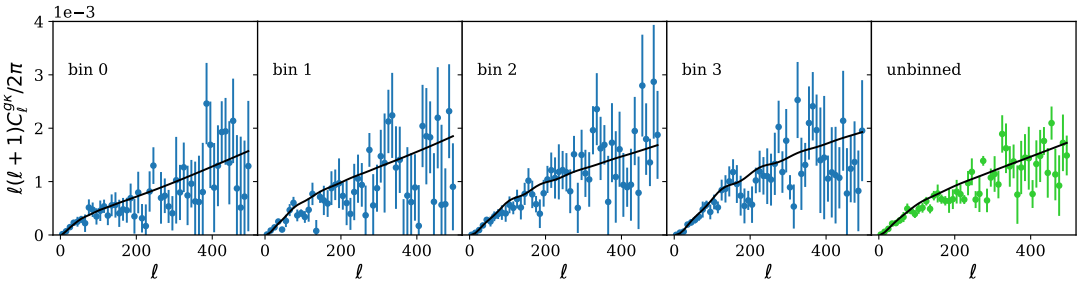

Figure 5.8 *The galaxy-lensing cross-correlation $C_\ell^{g\kappa}$ for each redshift slice and the unbinned case. The solid lines are theory with the best-fit $p(z)$ and the same galaxy biases as in Fig. 5.3.*

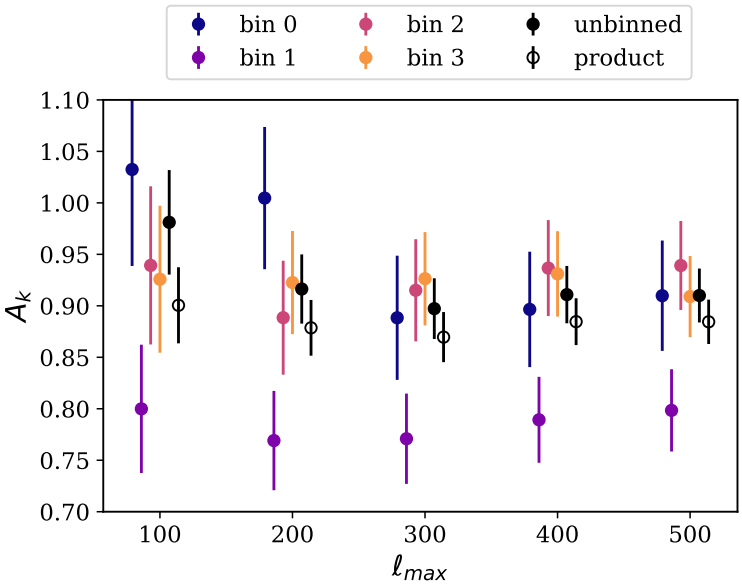

Figure 5.9 *The mean and 1-σ of A_κ likelihoods. Individual bins are shown in blue (bin 0), purple (bin 1), pink (bin 2), and orange (bin 3) points, while the product of the four bins is shown in black open circles. The solid black points show the unbinned case, using the set of best-fit $p(z)$.*

Our conclusion is that all of these options consistently yield A_κ close to 0.9, and that the deviation from the fiducial *Planck* prediction is real. In order to report an overall amplitude for A_κ, we need to combine the different redshift slices, which we do in the simple approximation that the slices are independent. Because this is not exact, we also consider an unbinned analysis in which all objects at $z < 0.8$ are combined; this gives closely consistent results to the outcome of averaging the four slices. We adopt the mean of the unbinned measurements using the two sets of photo-zs as our final result:

$$A_\kappa = 0.901 \pm 0.026. \tag{5.11}$$

This significant discrepancy with the fiducial model is one of the principal results of this work. The implications are discussed in Section 5.2.5. A particularly interesting point is that the overall amplitude of CMB lensing, dominated by LSS at $z \simeq 2$, is nevertheless consistent with the fiducial model. What we will show is that these two observations in combination require a matter density lower than the fiducial value.

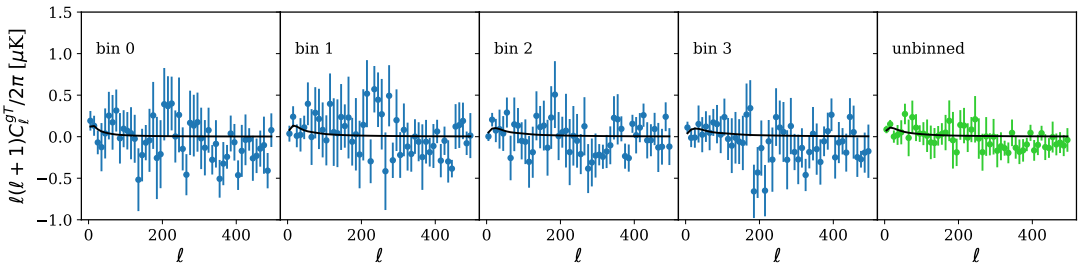

Figure 5.10 *The galaxy-temperature cross-correlation C_ℓ^{gT} for each redshift slice and unbinned case. The solid lines are the fiducial ΛCDM predictions with the best-fit $p(z)$ and the same galaxy biases as in Fig. 5.3.*

5.2.3 Cross-correlation with the temperature map

Fig. 5.10 shows the measurements of galaxy-temperature cross-correlations. The signal is dominated by noise at $\ell > 50$. The black solid line shows the theory prediction using the best-fit $p(z)$ and bias from galaxy auto-correlations. As with the lensing case, we introduce an ISW amplitude $A_{\rm ISW}$ in order to compare theory and data, such that $C_\ell^{\rm th} = A_{\rm ISW} b C_\ell^{\rm DM}$. In the two bias case, it is

$$C_\ell^{\rm th} = A_{\rm ISW}\left[b_1 C_\ell^{\rm DM;lin} + b_2 \Delta C_\ell^{\rm DM;nl}\right]. \tag{5.12}$$

The likelihood for $A_{\rm ISW}$ is then computed for each set of $p(z)$, then marginalised over. The marginalised likelihood for $A_{\rm ISW}$ is almost identical with that of the best-fit model, as shown in Table 5.3. Fig. 5.11 shows the likelihoods of $A_{\rm ISW}$ for each redshift slice (coloured) and combined (black) in the marginalised (solid line), mean parameter (circles), and best-fit (dotted line) model cases. The mean and width of individual curve are presented in Table 5.3. The combined likelihood shows a clear detection of the ISW signal, with $A_{\rm ISW} = 0.984 \pm 0.349$, excluding zero at 2.8σ.

In contrast to the CMB lensing signal, the temperature cross-correlation is thus in good agreement with the fiducial ΛCDM prediction of the ISW effect, although the intrinsically greater cosmic variance on the ISW signal means that we cannot exclude discrepancies at the same level as seen in the lensing signal. The overall modest S/N also prevents strong statements about the signal as a function of redshift, although $A_{\rm ISW}$ is positive and consistent with unity in all bins. The lowest signal is seen in our highest-redshift bin, $A_{\rm ISW} = 0.18 \pm 0.67$, which is interesting in the light of the report by [13] of a null signal at $z = 0.68$ using

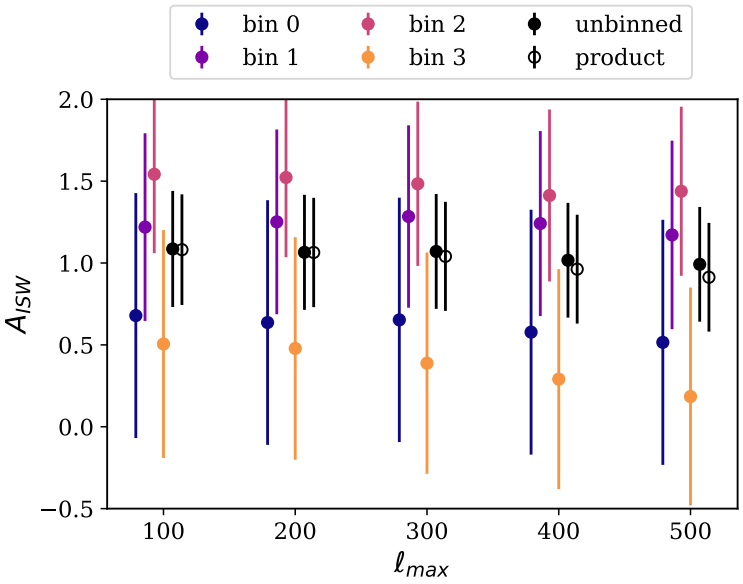

Figure 5.11 *The mean and 1-σ of $A_{\rm ISW}$ likelihoods. Individual bins are shown in blue (bin 0), purple (bin 1), pink (bin 2), and orange (bin 3) points, while the product of the four bins is shown in black open circles. The solid black points show the unbinned case, using the set of best-fit $p(z)$.*

a combined VST+SDSS sample of LRGs: $A_{\rm ISW} = -0.89 \pm 0.82$. Our signal is certainly closer to the fiducial $A_{\rm ISW} = 1$ than to this result, but the lack of a clear ISW signal in this bin remains.

5.2.4 Consistency checks

A tendency for the CMB lensing signal to lie below the fiducial model is seen consistently in all tomographic bins. It is also a robust feature, which does not alter with different treatments of the photometric redshifts. We summarise the results of a number of options that we considered in Fig. 5.12. We can consider our photometric redshifts or those of Z20; we can further restrict the Z20 sample to objects in the calibratable region of multicolour space; we can clip the photo-z catalogues to remove objects where the estimates are discrepant (we choose a threshold of $|\Delta z| = 0.05$); we can adjust one of the photo-z catalogues to remove any offset in $\langle \Delta z \rangle$ as a function of redshift; we can remove objects that are placed in different tomographic bins by the two catalogues. All of these options potentially alter the error distribution and hence the true $p(z)$ of the selection. The nuisance parameters governing these distributions were therefore re-optimised using the galaxy cross-correlations in each case. The impact of some

Table 5.3 *The linear and non-linear bias and constraints on A_κ and $A_{\rm ISW}$ for various cases at $\ell_{\rm max} = 500$. The first row shows the case where all $p(z)$ parameters are marginalized over. The second row shows the case for best-fit $p(z)$ parameters. The third and fourth rows show the cases using the photo-z from [314] (Z20) and that with the applied offset. The last row shows the case of using the AvERA model described in [22].*

Parameters	bin0	bin1	bin2	bin3	combined	Un-binned
Redshift	$0 < z \leq 0.3$	$0.3 < z \leq 0.45$	$0.45 < z \leq 0.6$	$0.6 < z \leq 0.8$	-	$0 < z \leq 0.8$
Marginalized over $p(z)$						
b_1	1.25 ± 0.01	1.53 ± 0.02	1.54 ± 0.01	1.86 ± 0.02	-	-
b_2	1.27 ± 0.01	1.85 ± 0.03	1.82 ± 0.01	2.23 ± 0.02	-	-
A_k	0.91 ± 0.05	0.82 ± 0.04	0.94 ± 0.04	0.90 ± 0.04	0.89 ± 0.02	-
$A_{\rm ISW}$	0.52 ± 0.78	1.20 ± 0.63	1.48 ± 0.61	0.18 ± 0.67	0.91 ± 0.33	-
Best-fit $p(z)$						
b_1	1.25	1.56	1.53	1.83	-	1.43
b_2	1.26	1.88	1.84	2.19	-	1.59
A_k	0.91 ± 0.05	0.80 ± 0.04	0.94 ± 0.04	0.91 ± 0.04	0.88 ± 0.02	0.91 ± 0.03
$A_{\rm ISW}$	0.52 ± 0.75	1.17 ± 0.58	1.44 ± 0.52	0.18 ± 0.67	0.91 ± 0.33	0.99 ± 0.35
Zhou et. al.						
b_1	1.25	1.54	1.55	1.90	-	1.44
b_2	1.26	1.87	1.90	2.21	-	1.62
A_k	0.91 ± 0.06	0.81 ± 0.04	0.93 ± 0.04	0.87 ± 0.04	0.87 ± 0.02	0.89 ± 0.03
$A_{\rm ISW}$	0.50 ± 0.79	1.03 ± 0.59	1.37 ± 0.55	0.20 ± 0.63	0.82 ± 0.33	0.98 ± 0.35
Offset						
b_1	1.28	1.52	1.54	1.89	-	1.45
b_2	1.30	1.86	1.87	2.20	-	1.64
A_k	0.89 ± 0.05	0.81 ± 0.04	0.93 ± 0.04	0.89 ± 0.04	0.87 ± 0.02	0.88 ± 0.03
$A_{\rm ISW}$	0.45 ± 0.81	1.05 ± 0.58	1.32 ± 0.56	0.25 ± 0.46	0.83 ± 0.33	0.99 ± 0.35
AvERA model						
b_1	1.16	1.34	1.25	1.46	-	1.23
b_2	1.11	1.50	1.45	1.75	-	1.33
A_k	0.97 ± 0.06	0.80 ± 0.04	0.91 ± 0.04	0.85 ± 0.04	0.87 ± 0.02	0.91 ± 0.03
$A_{\rm ISW}$	0.24 ± 0.35	0.48 ± 0.25	0.55 ± 0.23	0.07 ± 0.24	0.35 ± 0.13	0.39 ± 0.14

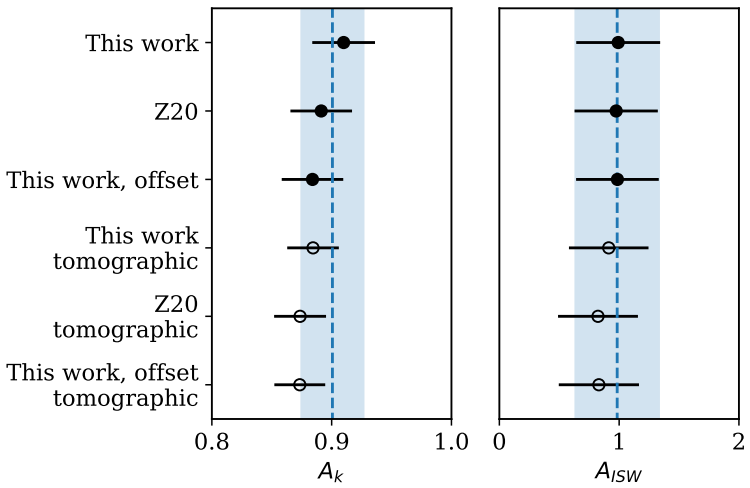

Figure 5.12 *Measurements of A_κ and $A_{\rm ISW}$ for various data selections at $\ell_{\rm max} = 500$ using the appropriate best-fit $p(z)$ for each set. The blue dashed line and band shows our default result, which is the average of the first two data points in each column. These represent a single unbinned analysis, as opposed to the average of the results for the various tomographic shells. The 'offset' results refer to the impact of the mean differences between our photo-zs and those of Z20 (see Section 4.2.4).*

of these different choices is shown in Fig. 5.12.

5.2.5 Implication of low A_κ

We first consider the simplest interpretation of our low A_κ amplitude for the galaxy-CMB lensing cross correlation in terms of parameters within the ΛCDM model. The lensing signal at low z has a direct linear dependence on the matter density fluctuation, which is proportional to the mean density times the relative fluctuation – i.e. to $\Omega_m\sigma_8$. The cross-correlation is also proportional to galaxy bias, but we have shown in Section 5.1 how that degree of freedom can be determined separately by including the galaxy auto-correlation data. At non-zero redshifts, the dependence on Ω_m becomes nonlinear as this parameter influences distances and evolution of density fluctuations. For our range of redshifts, the empirical density dependence of the amplitude is as $\Omega_m^{0.78}$, so that our result for A_κ produces the following constraint:

$$\sigma_8\Omega_m^{0.78} = 0.297 \pm 0.009. \tag{5.13}$$

The cosmology is fixed when determining bias parameters from galaxy clustering, and these bias parameters are then used to constrain cosmology from cross-correlations. This is acceptable, because the bias determined such that $b\sigma_8$ is matched to the overall amplitude of the measured galaxy clustering. The cross-correlation amplitude depends on $b\sigma_8^2$. Therefore, if we change the σ_8 parameter in fitting galaxy clustering (thus determining the corresponding bias parameters), the change in the cross-correlation amplitude will only depend on the change in σ_8. The amplitude of galaxy clustering is not sensitive to changes in Ω_m parameter, and thus also does not affect the determination of the bias parameter.

It is interesting to note that total CMB lensing itself produces a constraint of a similar form, but with a different density dependence:

$$\sigma_8\Omega_m^{0.25} = 0.589 \pm 0.020 \tag{5.14}$$

[228]. A straightforward combination of these two results yields

$$\Omega_m = 0.275 \pm 0.024; \quad \sigma_8 = 0.814 \pm 0.042; \tag{5.15}$$

the same normalisation as *Planck*, but a somewhat lower density.

It is interesting to compare these results with analogous constraints from weak galaxy lensing. Here the dependence on density is intermediate in strength. The constraints from the cosmic shear measurement of KiDS-1000 [15] and DES Y1 [291] are as follows:

$$\sigma_8\Omega_m^{0.5} = 0.416^{+0.013}_{-0.011} \qquad \mathrm{KiDS-1000} \tag{5.16}$$

$$\sigma_8\Omega_m^{0.5} = 0.428 \pm 0.015 \qquad \mathrm{DES-Y1} \tag{5.17}$$

which is in close consistency with what would be deduced from the CMB lensing results: $\sigma_8\Omega_m^{0.5} = 0.427$, as opposed to the fiducial 0.455. In combination, these three lensing results then give a clear preference for a model with a rather lower density than the *Planck* fiducial model, as illustrated in Fig. 5.13:

$$\Omega_m = 0.274 \pm 0.024; \quad \sigma_8 = 0.804 \pm 0.040. \tag{5.18}$$

It can be noted that the KiDS-1000 papers preferred to interpret their results in terms of a reduced σ_8, but a shift purely in normalisation is disfavoured by the

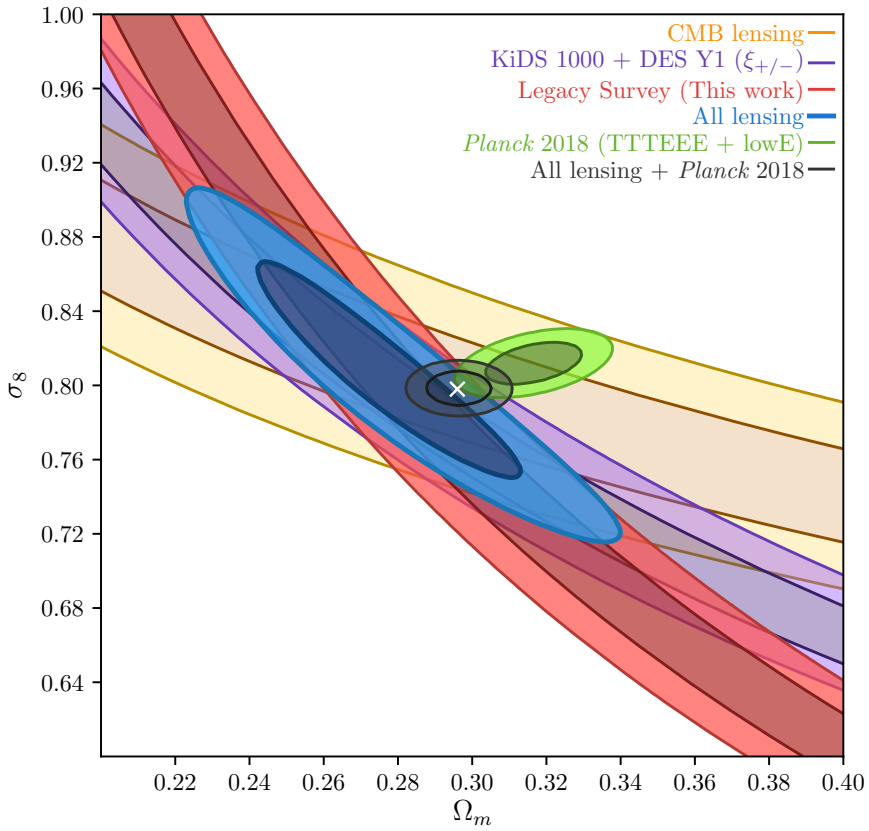

Figure 5.13 *Comparison of constraints on the $\Omega_m - \sigma_8$ plane; the contours contain 68% and 95% of the total probability. Note the consistent intersection of the three lensing-based results. The KiDS-1000 + DES Y1 constraint are for cosmic shear only. We use a Gaussian likelihood for DES Y1 and a skewed Gaussian using model 2 of [18] for KiDS-1000 to account for their asymmetric errors. This figure is produced by Shadab Alam, the author on the paper in which this section was published. The figure is adopted here as to maintain the clarity of discussion from that work.*

total CMB lensing amplitude, quite apart from our current results.

The conflict of this result with *Planck* is marked: $\Delta\chi^2 = 12$ on 2 degrees of freedom, which represents a p value of 2×10^{-3}. In these circumstances, we should be cautious in accepting the formal combination of the above lensing result with *Planck*, which is

$$\Omega_m = 0.296 \pm 0.006; \quad \sigma_8 = 0.798 \pm 0.006. \tag{5.19}$$

In fact, this unimaginative compromise model is arguably not ridiculous: it lies within the 95% confidence contours of both our combined lensing result and *Planck*. The value of Ω_m alone would represent a 2.7σ deviation from *Planck*,

but consistency in σ_8 is better and there is no prior reason to be more concerned about a deviation in one or other of these parameters. Nevertheless, agreement this weak is asking a lot of bad luck: we may be fairly sure that systematics are present, and the question is whether they lie in the data or in the theoretical framework. From the point of view of the actual values of Ω_m and σ_8, 'new physics' counts as just a further systematic on the same footing as data errors [25], but these alternatives are hardly equal in their implications.

5.2.6 Discussion

Imperfections in data

The most conservative assumption is that there are indeed imperfections in the data. If these were to lie on the lensing side, we would point the finger of suspicion at photometric redshifts, which are a dominant source of potential bias. We have discussed the reliability of the photo-zs used in this paper at some length, and a huge effort has been invested in this topic by galaxy weak lensing groups – using rather different data and methods to the approach taken here. On the CMB side, the exemplary thoroughness of the *Planck* analysis makes one reluctant to suggest any imperfection, but there are issues. Apart from the continuing puzzle of the well-known large-scale anomalies, there is the fact that the *Planck* TTTEEE data prefer an amplitude of CMB lensing that is *higher* than fiducial: $A_{\rm lens} = 1.180 \pm 0.065$, which represents some form of internal inconsistency. These issues were investigated in detail by [74], who argued that that the anomalies represented no more than slightly unusual statistical fluctuations in the *Planck* dataset and that there was no evidence of systematics at an important level. Where large-scale properties of the CMB are concerned, cosmic variance dominates and the many independent *Planck* maps can indeed give confidence that systematics are negligible. But in the noise-dominated regime, where the best results require the combination of all data subsets, residual systematics at the few-σ level are not so easy to rule out. The *Planck* constraint on Ω_m does depend significantly on the high$-\ell$ data, and so could be considered potentially less robust. We therefore think it is plausible that the compromise solution with $\Omega_m \simeq 0.296$ may be close to the truth. If we look at CMB constraints independent of *Planck*, ACT+WMAP yields $\Omega_m = 0.313 \pm 0.016$, which is easily consistent with 0.296; this work also has $A_{\rm lens}$ very close to unity [7].

Implications for the Hubble parameter

A slightly reduced matter density would also have the advantage of reducing the other tension that is currently the subject of much discussion: the Hubble parameter. The most robust inference concerning H_0 from the CMB comes from the main acoustic scale, which can be taken empirically as measuring the combination $\Omega_m h^3$ with negligible error [217]. If we use this as a basis for rescaling the fiducial model, the compromise $\Omega_m = 0.296$ would require $H_0 \simeq 69\,\mathrm{km\,s^{-1}Mpc^{-1}}$. This 2% increase from the fiducial value is still significantly below the direct determination of 74.03 ± 1.42 [244], but again would only require a modest level of systematics for consistency. Furthermore, taking seriously the $\Omega_m \simeq 0.274$ from the combined lensing data would imply a completely consistent $H_0 \simeq 71$.

Consideration of variations in h prompts us to ask whether the predicted A_κ depends on h. From Eq. 3.40, we can see that there is no explicit h dependence, since h times comoving distance is a function of redshift and Ω_m only. The scale at which σ_8 is determined is accessible to the range of ℓ under study, so changes in power-spectrum shape arising from changes in h would be expected to have a minor effect. In practice, we find $A_\kappa \propto h^{0.24}$, which is equivalent to a negligible $\Omega_m^{0.08}$ effect when considering variations with $\Omega_m h^3$ fixed.

It is undeniably depressing to be considering the possibility that one or more of the leading current cosmological datasets could be reporting results that contain systematic errors of close to 2σ, but equally we need to beware of too hastily declaring the existence of new physics as soon as we see a minor statistical discrepancy. Because there are in principle two distinct discrepancies, affecting $\Omega_m - \sigma_8$ and H_0, a single new addition to the cosmological model that solved both issues would demand to be taken seriously. But both the lensing and H_0 discrepancies have existed in the literature for some while, and it is fair to say that no compelling solution has emerged. Nevertheless, it is worth reviewing some selected candidates.

Massive neutrinos

It is known that neutrinos make a non-zero contribution to the non-relativistic density, with a summed mass of at least 0.06 eV ($\Omega_\nu h^2 > 0.00064$). Owing to free streaming, the neutrino distribution is close to homogeneous on the scales of

LSS, and therefore the lensing effect is reduced in two ways: the clumped mass is only the CDM, with a density $(1-f_\nu)\Omega_m$; this lower effective dark matter density slows growth since last scattering, reducing σ_8 today. At first sight, these effects sound as if they have the potential to close the gap between lensing results and *Planck*, but this is not so. Firstly note that we do not really need to be concerned with growth suppression for the interpretation of the lensing results themselves, since the lensing signal is directly proportional to the low-redshift normalisation. Furthermore, the standard definition of σ_8 (adopted by *Planck* and CAMB) is that it is the rms fractional fluctuation in the *total* matter density. The fractional fluctuation in the CDM density is thus $\sigma_8/(1-f_\nu)$, and this raised amplitude compensates for the lower clumped density, so that the lensing signal for a given Ω_m and σ_8 should be independent of the neutrino fraction. The only subtlety is that the growth between $z=1-2$ and $z=0$ will be slightly less than in ΛCDM for the given Ω_m. But this is a tiny effect: f_g is about $\Omega_m(z)^{0.6}$, so the relative f_g is $(1-f_\nu)^{0.6}$, so the mass fluctuations at $z=1-2$ are higher by of order $1+0.6f_\nu$ than in ΛCDM for a given $z=0$ normalisation, which is a negligible correction.

Therefore, all the dependence on neutrino fraction on the $\Omega_m-\sigma_8$ plane comes from *Planck*. Inspecting their chains, the effect is approximately $\sigma_8 \propto (1-f_\nu)^{2.2}$ and $\Omega_m \propto (1-f_\nu)^{-2.5}$. Although the predicted normalisation is reduced, as expected, the best-fit density rises and so the tension between primary CMB and lensing is *increased* if there is a non-minimal neutrino fraction.

Modified gravity

A more effective modification of theory concerns the strength of gravity. To avoid excessive complication, it is common to approach this in a form that includes two linear parameters that modify the scalar potentials Ψ and Φ, which describe fluctuations in the time and spatial parts of the metric. In the standard model, $\Psi=\Phi$ and the potentials satisfy the Poisson equation. The most transparent modification is to scale the forces for non-relativistic particles (from Ψ) and photons (from $\Psi+\Phi$) that result from a given mass fluctuation, δ, so that $\nabla^2\Psi \propto (1+\mu)\delta$ and $\nabla^2(\Psi+\Phi) \propto (1+\Sigma)\delta$ (e.g. Simpson et al. 2013). The motivation for modified gravity comes from late-time accelerated expansion, and therefore it is normally assumed that the modifications evolve as

$$(\mu(z),\Sigma(z)) = (\mu_0,\Sigma_0)\,\Omega_\Lambda(z), \tag{5.20}$$

so that modifications are unimportant at last scattering. Since ΛCDM seems to describe the expansion history well, it is also assumed that the modifications affect only perturbations. Thus the cosmological parameters inferred from the CMB should be unaffected in this framework, and therefore modified gravity can be used to close any gap between the predicted and observed lensing signal. There is a degeneracy here: for $\Sigma = 0$ (normal lensing strength), we can appeal to $\mu < 0$ to reduce the growth in fluctuations; alternatively, we can have normal growth with $\mu = 0$ and suppress the resulting lensing signal by appealing to $\Sigma < 0$. In either of these solutions, it would be understandable that the total CMB lensing signal is consistent with standard gravity, because it arises around $z = 2$, where the modifications are only just switching on. To achieve $A_\kappa \simeq 0.9$ at $z \simeq 0.5$, where $\Omega_\Lambda = 0.4$, we need either $\Sigma_0 = -0.25$, or $\mu_0 = -1.5$. The large value for μ_0 seems surprising at first sight, implying close to total suppression of LSS gravity at the present epoch. This is partly a consequence of the $\mu \propto \Omega_\Lambda(a)$ assumption, and also because μ suppression of the strength of gravity only alters the growth *rate*: to achieve significant reduction in δ at $z \simeq 0.5$ would require substantial alteration to the growth rate at much higher redshifts, which is hard to achieve in this model unless μ_0 is large. Such a model can be ruled out by other evidence, since it would imply a very non-standard growth rate at $z = 0.5$, whereas we know from redshift-space distortions that the rate is within about 10% of fiducial at this redshift [320].

In summary, then, an explanation of a low lensing amplitude via modified gravity must involve an alteration of the strength of light deflection by a given mass concentration, rather than reducing the amplitude of mass fluctuations. Such an explanation appears to be consistent and not in conflict with other evidence, but one could hardly call it compelling – not least because it has no impact on the H_0 tension; such a radical conclusion requires more than a single piece of evidence. In due course, we will have more accurate tomographic lensing and redshift-space distortion data where changes in the growth rate and strength of lensing with redshift can be measured, so that a progressive decline in the strength of lensing could be measured. Without such evidence, this hypothesis is at best provisional.

5.2.7 $A_{\rm ISW}$ and implication on AvERA model

An interesting approach that has been proposed with a view to explaining the high claimed ISW signal from superstructures is the AvERA model [234].

This is a radical framework that postulates a critical-density universe without a cosmological constant, but with averaging of an inhomogeneous expansion rate, leading to an apparent acceleration as measured by the mean effective Hubble parameter. The model can be adjusted so that the empirical $H(z)$ relation rather closely matches the standard ΛCDM case – which has the advantage that the conversion between distance and redshift remains as in the standard model, so that inferences from the CMB regarding density parameters and the shape of the matter power spectrum remain valid.

On the other hand, the *amplitude* of the spectrum is modified in this model, and the density growth rate $f_g \equiv d\ln\delta/d\ln a$ is rather different from ΛCDM. There is a spike above $f_g = 1$ around $z \simeq 2$ and in general the rate is higher than the standard model; thus, the required value of σ_8 at $z = 0$ has to be increased in order to be consistent with the amplitude of primordial fluctuations inferred from the CMB. A convenient fitting formula for the growth rate is

$$f_g(a) = \exp(-2.308a^2) + 0.549[1 + 11.569(\ln a + 1.222)^2]^{-1}. \tag{5.21}$$

Integration of this expression implies that $\sigma_8(z)$ for AvERA is above ΛCDM at high redshift, by as much as a factor 1.2 at $z = 1.5$. Conversely, the low-redshift evolution is slower and the amplitude of present-day matter fluctuations is about 5% lower than ΛCDM. The two models predict identical amplitudes at $z \simeq 0.08$. Thus, for redshifts relevant for our tomographic data, the AvERA model predicts a higher density fluctuation, so that the predicted amplitude of the linear ISW signature is greater. There will also be a greater degree of nonlinear evolution. We treat this by assuming that the nonlinearities can be estimated in the HALOFIT framework by taking the standard ΛCDM approach and increasing $\sigma_8(z)$ appropriately. This should be sufficient to indicate how important the increased nonlinearity might be (this will be more of a potential issue for lensing, where even weak lensing can be dominated by nonlinear structures on small enough angular scales).

We use the Planck 2018 Cosmological parameters [227], and set the power spectrum of AvERA to be identical to ΛCDM at $z = 8.55$ consistent with [22]. We use the fitting formula in Eq. 5.21, and interpolate the AvERA $H(z)$ and $R(z)$ as given by [22]. Fig. 5.14 shows the matter auto-correlation, matter-κ, and matter-T cross-correlations in AvERA and ΛCDM with both linear and non-linear power spectra, using the best-fit $p(z)$. As expected, the AvERA prediction has a higher amplitude than ΛCDM. The corresponding galaxy biases are significantly smaller

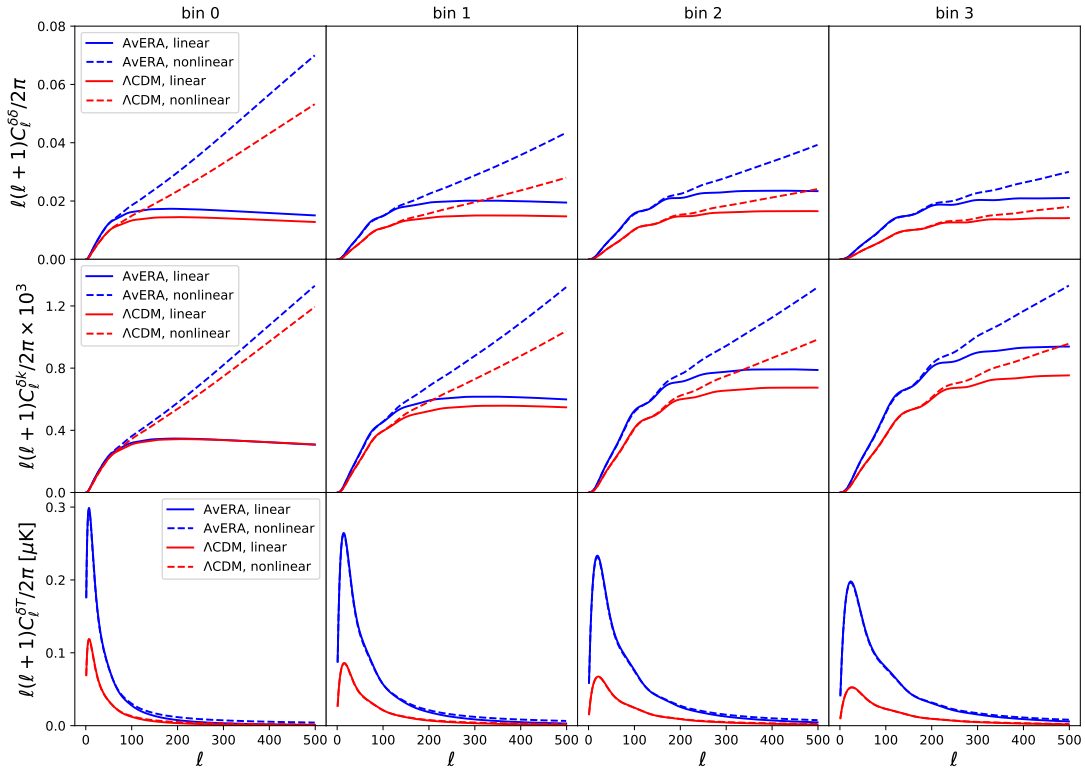

Figure 5.14 *The dark matter auto-correlation (top), the matter-κ cross-correlation (middle), and the matter-temperature cross-correlation (bottom) in ΛCDM (red) and AvERA (blue) model for the four tomographic bins using the best-fit $p(z)$. The solid lines show computation using linear power spectrum, and the dashed lines show that using non-linear power spectrum from* HALOFIT.

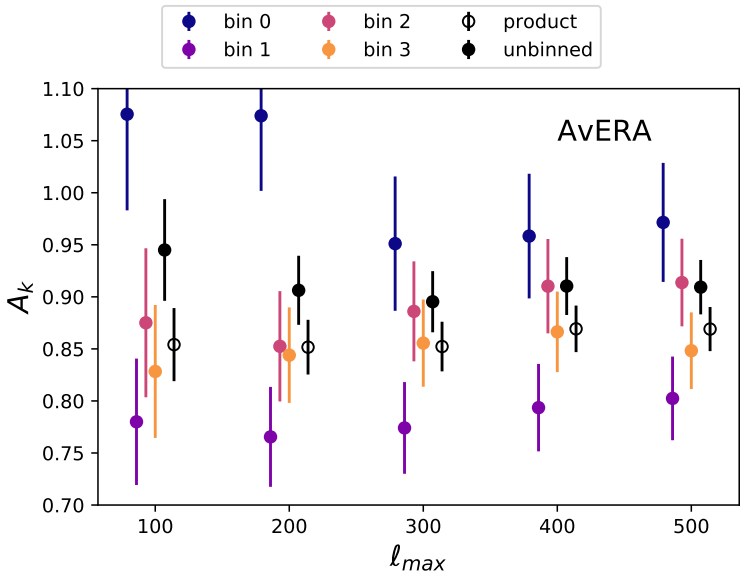

Figure 5.15 *The constraints for A_κ from the normalised likelihoods in the AvERA model using the best-fit $p(z)$ and fitted galaxy bias.*

in the AvERA case as shown in Table 5.3, but this effect is absorbed in the lensing cross-correlation, resulting in similar constraints on A_κ. The likelihoods for A_κ and $A_{\rm ISW}$ are obtained in Figs 5.15-5.16. In this case, we find $A_\kappa = 0.87 \pm 0.02$ for the product, and $A_\kappa = 0.91 \pm 0.03$ for the unbinned case. In the ISW case, the AvERA prediction is about three times as large as ΛCDM. The preferred amplitude is $A_{\rm ISW} = 0.35 \pm 0.13$ from the product of tomographic bins, and $A_{\rm ISW} = 0.39 \pm 0.14$ from the unbinned result. Adopting the unbinned case, this ISW result excludes unity at 4.4σ and we can be confident that the AvERA model greatly over-predicts the general level of ISW fluctuations.

5.3 Summary and discussion

We have performed a tomographic analysis of the cross-correlations between Legacy Survey galaxies and the *Planck* CMB lensing convergence and temperature maps, covering 17 739 deg^2. We obtained our own photometric redshifts for the Legacy Survey based on $g - r$, $r - z$, and $z - W_1$ colours, with a precision of $\sigma_z/(1 + z) = 0.012 - 0.015$. The galaxy sample is divided into four wide redshift bins between $z = 0$ and $z \simeq 0.8$. We model errors in photometric redshift with respect to calibration data sets via a modified Lorentzian function, and constrain the tails of the error distribution by requiring consistent prediction

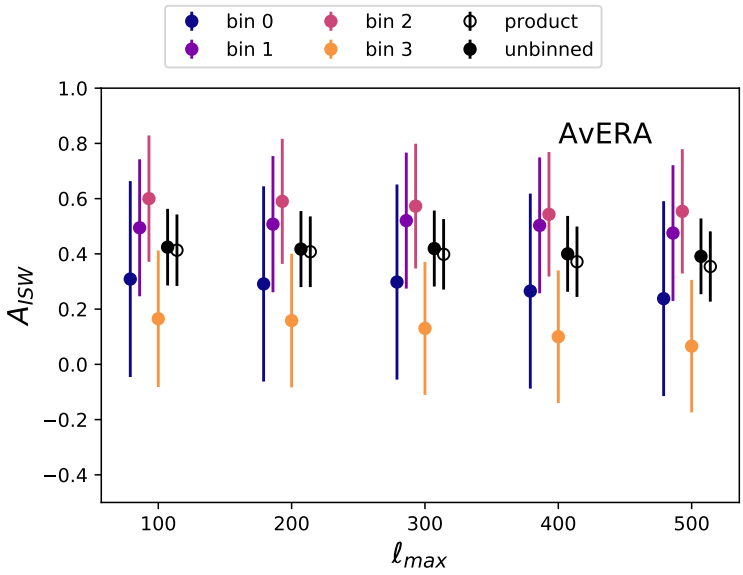

Figure 5.16 *The constraints for $A_{\rm ISW}$ from the normalised likelihoods in the AvERA model using the best-fit $p(z)$ and fitted galaxy bias.*

of the galaxy cross-correlation signal between different tomographic bins. This modelling incorporates a novel scheme for dealing with scale-dependent bias (Eq. 5.8), in which the linear and nonlinear parts of the matter power spectrum receive independent boosts to their amplitudes. The consistency of the galaxy clustering and its cross-correlations argues that the galaxy sample from the Legacy survey is robust, and that the properties of the photometric redshifts are understood.

We then proceeded to evaluate the cross-correlation between the tomographic galaxy maps and the CMB maps of temperature and lensing convergence. The results are compared with the predictions of the fiducial *Planck* cosmological model, marginalizing over the photo-z error parameters with weights given by the likelihood from fitting galaxy auto- and cross-correlations.

The amplitude for the ISW signal relative to the fiducial prediction is $A_{\rm ISW} = 0.98 \pm 0.35$, consistent with ΛCDM, as found by previous works, e.g. [280]. We also explored the AvERA model [234], which was developed in order to explain the claimed excess signal in the stacked ISW signal in supervoids. We find that in this model, $A_\kappa = 0.91 \pm 0.03$, and $A_{\rm ISW} = 0.39 \pm 0.14$, with significantly smaller galaxy biases compared to the ΛCDM case. Thus, the AvERA model achieves its aim of predicting an enhanced supervoid signal at the price of raising the overall level of ISW power to the point where it is inconsistent with observation, even given the relatively noisy nature of the ISW signal. If the supervoid signal is

found to persist in future studies, AvERA cannot be the explanation.

The amplitude of the CMB lensing signal is found to be significantly lower than the prediction of the fiducial *Planck* model, with a scaling factor $A_\kappa = 0.901 \pm 0.026$. We note that this lower amplitude is consistent with the results from an analysis of cross-correlation between CMB lensing and a DESI LRG sample based on the Legacy Survey data [140]. Our result can be translated into constraints on the parameter combination $\sigma_8\Omega_m^{0.78} = 0.297 \pm 0.009$. The total CMB lensing signal provides an alternative constraint on this plane, of $\sigma_8\Omega_m^{0.25} = 0.589 \pm 0.020$ [228], which also represents an amplitude lower than fiducial, although only by 1σ. In combination, these CMB lensing figures prefer a solution with a relatively low matter density of $\Omega_m \simeq 0.274$. These CMB lensing results are also in excellent agreement with the value of $\sigma_8\Omega_m^{0.5}$ deduced from weak galaxy lensing [15, 291]. Within the compass of ΛCDM, the model that does least violence to lensing and CMB data is

$$\Omega_m = 0.296 \pm 0.006, \quad \sigma_8 = 0.798 \pm 0.006, \tag{5.22}$$

and this is consistent with the 95% confidence ranges from both datasets. It is therefore worth taking seriously the possibility that the true cosmic density is substantially on the low side of the fiducial *Planck* estimate. Such a reduction would also reduce the H_0 tension, raising the best-fitting CMB value to around $69\,\mathrm{km\,s^{-1}Mpc^{-1}}$ – although this would still imply the existence of systematics in the direct H_0 data (see e.g. Efstathiou 2020).

We therefore face a situation where at least two of three currently dominant cosmological probes contain unrecognised systematics at the level of a few standard deviations, or the standard model must be extended. The choice between conservatism or revolution is perhaps not so easy in the current circumstances, but the next generation of experiments should settle the question beyond all doubt.

Chapter 6

Stacked CMB lensing and ISW signals around superstructures in the DESI Legacy Survey

6.1 Introduction

Chapter 5 has shown that the impact of LSS on the CMB from lensing and ISW is close to the LCDM prediction, within a discrepancy of order 10%. But the literature contains claims of much larger discrepancies in the amplitude of these foreground effects. Granett et al. [101] averaged CMB temperature maps at the positions of 50 objects identified as voids and clusters that had the most extreme density contrasts as measured using the SDSS LRG sample. By comparison to ΛCDM simulations, they claimed an excess ISW signal of 4σ significance. Subsequently, [40, 42, 144, 145] used stacking techniques and claimed an ISW signal that was higher than the ΛCDM prediction at moderate significance. [190] reported a signal consistent with ΛCDM using the whole void catalogue, rather than focusing on superstructures. Most recently, [146], hereafter K19, measured the stacked ISW signal using the DES supervoids with radius $R_v > 100\,h^{-1}\,\mathrm{Mpc}$, and found an amplitude relative to the ΛCDM prediction of $A_{\mathrm{ISW}} = 5.2 \pm 1.6$ in combination with BOSS. In a separate paper, [298] measured the stacked CMB lensing convergence signal for the same objects, and found no discrepancy with ΛCDM.

The anomalous ISW amplitude from supervoids is of interest in terms of modified gravity, where the screening mechanisms in some theories are less effective in empty regions [50]. However, there has not been a satisfactory explanation for this excess signal. [40] argued that the signal is unlikely to be caused by Sunyaev-Zel'dovich effects, non-Gaussianity, or modified gravity (see also Nadathur et al. 2012). Another possible explanation comes from the AvERA (Average Expansion Rate Approximation) model [22], which assumes an inhomogeneous expansion rate with $\Omega_\Lambda = 0$ and predicts a higher overall ISW signal by modifying the growth rate. However, [114] showed that the AvERA model prediction is inconsistent with galaxy-temperature cross-correlation results, so the ability of the AvERA model to account for the supervoid results is subject to doubt.

One needs to be cautious in interpreting the stacked results. Firstly, the definition of supervoids is not exactly the same in each case. In some cases, voids are defined in 3D density fields based on e.g., the ZOBOV algorithm [197], whereas in other cases the void definition is based on 2D smoothed density fields [e.g. 250]. Different void-finding algorithms can lead to different structures being selected. Secondly, the procedures involve various parameter choices such as the initial smoothing scale of the density field and threshold criteria for superstructure selection. Therefore, one needs to make sure that the final result does not depend on such choices.

Nevertheless, the reported anomalous ISW amplitude is usually at the 2-3σ level. There is a fair chance that they are statistical flukes. To clarify the situation, it is useful to use a bigger sample of galaxies for the analysis to beat down the dominant noise from sample variance. The aim of this work is to repeat the stacking analysis using superstructures in the DESI Legacy Imaging Survey. The large sky coverage reduces the noise due to cosmic variance. We use the galaxy maps produced in Chapter 4 [114], hereafter H21, based on photometric redshifts; the cross-correlation of these maps with the CMB lensing convergence and ISW effect provides a baseline for the ISW amplitude coming from superstructures only. We attempt to adopt the same void finding algorithm as in K19 based on the 2D maps, although the relatively high thickness of the photometric redshift bins means that our selected superstructures are not exactly comparable to those of K19. In order to reduce confirmation bias, we also adopt a 'blind' strategy where we fix our analysis pipeline using mock data based on cosmological N-body simulations, before we run the pipeline on the actual data.

The Chapter is organised in the following structure. Section 6.2 introduces

the data used for creating superstructures, the mock galaxy dataset, and the generated lensing convergence and ISW maps. The void finding procedure and covariance matrix is described in Section 6.3. We compare our superstructure catalogues from the real and mock data in Section 6.4 and present the stacking results in Section 6.5. Finally, we discuss the results and sum up in Section 6.6.

6.2 Simulation

We make use of the MultiDark Planck [MDPL2; 142] simulations with *Planck* 2013 Cosmology. The simulation is performed with a $1\,h^{-1}$Gpc box with 3840^3 particles using the L-Gadget 2 codes. The mass resolution of the simulation is $1.51 \times 10^9\,h^{-1}M_\odot$. The simulation assumes a flat ΛCDM cosmology with $\Omega_m = 0.307$, $\Omega_b = 0.048$, $h = 0.67$, $n_s = 0.96$ and $\sigma_8 = 0.823$. The dark matter halo catalogue for 32 snapshots between redshift 0 & 1 is processed using the ROCKSTAR[1] phase space halo finder [23], in order to construct galaxy lightcones. The simulation is publicly available through the CosmoSim database[2] [231, 240].

6.2.1 Simulated galaxy light-cones

We use the halo occupation distribution (HOD) model to generate simulated galaxy catalogues. We only use the measurements of linear and non-linear bias (H21) to find the best fit HOD parameters. We use a simplified version of the HOD model with only two free parameters corresponding to the characteristic mass of central ($M_{\rm cut}$) and satellite galaxies (M_1) as given in following equations:

$$p_{\rm cen} = \frac{1}{2}{\rm erfc}\left(\frac{\ln M_{\rm cut} - \ln M_{\rm halo}}{\sqrt{2}}\right) \tag{6.1}$$

$$\langle N_{\rm sat}\rangle = \frac{M_{\rm halo} - M_{\rm cut}}{M_1}, \tag{6.2}$$

where $p_{\rm cen}$ gives the probability of assigning a central galaxy to a halo with mass $M_{\rm halo}$ and $\langle N_{\rm sat}\rangle$ gives the mean number of satellite galaxies as the function of halo mass. The actual number of satellite galaxies for any given halo is drawn

[1] `https://bitbucket.org/gfcstanford/rockstar`
[2] `https://www.cosmosim.org/cms/simulations/mdpl2/`

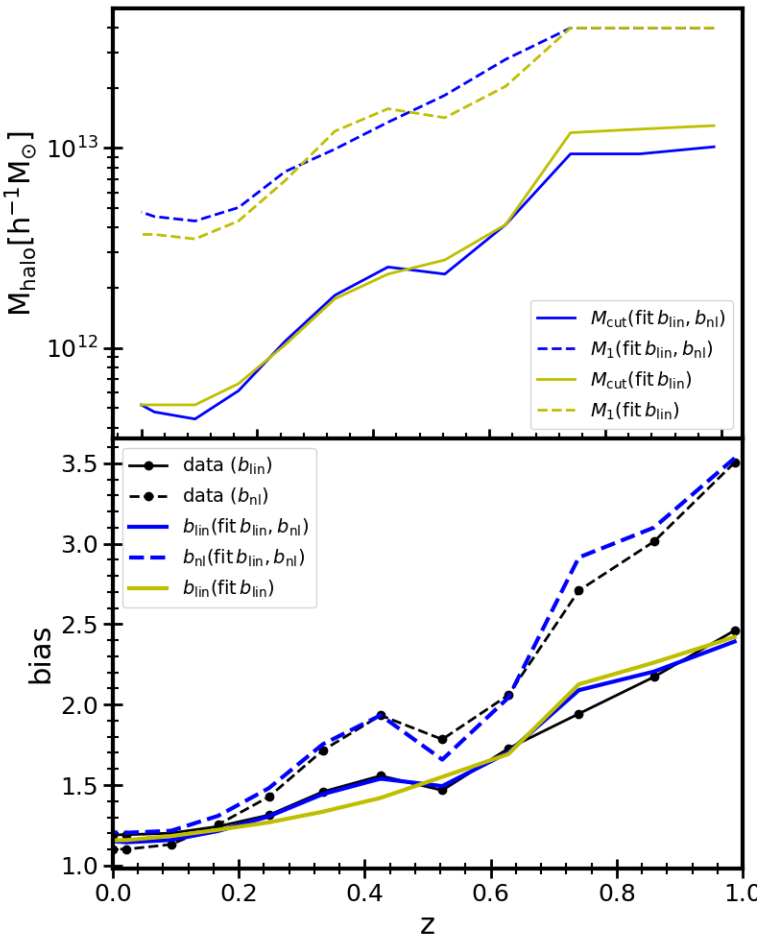

Figure 6.1 *Top panel shows the best fit HOD parameters as the function of redshift used to generate simulated galaxy catalogues. Bottom panel shows the evolution of linear and non-linear bias in mock with coloured lines. The black line shows the best fit linear and non-linear bias obtained for the data from [114]. This figure is made by Shadab Alam.*

from a Poisson distribution. We use main haloes (i.e. discarding subhaloes) from 32 snapshots between redshift 0 & 1 and determine the best fit HOD parameters by fitting the 3D galaxy power spectrum with linear and non-linear bias evolution as measured in the data (H21). The linear bias values in our mocks are defined using scales $0.05 < k < 0.1\,h\,\mathrm{Mpc}^{-1}$ and the non-linear bias uses the scales $0.5 < k < 2\,h\,\mathrm{Mpc}^{-1}$. Our best fit parameters are not very sensitive to the limits of scales used to define the linear and non-linear bias. The best fit HOD parameters along with galaxy bias are shown in the Figure 6.1. We have created two sets of mocks, one of which only matches the linear bias, and the other one also has non-linear bias matched. For the scales considered in this project, we confirm that the two mocks do not give rise to significantly different stacking signals from superstructures.

We then convert our galaxy catalogue into lightcone form by simply repeating the box and placing the observer at the origin in order to extract shells from each snapshot covering the comoving separation between consecutive snapshots. The simulation and data are matched in galaxy number density in each redshift slice. In order to include the photometric redshift effect, we assign to each galaxy a photometric redshift $z_p = z + \delta z$, where δz is drawn from the distribution of Eq. 4.1 with the parameters given by the best-fit $p(z)$ in each bin from H21. We then construct our tomographic slices by selecting galaxies in redshift bins using z_p. The resulting true redshift distribution is close to the best-fit $p(z)$ from the real data, as shown in Fig. 6.2. The same survey mask is applied to the mock as the DESI Legacy Survey data.

6.2.2 Making mock lensing convergence maps

In order to generate lensing convergence maps that are consistent with our simulated galaxy data, we perform the following integral using the Born approximation:

$$\kappa(\hat{\theta}) = \int_0^{r_{\max}} \frac{3H_0^2\Omega_m}{2c^2} \frac{(r_{\mathrm{LS}} - r)r}{r_{\mathrm{LS}}} \delta(r, \hat{\theta})\, dr, \tag{6.3}$$

where r_{LS} is the comoving distance between CMB and the lens plane and r is the comoving distance to the lens plane. The $\delta(r, \hat{\theta})$ is the matter overdensity in the direction $\hat{\theta}$ within a shell of width dr at distance r. To determine δ, we first create particle lightcone using snapshot by repeating the box and extracting

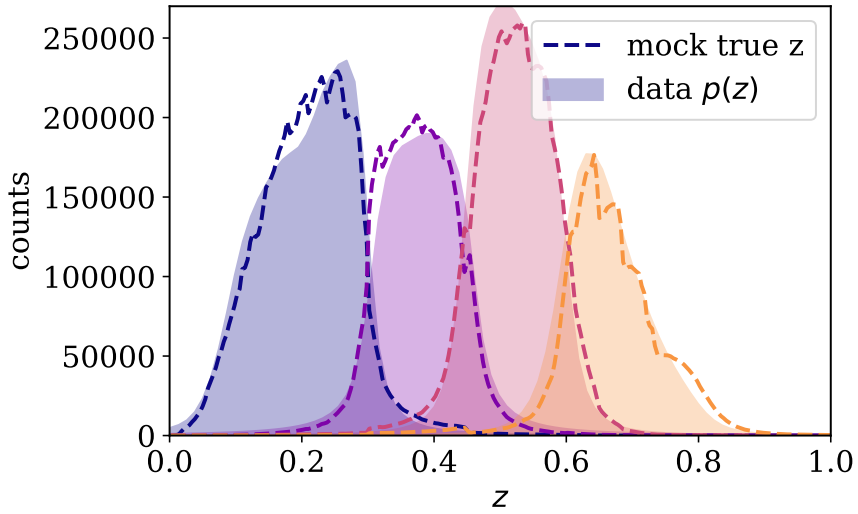

Figure 6.2 *The mock redshift distribution (dashed) is matched to observations by assigning a redshift error δz from the best-fit modified Lorentzian distribution used in [114] and the corresponding best-fit $p(z)$ from data (shaded) by fitting the galaxy auto- and cross-correlations in the four tomographic bins.*

a shell of particle at the location of 32 halo snapshot between redshift 0-1. But we have only three particle snapshots ($z \approx 0, 0.49, 1.02$) available compared to 32 halo snapshot. Therefore, for each halo snapshot shell we use the nearest particle snapshot and scale the over-density by ratio of growth at the halo snapshot to the growth at nearest particle snapshot. This gives us $\delta(r, \hat{\theta})$ which is then integrated using equation 6.3. In principle the full κ map should be integrated with $r_{\rm max} = \infty$. But since we are only concerned with the cross-correlation of galaxies with the convergence map, as long as we limit our integral to larger than the maximum galaxy redshift ($z \approx 0.9$) we will obtain unbiased results. Therefore we use $r_{\rm max}$ corresponding to $z_{\rm max} = 1.02$ to generate our lensing convergence map. We note that we use a HEALPIX pixelisation with $n_{\rm side} = 512$ to generate our convergence map.

6.2.3 Making ISW maps in simulations

Although the ISW signal arises from the linear evolution of the potential Φ, it has contributions from non-linear evolution. To include both of them, we follow the algorithm presented in Cai et al. [39], Seljak [261] to compute the time derivative

of the potential $\dot{\Phi}$ in Fourier space using

$$\dot{\Phi}(\mathbf{k},t) = \frac{3}{2}\left(\frac{H_0}{k}\right)^2 \Omega_{\rm m}\left[\frac{\dot{a}}{a^2}\delta(\mathbf{k},t) + \frac{i\mathbf{k}\cdot\mathbf{p}(\mathbf{k},t)}{a}\right], \tag{6.4}$$

where a is the expansion factor at z, $\mathbf{p}(\mathbf{k},t)$ is the Fourier transform of the momentum density fluctuation $\mathbf{p}(\mathbf{x},t) = [1+\delta(\mathbf{x},t)]\mathbf{v}(\mathbf{x},t)$, and $\delta(\mathbf{k},t)$ is the density contrast. We use the full particle data at the three snapshots mentioned above to compute $\dot{\Phi}(\mathbf{k},t)$ in Fourier space. We then interpolate $\dot{\Phi}$ in Fourier space according to the linear growth factor $G(a) = D(a)[1-f(a)]$ to obtain $\dot{\Phi}(\mathbf{k},t)$ at more epochs t between the original snapshots, where the times t are chosen such that their line-of-sight comoving spacing is $100\,h^{-1}\,$Mpc. The inverse Fourier transform of the above yields $\dot{\Phi}$ in real space on 3D grids. Follow Cai et al. [39], we then use Healpix to tessellate the sky, and follow Healpix pixel centres along the line of sights to interpolate and integrate $\dot{\Phi}$ values on grids to obtain the full ISW maps including the non-linear Rees-Sciama effect. Examples of the power spectra measured from these maps are shown in Fig. 6.3.

6.2.4 Quasi-linear ISW maps

With the expected high signal-to-noise from the galaxy-CMB lensing cross-correlation, we can also use the observed lensing signal around peaks and troughs to predict their corresponding ISW signal directly. This has the benefit of using one observable to predict the other. Using Eq. 6.3, we compute the lensing convergence κ for each direction $\hat{\theta}$ in each shell between $0 < z < 1$. We then follow methods in Section 3.3.2 and obtain the quasi-linear ISW map using Eq. 3.53 for each of the 30 shells, where r_0 is the comoving distance to the shell centre. These maps are then added together to produce the final (noise-free) ISW map. The comparison of the power spectra of the quasi-linear and full ISW maps is shown in Fig. 6.3. We can see that the two maps are most consistent in the range of $10 < \ell < 40$. At scales $\ell \lesssim 10$, the linear map gives unphysical modes whose amplitudes are much larger than the full computation. At smaller scales, where $\ell > 40$, the full computation gives a higher amplitude than the quasi-linear case. In the stacking analysis, we are mostly interested in structures of a few degrees, corresponding to $\ell \sim 100$.

An alternative method based on non-linear density evolution is mentioned earlier in Section 3.3.1. This method assumes spherical symmetry of the stacked void

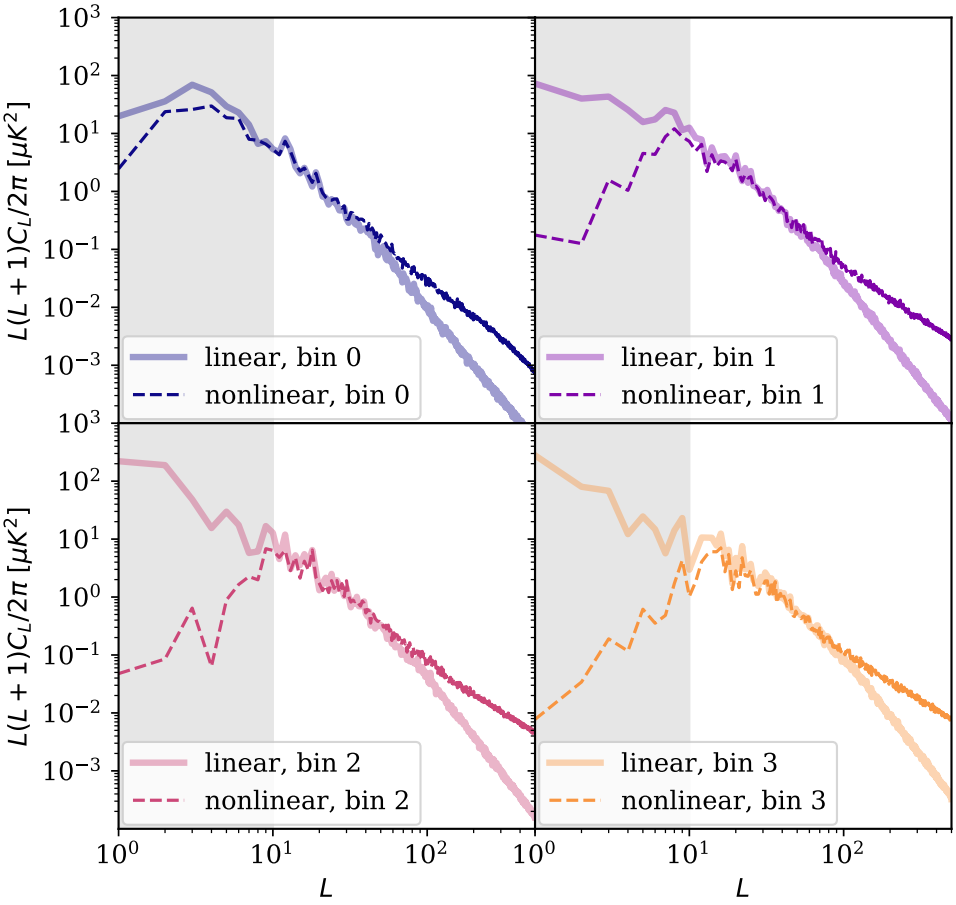

Figure 6.3 *The auto power spectra of simulated ISW maps for the mock catalogue in four tomographic slices. The full non-linear computations are shown with dashed lines and the quasi-linear approximations are shown with solid lines. The grey region indicates the low-ℓ range that is removed in the linear map.*

profile. This is generally the case for 3D voids. Void finders based on 2D density slices preferentially find elongated voids [145]. For our case, the redshift slice is $400 - 800\,h^{-1}$ Mpc in width, the voids found are more likely to be 'tunnels', and spherical symmetry is not applicable. Therefore, we use our simulations to predict the stacked ISW signal, which captures the non-linearity of the density evolution. As a comparison, we use this method to compute the linear theory prediction of the same signal, and demonstrate their differences.

6.3 Methods

6.3.1 Void finder

We follow the void finder algorithm in [250]. The finder takes the following steps:

1. We estimate the 2D density fluctuation on HEALPIX maps with $\delta = n/\bar{n} - 1$. We then apply a Gaussian smoothing of $\sigma = 20\,h^{-1}\,\mathrm{Mpc}/d(z)$, where $d(z)$ is the mean comoving distance to the tomographic slice. We then define pixels with $\delta < \delta_*$ as potential void centres. In practice, we fix δ_* to pick out the lowest 10% of the smoothed pixels, which is around $\delta_* = -0.2$.

2. Starting from the lowest density pixel in the potential void centres, we compute the mean density δ_i inside a circular shell of radii R_i and $R_i + \Delta R$ for each $R_i \in \{R\}$. ΔR is chosen to be $1\,h^{-1}\,\mathrm{Mpc}$. Once $\bar{\delta}_i > 0$ is encountered for the first time, we register $R_v = R_i + \Delta R/2$ as the void radius. In practice, we use the `query_disc` function in HEALPY to find pixels within a disc of angular size $\theta_i = R_i/d(z)$.

3. Once the void is found, we check the potential void centre list, and exclude any centre that is inside the existing void.

4. We then update the list of potential void centres and repeat steps (2)-(3) until the list is exhausted.

The free parameters in this finder algorithm are the initial smoothing σ and the density cut δ_*. A larger σ will result in the merging of smaller voids, and could lead to higher signal to noise [146, 250]. As a result of the merging of voids and the hierarchical void-finding procedure, the void catalogue can be different. Increasing δ_* would include shallower voids. However, this should not affect any deeper voids found with a lower δ_*. It is possible to find small but deep voids embedded in large shallower voids. We choose $\{R\}$ in the range $1\,h^{-1}\,\mathrm{Mpc} \leq R \leq 300\,h^{-1}\,\mathrm{Mpc}$, with an increment of $2\,h^{-1}\,\mathrm{Mpc}$ between each sample. After we obtain the void sample, we further exclude voids that have have less than 70% of their area inside the survey mask. An illustration of the procedure is shown in Fig. 6.5.

A major difference between this work and [146] is that our redshift slice is much thicker whereas they used slices of comoving size $100\,h^{-1}\,\mathrm{Mpc}$. In [146], due to

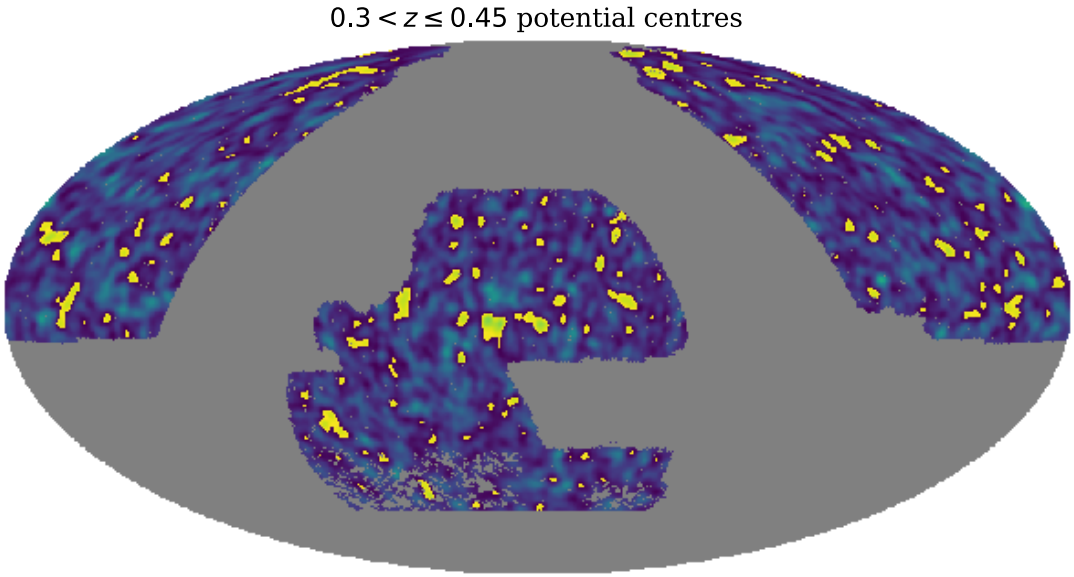

Figure 6.4 *An example of the void finding procedure using the tomographic slice in redshift range* $0.3 < z \leq 0.45$. *The highlighted pixels correspond to the potential void centres, selected on the smoothed density map with* $\delta < \delta_*$. *In this case,* $\delta_* = -0.15$. *The background intensity map shows the density fluctuation in this slice.*

the thin redshift slice, they also include a pruning of overlapping voids between different redshift bins by shifting the bin edges a few times. Thus, although the void finding algorithm is defined in 2D, their void catalogue is comparable to those found using 3D algorithms. We do not carry out this procedure here because we expect that the structures in the four tomographic bins are dominated at distinctive redshifts and thus not strongly correlated. The voids found here are likely to be 'tunnels' rather than spherical objects.

To find clusters, we apply the identical procedure to an inverted density map. Due to the lognormal shape of the smoothed density distribution of each map, we select the densest 5%, instead of 10%, pixels as potential centres. This choice gives similar numbers of clusters and voids in the final sample.

In order to obtain the stacked signal at the position of these superstructures, we rotate the map (in this case, the map can be galaxy density, lensing convergence, or temperature fluctuation) at the pixel level to place each superstructure centre at $(\theta, \phi) = (0, 0)$. We then stack the rotated maps scaled by the void radius R_v, on a grid with $0 \leq R \leq 3R_v$. To account for masks, we also perform the same

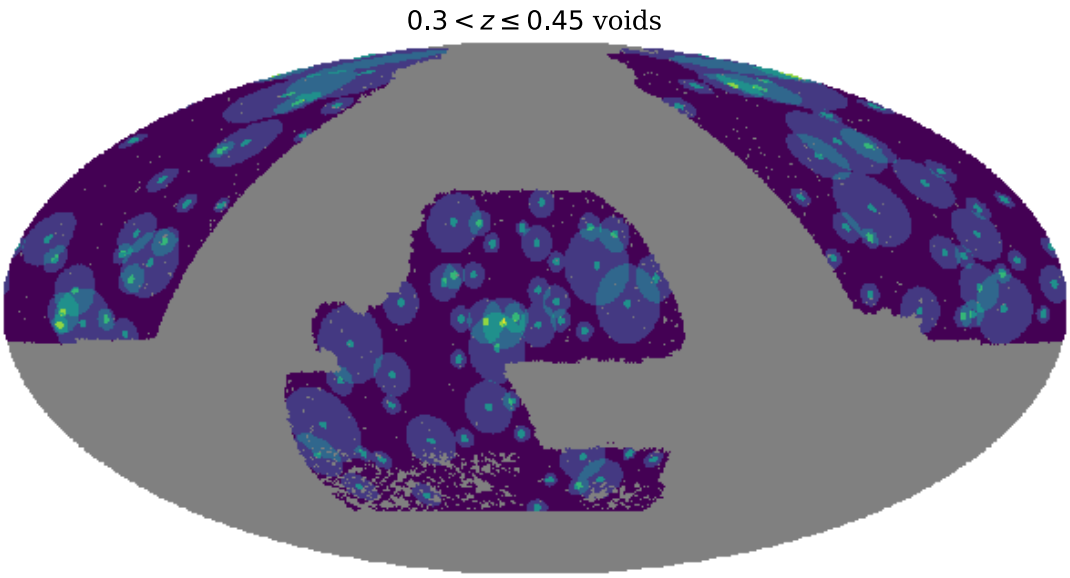

Figure 6.5 *The resulting void centres (shown highlighted dots) from Fig. 6.4 and their void radius (shown in fainter circles). Notice that some voids at survey boundaries are cut. Also notice that voids can overlap, in cases where deeper voids can be found inside shallower voids.*

rotation to the mask for each void. The stacked map is obtained by

$$P^{\rm stack} = \frac{\sum_i P_i^{\rm map}}{\sum_i P_i^{\rm mask}}, \tag{6.5}$$

where $P_i^{\rm map}$ is the pixel value for the map for i-th void, and $P_i^{\rm mask}$ is that for the mask. We extract the isotropic radial profile for these stacked images. Given the angular bins $\{\theta\}$, we measure the average signal in the ring between radii θ_i and θ_{i+1}, and assign the value to the middle of the angular bin.

6.3.2 Covariance matrix

We use three methods to estimate the covariance matrix for the stacked signal to account for the noise on the background CMB map as well as the foreground superstructure positions.

To capture the CMB noise, we generate 1000 random CMB maps with nside = 512 using the measured pseudo CMB temperature auto power spectrum, corrected by the fraction of sky lost due to the mask $\hat{C}_\ell = C_\ell / f_{\rm sky}$. The maps are then generated using the `synfast` function in HEALPY applied to C_ℓ, and multiplied by the *Planck* 2018 CMB mask. For comparison, we also use the *Planck* best-

fit ΛCDM CMB power spectrum[3], accounting for the pixel window function and the FWHM = 5 arcmin circular Gaussian smoothing. These methods give a consistent covariance matrix. We repeat the same stacking process for superstructures in each redshift slice on each of the random CMB maps and extract the averaged radial profile. The covariance matrix is computed by

$$C_{ij} = \frac{1}{N}\sum_{s}^{N}(x_i^s - \bar{x}_i)(x_j^s - \bar{x}_j), \tag{6.6}$$

where $N = 1000$ is the sample size, x_i^s is the measurement of i-th data component in the s-th sample, and $\bar{x}_i$ is the mean measurement of the i-th component. The inverse covariance is corrected by the Hartlap factor [116] with $C_{ij}^{-1} = (N - p - 1)/(N - 1)\langle C_{ij}^{-1}\rangle$, where $p = 15$ is the length of the data vector.

To estimate the errors due to the fluctuations of the foreground galaxy sample, we generate 1000 sets of random superstructure positions for each redshift bin within the survey mask, and compute the stacked signal on the *Planck* 2018 CMB temperature map. It should be noted that this assumes no correlation of the positions of the superstructures, which are in general not true: there will be close pairs of clusters, while it is unlikely to find two voids that are close to each other. Nevertheless, this method provides a rough estimate of the foreground random error. The covariance is computed using Eq. 6.6 and the inverse covariance is corrected by the Hartlap factor.

Finally, we estimate the covariance matrix from Jackknife subsampling by excluding one superstructure at a time in the given redshift bin. The sample size is equal to the number of superstructures in each bin, N_J. The resultant covariance matrix from Eq. 6.6 is multiplied by $(N_J - 1)$ to account for correlation between different Jackknife samples. The Jackknife covariance matrix is noisy with small sample size, i.e., in the lower redshift bins.

The comparison of the diagonal elements of the three covariance matrices for the void sample is shown in Fig. 6.6. For the cluster sample, the covariance is similar but with different number of objects in each bin. In all cases, there is close agreement between the three methods. Due to the small Jackknife sample size in bin 0, the diagonal elements are noisy compared to the other two methods. From here on, we will use the covariance matrix estimated from random void positions in our following analysis. The jackknife covariance is used for the case of the

[3] `http://pla.esac.esa.int/pla/#cosmology`

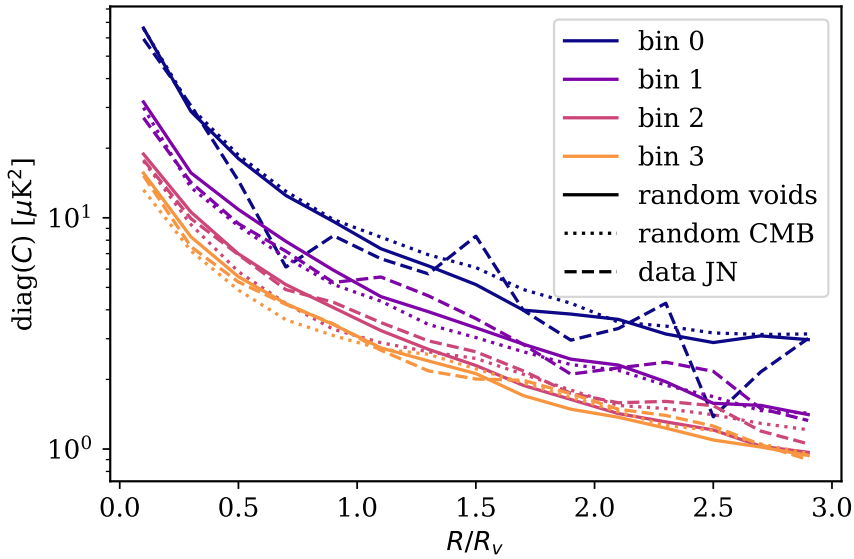

Figure 6.6 *The diagonal elements of the covariance matrices (in* $[\mu\mathrm{K}^2]$*) for the radial ISW stacked profile in each redshift bin (shown in different colours). The dotted lines show that from 1000 random CMB samples using the void positions in data, the solid lines show that from 1000 sets of void positions using the real CMB map, and the dashed lines show the Jackknife error from the actual data.*

stacking of all superstructures.

6.4 Superstructures

A summary of the numbers of voids and clusters found in each redshift bin is shown in Table 6.1 for both the mock and real data. In general, the data and the mock show good consistency in terms of the number of voids found and in the distribution of void radius. For clusters, the density cut δ_* in the finder algorithm is slightly larger in data compared to mock, and the number of clusters found is smaller especially in bin 2 and bin 3. The distribution of the radius in comoving length and central density (in the smoothed map) of these superstructures is shown in Fig. 6.7. The majority of the superstructures found have a radius of around $60\,h^{-1}\,\mathrm{Mpc}$, with an extended tail towards $R_v \sim 300\,h^{-1}\,\mathrm{Mpc}$. There is a small number of clusters in data that saturate at the maximum radius. It is pointed out in [145] that there is an anti-correlation between the depth and the size of the superstructures. There is, however, no clear trend in the voids and clusters found here. The minimum R_v at fixed central density increases with the central density becoming more extreme.

The stacked galaxy density profiles are shown in the upper panel of Fig. 6.8 for both voids and clusters. The agreement between mock (solid bands) and real data (circles for voids and squares for clusters) is good. The dotted lines show the profile divided by linear galaxy bias in each case. The agreement between data and simulation using linear bias is expected for voids, as discussed in [229]. At $R > R_v$, the stacked density profile changes sign and peaks at $R \sim 1.3R_v$, before falling to zero at larger scales. This suggests that on average, the voids found are surrounded by overdensities and clusters are surrounded by underdensities, consistent with other findings in the literature (e.g. [110]).

6.5 Results

6.5.1 Stacked lensing map

We stack the the *Planck* 2018 lensing convergence map with $\ell_{\rm max} = 2048$ and the simulated lensing convergence map at superstructure positions in real and mock data respectively. Prior to stacking, we smoothed the lensing maps with a Gaussian kernel with FWHM = 1° to suppress the small scale power for the purpose of map rotation at the pixel level, and this is done consistently in both data and simulation.

The lower panel of Fig. 6.8 shows the stacked radial profile of the κ-map. Similar to the case of the stacked galaxy density profile, the change of sign with a peak at $R \approx 1.3R_v$ is also present in the stacked κ profiles. For voids, the real and mock datasets show good consistency in general. For clusters, however, the simulation over-predicts the lensing signal in bin 3 significantly for $R < R_v$. Combining clusters in all four redshift bins, we find that the simulation also shows a 30% excess compared to data, because the sample is dominated by the highest redshift bin. Due to the slightly more extended R_v distribution in the real data compared to the mock, especially in the highest redshift bin (see Fig. 6.7), we check whether including a weight based on the ratio of the two R_v distributions can reduce the difference between the data and mock. However, the inclusion of this weight does not change the signal significantly. We characterise the consistency between simulation result and data using the lensing amplitude A_κ, where $\kappa_{\rm data} = A_\kappa \kappa_{\rm th}$. Assuming Gaussian likelihoods with $\mathcal{L} \propto \exp(-\chi^2/2)$ and using the Jackknife covariance for the combined case, we find $A_\kappa = 0.937 \pm 0.087$ for all voids and

Table 6.1 *Summary of various parameters used in void finding and the number of voids in each redshift slice. The first row shows the mean redshift computed from the best-fit redshift distribution in our previous work. The second row shows the smoothing scales for the density maps in units of degrees, which correspond to a comoving length of* $20\,h^{-1}\,\mathrm{Mpc}$ *for each slice. The third row shows the density cut, where* $\delta < \delta_*$ *are selected as potential void centres. The last row shows the number of voids found in each bin, after excluding voids that have less than* 70% *of their area inside the survey mask.*

Redshift bin	$0 < z \leq 0.3$	$0.3 < z \leq 0.45$	$0.45 < z \leq 0.6$	$0.6 < z \leq 0.8$
Mock				
Mean redshift	0.210	0.376	0.521	0.667
linear bias	1.19	1.40	1.49	1.76
Smoothing scale [deg]	1.92	1.12	0.84	0.68
δ_* (voids)	−0.11	−0.14	−0.14	−0.15
N (voids)	28	108	209	364
δ_* (clusters)	0.11	0.15	0.15	0.16
N (clusters)	31	119	230	378
Data				
Mean redshift	0.207	0.376	0.522	0.663
linear bias	1.25	1.56	1.52	1.83
Smoothing scale [deg]	1.93	1.09	0.84	0.69
δ_* (voids)	−0.11	−0.14	−0.14	−0.15
N (voids)	33	111	223	332
δ_* (clusters)	0.12	0.16	0.16	0.18
N (clusters)	38	97	185	282

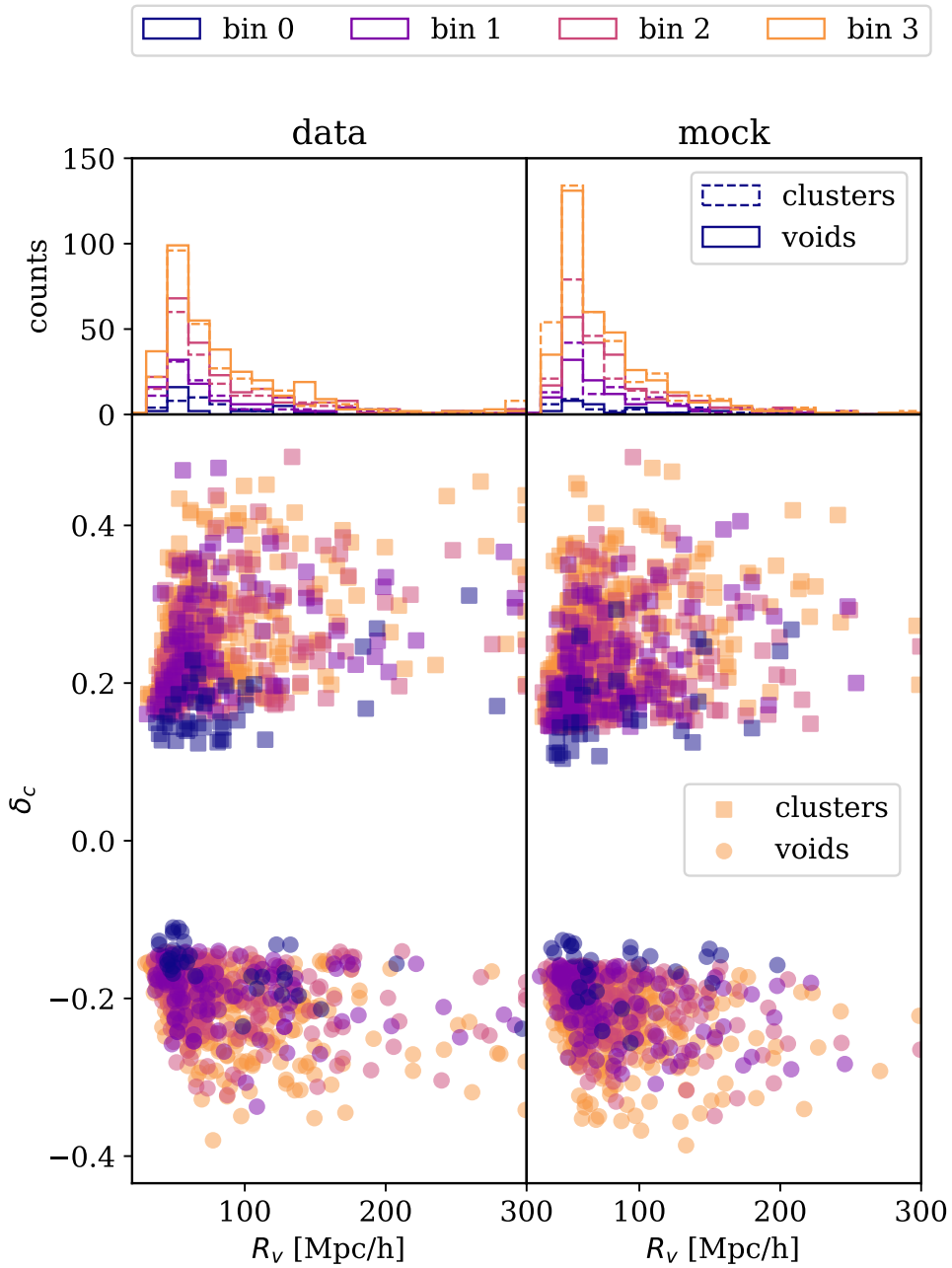

Figure 6.7 *Superstructure size and central density in real and mock data. The radius is defined as when the mean density measured within a ring of central radius R and width $1\,h^{-1}\,\mathrm{Mpc}$ first become positive.*

$A_\kappa = 0.712 \pm 0.076$ for all clusters. Assuming independence, this difference is formally 1.9σ, so hardly compelling evidence of an inconsistency; the combined result gives $A_\kappa = 0.811 \pm 0.057$.

In H21, the measured the angular cross-correlation between CMB lensing and galaxy overdensity also has a lower amplitude, $A_\kappa = 0.901 \pm 0.026$, given the best-fit *Planck* 2018 cosmological parameters, $\sigma_8 = 0.811$ and $\Omega_m = 0.315$. We further measure the angular cross-correlation $C_\ell^{g\kappa}$ of the mock and compare it with data. In order to account for the difference in the galaxy bias, we include galaxy auto-correlation C_ℓ^{gg}, and compare the bias-independent quantity $R = C_\ell^{g\kappa}/(C_\ell^{gg})^{-1/2}$. The lensing amplitude A_κ is then given by $A_\kappa = R^{\rm data}/R^{\rm mock}$. We compare the binned modes with $10 \leq \ell < 500$, assuming a diagonal covariance where the diagonal terms, following equations (12) and (13) in H21. We obtain the following values for A_κ in the four bins: 0.84 ± 0.06, 0.81 ± 0.05, 0.86 ± 0.04, 0.79 ± 0.04, and for the unbinned case, $A_\kappa = 0.85 \pm 0.03$, consistent with the stacked result. This may suggest that the lower lensing signal is likely contributed by high density peaks.

6.5.2 Stacked ISW map

We remove $\ell < 10$ modes from the *Planck* 2018 CMB temperature map and the simulated ISW map to reduce the effect of the imperfectly simulated large-scale modes in the simulated ISW map as shown in Fig. 6.3. A comparison of the stacked ISW profiles in data and simulation is presented in Fig. 6.9. The linear theory prediction from the lensing potential gives consistent result as does the full non-linear calculation, shown in the solid and shaded lines. Given the size of the error, the data show general consistency with the simulation. In the void case, it is noticeable that in bin 1, the data have a larger signal in $R < R_v$, whereas in bin 0, the data measurement is slightly positive. The level of fluctuations in the four measurements suggest that these deviations are not statistically significant. We use the covariance matrix obtained from 1000 sets of random void positions to quantify the consistency between data and simulation. Given 15 degrees of freedom, the χ^2 for each redshift bin is 8.9, 11.1, 16.2, 11.8. The null test of the data signal gives χ^2 of 8.1, 12.7, 15.2, 10.2. In general, the data do not show a preference for the simulation prediction over a null signal. For clusters, similar level of statistical fluctuations are present, with $\chi^2 = 11.3, 7.6, 10.8, 16.1$ for data compared to simulation, and $\chi^2 = 10.5, 8.9, 11.3, 17.3$ for the null test.

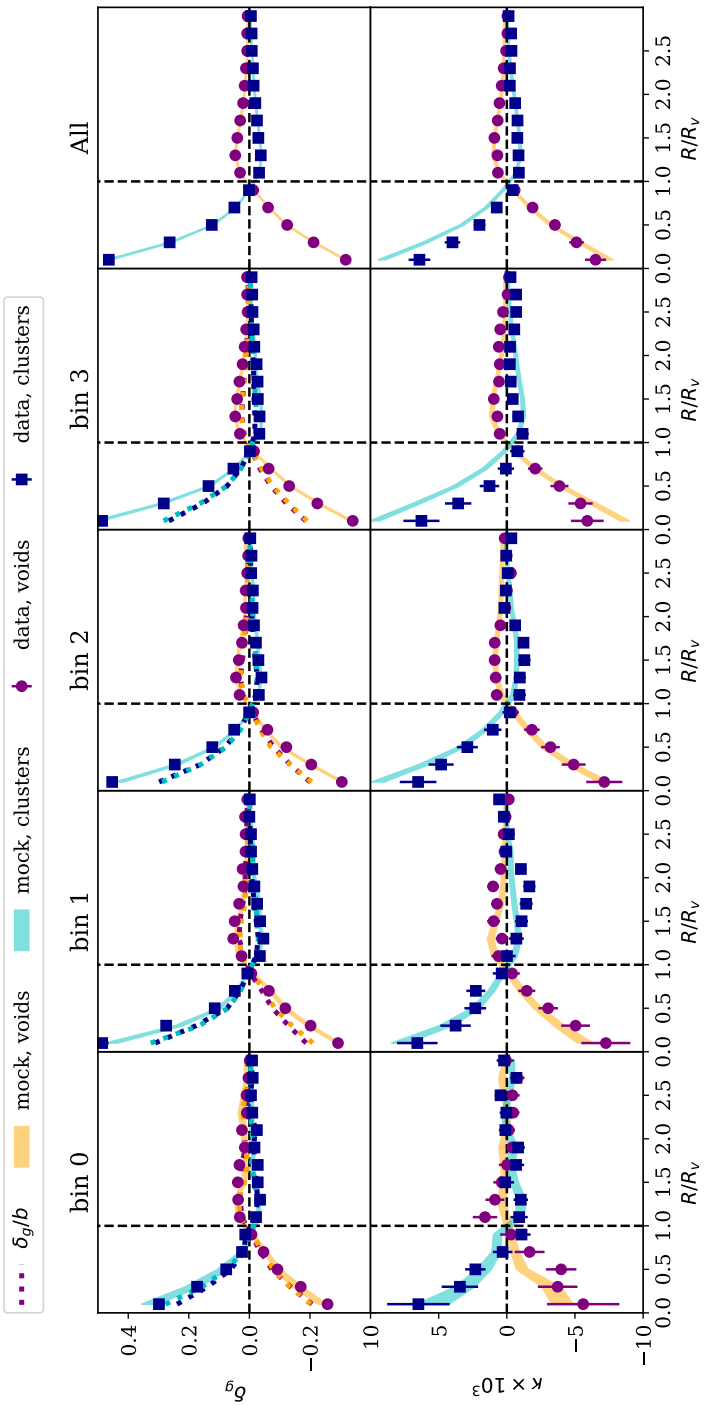

Figure 6.8 *Upper panel: The averaged radial profile of stacked galaxy density in each redshift bin at the superstructure positions found in simulation (solid band) and data (points). The dotted lines show the mean profile divided by the linear galaxy bias measured in simulation and data respectively. Lower panel: The averaged radial profile of stacked CMB lensing convergence. The lensing map have been smoothed by a Gaussian kernel of* FWHM $= 1^\circ$ *to suppress the small scale power for the purpose of map rotation at the pixel level. The error bars come from Jackknife sampling of the voids in each redshift bin.*

Combining voids in all four bins, we find that $\chi^2 = 12.6$ for simulation and 10.1 for a null signal. The larger χ^2 for the simulation is probably due to the slightly negative signal at $R > R_v$ opposed to positive. The combined cluster result shows $\chi^2 = 11.1$ for simulation and 15.1 for null signal. We characterise the consistency between simulation result and data using the ISW amplitude $A_{\rm ISW}$, where $\Delta T_{\rm data} = A_{\rm ISW}\Delta T_{\rm th}$. Assuming Gaussian likelihoods with $\mathcal{L} \propto \exp(-\chi^2/2)$, we find $A_{\rm ISW} = -0.10 \pm 0.69$ for all voids and $A_{\rm ISW} = 1.52 \pm 0.72$ for all clusters. The combined result gives $A_{\rm ISW} = 0.68 \pm 0.50$. Therefore, given the size of the error, the measurements are fully consistent with the ΛCDM prediction; however, there is also no clear detection of this signal.

6.5.3 Comparison with K19

We investigate the possible causes of the excess signal in K19. We have tried to apply the same void finding algorithm as K19, but there are a few differences. Firstly, they used redshift bins with a comoving width of $100\,h^{-1}\,$Mpc between $0.2 < z < 0.9$, whereas our bins are much wider. Secondly, due to the larger galaxy bias of the redMaGiC sample, they use a fixed $\delta_* = -0.3$ in the void finding algorithm across all redshift bins, and a comoving smoothing scale of $50\,h^{-1}\,$Mpc. In our fiducial setting, we have chosen to define δ_* to correspond to the lowest 10% in density, and applied a comoving smoothing scale of $20\,h^{-1}\,$Mpc. Thirdly, in K19 a subsample of supervoids with $R_v > 100\,h^{-1}\,$Mpc in particular gave the excess signal, whereas in our fiducial void sample, we do not make selections based on void properties. Finally, the void sample in K19 is only within the DES footprint, whereas our sample covers a larger region.

To begin with, we make the assumption that differences in the void finding process would not lead to an inconsistent stacking signal, because the underlying structures found should correspond to the same physical underdensities. In this case, one possibility could be that the excess is only contributed by the supervoids with $R_v > 100\,h^{-1}\,$Mpc.

Thus, we look at such subsample with our fiducial setting. This gives a total of 151 simulated voids, and 187 voids in the actual data. This number is smaller than one would expect from the K19 sample, which comprises 87 voids with $R_v > 100\,h^{-1}\,$Mpc within the DES footprint, if it were extended about 3 times to the same size as the Legacy Survey. This difference can be attributed to the thicker redshift slices used in our analysis. An additional factor is that most of

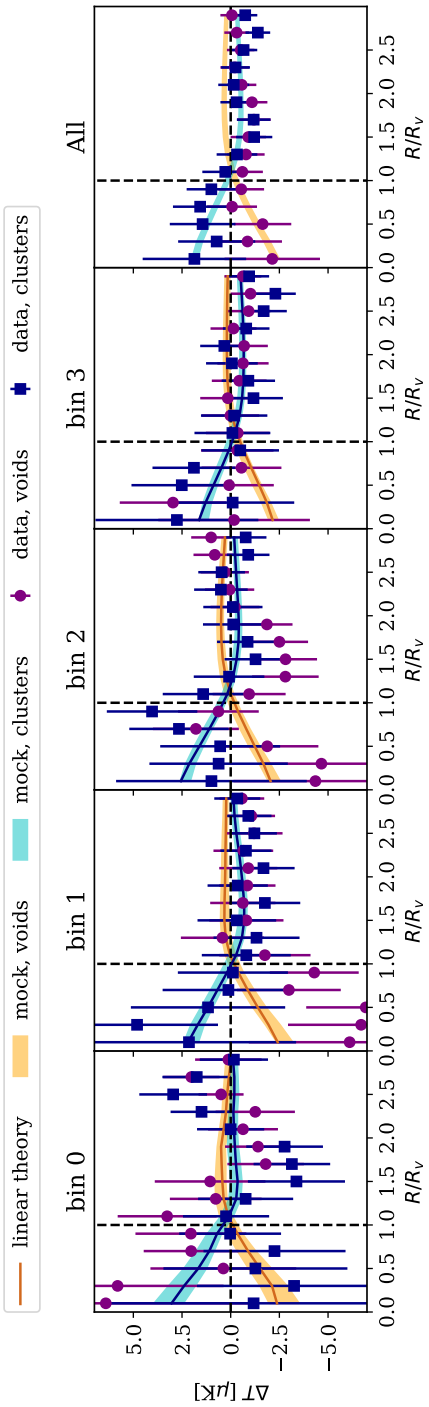

Figure 6.9 *The averaged radial profile of stacked ISW temperature in each redshift bin at the void positions found in the mock (yellow band) and real data (purple data points). The simulation prediction using linear theory is shown by the solid orange lines. For data, we use the Planck 2018 CMB temperature map. For both maps, the $\ell < 10$ modes are removed. The error bars come from Jackknife sampling of the voids in each redshift bin.*

the DES Y1 region is masked owing to our completeness cut, thus we may also lose a number of voids from that area. The stacked ISW profiles are shown in Fig. 6.10. The overall signal from data (purple dots) shows good consistency with our simulation results (yellow band). On the same plot, we also copy the results from K19. While their theoretical prediction (grey solid line) seems to be smaller than ours, their void signal from the DES sample (blue band) is much stronger. The difference in the theoretical prediction is plausibly due to the difference involved in the void finding procedure. Using the covariance matrix from 1000 sets of random void samples, the χ^2 is 16.3 compared to simulation and 16.5 compared to a null signal with DOF = 15. This suggests that in our fiducial sample, the large voids with $R_v > 100\,h^{-1}\,\mathrm{Mpc}$ do not cause an excess ISW signal.

Another possibility is that the K19 excess is due to cosmic variance. To test this, we apply the same survey mask from the DES footprint, giving a subsample of 173 voids. Among these, 40 voids have $R_v > 100\,h^{-1}\,\mathrm{Mpc}$. As shown in Fig. 6.10, the stacked signal using all voids within the DES footprint (brown squares) is consistent with zero, but selecting the large voids (pink star) does result in a mean signal closer to that measured in K19. However, given the size of the error bars, the overall signal is consistent with both a null signal and the simulation prediction.

The above investigation suggests that the excess signal may be due to difference in the redshift binning and parameter choices in the void finding process. Thus, we try to follow as closely as possible the procedure outlined in K19 (and references therein) in order to see if we can reproduce their signal. We split our photometric sample in the redshift range $0.2 < z < 0.8$ into bins of comoving width of $100\,h^{-1}\,\mathrm{Mpc}$. We exclude bins beyond $z \approx 0.7$ due to a sharp drop in number density. This gives a total of 11 redshift bins. We also create another sample that has a matched colour distribution in $g - W_1$ vs $r - z$ and $g - r$ vs $r - z$ as the DESY1A1 RedMaGiC sample. The details of the selection criteria can be found in Appendix A. Such a selection removes about half of the sample compared to the unmatched one. To account for the masked DES Y1 region, we relax the completeness threshold for the mask to 30% so that most of the DES Y1 region is now included. The completeness weighting and stellar density correction is then applied to each density map. Finally, due to the large photo-z tail, we expect neighbouring bins to overlap significantly. In K19, a careful pruning of voids was applied by shifting the redshift binning by a small amount. In this case we apply a

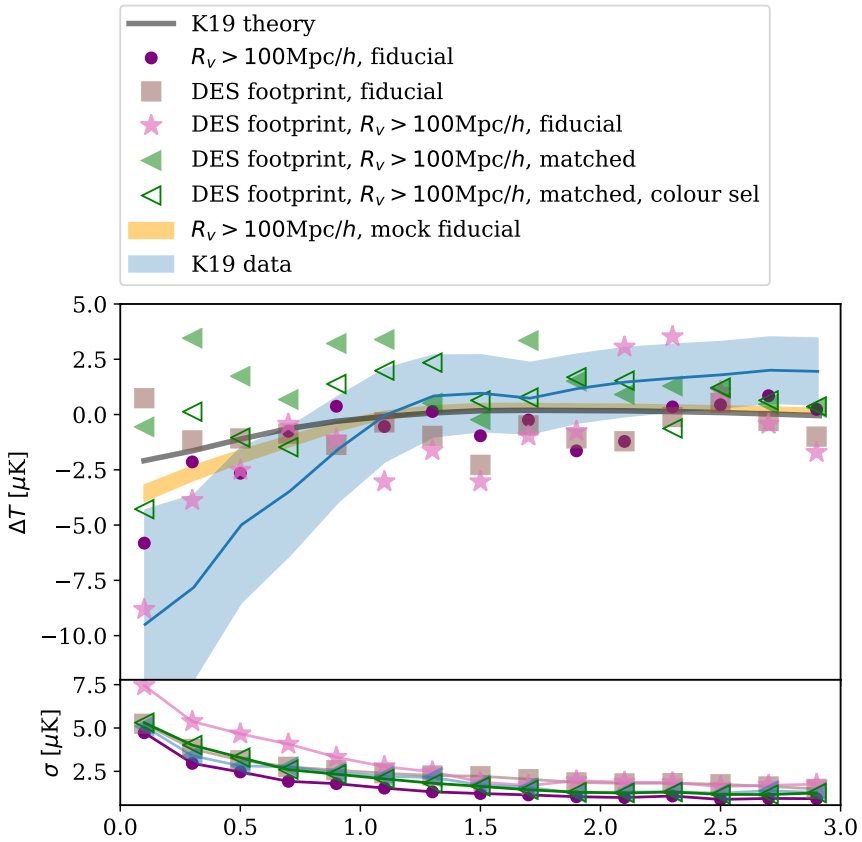

Figure 6.10 *Stacked void profiles for a few subsamples chosen to match the K19 measurements (data shown as a blue band and theory shown as a grey solid line). The subsamples involving our fiducial setting include: selection of void radius $R_v > 100\,h^{-1}\,\mathrm{Mpc}$ (purple circle); selection within the DES footprint (brown square); and selection within DES footprint as well as cut on R_v (pink star). We also consider subsamples that are more closely matched to K19 in the void finding process within the DES footprint with and without a redMaGiC-like colour selection (shown in open and filled green triangles). The error bars given by Jackknife resampling are shown in the lower panel.*

simplified version, where for neighbouring bins we remove the voids in the higher redshift bin if their centre lies within $0.5R_v$ of the voids in the lower redshift bin. We check that this removes most of the overlapping voids. We also apply the same smoothing scale as in K19, $\sigma = 50\,h^{-1}$ Mpc, in void finding. We find 75 and 64 voids with $R_v > 100\,h^{-1}$ Mpc inside the DES footprint with and without colour space constraints respectively, comparable to the 87 sample in K19. The stacked signal at these void centres are shown in Fig. 6.10 as green open triangles (with colour selection) and filled triangles (without colour selection). These signals are slightly positive at $R < R_v$, and do not reproduce the excess signal shown in K19 (open black triangles). Thus, the excess signal may be due to other details in the void catalogue construction. For example, the small redshift bins can be affected by the uncertainty of our photo-z sample, which has a median of $|\Delta z| = 0.027$ but with a large non-Gaussian tail.

To summarise, we have attempted to compare the ISW signal from our void sample with K19, by investigating cuts on the void size, cosmic variance, and void-finding procedure. In the first two cases, we do not see a clear deviation from our simulation prediction based on the ΛCDM cosmology. In the last case, we obtain a signal that is consistent with ΛCDM, rather than about three times larger than the theoretical prediction from K19. This difference may be caused by details in the galaxy catalogue such as the galaxy sample and the photometric redshifts.

6.5.4 Searching for higher ISW signal

In this Section we look at the dependence of the signal-to-noise of the stacked ISW profile on supercluster properties. The purpose of Section is to see whether the excess ISW can be reproduced in by applying specific selections, rather than trying to claim a higher significance detection. Specifically we focus on R_v and δ_c, and in each case, we split the sample into the most extreme 10% and 50%, and compare the SNR with the full sample. We use the simulation to determine the mean expected signal (thus the signal itself is noise free) and we show realistic errors by computing the covariance from 1000 sets of random void positions within the DESI Legacy Survey footprint, and stack using the *Planck* CMB map. As shown in the upper panel in Fig. 6.11, selecting the 10% most extreme objects in terms of R_v or δ_c can boost the predicted ISW signal by about a factor of 2. From the lower panel in Fig. 6.11, it is clear that the larger R_v has a smaller

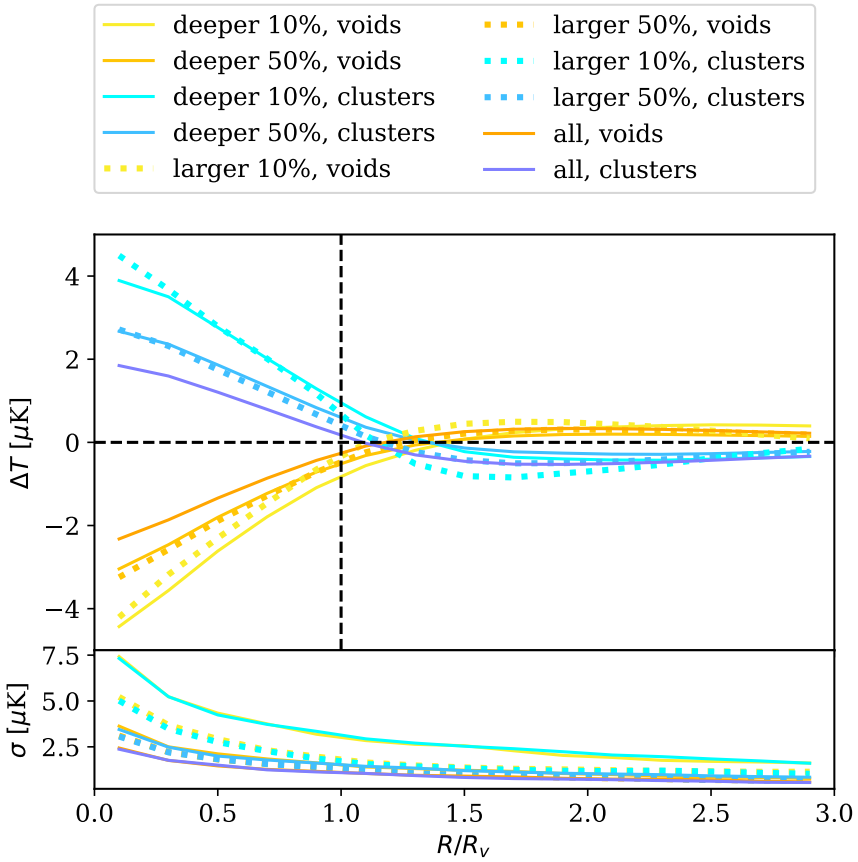

Figure 6.11 *Stacked ISW profile split by central depth δ_c (solid line) and size R_v (dotted line) using superstructures in the mock catalogue. The split is using the most extreme 10%, 50%, and the full sample in each case. Error bars are given by 1000 sets of random void stacking using the* Planck *CMB map.*

uncertainty compared to the more extreme δ_c selections with the same number of objects. This may be due to that fact that with the larger R_v selection, the stacked profile is effectively averaging over a larger scale on the CMB map, thus reducing the noise on the profile.

We measure the constraints on $A_{\rm ISW}$ for these selections in data. Focusing on the 10% and 50% of the superstructures with largest R_v, we find that the data measurements show an increased signal especially in density peaks, with $A_{\rm ISW} = 0.10 \pm 0.99, 0.57 \pm 0.71$ for voids and $A_{\rm ISW} = 1.47 \pm 0.77, 2.59 \pm 0.73$ for clusters. Limiting the sample to the 10% and 50% with the most extreme δ_c, we find that the data do not show significant boost in the ISW signal, and $A_{\rm ISW} = 0.15 \pm 1.24, 0.32 \pm 0.89$ for voids and $A_{\rm ISW} = 0.83 \pm 1.26, 0.25 \pm 0.89$ for clusters. Combining the voids and clusters in the δ_c selection, one finds $A_{\rm ISW} = 0.75 \pm 0.83, 0.58 \pm 0.59$ for the 10% and 50% of the total sample, which does not improve

the significance of the signal compared to the full sample. On the other hand, in the R_v case, $A_{\rm ISW} = 0.96 \pm 0.61, 1.55 \pm 0.51$. The constraints on R_v from the higher R_v subsamples and the full sample is statistically consistent with 0.3σ and 1.2σ for the 10% and 50% cases respectively. Therefore, by constraining on a larger R_v sample, it is statistically possible to obtain a larger mean ISW signal, leading to a more significant detection of the ISW amplitude $A_{\rm ISW}$. However, we emphasise that this selection is *a posteriori* and one should be careful in interpreting these results because of the *look-elsewhere effect*. This effect refers to that, by repeating certain measurements multiple times (or searching over a wide range of parameter space in the continuous case), the possibility of getting a higher signal due to random fluctuations also increases [180, 264]. The significance of an anomaly can be overestimated in this way which leads to biased conclusions. This effect can be accounted for using a number of simulations or analytically, e.g. [21].

6.6 Conclusions

In this Chapter we have constructed a catalogue of superstructures, using tomographic data with $0 < z < 0.8$ in the DESI Legacy Imaging Survey. We adopt the void finding algorithm described in [250], taking the lowest 10% and highest 5% pixels of the galaxy density field after 2D Gaussian smoothing with $\sigma = 20\,h^{-1}\,$Mpc. The aim has been to test the excess ISW signal from supervoids claimed in the literature [101, 146]. To compare our results with the ΛCDM model prediction, we constructed a mock catalogue using the *Multidark* simulation. The galaxy number density, linear, and non-linear galaxy biases are matched to those found in our previous work on the DESI Legacy Imaging Survey (Hang et al. 2021: H21), and we applied a redshift error to match the photo-z precision found in H21. The properties of the superstructures and the stacked galaxy density profiles around these superstructures are consistent between the mock and the data. We also created the corresponding lensing convergence and ISW maps.

We then looked at the stacked CMB lensing convergence and CMB temperature using the *Planck* 2018 maps at the centre of these superstructures, scaled by the void/cluster radius R_v. The comparison between the stacked lensing signal agrees well in the void case, but the cluster signal seems to be slightly over-predicted in the highest redshift bin. Using the covariance matrix from 1000 sets of randomised superstructure positions, we quantify the consistency between

simulation and data via the lensing amplitude A_κ, and find $A_\kappa = 0.81 \pm 0.06$ from combining the voids and clusters. This is largely driven by the highest redshift bin, which contains the most clusters. In H21, we favoured a lensing amplitude of $A_\kappa = 0.90 \pm 0.03$ compared to the theoretical prediction from the *Planck* 2018 best-fit cosmology, using cross-correlation in spherical harmonic space (therefore essentially utilising all pixels, rather than density peaks and troughs). This lower amplitude of the CMB lensing signal is consistent with our result from superstructures, although we note that the voids and clusters are in 1.9σ tension, with $A_\kappa = 0.937 \pm 0.087$ for all voids and $A_\kappa = 0.712 \pm 0.076$ for all clusters. Despite this, the level of disagreement between our mocks and data for the lensing signal is negligibly small for the purpose of ISW study, as its measurement is much noisier.

The stacked ISW signals are in general consistent with simulation results – but also with a null signal, reflecting the low signal-to-noise of the ISW effect. Specifically, we do not detect a significant signal from the void catalogue, and only a marginal signal from clusters. Combining the superstructures, we find the ISW amplitude to be $A_{\rm ISW} = 0.68 \pm 0.50$, somewhat weaker than the cross-correlation result from H21 which gave $A_{\rm ISW} = 1.10 \pm 0.31$ (although both measurements are consistent). Therefore, we do not claim a detected ISW signal using this sample.

We compare our results with K19, [146], who reported a 3σ excess of ISW signal compared to ΛCDM prediction from supervoids with void radius $R_v > 100\,h^{-1}\,$Mpc, using the DES redMaGiC sample within similar redshift range. Using our fiducial settings described above, we do not find any excess signal from voids with the same size cut, or within the same survey mask. Two subsamples are then constructed to match the redshift binning and void finding procedure in K19 as closely as possible within the DES footprint, with and without a redMaGiC-like colour selection. The stacked ISW profiles from the voids found in these samples also do not show any anomalous signal.

Lastly, we look at the dependence of the ISW signal on the void properties and discuss whether this can be used to explain a higher detection of the ISW signal from suitably chosen superstructures. We show that the mean ISW signal from the mock dataset is amplified by excluding smaller or less extreme superstructures, while the shot noise increases. Applying the same selections to the data, we find no significant improvement in the constraint on the ISW amplitude $A_{\rm ISW}$ from more extreme superstructures, although there is a boost in $A_{\rm ISW}$ from density peaks with larger R_v. The most extreme subset conditioning on

the largest R_v gives $A_{\rm ISW} = 0.96 \pm 0.61$, and the 95% upper limit is 2.16. However, we emphasise that the selection of the subset is not *a priori*. The increase in the signal is likely overestimated due to random statistical fluctuations, or the look-elsewhere effect.

In summary, then, our results from investigating the impact of superstructures on the CMB do not reveal any compelling discrepancy with ΛCDM. The CMB lensing results for superstructures independently favour an approximately 10% reduction in amplitude relative to the *Planck* 2018 prediction, in very close agreement with our conclusion from the overall galaxy-lensing cross-correlation in H21, which we argued favoured a matter density at the low end of the range permitted by *Planck*. The evidence for this reduced lensing amplitude is present in both voids and clusters although the latter favour a stronger signal at the 1.9σ level; it will be interesting to see if this tension becomes more significant in future datasets. Similarly, the ISW signal from stacked superstructures is consistent with the H21 cross-correlation result, and not in significant disagreement with ΛCDM. Formally, the 95% confidence upper limit on $A_{\rm ISW}$ from superstructures is 1.51, and therefore we do not reproduce literature claims of anomalous superstructure ISW signals at several times the ΛCDM prediction. We have tried to vary our analysis in order to mimic more closely the selection involved in these claims, but have not succeeded in raising the ISW signal. Presumably some small differences in method remain. But the important point is that any such excess is apparently not robust, since we were not able to produce an excess signal even by exploring a number of alternative forms of superstructure selection.

Chapter 7

Closing Remarks

Over the last few decades, a cosmological concordance has been established by observations of the CMB and the spatial distribution of galaxies. However, our ignorance of the nature of dark matter and dark energy, which comprise 95% of the Universe, is unsatisfying. Various models of dark energy and modifications to General Relativity have been postulated in order to solve this mystery. The growth and evolution of large-scale structures, as the result of the competition between gravity and expansion caused by dark energy, is an excellent testing ground for possible deviations from the standard cosmological model. In this thesis, I have performed two such tests using redshift-space distortion and the correlation between CMB and large-scale structures. I will now briefly summarise the main results presented in this thesis, and provide an outlook for possible future works.

7.1 Summary

In Chapter 2, I measured RSD from the two-point cross-correlation between galaxies and groups using the GAMA survey. To reveal the dependence of the RSD signal on tracers, I split galaxies into red and blue subsamples, and groups into three stellar mass bins. The resultant 2D correlation functions show a clear trend in colour and group mass, as expected, especially at non-linear scales where the 'Fingers of God' dominates (Fig. 2.9). Applying a linear model with an appropriate minimum scale cut on the measurements, and testing against GAMA

mock catalogues, I measured a growth rate $f\sigma_8 = 0.25 \pm 0.15$, consistent across different subsamples and also with the *Planck* 2018 result (Fig. 2.15).

The imprints of galaxy clustering on the CMB is useful for constraining cosmological parameters such as the growth rate via CMB lensing, and the dark energy equation of state via the ISW effect. In Chapter 4, I used the public DESI Legacy Survey, which provides the deepest wide-area multicolour CCD imaging, to conduct angular cross-correlation for the above purposes. The challenge was to obtain robust photometric redshifts for the galaxies given limited photometric bands. I assigned photometric redshifts to over 70% of galaxies in the Legacy Survey using a 3D colour grid calibrated by spectroscopic galaxy samples, and separated the galaxy sample into four tomographic bins between $0 < z < 0.8$ (Fig. 4.6).

In Chapter 5 I measured the angular cross-correlation C_ℓ of galaxy densities with the Planck lensing convergence and temperature maps. To pin down the galaxy bias and photo-z parameters, I fitted the ten galaxy auto- and cross-correlations between the four redshift bins. The best-fit parameters are used in the CMB cross-correlation analysis, and I tested that marginalisation over the nuisance parameters do not have a significant effect on the constraints of the final lensing and ISW amplitudes. Interestingly, I discovered a low lensing amplitude $A_\kappa = 0.901 \pm 0.026$, more than 3σ below the fiducial value given by *Planck*. The result was translated to a constraint on the $\Omega_m - \sigma_8$ plane (Fig. 5.13), reinforcing the existing lensing tension with *Planck*. The result shows that the combined lensing data favours a lower density than *Planck*, rather than a reduced normalisation. I also reported a 2.8σ detection of the ISW signal with $A_{\rm ISW} = 0.98 \pm 0.35$.

In Chapter 6, I constructed a superstructure catalogue for the tomographic bins to measure the stacked signals from CMB lensing and temperature. The large survey area covered by the DESI Legacy Survey effectively reduces the impact of cosmic variance, and is ideal for the investigation of the 'excess ISW signal' from supervoids claimed by many in literature. I used a realistic mock catalogue with matched galaxy bias with data and its corresponding lensing convergence and ISW maps to compute the expected signal in the ΛCDM model. I measured a lensing amplitude $A_\kappa = 0.81 \pm 0.06$ (Fig. 6.8), consistent with that found in Chapter 5. The ISW amplitude is detected with mild statistical significance, $A_{\rm ISW} = 0.68 \pm 0.50$. However, it indicates no clear deviation from the ΛCDM prediction (Fig. 6.9), with a 95% upper limit of 1.51. By splitting

the superstructures into different subsamples, I found that the signal is boosted with a minimum size cut from superclusters. However, because this choice is *a posteriori*, the result can be overestimated due to the look-elsewhere effect.

7.2 Future outlooks

An extension to the work presented in Chapter 2 would be to push the RSD modelling into quasi-linear scales where the GAMA data has a higher signal-to-noise ratio. I plan to apply the streaming model with a separation of the 1- and 2-halo contributions. While a tighter constraint on $f\sigma_8$ may be obtained, the modelling can also reveal dependence of the 1-halo parameters on different group mass and galaxy types. At small scales, non-linear galaxy bias can be a complication. Recently, it is pointed out in [201] that, depending on the way the galaxy sample is split, anisotropic assembly bias can also affect quadruple moment.

The size and quality of the DESI Legacy Survey photo-z catalogue constructed in Chapter 4 permits a range of interesting further investigations. One possible extension of the current study can be to focus on different galaxy tracers in the DESI Legacy Survey, such as splitting by colour and luminosity. These subsamples will allow me to check that our results are robust with respect to e.g. the treatment of scale-dependent bias. The cross-correlation between different galaxy tracers can also improve our understanding of the assembly history of galaxies and halos via assembly bias [92, 312].

Another interesting extension is the cross-correlation between the tomographic density maps and the *Planck* CMB Compton-y maps via the thermal Sunyaev-Zel'dovich (tSZ) effect (e.g. [143]). The signal directly probes the total thermal energy of hot gas in clusters, haloes, and intergalactic medium, which can be modulated by processes such as radiative cooling and AGN feedback. The understanding of baryonic feedback is crucial for improving cosmological parameter constraints at non-linear scales. Strong stellar and AGN feedback can affect the matter power spectrum at scales up to $\sim 1\mathrm{Mpc}/h$, first demonstrated in [321] using hydrodynamic simulations. The hot gas ejected from AGN suppresses the power at these intermediate scales at the percent level. [262] further points out that such effects can bias weak lensing shear measurements due to redistribution of baryons. The current solution in the lensing community is to marginalise over

various baryonic effects, subsequently increasing the error budget. The study of baryonic effects through cross-correlation between tSZ and the galaxy field could potentially be a remedy.

In recent years, voids have become a competitive probe for cosmology and structure formation (e.g. [110, 192]) via RSD and the Alcock-Paczynski (AP) effect due to their enhanced linearity at small scales. Voids are also ideal laboratories to test deviations from the standard cosmological model, because their abundance and profile are sensitive to modified gravity, evolving dark energy [41], and neutrino mass [313]. The supervoid catalogue constructed in Chapter 6 can be used for statistical studies assisted with non-standard cosmological simulations. When combined with the split tracers as proposed above, it also has the potential to reveal void-galaxy connection and the dependence of galaxy properties on their environments.

Looking ahead, the field of observational cosmology is expecting a major leap with the scope of next-generation galaxy surveys and CMB experiments. Tests of structure growth mentioned in this thesis, RSD and galaxy-CMB cross-correlation, can be performed to unprecedented precision. With the enhanced signal-to-noise, these experiments will push parameter constraints to percent or sub-percent level so that different cosmological models can be distinguished. For example, DESI [60, 175], which has recently started its 1% survey, is designed to significantly advance the BAO and RSD measurements. Covering a vast sky area of 14,000 deg^2, DESI will take spectra for over 30 million galaxies and quasars out to $z \sim 3.5$. This dataset is expected to improve constraints on the growth rate by a factor of 4-10 compared to previous results [89] (see also Fig. 7.1). The combination of different probes and across different datasets can lead to even stronger constraints [129]. In particular, DESI contains a dedicated high density galaxy sample, the Bright Galaxy Sample (BGS), at $z < 0.4$. This sample, similar to the GAMA survey but much larger in area, is ideal for RSD analysis with groups and galaxies as mentioned in Chapter 2 with significantly improved statistical power.

The space-based Euclid mission [158], expected to be launched in late 2022, will provide a great leap forward in weak lensing cosmology, another major test for gravity. Equipped with multi-band photometry and excellent imager, Euclid will scan a sky area of 15,000 deg^2, delivering exquisite shape measurements of 30 galaxies per arcmin^2 to as far as $z \sim 2$. Compared to ground-based surveys, Euclid does not suffer from systematics caused by the Earth's atmosphere, and is

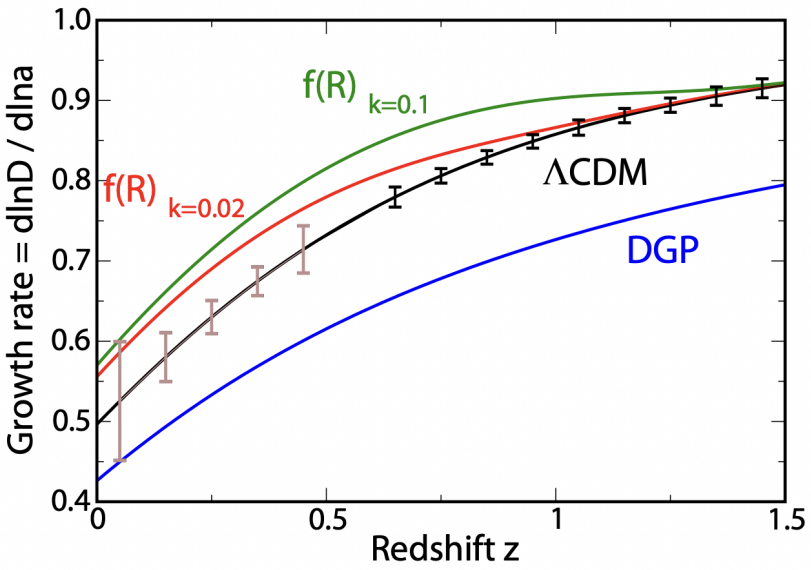

Figure 7.1 *The forecast of growth rate measurements from DESI as a function of redshift. The light pink error bars are from the Bright Galaxy Sample (BGS) at $z < 0.4$. The ΛCDM model is plotted in black solid line, and the coloured lines show two $f(R)$ modified gravity models [167] and the Dvali-Gabadadze-Porrati (DGP) braneworld model [71]. The $f(R)$ models are scale-dependent, and two cases with $k = 0.02\,h\,\mathrm{Mpc}^{-1}$ and $k = 0.1\,h\,\mathrm{Mpc}^{-1}$ are shown. These theories can be distinguished given the forecasted error bar. The plot is adopted from Huterer et al. [129].*

able to extend the measurable wavelength to near infrared. This permits precise systematic control and photo-z calibration, essential for interpreting the lensing signal. Euclid will determine the dark energy equation of state to 1% and improve the growth rate measurement by a factor of 30 compared to current results.

The Legacy Survey of Space and Time (LSST) [151] at the Vera C. Rubin Observatory will bring the size of cosmological surveys to the next level. Starting around 2022-2023, LSST will chart almost the entire sky with 30,000 deg^2, observing $\sim$ 10 billion stars and galaxies and generating petabytes of data during its 10-year operation. In addition to a boost in statistical power, hundreds of repeated visits in the main survey area of LSST allow fine control of systematics and null tests, making it suitable for a wide range of scientific purposes.

We also expect major advances in CMB observations in the near future. For example, CMB Stage 4[1] is a set of ground-based experiments that consists of 21 telescopes at the South Pole and in the Chilean Atacama desert, targeting at wide area and high resolution CMB observations. With an order of magnitude increase in the number of detectors, the sensitivity and depth of these experiments will not only greatly improve the current constraints, but also permit a test of inflationary theories. The cross-correlation analysis with large-scale structures similar to Chapter 5 will greatly benefit from these upgraded CMB maps, as the constraints on the lensing amplitude A_κ is limited by the current CMB resolution.

In light of these high precision surveys, I believe that it is a particular exciting time for cosmology. One should be prepared to embrace one of the two possible outcomes: either the discrepancy persists, thus pointing to strong evidence for new physics, or it vanishes due to a better knowledge of systematic errors, hereby proving another triumph for General Relativity and the ΛCDM model. In any case, unbiased interpretation of these measurements are vital – non-linear effects and unaccounted systematics may easily shift the parameter constraint at percent or sub-percent level. Therefore, it will also be a flourishing time for novel cosmological probes and theoretical efforts.

Finally, tests for fundamental theories of physics, i.e. General Relativity and the Standard Model of particle physics, upon which cosmology stands, are also carried out extensively in other branches of physics. For example, since its first detection in 2016, the LIGO/Virgo Collaboration now has a collection of 50 gravitational wave events. Moreover, in 2020, they found a $2.6M_\odot$ object lying in the 'mass gap'

[1] `https://cmb-s4.org/`

between a neutron star and black hole [3], posing challenges to the current model for the formation and mass distribution of coalescing compact binaries. Not long after the breathtaking photo of the supermassive black hole at the centre of M87 taken by the Event Horizon Telescope (EHT) [79], earlier this year, the light polarisation was also detected around this black hole, revealing signatures of a magnetic field [80, 81]. The consistency of observation and modelling shows a great triumph for General Relativity tested in the strong field regime. Outside the field of astronomy, the Large Hadron Collider (LHC) has reported a mild violation of lepton universality in the beauty-quark decays at 3.1σ level [150] earlier this year. Several weeks before the completion of this thesis, the Muon $g-2$ experiment at Fermilab revealed a 4.2σ tension in the measured muon magnetic anomaly in combination with a previous experiment [4]. These results, although still tentative by the standard of particle physics, could shake the foundation of the Standard Model. Therefore, it may well be the case that a breakthrough in cosmology can come unexpectedly from outside of its realm, and vice versa. In my opinion, with great advance in theory and technology, the future is bright for cosmology.

Appendix A

Matching redMaGiC colour selection

In order to match the DESY1A1 redMaGiC galaxies as closely as possible, we compare their distribution in colour-colour space with a subsample of DECaLS galaxies in the same region (Fig. A.1). We apply cuts in the $g - r$ versus $r - z$ plane based on the ratio of the normalized distribution. We exclude regions in this space where the ratio is smaller than a threshold set to 0.5. Such a exclusion does not affect the redMaGiC sample (about 92% of our objects remain), but it results in a cut in low-redshift DECALS galaxies. The selected DECALS sample contains 1.8 million galaxies, about 3 times the redMaGiC sample. Fig. A.2 shows the selected region in the colour-colour plane for our full sample used in Section 6.5.3 in the redshift range $0.2 < z < 0.8$ in the north and south part of the DESI Legacy Survey.

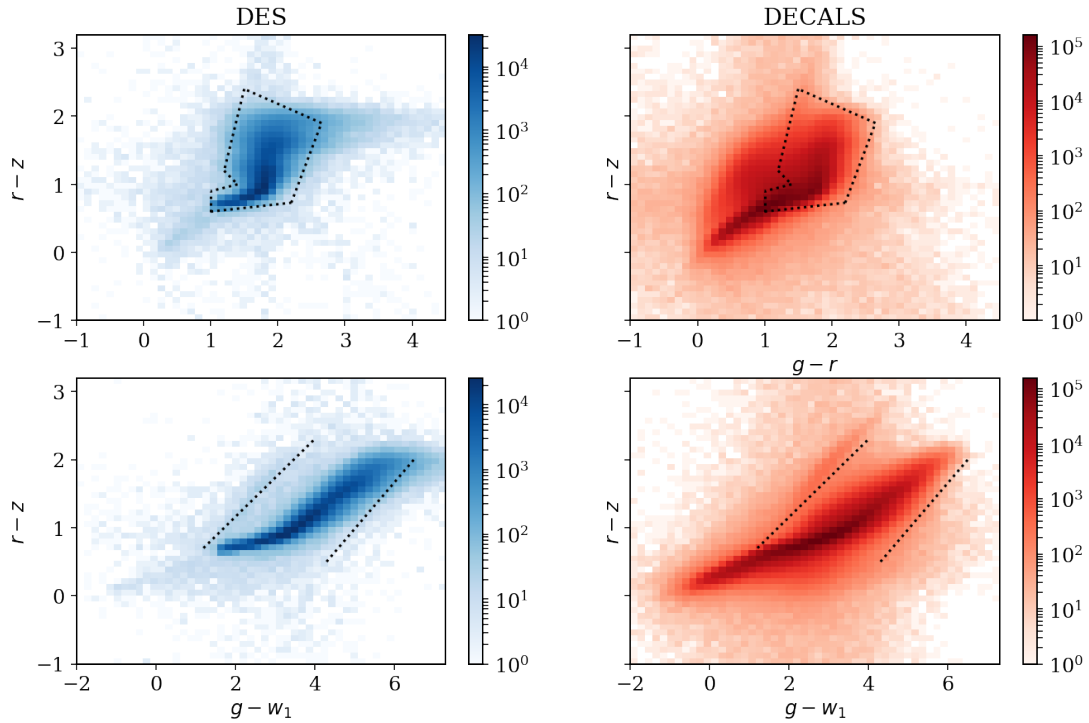

Figure A.1 *The comparison of redMaGiC (left, blue) and DECALS (right, red) samples in the same sky area in $g-r$ and $r-z$ plane (upper panel), and in $g-w_1$ and $r-z$ plane (lower panel). DECALS contains a large number of bluer objects compared to redMaGiC. The thin strip on the left side of the main sequence is likely to be residual stars. The black dotted box is the region used to take ratios.*

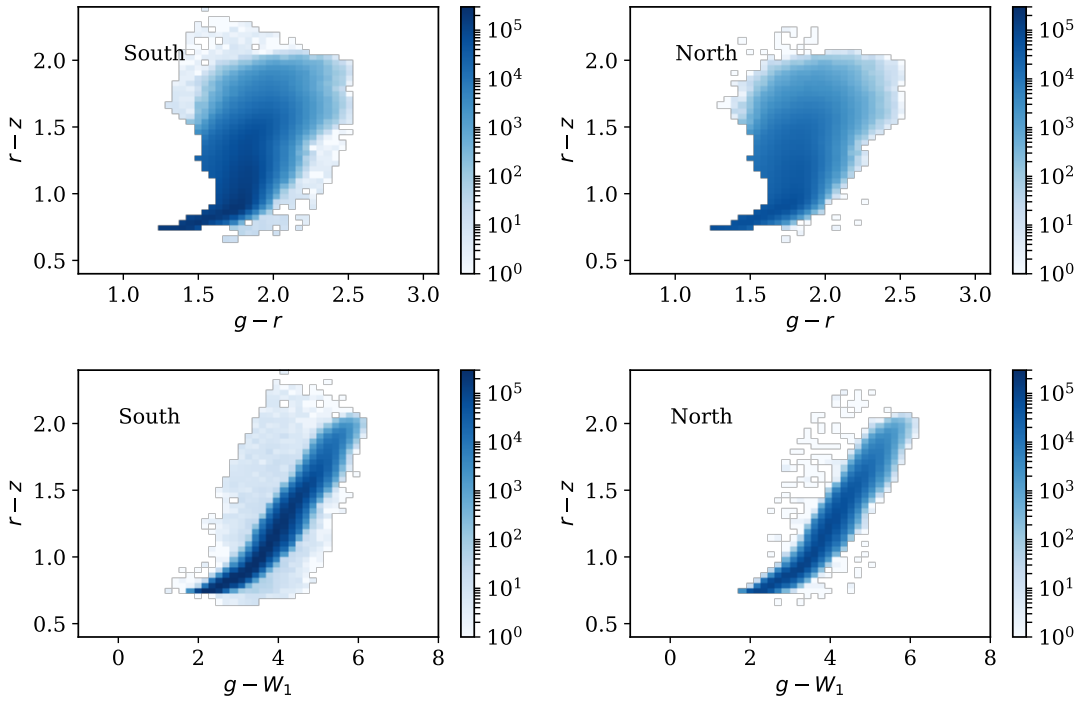

Figure A.2 *The selection in $g-r$ vs $r-z$ and $g-W_1$ vs $r-z$ colour space for the DESI Legacy Survey galaxy sample in the north and south regions respectively to match the DESY1A1 redMaGiC sample.*

Bibliography

[1] Abbott B. P., et al., 2017, Nature, 551, 85

[2] Abbott T. M. C., et al., 2020a, Phys. Rev. D, 102, 023509

[3] Abbott R., et al., 2020b, The Astrophysical Journal, 896, L44

[4] Abi B., et al., 2021, Physical Review Letters, 126

[5] Afshordi N., 2004, Phys. Rev. D, 70, 083536

[6] Ahumada R., et al., 2020, ApJS, 249, 3

[7] Aiola S., et al., 2020, arXiv e-prints, p. arXiv:2007.07288

[8] Alam S., et al., 2015, ApJS, 219, 12

[9] Alam S., et al., 2017, MNRAS, 470, 2617

[10] Allen S. W., Evrard A. E., Mantz A. B., 2011, ARA&A, 49, 409

[11] Almosallam I. A., Jarvis M. J., Roberts S. J., 2016, MNRAS, 462, 726

[12] Anderson L., et al., 2014, Monthly Notices of the Royal Astronomical Society, 441, 24–62

[13] Ansarinejad B., Mackenzie R., Shanks T., Metcalfe N., 2020, MNRAS, 493, 4830

[14] Arnouts S., Cristiani S., Moscardini L., Matarrese S., Lucchin F., Fontana A., Giallongo E., 1999, MNRAS, 310, 540

[15] Asgari M., et al., 2021, A&A, 645, A104

[16] Aubourg E., et al., 2015, Physical Review D, 92

[17] Bahcall N. A., Fan X., 1998, ApJ, 504, 1

[18] Barlow R., 2003, arXiv e-prints, p. physics/0306138

[19] Bartelmann M., Schneider P., 2001, Phys. Rep., 340, 291

[20] Basilakos S., Pouri A., 2012, MNRAS, 423, 3761

[21] Bayer A. E., Seljak U., 2020, J. Cosmology Astropart. Phys., 2020, 009

[22] Beck R., Csabai I., Rácz G., Szapudi I., 2018, MNRAS, 479, 3582

[23] Behroozi P. S., Wechsler R. H., Wu H.-Y., 2013, ApJ, 762, 109

[24] Benítez N., 2000, ApJ, 536, 571

[25] Bernal J. L., Peacock J. A., 2018, J. Cosmology Astropart. Phys., 2018, 002

[26] Bertacca D., Maartens R., Raccanelli A., Clarkson C., 2012, J. Cosmology Astropart. Phys., 2012, 025

[27] Beutler F., Dio E. D., 2020, Journal of Cosmology and Astroparticle Physics, 2020, 048–048

[28] Bianchi D., Chiesa M., Guzzo L., 2015, MNRAS, 446, 75

[29] Birrer S., et al., 2019, MNRAS, 484, 4726

[30] Blake C., et al., 2011, MNRAS, 415, 2876

[31] Blake C., et al., 2013, MNRAS, 436, 3089

[32] Bond J. R., et al., 1991, ApJ, 379, 440

[33] Bond J. R., Kofman L., Pogosyan D., 1996, Nature, 380, 603

[34] Bonnett C., et al., 2016, Phys. Rev. D, 94, 042005

[35] Bonvin C., Hui L., Gaztañaga E., 2014, Phys. Rev. D, 89, 083535

[36] Brammer G. B., van Dokkum P. G., Coppi P., 2008, ApJ, 686, 1503

[37] Brooks S. P., Gelman A., 1998, Journal of computational and graphical statistics, 7, 434

[38] Cai Y.-C., Cole S., Jenkins A., Frenk C., 2009, MNRAS, 396, 772

[39] Cai Y.-C., Cole S., Jenkins A., Frenk C. S., 2010, MNRAS, 407, 201

[40] Cai Y.-C., Neyrinck M. C., Szapudi I., Cole S., Frenk C. S., 2014, ApJ, 786, 110

[41] Cai Y.-C., Padilla N., Li B., 2015, MNRAS, 451, 1036

[42] Cai Y.-C., Neyrinck M., Mao Q., Peacock J. A., Szapudi I., Berlind A. A., 2017, MNRAS, 466, 3364

[43] Carbone C., Petkova M., Dolag K., 2016, J. Cosmology Astropart. Phys., 2016, 034

[44] Carrasco Kind M., Brunner R. J., 2013, MNRAS, 432, 1483

[45] Castorina E., White M., 2018, MNRAS, 476, 4403

[46] Cavuoti S., Amaro V., Brescia M., Vellucci C., Tortora C., Longo G., 2017, MNRAS, 465, 1959

[47] Cawthon R., et al., 2018, MNRAS, 481, 2427

[48] Chen H.-Y., Fishbach M., Holz D. E., 2018, Nature, 562, 545

[49] Choquet-Bruhat Y., 2014, Introduction to General Relativity, Black Holes, and Cosmology. Oxford University Press

[50] Clampitt J., Cai Y.-C., Li B., 2013, MNRAS, 431, 749

[51] Clifton T., Ferreira P. G., Padilla A., Skordis C., 2012, Phys. Rep., 513, 1

[52] Cole S., 2011, MNRAS, 416, 739

[53] Cole S., Kaiser N., 1989, MNRAS, 237, 1127

[54] Cole S., Fisher K. B., Weinberg D. H., 1994, MNRAS, 267, 785

[55] Coles P., Jones B., 1991, MNRAS, 248, 1

[56] Colombi S., 1994, ApJ, 435, 536

[57] Cooray A., 2002, Phys. Rev. D, 65, 083518

[58] Cooray A., Sheth R., 2002, Elsevier, 372, 1

[59] Crittenden R. G., Turok N., 1996, Phys. Rev. Lett., 76, 575

[60] DESI Collaboration et al., 2016, The DESI Experiment Part I: Science,Targeting, and Survey Design (`arXiv:1611.00036`)

[61] Darwish O., et al., 2020a, arXiv e-prints, p. arXiv:2004.01139

[62] Darwish O., et al., 2020b, arXiv e-prints, p. arXiv:2004.01139

[63] Davis M., Peebles P. J. E., 1983, ApJ, 267, 465

[64] Dawson K., et al., 2015, The Astronomical Journal, 151

[65] Dekel A., Lahav O., 1999, ApJ, 520, 24

[66] Desjacques V., Jeong D., Schmidt F., 2018, Phys. Rep., 733, 1

[67] Dey A., et al., 2016, in Ground-based and Airborne Instrumentation for Astronomy VI. p. 99082C, doi:10.1117/12.2231488

[68] Dey A., et al., 2019, AJ, 157, 168

[69] Doux C., Penna-Lima M., Vitenti S. D. P., Tréguer J., Aubourg E., Ganga K., 2018, MNRAS, 480, 5386

[70] Driver S. P., et al., 2009, Astronomy and Geophysics, 50, 5.12

[71] Dvali G., Gabadadze G., Porrati M., 2000, Physics Letters B, 485, 208

[72] Efstathiou G., 2020, arXiv e-prints, p. arXiv:2007.10716

[73] Efstathiou G., Bond J. R., 1999, MNRAS, 304, 75

[74] Efstathiou G., Gratton S., 2019, arXiv e-prints, p. arXiv:1910.00483

[75] Eisenstein D. J., et al., 2005, ApJ, 633, 560

[76] Eisenstein D. J., Seo H.-J., Sirko E., Spergel D. N., 2007, ApJ, 664, 675

[77] Epstein R., 1983, MNRAS, 205, 207

[78] Escoffier S., et al., 2016, preprint, (arXiv:1606.00233)

[79] Event Horizon Telescope Collaboration et al., 2019, ApJ, 875, L1

[80] Event Horizon Telescope Collaboration et al., 2021a, ApJ, 910, L12

[81] Event Horizon Telescope Collaboration et al., 2021b, ApJ, 910, L13

[82] Farrow D. J., et al., 2015, MNRAS, 454, 2120

[83] Feng J. L., 2010, ARA&A, 48, 495

[84] Ferreira P. G., Skordis C., 2010, Phys. Rev. D, 81, 104020

[85] Fisher K. B., 1995, ApJ, 448, 494

[86] Fisher K. B., Scharf C. A., Lahav O., 1994, MNRAS, 266, 219

[87] Flaugher B., et al., 2015, AJ, 150, 150

[88] Folatelli G., et al., 2010, AJ, 139, 120

[89] Font-Ribera A., McDonald P., Mostek N., Reid B. A., Seo H.-J., Slosar A., 2014, Journal of Cosmology and Astroparticle Physics, 2014, 023–023

[90] Friedrich O., Seitz S., Eifler T. F., Gruen D., 2016, MNRAS, 456, 2662

[91] Fukushige T., Makino J., 2001, ApJ, 557, 532

[92] Gao L., White S. D. M., 2007, MNRAS, 377, L5

[93] Giannantonio T., Scranton R., Crittenden R. G., Nichol R. C., Boughn S. P., Myers A. D., Richards G. T., 2008, Phys. Rev. D, 77, 123520

[94] Giannantonio T., et al., 2016, MNRAS, 456, 3213

[95] Giblin B., et al., 2021, A&A, 645, A105

[96] Gil-Marín H., Noreña J., Verde L., Percival W. J., Wagner C., Manera M., Schneider D. P., 2015, MNRAS, 451, 539

[97] Gonzalez-Perez V., Lacey C. G., Baugh C. M., Lagos C. D. P., Helly J., Campbell D. J. R., Mitchell P. D., 2014, MNRAS, 439, 264

[98] Górski K. M., Hivon E., Banday A. J., Wand elt B. D., Hansen F. K., Reinecke M., Bartelmann M., 2005, ApJ, 622, 759

[99] Graff P., Feroz F., Hobson M. P., Lasenby A., 2014, MNRAS, 441, 1741

[100] Graham M. L., Connolly A. J., Ivezić Ž., Schmidt S. J., Jones R. L., Jurić M., Daniel S. F., Yoachim P., 2018, AJ, 155, 1

[101] Granett B. R., Neyrinck M. C., Szapudi I., 2008, ApJ, 683, L99

[102] Gross M. A. K., Somerville R. S., Primack J. R., Holtzman J., Klypin A., 1998, MNRAS, 301, 81

[103] Gunn J. E., Gott J. R. I., 1972, ApJ, 176, 1

[104] Guo H., Zehavi I., Zheng Z., 2012, ApJ, 756, 127

[105] Guo Q., White S., Angulo R. E., Henriques B., Lemson G., Boylan-Kolchin M., Thomas P., Short C., 2013, MNRAS, 428, 1351

[106] Guo H., et al., 2014, MNRAS, 441, 2398

[107] Guzzo L., et al., 2008, Nature, 451, 541

[108] Hamana T., et al., 2020, PASJ, 72, 16

[109] Hamaus N., Seljak U., Desjacques V., 2012, Phys. Rev. D, 86, 103513

[110] Hamaus N., Pisani A., Choi J.-A., Lavaux G., Wandelt B. D., Weller J., 2020, J. Cosmology Astropart. Phys., 2020, 023

[111] Hamilton A. J. S., 1992, ApJ, 385, L5

[112] Hamuy M., Phillips M. M., Suntzeff N. B., Schommer R. A., Maza J., Aviles R., 1996, AJ, 112, 2391

[113] Han J., et al., 2015, MNRAS, 446, 1356

[114] Hang Q., Alam S., Peacock J. A., Cai Y.-C., 2021, MNRAS, 501, 1481

[115] Harrison E. R., 1970, Phys. Rev. D, 1, 2726

[116] Hartlap J., Simon P., Schneider P., 2007, A&A, 464, 399

[117] Hawkins E., et al., 2003, MNRAS, 346, 78

[118] Hikage C., 2014, MNRAS, 441, L21

[119] Hikage C., et al., 2019, PASJ, 71, 43

[120] Hildebrandt H., et al., 2010, A&A, 523, A31

[121] Hildebrandt H., et al., 2017, MNRAS, 465, 1454

[122] Hildebrandt H., et al., 2020, A&A, 633, A69

[123] Hinshaw G., et al., 2013, ApJS, 208, 19

[124] Ho S., Hirata C., Padmanabhan N., Seljak U., Bahcall N., 2008, Phys. Rev. D, 78, 043519

[125] Hu W., 2000, Phys. Rev. D, 62, 043007

[126] Hu W., Dodelson S., 2002, ARA&A, 40, 171

[127] Hu W., Sugiyama N., 1995, ApJ, 444, 489

[128] Hubble E., 1929, Proceedings of the National Academy of Science, 15, 168

[129] Huterer D., et al., 2015, Astroparticle Physics, 63, 23

[130] Ilbert O., et al., 2009, ApJ, 690, 1236

[131] Jackson J. C., 1972, MNRAS, 156, 1P

[132] Jenkins A., Frenk C. S., White S. D. M., Colberg J. M., Cole S., Evrard A. E., Couchman H. M. P., Yoshida N., 2001, MNRAS, 321, 372

[133] Jennings E., Baugh C. M., Pascoli S., 2011, MNRAS, 410, 2081

[134] Joudaki S., et al., 2020, A&A, 638, L1

[135] Juszkiewicz R., Springel V., Durrer R., 1999, APJL, 518, L25

[136] Kaiser N., 1984, ApJ, 284, L9

[137] Kaiser N., 1987, MNRAS, 227, 1

[138] Kaiser N., 1992, ApJ, 388, 272

[139] Kilbinger M., et al., 2013, MNRAS, 430, 2200

[140] Kitanidis E., White M., 2021, MNRAS, 501, 6181

[141] Kitanidis E., et al., 2020, MNRAS, 496, 2262

[142] Klypin A., Yepes G., Gottlöber S., Prada F., Heß S., 2016, MNRAS, 457, 4340

[143] Koukoufilippas N., Alonso D., Bilicki M., Peacock J. A., 2020, MNRAS, 491, 5464

[144] Kovács A., 2018, MNRAS, 475, 1777

[145] Kovács A., et al., 2017, MNRAS, 465, 4166

[146] Kovács A., et al., 2019, MNRAS, 484, 5267

[147] Kraljic K., et al., 2018, MNRAS, 474, 547

[148] Kravtsov A. V., Klypin A. A., 1999, ApJ, 520, 437

[149] Krolewski A., Ferraro S., Schlafly E. F., White M., 2020, J. Cosmology Astropart. Phys., 2020, 047

[150] LHCb collaboration et al., 2021, Test of lepton universality in beauty-quark decays (arXiv:2103.11769)

[151] LSST Dark Energy Science Collaboration 2012, Large Synoptic Survey Telescope: Dark Energy Science Collaboration (arXiv:1211.0310)

[152] Lahav O., Lilje P. B., Primack J. R., Rees M. J., 1991, MNRAS, 251, 128

[153] Laigle C., et al., 2016, ApJS, 224, 24

[154] Lam T. Y., Schmidt F., Nishimichi T., Takada M., 2013, Phys. Rev. D, 88, 023012

[155] Lamoreaux S. K., 1997, Phys. Rev. Lett., 78, 5

[156] Landy S. D., Szalay A. S., 1993, ApJ, 412, 65

[157] Lang D., Hogg D. W., Mykytyn D., 2016, The Tractor: Probabilistic astronomical source detection and measurement (ascl:1604.008)

[158] Laureijs R., et al., 2011, Euclid Definition Study Report (arXiv:1110.3193)

[159] Lee J., Shandarin S. F., 1999, ApJ, 517, L5

[160] Leistedt B., Hogg D. W., 2017, ApJ, 838, 5

[161] Lemson G., Virgo Consortium t., 2006, arXiv e-prints, pp astro–ph/0608019

[162] Lewis A., Bridle S., 2002, Phys. Rev. D, 66, 103511

[163] Lewis A., Challinor A., Lasenby A., 2000, ApJ, 538, 473

[164] Lilje P. B., Efstathiou G., 1989, MNRAS, 236, 851

[165] Limber D. N., 1953, ApJ, 117, 134

[166] Lin Y.-T., Mohr J. J., 2004, ApJ, 617, 879

[167] Linder E. V., 2009, Phys. Rev. D, 80, 123528

[168] Liske J., et al., 2015, MNRAS, 452, 2087

[169] Loveday J., et al., 2012, MNRAS, 420, 1239

[170] Loveday J., et al., 2018, MNRAS, 474, 3435

[171] Ma C.-P., Bertschinger E., 1995, The Astrophysical Journal, 455, 7

[172] Malavasi N., et al., 2017, MNRAS, 465, 3817

[173] Malz A. I., Hogg D. W., 2020, arXiv e-prints, p. arXiv:2007.12178

[174] Martel H., Shapiro P. R., Weinberg S., 1998, ApJ, 492, 29

[175] Martini P., et al., 2018, in Evans C. J., Simard L., Takami H., eds, Society of Photo-Optical Instrumentation Engineers (SPIE) Conference Series Vol. 10702, Ground-based and Airborne Instrumentation for Astronomy VII. p. 107021F (arXiv:1807.09287), doi:10.1117/12.2313063

[176] Matsubara T., 2000, ApJ, 535, 1

[177] McDonald P., Seljak U., 2009, J. Cosmology Astropart. Phys., 10, 007

[178] McGill C., 1990, MNRAS, 242, 428

[179] Merson A. I., et al., 2013, MNRAS, 429, 556

[180] Miller R. G., 1966, Simultaneous statistical inference [by] Rupert G. Miller, Jr. McGraw-Hill New York

[181] Miller R. G., 1974, Biometrika, 61, 1

[182] Mo H. J., White S. D. M., 1996, MNRAS, 282, 347

[183] Mo H. J., Jing Y. P., Borner G., 1997, MNRAS, 286, 979

[184] Mohammad F. G., et al., 2016, MNRAS, 458, 1948

[185] Mohammad F. G., et al., 2018, A&A, 610, A59

[186] Monaco P., 1995, ApJ, 447, 23

[187] Mörtsell E., Dhawan S., 2018, J. Cosmology Astropart. Phys., 2018, 025

[188] Mukhanov V., 2005, Physical Foundations of Cosmology. Cambridge University Press, Oxford

[189] Mukhanov V. F., Feldman H. A., Brandenberger R. H., 1992, Phys. Rep., 215, 203

[190] Nadathur S., Crittenden R., 2016, ApJ, 830, L19

[191] Nadathur S., Hotchkiss S., Sarkar S., 2012, J. Cosmology Astropart. Phys., 2012, 042

[192] Nadathur S., Carter P. M., Percival W. J., Winther H. A., Bautista J. E., 2019, Phys. Rev. D, 100, 023504

[193] Navarro J. F., Frenk C. S., White S. D. M., 1997, ApJ, 490, 493

[194] Navarro J. F., et al., 2004, MNRAS, 349, 1039

[195] Navarro J. F., et al., 2010, MNRAS, 402, 21

[196] Newman J. A., et al., 2013, ApJS, 208, 5

[197] Neyrinck M. C., 2008, MNRAS, 386, 2101

[198] Nishizawa A. J., 2014, Progress of Theoretical and Experimental Physics, 2014, 06B110

[199] Nock K., Percival W. J., Ross A. J., 2010, MNRAS, 407, 520

[200] Norberg P., Baugh C. M., Gaztañaga E., Croton D. J., 2009, MNRAS, 396, 19

[201] Obuljen A., Percival W. J., Dalal N., 2020, Journal of Cosmology and Astroparticle Physics, 2020, 058–058

[202] Padilla N. D., Merchán M. E., Valotto C. A., Lambas D. G., Maia M. A. G., 2001, ApJ, 554, 873

[203] Padmanabhan N., Xu X., Eisenstein D. J., Scalzo R., Cuesta A. J., Mehta K. T., Kazin E., 2012, MNRAS, 427, 2132

[204] Peacock J., 2003, Cosmological Physics, 5 edn. Cambridge University Press

[205] Peacock J. A., 2007, MNRAS, 379, 1067

[206] Peacock J. A., 2016, in van de Weygaert R., Shandarin S., Saar E., Einasto J., eds, IAU Symposium Vol. 308, The Zeldovich Universe: Genesis and Growth of the Cosmic Web. pp 125–142, doi:10.1017/S1743921316009741

[207] Peacock J. A., Bilicki M., 2018, MNRAS, 481, 1133

[208] Peacock J. A., Dodds S. J., 1994, MNRAS, 267, 1020

[209] Peacock J. A., Heavens A. F., 1990, MNRAS, 243, 133

[210] Peacock J. A., Smith R. E., 2000, MNRAS, 318, 1144

[211] Peacock J. A., et al., 2001, Nature, 410, 169

[212] Peccei R., Quinn H., 1977, Physical Review Letters - PHYS REV LETT, 38, 1440

[213] Peebles P. J. E., 1967, ApJ, 147, 859

[214] Peebles P. J. E., 1980, The large-scale structure of the universe

[215] Peebles P. J. E., Yu J. T., 1970, ApJ, 162, 815

[216] Penzias A. A., Wilson R. W., 1965, ApJ, 142, 419

[217] Percival W. J., et al., 2002, MNRAS, 337, 1068

[218] Percival W. J., Cole S., Eisenstein D. J., Nichol R. C., Peacock J. A., Pope A. C., Szalay A. S., 2007, MNRAS, 381, 1053

[219] Perlmutter S., et al., 1999, ApJ, 517, 565

[220] Phillips M. M., 1993, ApJ, 413, L105

[221] Phillips M. M., Wells L. A., Suntzeff N. B., Hamuy M., Leibundgut B., Kirshner R. P., Foltz C. B., 1992, AJ, 103, 1632

[222] Pietrzyński G., et al., 2013, Nature, 495, 76

[223] Planck Collaboration 2014, A&A, 571, A17

[224] Planck Collaboration et al., 2016a, A&A, 594, A15

[225] Planck Collaboration et al., 2016b, A&A, 594, A21

[226] Planck Collaboration et al., 2020a, A&A, 641, A1

[227] Planck Collaboration et al., 2020b, A&A, 641, A6

[228] Planck Collaboration et al., 2020c, A&A, 641, A8

[229] Pollina G., Hamaus N., Dolag K., Weller J., Baldi M., Moscardini L., 2017, MNRAS, 469, 787

[230] Pope A. C., Szapudi I., 2008, MNRAS, 389, 766

[231] Prada F., Klypin A. A., Cuesta A. J., Betancort-Rijo J. E., Primack J., 2012, MNRAS, 423, 3018

[232] Press W., Schechter P., 1974, ApJ, 187, 425

[233] Raccanelli A., Samushia L., Percival W. J., 2010, MNRAS, 409, 1525

[234] Rácz G., Dobos L., Beck R., Szapudi I., Csabai I., 2017, MNRAS, 469, L1

[235] Rau M. M., Seitz S., Brimioulle F., Frank E., Friedrich O., Gruen D., Hoyle B., 2015, MNRAS, 452, 3710

[236] Raveri M., Hu W., 2019, Phys. Rev. D, 99, 043506

[237] Reid B. A., White M., 2011, MNRAS, 417, 1913

[238] Reid B. A., et al., 2012, MNRAS, 426, 2719

[239] Renk J., Zumalacárregui M., Montanari F., Barreira A., 2017, J. Cosmology Astropart. Phys., 2017, 020

[240] Riebe K., et al., 2013, Astronomische Nachrichten, 334, 691

[241] Riess A. G., Press W. H., Kirshner R. P., 1995, ApJ, 438, L17

[242] Riess A. G., et al., 1998, AJ, 116, 1009

[243] Riess A. G., et al., 2016, The Astrophysical Journal, 826, 56

[244] Riess A. G., Casertano S., Yuan W., Macri L. M., Scolnic D., 2019, ApJ, 876, 85

[245] Robotham A. S. G., et al., 2011, MNRAS, 416, 2640

[246] Rubin V. C., Ford W. K. J., Thonnard N., 1978, ApJ, 225, L107

[247] Sadeh I., Abdalla F. B., Lahav O., 2016, PASP, 128, 104502

[248] Samushia L., et al., 2013, MNRAS, 429, 1514

[249] Sánchez C., et al., 2014, MNRAS, 445, 1482

[250] Sánchez C., et al., 2017, MNRAS, 465, 746

[251] Sawangwit U., Shanks T., Cannon R. D., Croom S. M., Ross N. P., Wake D. A., 2010, MNRAS, 402, 2228

[252] Schaan E., Ferraro S., Seljak U., 2020, arXiv e-prints, p. arXiv:2007.12795

[253] Schäfer J., Strimmer K., 2005, Statistical applications in genetics and molecular biology, 4

[254] Schlegel D. J., Finkbeiner D. P., Davis M., 1998, ApJ, 500, 525

[255] Schmidt S. J., et al., 2020, arXiv e-prints, p. arXiv:2001.03621

[256] Schneider P., 2006, Extragalactic Astronomy and Cosmology

[257] Schutz B. F., 1986, Nature, 323, 310

[258] Scoccimarro R., 2004, Phys. Rev. D, 70, 083007

[259] Scoccimarro R., Feldman H. A., Fry J. N., Frieman J. A., 2001, ApJ, 546, 652

[260] Scodeggio M., et al., 2018, A&A, 609, A84

[261] Seljak U., 1996, ApJ, 460, 549

[262] Semboloni E., Hoekstra H., Schaye J., van Daalen M. P., McCarthy I. G., 2011, MNRAS, 417, 2020

[263] Seo H.-J., et al., 2010, ApJ, 720, 1650

[264] Shaffer J., 1995, Annual Review of Psychology, 46, 561

[265] Sheth R. K., 1996, MNRAS, 279, 1310

[266] Sheth R. K., Tormen G., 1999, MNRAS, 308, 119

[267] Sheth R. K., Mo H. J., Tormen G., 2001a, MNRAS, 323, 1

[268] Sheth R. K., Hui L., Diaferio A., Scoccimarro R., 2001b, MNRAS, 325, 1288

[269] Sheth R. K., Diaferio A., Hui L., Scoccimarro R., 2001c, MNRAS, 326, 463

[270] Silk J., 1967, Nature, 215, 1155

[271] Simpson F., et al., 2013, MNRAS, 429, 2249

[272] Singh S., Mandelbaum R., Brownstein J. R., 2017, MNRAS, 464, 2120

[273] Singh S., Mandelbaum R., Seljak U., Rodríguez-Torres S., Slosar A., 2020, MNRAS, 491, 51

[274] Slepian Z., et al., 2015, arXiv e-prints, p. arXiv:1512.02231

[275] Slipher V. M., 1917, Proceedings of the American Philosophical Society, 56, 403

[276] Smith R. E., et al., 2003, MNRAS, 341, 1311

[277] Smith R. E., Hernández-Monteagudo C., Seljak U., 2009, Phys. Rev. D, 80, 063528

[278] Somerville R. S., Davé R., 2015, ARA&A, 53, 51

[279] Springel V., et al., 2017, Nature, 435, 629

[280] Stölzner B., Cuoco A., Lesgourgues J., Bilicki M., 2018, Phys. Rev. D, 97, 063506

[281] Suzuki N., et al., 2012, The Astrophysical Journal, 746, 85

[282] Takahashi R., Sato M., Nishimichi T., Taruya A., Oguri M., 2012, ApJ, 761, 152

[283] Taruya A., Nishimichi T., Saito S., 2010, Phys. Rev. D, 82, 063522

[284] Taylor A. N., Kitching T. D., 2010, MNRAS, 408, 865

[285] Taylor E. N., et al., 2011, MNRAS, 418, 1587

[286] Taylor E. N., et al., 2015, MNRAS, 446, 2144

[287] The Dark Energy Survey Collaboration 2005, arXiv e-prints, pp astro–ph/0510346

[288] Tinker J. L., 2007, MNRAS, 374, 477

[289] Tinker J. L., Robertson B. E., Kravtsov A. V., Klypin A., Warren M. S., Yepes G., Gottlöber S., 2010, ApJ, 724, 878

[290] Treyer M., et al., 2018, MNRAS, 477, 2684

[291] Troxel M. A., et al., 2018a, Phys. Rev. D, 98, 043528

[292] Troxel M. A., et al., 2018b, MNRAS, 479, 4998

[293] Tytler D., O'Meara J. M., Suzuki N., Lubin D., 2000, Physica Scripta Volume T, 85, 12

[294] Uhlemann C., Codis S., Pichon C., Bernardeau F., Reimberg P., 2016, MNRAS, 460, 1529

[295] Valageas P., 2009, A&A, 508, 93

[296] Vale A., Ostriker J. P., 2004, MNRAS, 353, 189

[297] Verde L., Wang L., Heavens A. F., Kamionkowski M., 2000, MNRAS, 313, 141

[298] Vielzeuf P., et al., 2021, MNRAS, 500, 464

[299] Wang L., Steinhardt P. J., 1998, ApJ, 508, 483

[300] Wechsler R. H., Tinker J. L., 2018, ARA&A, 56, 435

[301] Weinberg S., 2008, Cosmology, 1 edn. Oxford University Press

[302] White S. D. M., Rees M. J., 1978, MNRAS, 183, 341

[303] White M., Hernquist L., Springel V., 2001, ApJ, 550, L129

[304] Williams G. G., Olszewski E., Lesser M. P., Burge J. H., 2004, in Moorwood A. F. M., Iye M., eds, Society of Photo-Optical Instrumentation Engineers (SPIE) Conference Series Vol. 5492, Ground-based Instrumentation for Astronomy. pp 787–798, doi:10.1117/12.552189

[305] Wojtak R., Hansen S. H., Hjorth J., 2011, Nature, 477, 567

[306] Wong K. C., et al., 2020, MNRAS, 498, 1420

[307] Wright E., et al., 2010, AJ, 140, 1868

[308] Yang X., Mo H. J., van den Bosch F. C., Weinmann S. M., Li C., Jing Y. P., 2005, MNRAS, 362, 711

[309] Yang X., Mo H. J., van den Bosch F. C., 2008, ApJ, 676, 248

[310] Yoo J., Seljak U., 2015, MNRAS, 447, 1789

[311] Zehavi I., et al., 2011, ApJ, 736, 59

[312] Zehavi I., Contreras S., Padilla N., Smith N. J., Baugh C. M., Norberg P., 2018, ApJ, 853, 84

[313] Zhang G., Li Z., Liu J., Spergel D. N., Kreisch C. D., Pisani A., Wandelt B. D., 2020, Phys. Rev. D, 102, 083537

[314] Zhou R., et al., 2020, arXiv e-prints, p. arXiv:2001.06018

[315] Ziman J., 1972, Principles of the Theory of Solids. Cambridge University Press, https://books.google.co.uk/books?id=o4woMNO-C3sC

[316] Zou H., et al., 2017, PASP, 129, 064101

[317] Zu Y., Weinberg D. H., 2013, MNRAS, 431, 3319

[318] Zwicky F., 1933, Helvetica Physica Acta, 6, 110

[319] de la Torre S., Guzzo L., 2012, MNRAS, 427, 327

[320] eBOSS Collaboration et al., 2020, arXiv e-prints, p. arXiv:2007.08991

[321] van Daalen M. P., Schaye J., Booth C. M., Dalla Vecchia C., 2011, MNRAS, 415, 3649